Development of Novel Synthetic Methodologies for the Preparation of Multifunctional Ferrite-Reduced Graphene Oxide Nanocomposites and Study of Their Microwave Absorption and Catalytic Properties

THESIS

Submitted in partial fulfillment
of the requirements for the degree of
DOCTOR OF PHILOSOPHY

by

Debabrata Moitra

Under the Supervision of
Dr. Narendra Nath Ghosh

BITS Pilani
Pilani | Dubai | Goa | Hyderabad

BIRLA INSTITUTE OF TECHNOLOGY AND SCIENCE, PILANI

2018

BIRLA INSTITUTE OF TECHNOLOGY AND SCIENCE PILANI

(RAJASTHAN)

CERTIFICATE

This is to certify that the thesis entitled **"Development of Novel Synthetic Methodologies for the Preparation of Multifunctional Ferrite-Reduced Graphene Oxide Nanocomposites and Study of Their Microwave Absorption and Catalytic Properties"** and submitted by **Debabrata Moitra,** ID No. 2014PHXF0403G for award of Ph.D. Degree of the Institute, embodies original work done by him under my supervision.

Signature in full of the Supervisor: *Narendranath Ghosh*

Name in capital block letters: **Dr. NARENDRA NATH GHOSH**

Designation: Professor

Date: 30.8.2018

ABSTRACT

In this thesis, synthesis of three different multifunctional ferrite-Reduced Graphene Oxide (RGO) nanocomposites (e.g. $Ni_{0.8}Zn_{0.2}Fe_2O_4$-RGO, $CoFe_2O_4$-RGO, and $BiFeO_3$ nanowire-RGO) and their structural characterizations have been discussed. Two different methodologies were employed for the synthesis of these nanocomposites (i) an *'in situ'* co-precipitation reduction technique was developed to prepare $Ni_{0.8}Zn_{0.2}Fe_2O_4$-RGO (NZF-RGO) and $CoFe_2O_4$-RGO (CF-RGO) nanocomposites and (ii) a facile hydrothermal technique was employed to prepare $BiFeO_3$ nanowire-RGO (BFO RGO) nanocomposites.

The multifunctional performances of these nanocomposites have been demonstrated for two important applications (i) microwave absorption in X-band region, and (ii) magnetically separable catalyst for multiple reactions.

The microwave absorption properties of all these synthesized nanocomposites exhibited more than 99% minimum reflection loss (RL) in the X-band region (8.2-12.4 GHz). The minimum RL for 50NZF-50RGO, 85CF-15RGO, and 97BFO-3RGO were found to be -19.99 dB at 11.58 GHz, -31.31 dB at 9.05 GHz, and -28.68 dB at 10.68 GHz when the absorber thickness was 1.8 mm, 2.15 mm, and 1.55 mm respectively.

The catalytic activities of the synthesized nanocomposites have been investigated for the following reactions: (i) decolorization of various synthetic organic dyes (such as 4-nitrophenol, Methyl Orange, and Rhodamine B) and a herbicide (trifluralin) via reduction reaction with $NaBH_4$ in aqueous medium, (ii) photo degradation of Methyl orange, Methylene blue, Rhodamine B, and a mixture of dyes under visible light exposure, (iii) Biginelli reaction to synthesize dihydropyrimidinone derivatives in solvent less condition, (iv) Click reaction to synthesize triazoles, and (v) epoxidation of styrene. All of the synthesized nanocomposites exhibit high catalytic activities for reactions mentioned above. BFO-RGO exhibit versatile catalytic activity towards multiple reactions. Magnetic recovery of the magnetically separable catalysts and their reusability tests has also been performed. The recovered catalysts exhibit the retention of their catalytic efficiency for the consecutive reaction up to 5 catalytic cycles.

Declaration

This is to certify that the material embodied in the present work, entitled **"Development of Novel Synthetic Methodologies for the Preparation of Multifunctional Ferrite-Reduced Graphene Oxide Nanocomposites and Study of Their Microwave Absorption and Catalytic Properties"**, is based on my original research work. It has not been submitted, in part or full, for any other diploma or degree of any University/Institution Deemed to be University and College/Institution of National Importance. References from other works have been duly cited at the relevant places.

Signature of the Candidate: Debabrata Moitra

Name in capital block letters: **DEBABRATA MOITRA**

Date: 30/8/2018

Acknowledgements

I wish to express my sincere gratitude to my supervisor, Dr. N. N. Ghosh for his continuous support, motivation and encouragement throughout the duration of my research work. I am deeply indebted to him for his thoughtful guidance, patience, expertise and their invaluable suggestions.

I am extremely grateful to Prof. S. Bhattacharyya (Vice Chancellor, BITS, Pilani), Prof. G. Raghurama (Director, BITS, Pilani, K K Birla Goa Campus), Prof. S. K. Verma, (Dean, Academic Research (Ph. D. Programme), BITS, Pilani), Dr. P. K. Das (Associate Dean, Academic Research, BITS Pilani, K K Birla Goa Campus) and Prof. Sunil Bhand (Dean, Sponsored Research and Consulting, BITS Pilani) for providing me with the facilities to conduct my research work at BITS Pilani, K K Birla Goa Campus.

I am also thankful to Dr. Anjan Chattopadhyay, Head, Department of Chemistry for the facilities and the help provided as well as for his encouragement during my work. I extend my sincere thanks to Prof. A. P. Koley (Professor of Chemistry and Associate Dean, Instruction Division), my Doctoral Advisory Committee members Dr. Amrita Chatterjee (Associate Professor, Department of Chemistry) and Dr. Ram Shanker Patel (Assistant Professor, Department of Physics). I want to thank Dr. Mainak Banerjee, Dr. R. N. Behera, Dr. Anjan Chattopadhyay, Dr. P. Bhavana and Dr. N. N. Ghosh (Doctoral Research Committee of Department of Chemistry) for their valuable advice, motivation and their support at various phases of my work.

I am indebted to Prof. Paul A. Millner, Mr. Martin Fuller (University of Leeds, UK), Dr. S. R. Vadera, Dr. M. K. Patra (DRDO Lab, Jodhpur) for extending the experimental facilities in their lab.

I am grateful to my ex-research colleagues Dr. Shubhenjit Hazra, Dr. Dayananda Desagani, Dr. Barun Kumar Ghosh, for their help, motivation and valuable suggestions. I am also thankful to them for guiding me in instrumental analysis. I also thank my

fellow research scholars, Mr. Madhurya Chandel and Ms. Priyanka Makkar for helping me in various ways.

I am extremely thankful to all of my fellow research scholar colleagues from BITS Pilani, K K Birla Goa Campus. I will always be grateful to them for their support throughout my research work.

I am thankful to the Mr. Samyak Dhole and Mr. Chayan Anand undergraduate students, BITS Pilani, K K Birla Goa Campus, for their help during my research work.

I am thankful to Mrs. Princy Johnson and Mr. Digambar Waingankar, (Senior Lab Technician, Department of Chemistry) for their help and co-operation.

I also thank the non-teaching staff of BITS Pilani, K K Birla Goa Campus for their kind help.

It is now my turn to thank those people who stood by my side for completion of my thesis work. I would like to greatly acknowledge the constant motivating support I received from my parents, my family during the entire PhD journey. First of all, I am really grateful to my beloved parents, Mr. Satinath Moitra and Mrs. Gouri Moitra who took all the liabilities regarding all the family matters and gave me the encouragements to complete this thesis work. Without their immense love and support this dissertation would not have been possible. I am also thankful to my wife Dr. Manjima Moitra. I dedicate this dissertation to my entire family.

Debabrata Moitra

Table of Contents

2. Synthesis of $Ni_{0.8}Zn_{0.2}Fe_2O_4$-RGO: Excellent Microwave Absorber and Highly Efficient Magnetically Separable Recyclable catalyst for Dye Degradation

3. Synthesis of CoFe₂O₄-RGO: Excellent Microwave Absorber and Highly Efficient Magnetically Separable Recyclable Photocatalyst for Dye Degradation

4. Synthesis of BiFeO₃ nanowire-RGO: Excellent Microwave Absorber and Versatile, Magnetically Separable and Reusable Catalyst towards Multiple Organic Reactions

List of Tables

List of Figures

List of Schemes

List of Abbreviations and Symbols

Abbreviations/Symbols	Description
4-AP	4-Aminophenol
4-NP	4-Nitrophenol
Å	Angstrom
Ar	Argon
a.u.	arbitrary unit
BET	Brunauer, Emmett and Teller
CVD	Chemical vapor deposition
DMF	Dimethylformamide
DNA	Deoxyribonucleic acid
DRS	Diffuse reflectance spectra
DSC	Differential scanning calorimetry
dB	Decibel
EIS	Electrochemical Impedance measurements
EMI	Electromagnetic interference
EDS	Energy dispersive X-Ray spectra
ET	Electron transfer
FLG	Few-layer graphene
H_c	Coercivity
g	Grams
GO	Graphene Oxide
GHz	Gigahertz
h	Hours
$h\nu$	Photon energy
k_{app}	Apparent rate constant
L	Liter
MB	Methylene Blue
MO	Methyl Orange
min	Minute
mm	Millimetre
M_s	Saturation Magnetization

MHz	Megahertz
nm	Nanometer
NMR	Nuclear Magnetic Resonance
PEG	Polyethylene glycol
PVA	Polyvinyl alcohol
PVDF	Polyvinylidene difluoride
PET	Polyethylene terephthalate
RAMs	Radar Absorbing Materials
RAS	Radar Absorbing Structure
RGO	Reduced graphene oxide
RhB	Rhodamine B
RL	Reflection loss
SBA-15	Santa Barbara Amorphous-15
FESEM	Field Emission Scanning Electron Microscope
FT-IR	Fourier-transform infrared spectroscopy
TEM	Transmissions Electron Microscope
TBHP	tert-butyl hydroperoxide
TPa	Terapascal
UHV	Ultra-high vacuum
VSM	Vibrating Sample Magnetometer
XRD	X-ray diffraction
λ_{max}	Wavelength of maximum absorption
$\sigma(T)$	Temperature-dependent electrical conductivity
f	Frequency of the electromagnetic wave
d	Absorber thickness
c	Velocity of light
Z_0	Free space impedance
Z_{in}	Absorber impedance
μ_r	Relative complex permeability
ε_0	Permittivity of free space
ε_r	Relative complex permittivity
ε'	Real part of permittivity
μ'	Real part of permeability

Keywords

Chapter 1

Introduction

1.1 Scope of the work

(i)   Development of simple chemical methodologies to prepare Reduced Graphene Oxide-Ferrite nanoparticle-based nanocomposites

(ii)   Investigations on the microwave absorption property of the synthesized nanocomposites.

(iii)   Use of the synthesized nanocomposites as a magnetically separable catalyst for some important reactions.

1.2 Introduction

In this thesis, development of multifunctional Reduced Graphene Oxide-ferrite nanocomposites $(Ni_{0.8}Zn_{0.2}Fe_2O_4]_x$-$[RGO]_{1-x}$, $[CoFe_2O_4]_x$-$[RGO]_{1-x}$, $[BiFeO_3]_x$-$[RGO]_{1-x}$ where $(x = 0-1))$ has been described. The multifunctional performances of these nanocomposites have been demonstrated for two important applications (i) microwave absorption in X-band region (8.2-12.4 GHz), and (ii) magnetically separable catalyst for different reactions.

In the next section (1.2.1) detailed literature survey on the microwave absorption of materials has been discussed giving particular emphasis on graphene-based materials. Then in the following section (1.2.2) the importance of the reactions, which have been chosen in the present study, has been described.

1.2.1 Literature survey on Microwave absorption of materials

1.2.1.1 Microwave absorbers

Nowadays, with the rapid development of wireless communication and other electronic devices, electromagnetic interference (EMI) has become a concern for its potential adverse effects on living systems and the human body [1-6]. Overexposure to microwave radiation through the excessive use of mobile phones, personal computers, local area network, television, radar systems, etc. can cause a severe interruption in electronically controlled systems [7-9]. Moreover, it is suspected that microwave exposure might be harmful to the biological systems because it may increase the possibility of cancer,

weaken immune response, damage DNA in brain cells, increase heart beat rate, etc.[7,10-13]. Therefore, to overcome these EMI related problems, there is currently focused effort by scientists to develop efficient microwave absorbing materials which can absorb unwanted electromagnetic signals. Microwave absorbers with high efficiency and broadband absorption in X-band region (8.2-12.4 GHz) find potential applications in military applications, particularly in stealth technology [9,14,15]. In defense, the use of Radar Absorbing Materials (RAMs), which are capable of absorbing microwave radiation in the X-band region, is very much required to stealth an object by reducing its radar cross section (RAS). At present, the next generation radar stealth equipment demands novel RAMs with advanced features, namely, lightweight, thin layers, strong absorption and wide effective bandwidth. 'Light, thin, strong and wide' are the key features of new electromagnetic wave absorbing materials [16,17], which are in high demand.

1.2.1.2 Microwave absorption mechanism

Dielectric loss, magnetic loss, and impedance matching are the main factors which dictate the microwave absorption performance of a material [18-22]. In case of nonmagnetic materials, attenuation mechanism of the microwave absorber mainly proceeds via dielectric loss. Conduction loss and relaxation loss, which are governed by the conductivity, and polarization of the material, also play essential roles [18,23]. Intrinsic conduction and hopping conduction are responsible for the conductivity of the materials, and hopping conduction generally dominates the conductivity of the materials [24]. The polarization of the material generates from the presence of functional groups, defects, and the interface between different components of the material [18,25-27]. Interface polarization occurs at frequency region (< GHz), whereas other attenuation (originate from atomic, ionic, and electron polarization) occurs at high frequency [28-30]. Conduction losses mainly dominate in metallic, high conductive materials, whereas dipolar losses dominate in dielectric insulators.

In case of magnetic materials along with conduction losses, magnetic losses (e.g., hysteresis, domain wall resonance, and electron spin resonance) also play important roles [3,31-34].

To evaluate the microwave absorption properties of the materials the complex permittivity (ε' and ε'' stand for real and imaginary permittivity, respectively) and permeability (μ' and μ'' stand for real and imaginary permeability respectively) of the samples are generally measured [7,11,35,36].

The complex permittivity and dielectric tangent loss ($\tan \delta_e$) can be expressed as equation 1.1 and 1.2 [35, 37-40].

$$\varepsilon = \varepsilon_0 \left(\varepsilon' - i\varepsilon''\right) \qquad (1.1)$$

$$\tan \delta_e = \frac{\varepsilon''}{\varepsilon'} = \frac{\sigma}{2\pi f \varepsilon_0 \varepsilon'} \qquad (1.2)$$

where the permittivity of free space ($\varepsilon_0 = 8.86 \times 10^{-12}$ F/m) in a vacuum [41], the real part ε' is the relative dielectric constant, and the imaginary part ε'' is the effective relative dielectric loss factor.

According to the free electron theory [1,3,23,35,42-44], ε'' can be expressed as:

$$\varepsilon'' \approx \sigma(T)/2\pi\varepsilon_0 f \qquad (1.3)$$

where $\sigma(T)$ is temperature-dependent electrical conductivity caused by ionic conduction and displacement current, f is frequency, and ε_0 is the dielectric constant in a vacuum. Equation 1.3 shows that $\sigma(T)$ plays an essential role in measuring dielectric loss parameter ε''.

Polarization loss also contributes to the dielectric loss in addition to the conduction loss in a nonmagnetic material. According to Debye dipolar relaxation theory [1-3,35,45-47], the relative complex permittivity ε_r can be expressed as equation 1.4:

$$\varepsilon_r = \varepsilon' + i\,\varepsilon'' = \varepsilon_\infty + \frac{\varepsilon_s - \varepsilon_\infty}{1 + i2\pi f \tau_0} \qquad (1.4)$$

$$\varepsilon' = \varepsilon_\infty + \frac{\varepsilon_s - \varepsilon_\infty}{1 + (i2\pi f \tau_0)^2} \qquad (1.5)$$

$$\varepsilon'' = \frac{2\pi f \tau_0 (\varepsilon_s - \varepsilon_\infty)}{1 + (2\pi f \tau_0)^2} + \frac{\sigma(T)}{2\pi f \epsilon_0} \qquad (1.6)$$

Equations (1.5) and (1.6) can be deduced from equation (1.4). From equation (1.5) and (1.6), the relationship between ε' and ε'' can be expressed as

$$(\varepsilon' - \frac{\varepsilon_s + \varepsilon_\infty}{2})^2 + (\varepsilon'')^2 = (\frac{\varepsilon_s - \varepsilon_\infty}{2})^2 \qquad (1.7)$$

Here, f is frequency, ε_s and ε_∞ are the stationary permittivities and optical dielectric constant at high-frequency limit respectively, σ is electrical conductivity, τ_0 is polarization relaxation time, which is relevant to temperature. τ_0 can be written as: [23,42,48,49]

$$\tau_0 = \frac{1}{2v} e^{U/kT} \qquad (1.8)$$

where U is the activation energy, k is constant, v is the lattice vibration frequency, and T is the temperature.

According to Cao et al. with the increase in temperature, the relaxation time becomes shorter [27,42]. Hence, ε′ increases due to the enhancement of electron polarization at elevated temperature. However, the degree of dipole orientation also increases with increasing temperature, so ε″ also increases. But, the energy which is required to overcome the frequency during the orientation of the dipole decreases with rising temperature [27]. This factor leads to decrease the value of ε″. Therefore, temperature plays a crucial role in determining the dielectric loss of the absorbing material.

Debye dipolar relaxation of microwave absorbers can be determined from the Cole-Cole semicircle plots of ε' versus ε'', where each semicircle represents one Debye relaxation process [35]. The presence of more than one semicircle for each sample suggests the existence of multiple Debye dipolar relaxation process [3]. Under alternating electromagnetic radiation, the lags of induced charges originating from composite interfaces, which meet the externally applied field, lead to the relaxation and transform the electromagnetic energy in to thermal energy [2,3]. During this relaxation process, the EM wave attenuates to a certain degree. Meanwhile, the Maxwell−Wagner−Siller polarization also contributes towards the consumption of EM waves [1,50]. This phenomenon mostly appears in the heterogeneous media, as the accumulation of virtual charge occurs at the interfaces, and the large dipoles form on particles or clusters [1- 3,45,50,51]. This polarization depends on the conductivity and permittivity of the constituents of the composites.

The values of relative complex permeability for magnetic microwave absorbing material can be expressed as [28,35,52]

$$\mu_r = \mu' - j\mu''. \tag{1.9}$$

The magnetic tangent loss (tan δ_μ) can be determined from equation (1.10) [35]

$$\tan \delta_\mu = \frac{\mu''}{\mu'} \tag{1.10}$$

Theoretically, the magnetic loss of magnetic materials is related to hysteresis loss, domain wall resonance, exchange resonance, eddy current loss, and natural resonance [3,31-35,53,54]. However, hysteresis loss can be neglected when a weak field is applied [3,35]. As the domain wall contribution towards magnetic loss usually occurs in the megahertz frequency range its contribution can also be neglected in the present case (8-12 GHz) [3,55]. Exchange resonance also makes a very little contribution to magnetic loss in the high-frequency range 8-12 GHz [56]. Therefore, the contributing factors which should be considered for magnetic loss in the present case are eddy current loss and natural resonance in the microwave frequency band [57,58]. The effect of eddy current loss can be estimated using the following equation: [1-3,35,47,59]

$$\mu'' \approx 2\pi \, \mu_0 \, (\mu')^2 \, \sigma \, d^2 f / 3 \tag{1.11}$$
$$C_0 = \mu'' \, (\mu')^{-2} f^{-1} = 2\pi \, \mu_0 \, d^2 \sigma \tag{1.12}$$

where C_0 is eddy current coefficient, μ_0 is permeability in vacuum, d is the thickness of the absorber and σ is electrical conductivity of the composite. When the value of $\mu'' \, (\mu')^{-2} f^{-1}$ does not change with increasing frequency then it can be assumed that the eddy current loss is contributing towards magnetic loss [1,3,35,59]. Another important factor which contributes to the magnetic loss is the natural resonance and can be described by natural resonance equation (equation 1.13): [1,35,59,60]

$$2\pi f_r = \gamma H_a \tag{1.13}$$
$$H_a = 4|K_1|/3\mu_0 M_s \tag{1.14}$$
$$K_1 = \mu_0 M_s H_c / 2 \tag{1.15}$$

where H_a is anisotropy energy, γ is gyromagnetic ratio, $|K_1|$ is anisotropy coefficient, μ_0 stands for permeability in free space ($4\pi \times 10^{-7}$ Hm^{-1}), H_c is coercivity, M_s is saturation magnetization and f_r is the resonance frequency.

1.2.1.3 Graphene as microwave absorber

Over the last few years, graphene has attracted immense attention to the scientists and technologists. Several researchers are exploring the possibility of application of graphene as microwave absorber due to its exceptional structural properties, namely high mechanical flexibility [4,8,39,45,60,61], low density, a 2-dimensional honeycomb structure with sp^2 hybridized C-atom [61-64], an unusual electronic structure near the Fermi level [39,65]. Graphene shows (i) weak skin effect due to its ultrathin thickness (single layer graphene), (ii) excellent optical transmittance, (iii) resonance effect due to its layered structure and high surface area (2675 m^2/g), (iv) strong mechanical strength (~1 TPa) and large aspect ratios, which are also beneficial for microwave absorption, (v) interfacial polarization due to the large interface, (vi) remarkable conduction loss due to excellent electrical conductivity and the high dielectric constant, (vi) enhanced polarization loss due to the presence of defects [18,66-69]. In view of these factors, it was expected that graphene could act as a good microwave absorbing material.

1.2.1.4 Preparation of graphene and graphene-based materials

In 2004, Andre Geim and Konstantin Novoselov demonstrated that monolayer graphene sheets can be obtained by cleaving a graphite crystal with an adhesive tape [70]. However, the graphene sheets, obtained by this process, are usually several microns in size with irregular shapes, and their azimuthal orientation is difficult to control [71]. Furthermore, when graphene is prepared in large scale using this method, its electronic transport property somehow deteriorates [71-73]. Hence this synthesized graphene lacks its quality of technological and commercial applications.

For the large-scale synthesis of graphene, physical methods (such as chemical vapor deposition (CVD)) or chemical methods, (e.g., Hummer's approach), are generally utilized [68,72-79].

1.2.1.4.1 Synthesis of graphene by CVD method

In this method, the growth of graphene occurs when a carbon-containing gas (such as CH_4) is exposed to the transition metal surface (such as Ni, Cu, etc.) at a high temperature. CVD method is generally used for the production of graphene films having a large area and low defect concentration [71,80]. Reina et al. [81] have prepared continuous graphene films having lateral size up to ~20 μm by using an ambient pressure CVD on polycrystalline Ni. The graphene thus produced contained 1-12 layers [81]. Wu et al. have reported the synthesis of few layers of graphene by a simple thermal CVD approach. Here, first 500-nm-thick Cu was magnetron sputtered onto the 200 nm thermally oxidized Si <100> 4-inch wafers. Then, the wafer was annealed at 850 °C for 30 min in a mixture of H_2 and Ar atmosphere. Then the growth of graphene was initiated by introducing CH_4 [73]. One of the major advantages of using CVD method for graphene synthesis is that the graphene produced by this method possess with less structural and electronic disorder or defects. The graphene prepared by CVD approach usually shows very high conductivity (5.25×10^6 S m^{-1}, 5.64×10^6 S m^{-1}, and 5.92×10^6 S m^{-1} for monolayer, double layer, and triple layer graphene, respectively) [82]. However, CVD method needs expensive substrate materials and infrastructure, which limits its applications for large-scale production.

1.2.1.4.2 Synthesis of Graphene oxide (GO) and Reduced Graphene oxide (RGO) by chemical methods

After the discovery of graphene, some of its derivatives, such as graphene oxide (GO) and reduced graphene oxides (RGO) have also attracted the attention of researchers. One of the most popular methods of GO preparation is Hummers' method [83]. In this process, graphite powder is oxidized chemically by a mixture of potassium permanganate ($KMnO_4$) and concentrated sulfuric acid (H_2SO_4). Though permanganate is used as an oxidant in this process, however, the main active species is dia manganese heptoxide.

$$KMnO_4 + 3\,H_2SO_4 \longrightarrow K^+ + MnO_3^+ + H_3O^+ + 3HSO_4^-$$

$$MnO_3^+ + MnO_4^- \longrightarrow Mn_2O_7$$
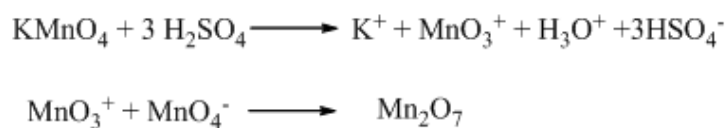
Scheme 1 Formation of dimanganese-heptoxide (Mn_2O_7) from $KMnO_4$ in the presence of strong acid

The reaction between potassium permanganate and sulfuric acid forms a dark red oil, which is diamanganese heptoxide. This bimetallic heptoxide is far more reactive than its monometallic tetraoxide counterpart. It detonates expanded graphite when comes in contact at a temperature higher than 55 °C [84,85]. This oxidation process of graphene leads to form Graphene Oxide (GO) [86]. GO contains many chemically reactive oxygen functionalities, (e.g., carboxylic acid groups at the edges and epoxy and hydroxyl groups on the basal plane) [39]. Due to the presence of the functional groups and defects, the sp^2 bonding network in GO disrupts, and the number of free electrons decreases. This results in the poor conducting ability of GO in comparison with pure Graphene [39,86,87].

RGO is generally prepared by removing oxygen-containing functional groups of GO by employing a reduction process [88]. Different reductions processes have been explored to convert GO to RGO. Depending upon the reduction processes the synthesized RGO possess different amount and type of residual functional groups, which in turn affect the performance of the material [89]. For the chemical reduction of GO, hydrazine monohydrate or dimethylhydrazine has been extensively used [68,75,90]. Stankovich et al. have successfully reduced GO (synthesized by Hummers method) by using a chemical reduction method. In the typical process, GO was first dispersed in water and then refluxed in the presence of Hydrazine hydrate at 100 °C for 24 h. This produced a solid black precipitate of RGO [68]. Wang et al. have reported the synthesis of RGO by reducing GO in the presence of hydrazine and ammonia solution at 95 °C for 1h [91]. However, reduction of GO with hydrazine some time also introduces heteroatom impurities, such as N_2 which form amines, hydrazones or other similar functional groups [92]. Therefore, some other reducing agent, such as $NaBH_4$, was found more effective in reducing GO. $NaBH_4$ was more effective in reducing C=O groups but showed moderate efficiency in the reduction of epoxide and carboxylic acid [93]. Shin et al. have reported the reduction of GO film, which was prepared by spray technique on a polyethylene terephthalate (PET) substrate. This, GO films, was reduced by dipping it in an aqueous $NaBH_4$ solution [92]. Other reductants, which were used for the chemical transformation of GO to RGO are hydroquinone [94], gaseous H_2 [95], Alkaline solution [96,97], ascorbic acid [98], etc. Apart from using chemical reagents for reduction of GO, some other reduction techniques were also used to synthesize RGO from GO. Hun et al. have reported the effect of microwave irradiation technique for reduction of graphene oxide films. Here, few-layer graphene (FLG) sheets were prepared by using the electrochemical

exfoliated method. The reduction process was carried out with a microwave power as low as 42 W at below 250 °C in air [99]. Zhou et al. have reported an electrochemical reduction method for the synthesis of RGO. In this method, graphene oxide slurry was first obtained by the modified Hummers method. GO films were fabricated on substrate surfaces by spray coating. After that, linear sweep voltammetry was performed to GO films on quartz in sodium phosphate buffer solution to produce electro-reduce graphene oxide films [100]. McAllister et al. have reported a thermal expansion technique to produce functionalized graphene sheets. In this method, GO was prepared according to the Staudenmaier method. The GO slurry was then spray-dried. Thermal exfoliation of GO was achieved by heating it at 1050 °C in Ar atmosphere for 30s [74]. Wang et al. have reported a solvothermal method for the synthesis of RGO. In this technique, GO was first prepared by a modified Hummers method. Then GO was dispersed in DMF and kept under a solvothermal condition in the presence of hydrazine at 180 °C to reduce Graphene Oxide [101]. The reduction process helps to restore the structure of pristine graphene to a large extent in the structure of RGO. Therefore, RGO exhibits better electrical conductivity than that of GO [88].

1.2.1.5 Microwave absorption property of Graphene, GO, and RGO

As graphene posses several excellent structural properties (in terms of mechanical, electrical, and chemical), its use as microwave absorber has been explored by several researchers [15,88,102]. Wu et al. have reported -9.2 dB at 13.4 GHz of reflection loss value for few layers of graphene prepared by CVD method [73]. The microwave absorption of pristine graphene is limited by its high conductivity and poor dispersion ability in the matrix. The high electrical conductivity of pristine graphene is a major weakness towards its microwave absorption ability. Its electromagnetic parameters are too high to meet the requirements of impedance match which leads to intense reflection and weak absorption [39]. Therefore, to improve the microwave absorption ability of graphene, the strategy taken by some researchers is to decrease the conductivity of graphene by introducing functional groups (e.g., C=O, COOH) in its structure, which can destroy some of its hexagonal rings [29]. The introduction of defects and functional groups by controlled oxidation and reduction process helps to widen the band gap of graphene [39,86,87]. The opening of the band gap in graphene can allow the separation of electron and hole [103]. This leads to a new electron conduction phenomenon. The

presence of defects can improve not only the impedance match characteristic but also introduces defects polarization relaxation, and electronic dipole relaxation which are critical for its potential use as RAMS [103]. Wang et al. had reported an improvement of RL_{min} value when GO was converted to RGO. The RL_{min} value of reduced RGO was -7.0 dB, while graphite under the same condition showed below -1.0 dB [91]. However, the RL min values of RGO was still less than the minimum expected value of a microwave absorber, which is -10 dB (called as effective reflection loss value, corresponding to 90% of absorption and attenuation). The microwave absorption properties of pristine graphene, GO, and RGO is listed in Table 1.1.

Table 1.1: Microwave absorption of GO and RGO synthesized by various methods.

Sample	Preparation method	Minimum RL (dB)	Absorber thickness (mm)	Corresponding frequency (GHz)	Reference
a) Compressed Graphene foam b) Graphene foam	GO dispersed in ethanol solution was solvothermally treated at 180 °C for 12h to form an ethanol-filled intermediate. Then freeze dried and annealed at 600 ºC for 1h in an argon atmosphere.	a) -35.51 b) -30.50	a) 0.9 -1 b) 9-10	2-18, 26.5-40, and 75-110	[15]
Graphene	CVD method at 850 ºC for 30 min	-9.2	5 layer	13.4	[73]

RGO	Reducing GO with hydrazine to prepare r-GO.	-7	2	6.5	[91]
GO	Improved Hummers' Method (KMnO$_4$ and H$_2$SO$_4$/H$_3$PO$_4$ mixture).	a) -28.5 b) -8	a) 5 b) 1.5	a) 2.6 b) 10.5	[104]
RGO	RGO was prepared by reduction of GO with mixed gas of hydrogenand argon at 450 ºC for 1h.	-10	2	16	[105]
RGO	Reducing GO with hydrazine.	-6.11	2	6.1	[106]
RGO	Solvothermal at 200 ºC for 8h in the presence of ethylene glycol.	-8.0	4	2.4	[107]
Ultrathin lightweight graphene	Ultrathin graphene was produced by the solution based reduction of graphene oxide with hydriodic acid and acetic acid, and then freeze-dried .	-42	2.1	12.4	[108]

Therefore, the microwave absorption properties of CVD graphene, as well as GO and RGO, which were prepared by chemical oxidation /reduction methods, are still far from

the practical application. Moreover, low stability of GO or RGO at high temperature also restrict their potential use as a microwave absorber [39,65,86,87]. Therefore, different strategies are adopted by several researchers to achieve good microwave absorption of graphene-based absorbers, such as (i) incorporation of a conducting materials in GO, so that the lower dielectric GO, and relatively higher permittivity value of the conductive material can lead to a moderate permittivity value, (ii) incorporation of poor conducting materials in RGO to achieve moderate permittivity value [29].

Several types graphene-based composites have been explored by the researchers. Some of the graphene (or RGO) based composites are graphene-polymer composites, graphene-ceramic composites, graphene-based carbon material, graphene-magnetic metal nanocomposites, graphene-ferrite composites, etc. [18]. Development of graphene-based microwave absorbing materials has been reviewed by Meng et al. [103], Li et al. [18], and Lv et al. [29]. In this review articles significance of graphene composites as microwave absorber, their synthesis and microwave absorption mechanisms have been discussed in details and up to date details references are cited therein. However, the quest for new graphene-based high performing microwave absorber is still on.

As ferrites offer several advantages towards microwave absorption which are discussed in section (1.2.1.6) therefore, present study mainly focuses the use of graphene-ferrite nanocomposites as microwave absorber.

1.2.1.6. Ferrites as microwave absorber

For the last few years, ferrites, which are one of the most important members of the magnetic materials family, have been widely investigated as microwave absorber [60,109-112]. Magnetic materials can exhibit their potential to be used as microwave absorber, because of their better impedance matching property than dielectric materials [56]. Ferrites offer improved complex permeability parameters (μ_r). A higher μ_r value results in a larger impedance matching value [56].

Ferrites are generally classified as (i) spinel ferrite (e.g., $NiFe_2O_4$, $CoFe_2O_4$, etc.), (ii) hexagonal ferrite ($BaFe_{12}O_{19}$, $SrFe_{12}O_{19}$, etc.), and (iii) Garnet ferrite ($Yb_3Fe_2(FeO_4)_3$, etc.) [18, 113, 114]. Their microwave absorption property is mainly associated with their

ferromagnetic resonance [59,115-121]. Several other loss mechanisms, such as eddy current loss, hysteresis loss, residual loss, intragranular and domain wall loss are also contributed to the microwave absorption properties [35,50,59,122]. In case of soft ferrite with inverse spinel structure (e.g., $NiFe_2O_4$), the ferromagnetism originates from the magnetic moment of antiparallel spins between Fe^{3+} ions (tetrahedral sites) and Ni^{2+} ions (octahedral sites). As these materials possess high saturation magnetization and Snoek's limit, large coercivity, they exhibit high complex permeability over a wide frequency range [112]. Soft ferrites show microwave absorption generally in the megahertz range, and hexaferrites are in the gigahertz range [123-126]. Microwave absorption properties of some of the ferrite nanoparticles are listed in Table 1.2

Table 1.2: Microwave absorption properties of various ferrites based composites and their synthesis methods

Samples	Preparation Method	Minimum Reflection loss (dB)	Corresponding Frequency (GHz)	Absorber thickness (mm)	Effective band width (RL<-10dB) (GHz)	References
60 wt % $ZnO/CoFe_2O_4$	Co-recipitation method 90 °C for 2h	-28.3	8.6	-	4.1 to 13	[9]
$NiFe_2O_4$	Hydrothermal at 180 °C for 6h	-24	9.5	3.5	8.5 to 13	[10]
$Ni_{0.8}Zn_{0.2}Fe_2O_4$	Co-precipitation method at 120 °C for 12h	-13.61	10.72	1.9	9.8 to 12	[11]
$CoFe_2O_4$	Co-precipitation method 120 °C for 12h	-55	9.25	2	8.2 to 10.8	[52]

$CoFe_2O_4$ nanorod	Hydrothermal at 150 °C for 15h.	-14.9	7.8	2.0	6.9 to 8.5	[62]
$CoFe_2O_4$ hollow	Hydrothermal at 160 °C for 24h followed by calcination 550 °C for 0.5h under argon atmosphere.	-11.7	7.2	2.0	6.7 to 8	[63]
$(Mn_{0.2}Ni_{0.4}Zn_{0.4}Fe_2O_4)_x$ $-(BaFe_{12}O_{19})_{1-x}$	One-pot precursor based method 800 °C for 4h.	-25	8.2	3.5	-	[109]
Ni Zn ferrite	Calcined at 1200 °C for 2h	-16	10.6	2	-	[127]
$(Ni_{0.4}Co_{0.2}Zn_{0.4})Fe_2O_4$	Sintered at 1250 °C for 2h.	-17.01	6.1	3	-	[128]
Ag core shell $Ni_{0.5}Zn_{0.5}Fe_2O_4$	Hydrothermal at 180 °C for 3h.	-25	9.0	1-2	-	[129]
Rugby Shaped $CoFe_2O_4$	Hydrothermal at 160 °C for 30h followed by calcinations at 550°C for 3h.	-34.1	13.4	2.5	2.6	[130]
$Ni_{0.5}Co_{0.5}Fe_2O_4$	Co-precipitation at 85 °C.	-18	2.47	1.5	-	[131]
$(NiFe_2O_4)_{0.85}-$ $(SrFe12O19)_{0.15}$	One pot precursor based method 800 °C for 4h	-17	8.2	3.2	-	[132]

$(Ni_{0.65}Zn_{0.35}Fe_2O_4)_{0.85}$-$(BaFe_{12}O_{19})_{0.15}$	One pot precursor based method 800 °C for 4h	-21	9.86	3.05	-	[133]
$Co_{0.6}Zn_{0.4}Fe_2O_4$ nanofiber.	Calcination at 700 °C for 2h	-16	10.6	2.9	7.8 to 16.8	[134]

As magnetic loss mechanism is mainly responsible for the microwave absorption property of ferrites, they are incapable of producing a significant amount of dielectric loss and magnetic loss simultaneously [7,56,109,132,134-137]. This factor limits their capability of microwave absorption over broadband. Moreover, the requirements of high weight ratios of ferrite powders (~60-80 %) in the microwave absorbing coating and higher thickness are major limitations of usage of pure ferrites as lightweight microwave absorber [7,134,138].

To overcome this limitation, combining magnetic nanoparticles with graphene to form a composite material is an attractive strategy [18,29,35]. As the loss mechanism of graphene is mainly based on dielectric loss, its microwave absorption properties are insufficient for wide range application [1,8,39]. Therefore, through the introduction of magnetic materials (e.g., ferrite nanoparticles) the microwave absorption property of graphene can be improved significantly. Recently, several graphene-ferrite nanocomposites have been explored to develop high performing microwave absorbers. Microwave absorption properties of some of the ferrite-graphene nanocomposites and their synthesis methods are listed in Table 1.3.

Table 1.3: Microwave absorption properties of various ferrites-graphene based composites and their synthesis methods

Samples	Preparation Method	Minimum Reflection loss (dB)	Corresponding Frequency (GHz)	Absorber thickness (mm)	Effective bandwidth (RL< -10dB) (GHz)	References
Fe_3O_4/graphene capsules (GCs)	Hydrothermal at 200 °C for 24h.	-32	8.76	3.5	5.4 to 17	[1]
$NiFe_2O_4$/r-GO	Hydrothermal at 180 °C for 24h.	-42	6.5	5	5.3	[2]
Co-doped NiZn ferrite/graphene nanocomposites	Hydrothermal at 180 °C for12h.	-53.5	9.6	3.1	4.8	[3]
$ZnFe_2O_4$/RGO	Hydrothermal at 180 °C for12h.	-29.3	16.7	1.6	2.6	[4]
85CF-15RGO	Co-precipitation reduction at 160 °C at 16h.	-31.13	9.05	2.15	2.72	[7]
$50N_{0.8}Z_{0.2}Fe_2O_4$-50RGO nanocomposite	Co-precipitation reduction at 120 °C at 12h.	-19.99	11.58	1.8	10.22-12.4	[11]
BFO-RGO	Hydrothermal at 140 °C for 24h.	-28.68	10.68	1.55	2.1	[35]
5 wt. % filler RGO/ $MnFe_2O_4$/PVDF	Hydrothermal at 140 °C for 12h.	-29	9.2 z	3	8-12.88	[59]
RGO/ Fe_3O_4	Co-precipitation at 80 °C for 2h.	-44.6	6.6 G	3.9	4.3	[60]

Graphene-Fe$_3$O$_4$	Heated at 200 °C for 24h.	-20	16	5		[61]
CoFe$_2$O$_4$ nanorod/ Graphene	Hydrothermal at 150 °C for 15h.	-25.8	16.1	2.0	4.5	[62]
CoFe$_2$O$_4$ hollow/ Graphene	Hydrothermal at 160 °C for 24h followed by calcination 550 °C for 0.5h under argon atmosphere.	-18.5	12.9	2	3.7	[63]
BaFe$_{12}$O$_{19}$@RGO	Calcination at 900 °C for 2h.	-32		3		[64]
RGO/ Fe$_3$O$_4$	Solvothermal method 200 ºC for 8h	-26.4	5.3	4.0	2.8	[107]
30 wt.% hollow Fe$_3$O$_4$/RGO	Solvothermal method 200 °C for 12h.	-24	12.9	2.0	4.9	[126]
Fe$_3$O$_4$-Fe/G composite	Calcination at 420 °C for 3h	-30	4.72	2.0	6.2	[139]
Graphene/Fe$_3$O$_4$	Hydrothermal route 220 ºC for 72h	-40.36	7.04	5.0	9.5	[140]
(RGO)/CoFe$_2$O$_4$ composite	Hydrothermal route at 180 °C for 10h	-47.9	12.4	2.3	5.6	[141]
NiFe$_2$O$_4$ nanorod -graphene	Solvothermal 150 °C for 15h.	-29.2	16.1	2.0	13.6-18	[142]
10 wt. % filler RGO/Co$_3$O$_4$/ PVDF	Hydrothermal at 140 °C for 12h.	-25	11.6	4	7.5-12	[143]

1.2.2 Literature survey on graphene-based catalysts

1.2.2.1 Graphene ferrite based nanocomposites as catalyst

It is a well-known fact that nanoparticles exhibit high catalytic activities owing to their high surface area [144,145]. However, nanoparticles also suffer from some limitations, such as (i) tendency of agglomeration of nanoparticles sometimes caused the reduction of their catalytic efficiency and (ii) difficulty in recovering the nanocatalyst for recycling as well as purification of the products [11,144,146]. These factors limit the large-scale practical applications of nanocatalyst. To overcome these limitations, immobilization of catalytically active nanoparticles on the surface of a support matrix is an attractive approach. Graphene (or RGO) is a promising candidate as catalyst support because of the following reasons (i) graphene (RGO) provides high surface area to immobilize catalytically active nanoparticles, (ii) the functional groups, which are present on RGO surface, helps to anchor the nanoparticles, (iii) immobilization of nanoparticles prevents their agglomeration. (iv) The high surface area of graphene/ RGO helps to absorb reactant molecules on the surface of the catalyst, catalytically active centers become more accessible to the reactant molecules, (v) the high conducting nature of graphene/RGO helps faster reactions. (vi) Graphene provides mechanically strong but flexible support [7,11,144,147-155].

In addition to the above-mentioned advantages, RGO-ferrite based catalysts also offer an important advantage. Due to the magnetic nature of RGO-ferrite nanocomposites, they can easily be separable from the reaction mixture after completion of the reaction. This easy magnetic recovery feature of RGO-ferrite nanocomposites makes them attractive catalysts for various reactions [155-173]. The application of the graphene-based nanocomposites as catalysts has been discussed in details with updated referencing in the review articles written by Hu et al. [174], and Zhang et al. [175].

In the presents study the following catalysis reactions were investigated where different RGO-ferrite nanocomposites were used as a catalyst: (i) decolorization of synthetic organic dyes, (ii) Styrene Epoxidation, (iii) Synthesis of Triazoles by 'click reaction' and (iv) Synthesis of dihydropyrimidinone derivatives by Biginelli reaction. A brief discussion about the importance of these reactions is given below

1.2.2 2 Degradation of dyes in water

Several industries, such as dyestuff, textile, paper, plastic, rubber, leather, printing, cosmetics, food processing, pharmaceuticals, etc., use varieties of dyes to color their products[176-178]. Worldwide over 10,000 different dyes are used in various industries and $\sim 7 \times 10^5$ tons of dyes are produced annually [179-182]. However, the degree of fixation of dyes to the products (e.g., fabrics) is not always complete, and as a result, these industries discharge dye containing effluents in the environment particularly onto the soil and aquatic systems. It has been estimated that ~ 2-50 % of dyes are lost in the effluent during dyeing process depending upon the nature of the dye and process employed for dyeing [183, 184]. Water pollution due to the discharge of colored effluents from industries is one of the major environmental concerns. Strong color of dyes and pigments to the receiving aquatic ecosystem possesses serious esthetic and ecological problems, such as inhibition of benthic photosynthesis [185]. Moreover, some of these dyes are toxic and carcinogenic in nature [186]. Thus, a synthetic dye containing effluents pose a direct long-term threat to amphibians and aquatic lives. This eventually threatens the lives of the earth including human beings because of their heavy reliance on water and aquatic products for survival [177]. One of the important characteristics of the synthetic dyes is that they are resistant to decolorize by different physical, chemical and biological agents. Therefore, they generally do not degrade or decolorize in conventional wastewater treatment processes. Hence, there is an urgent need for the development of efficient treatment methods for waste effluents of textile and dye-based industries.

Varieties of physical, chemical and biological techniques have been adopted to treat dye containing effluents [183,187-189]. Physical processes include adsorption method, coagulation-flocculation technique, membrane filtration, ion-exchange technique, etc. [183,187,188,190-192]. Most of the physical processes, which are conventionally used to treat dye containing wastewater, suffer from several limitations. For example, adsorption process is a slow process and is not very effective for the highly colored wastewater. In case of membrane separation process, apart from the slow separation rate, the special requirement of filtration, ultra-high vacuum (UHV) conditions, frequent clogging of membrane pores by organic pollutants make this process limited use for the dye effluent treatment. Generation of huge amount of sludge is the main disadvantage of coagulation-

flocculation based methods. Another problem of physical treatment techniques is that in most of the time complete degradation of dyes is not possible. Biodegradation is not an efficient method for the dyes having complex aromatic structure. Use of pure cultures (algal, fungal and bacterial) is not very effective for wastewater containing various types of dyes, because most of the isolated cultures are dye specific [185,186,193]. Hence, use of these methods on a large scale is impracticable.

For the last few years, the catalytic reduction of water-soluble dyes over heterogeneous catalysts has gained immense attention as an alternative route to the physical methods for treatment of dye containing wastewater, because it offers high efficiency [176]. Several authors have reported various metal nanoparticle based catalysts for the reduction of various dye molecules to their colorless forms [194-206]. Reduction reactions of synthetic dyes (such as Methyl Orange, Congo Red, Methylene Blue, Rhodamine B, etc.) and aromatic nitro compounds (e.g., 4- nitrophenol) by catalysts have been widely reported as model reactions to evaluate the catalytic efficiency of the synthesized catalysts [207-211].

1.2.2 3 Styrene Epoxidation

Over the last few years olefin epoxidation has gained immense interest due to a wide range of applications of epoxide, such as useful and versatile intermediate for the synthesis of many pharmaceutical products, fine chemicals, commodities, etc. [212-215]. The epoxidation of styrene can be presented by the chemical following equation:
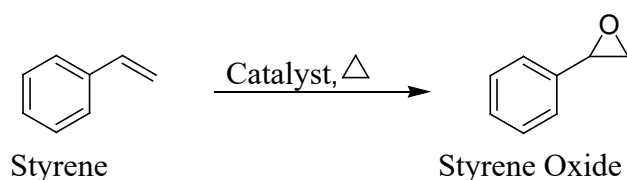
Epoxidation of olefins is one of the main routes for the production of epoxides [214]. However, epoxidation of styrene is very difficult because of the presence of the olefinic group in the terminal position [216]. Some of the limitations associated with the conventional epoxidation processes (such as non-catalytic process using chlorine, co-epoxidation process, organic peroxide and peracid-based catalytic process, etc.) are (i) most of these processes are not environment friendly, (ii) capital-intensive, (iii)

production of large amount of chloride-laden sewage in chlorine-based processes, (iv) peracids are corrosive and also generate large amount of by-products and waste products, (v) separation problem for homogeneous catalysts [147,148,215,217-224]. Hence, there is enormous interest in developing novel heterogeneous catalysts for epoxidation reactions.

Commonly Titanium silicate molecular sieves (e.g., TS-1 (Ti-MFI), TS-2 (Ti-MEL), etc.) are used widely as a catalyst for epoxidation of olefinic compounds with H_2O_2. However, several challenges, such as sometimes poor selectivity (5-10% for styrene oxide), higher production cost, relative difficulty in separation, leaching of Ti under harsh reaction conditions still exist [217]. Therefore, continuous efforts are on to overcome these limitations.

1.2.2 4 Synthesis of Triazoles by 'click reaction.'

Synthesis of Triazoles by 'click reaction,' introduced by Sharpless and co-workers [225], have received considerable interest because of the useful applications of triazoles as biologically active compounds, agrochemicals, pharmaceuticals, drug molecules with significant anti-HIV activity, antimicrobial activity against Gram-positive bacteria etc.[226]. One of the representative reactions can be presented as:
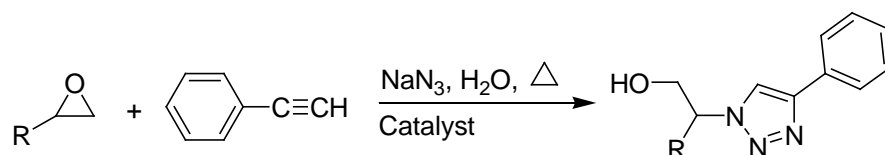
Several authors have reported Cu based catalysts for the synthesis of triazole derivatives including Cu^{II}-hydrotalcite [226], mesoporous CuO [227], Copper(I)-Zeolite [228], 4'-Phenyl-2,2':6',2''-Terpyridine Copper(II) complex immobilized on activated multiwalled carbon nanotubes [229], CuFe$_2$O$_4$ nanoparticles [230], CuI [231], copper(I)@phosphorated SiO$_2$ [232], Copper nanoparticles on activated carbon [233], [(NHC)CuCl] complex [234], CuSO$_4$.5H$_2$O with a sodium ascorbate additive [235], Silica-Immobilized NHC–Cu(I) [236], Polystyrene-supported ionic liquid copper complex [237], etc. However, in some cases the limitations which are associated with these procedures are elevated reaction temperature [226, 238], formation of undesired products, low yields, use of homogeneous catalysts, harsh reaction conditions to synthesize the catalysts, etc. [226, 232, 239]. Moreover, use of magnetically separable

catalysts for synthesis of β-hydroxy triazoles by employing epoxides as starting compounds and 1,3 dipolar cycloaddition are limited in literature.

1.2.2 5 Synthesis of dihydropyrimidinone derivatives by Biginelli reaction

Biginelli condensation involves one-pot multicomponent condensation of an aldehyde, β-ketoester/ β-diketone, and urea/thiourea, for preparation of dihydropyrimidinone derivative [240-243] and can be presented as follows:
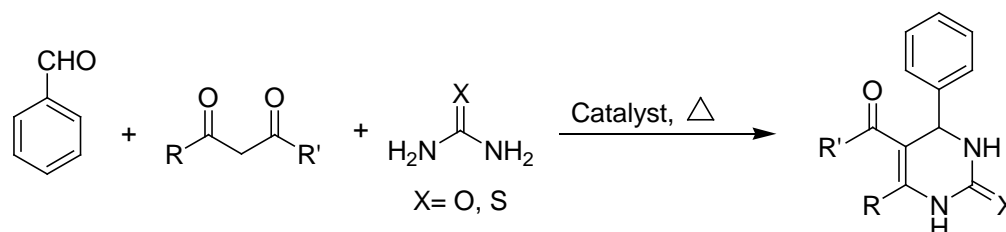
Synthesis of DPHMs and derivatives are important because of their wide range pharmaceutical and therapeutic applications such as anti-inflammatory agents, calcium channel blockers, antihypertensive, anti-tumor, adrenergic and neuropeptide antagonists etc. [240,243,244]. As original Biginelli reaction suffers from some serious limitations (such as use of strong acidic catalyst, poor yield, etc.)[240] several improved procedures involving heterogeneous catalysts have been reported. For example, Fe_3O_4@mesoporous SBA-15 [240], Fe_3O_4@SiO_2-imid-$H_3PMo_{12}O_{40}$ [243], MnO_2-MWCNT [245], Acidic Choline-Based Ionic Liquids [246], sulfonated-phenylacetic acid coated Fe_3O_4 [247], cellulose sulfuric acid [247], nano ZnO [248], SiO_2-$CuCl_2$ [249], Nafion-Ga [250], etc. have been reported for Biginelli reaction. But, despite the efforts made in recent years for Biginelli reaction, difficulty in catalyst recovery and complicated procedures for catalyst preparation remain as typical problems.

1.3 Gaps in existing literature

1) A persistent and urgent demand exists for the development of microwave absorber with advanced features, namely lightweight, thin layers, strong adsorption, and wide effective bandwidth. Microwave absorber effective in X-band region is very much required for stealth application in military applications.

2) Though ferrite materials are well studied for microwave absorptions, but most of the ferrites suffer from one or more of the following limitations such as (i) high density, (ii) poor environmental stability, (iii) narrow wave absorbing band, (iv) poor flexibility, etc. These factors restrict their wide applications as microwave absorber.

3) Though several graphene (or RGO)-ferrite based nanocomposites have been reported by several researchers, but in most of the cases, the synthesized routes are complicated in nature. Therefore, the scope exists to develop simple, but novel and cost-effective synthetic methodology which can produce RGO-ferrite based nanocomposites.

4) Application of RGO-ferrites based nanocomposites as a magnetically separable catalyst for Biginelli reaction, click reaction, and epoxidation reaction has not yet well investigated. To the best of our knowledge, the use of RGO-Ferrites composites as a versatile catalyst for multiple organic reactions has not yet reported.

1.4 Objectives

1) Development of simple but novel aqueous solution based chemical methodologies for preparation of RGO-ferrite nanoparticles.

2) Detailed investigations on the structure and magnetic properties of the synthesized nanocomposites.

3) Investigation on the microwave absorption property of the synthesized nanocomposites in X band region.

4) Investigations on the catalytic activities of the synthesized nanocomposites for the following reaction (i) decolorization of synthetic organic dyes, (ii) Styrene Epoxidation, (iii) Synthesis of Triazoles by 'click reaction', and (iv) Synthesis of dihydropyrimidinone derivatives by Biginelli reaction.

5) Magnetic recovery of the catalyst after completion of the reaction and their reusability tests.

1.5 Organization of thesis

In this thesis, synthesis protocol of three different Reduced Graphene Oxide (RGO)-ferrite based nanocomposites (e.g. $(Ni_{0.8}Zn_{0.2}Fe_2O_4]_x$-$[RGO]_{1-x}$, $[CoFe_2O_4]_x$-$[RGO]_{1-x}$, $[BiFeO_3]_x$-$[RGO]_{1-x}$ where (x = 0-1)) have been described (Chapter 2, 3, and 4). Then the synthesized nanocomposites were tested for two different applications (i) microwave absorption in X-band region, and (ii) magnetically separable catalyst for multiple reactions.

Chapter 1: This chapter contains (i) scope of work, (ii) literature survey on microwave absorption material, (ii) importance of the catalysis reactions, which were chosen (iv) gap in existing research, (v) objective of present study and organization of this thesis.

Chapter 2: This chapter describes the synthesis of $Ni_{0.8}Zn_{0.2}Fe_2O_4$-RGO (NZF-RGO) nanocomposites with different weight ratios of NZF and RGO by '*in situ*' co-precipitation reduction method. Their (i) structural characterizations, (ii) microwave absorption property in X-band region and (iii) the catalytic activities towards the reduction of synthetic dyes (4-nitrophenol, Methyl orange, Rhodamine B) as well as herbicide (trifluralin) in presence of excess $NaBH_4$ in aqueous medium and magnetic separation of NZF-RGO after catalysis reactions and its reusability tests are described.

Chapter-3: This chapter describes the synthesis of $CoFe_2O_4$-RGO (CF-RGO) nanocomposites with different weight ratios of CF and RGO by '*in situ*' co-precipitation reduction method. Their (i) structural characterizations, (ii) microwave absorption property in X-band region and (iii) photocatalytic activity towards degradation of synthetic organic dyes (e.g., Methyl Orange, Methylene Blue, Rhodamine B and Dye mixture) were investigated under visible light generated from a 100W reading lamp in the presence of H_2O_2.

Chapter 4: This chapter describes the synthesis of $BiFeO_3$ nanowire-Reduced Graphene Oxide (BFO-RGO) nanocomposite with different weight ratios of BFO and RGO by a hydrothermal method. Their (i) structural characterizations, (ii) microwave absorption

property in X-band region and (iii) excellent catalytic activity towards Biginelli reaction, click reaction, styrene epoxidation and decolorization of 4-nitrophenol and trifluralin via reduction reaction with $NaBH_4$ and magnetic separation of BFO-RGO after catalysis reactions and its reusability tests were investigated.

Chapter 5: This chapter contains (i) summary of results including comparison of catalysis property and microwave absorption property of the synthesized nanocomposites with already reported similar type of nanocomposites, (ii) conclusions, and (iii) scope of future work.

1.6 Details of the Instruments used for the current investigations

Here details of the instruments which were used to characterize the synthesized catalyzed and to investigate the catalysis reactions are provided.

Room temperature powder X-ray diffraction (XRD) patterns of the synthesized materials were recorded using a powder X-ray diffractometer (Mini Flex II, Rigaku) with Cu K_α radiation at a scanning speed of $2°$ min^{-1}.

Transmissions Electron Microscope (TEM) images of the samples were obtained using a JEOL JEM 1400, Japan. Field Emission Scanning Electron Microscope (FESEM) images and Energy Dispersive X-Ray spectra (EDS) were obtained using Quanta 250 FEG (FEI) and EDAX ELEMENT electron microscope respectively.

Multiple point BET surface areas and pore structures were measured with a surface area and porosity analyzer (Micromeritics Tristar 3000). Before the analysis, samples were degassed at 150 °C for ~6 h under N_2 atmosphere.

UV-vis diffuse reflectance spectra (DRS) analysis was recorded using JASCO V-770 spectrophotometer and energy band gap was calculated from the plot of Kubelka-Munk function versus photon energy.

Differential scanning calorimetric (DSC) analysis was carried out for melting point determination using a DSC-60 (Shimadzu, Japan).

Fourier transform infrared spectra of the samples were recorded by infrared spectrophotometer (IRAffinity-1, Shimadzu, Japan).

Raman spectra were taken on a Renishawin Via Raman microscope with a 633 nm laser excitation. To obtain spectra from Raman spectroscopy powder samples were used.

Electrochemical Impedance measurements [7]

IVIUMSTAT (10V/5A/8MHz) workstation was used to perform Electrochemical Impedance measurements and the measurements were carried out in the frequency range 0.01−10000 Hz at an open circuit potential with alternating current amplitude of 0.01 V. The test electrode was fabricated by mixing 80 wt % of active materials, 10 wt % acetylene black, and 10 wt % polyvinylidene difluoride in N-methyl-2-pyrrolidene. Then the slurry was coated on a Cu wire by dip coating using a dip coater Xdip-SV1 (Apex Eqipments) and vacuum dried at 60 °C for 24h. A three-electrode cell was constructed using Ag/AgCl electrode as the reference electrode, the as-prepared electrode as a working electrode and platinum wire electrode as the counter electrode. EIS measurements were carried out in 3M KOH solution.

Room temperature magnetization with respect to an external magnetic field was measured for the synthesized catalysts using a Vibrating Sample Magnetometer (VSM) (EV5, ADE Technology).

^{1}H NMR (Nuclear Magnetic Resonance) spectra were recorded on a BRUKER 800 ULTRA SHIELD PLUS (400 MHz) instrument using deuterated solvent.

Microwave absorption measurements

HP 8510 Vector Network Analyzer was used for the measurement of microwave absorption of the synthesized nanocomposites in X-band (8.2-12.4 GHz) range. Reflection loss (RL) was calculated using the measured values of complex permittivity and permeability. To prepare the samples for this purpose, nanocomposite powders were first mixed with aqueous solution of 10 wt. % polyvinyl alcohol (PVA), which acted as a

binder and the mixture was dried. This mixture was further ground to powders and then compressed under a pressure of 10 tons and shaped into a rectangular pellet with the size of 10.16 mm × 22.86 mm × 2 mm, so as to fit exactly into the rectangular waveguide of X-band.

The frequency dependence of reflection loss (RL) values of the as-synthesized samples was estimated from the complex permittivity ($\varepsilon_r = \varepsilon' - j\varepsilon''$) and permeability ($\mu_r = \mu' - j\mu''$) using a single-layered plane wave absorber model, proposed by Naito and Suetake[11,35,251].

$$Z_{in} = Z_0(\mu_r/\varepsilon_r)^{1/2} \tan h\left[j\left(\frac{2\pi fd}{c}\right)(\mu_r.\varepsilon_r)^{1/2}\right] \qquad (1.16)$$

$$RL = 20\log\left|\frac{Z_{in} - Z_0}{Z_{in} + Z_0}\right| \qquad (1.17)$$

Where f is the microwave frequency, d is the absorber thickness, Z_0 is the impedance of free space and Z_{in} is the input impedance of absorber.

To obtain the RL values of the absorber with different thickness MATLAB simulation was used.

Chapter 2

Synthesis of Ni$_{0.8}$Zn$_{0.2}$Fe$_2$O$_4$-RGO: Excellent Microwave Absorber and Highly Efficient Magnetically Separable Recyclable catalyst for Dye Degradation
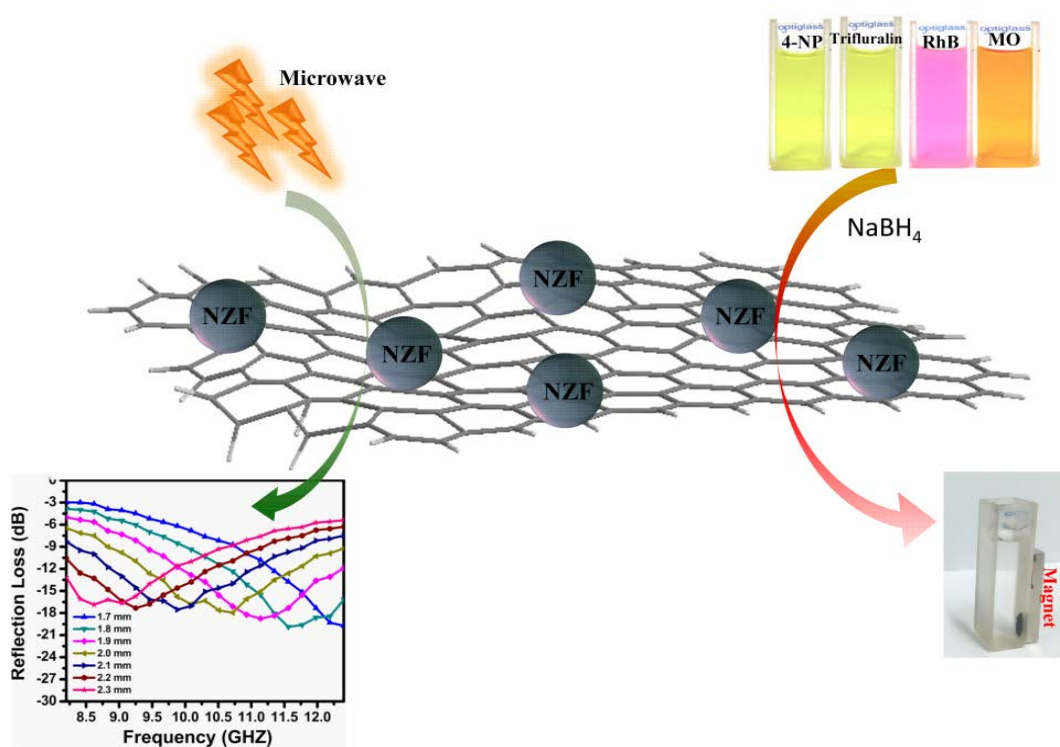
In this chapter an *'in-situ'* co-precipitation reduction method has been reported for the preparation of Ni$_{0.8}$Zn$_{0.2}$Fe$_2$O$_4$-RGO (NZF-RGO) nanocomposites with different weight ratios of NZF and RGO. Their (i) structural characterizations, (ii) microwave absorption property in X-band region and (iii) the catalytic activities towards the reduction of synthetic dyes (4-nitrophenol (4-NP), Methyl orange (MO), Rhodamine B (RhB)) as well as herbicide (trifluralin) in presence of excess NaBH$_4$ in aqueous medium and magnetic separation of NZF-RGO after catalysis reactions and its reusability tests will described [11].

2.1 Experimental procedure[11]

2.1.1 Materials required

Nickel nitrate Ni(NO$_3$)$_2$.6H$_2$O, Zinc nitrate Zn(NO$_3$)$_2$.6H$_2$O, Iron nitrate Fe(NO$_3$)$_3$.9H$_2$O, Sodium hydroxide (NaOH), Sodium nitrate NaNO$_3$, Sulphuric acid (H$_2$SO$_4$), Potassium permanganate (KMnO$_4$) and 30% H$_2$O$_2$ solution were purchased from Merck, India and Graphite powder (bought from Sigma Aldrich with mean particle size of < 20 µm) and used without further purification. Methyl orange (MO), Trifluralin, and Rhodamine B (RhB) were purchased from Sigma Aldrich. 4-Nitrophenol (4-NP), and sodium borohydride (NaBH$_4$) were purchased from Acros Organics. All reagents were of analytical reagent grade and used as received. Millipore water (18 MΩ) was used throughout the study.

2.1.2 Synthesis of Ni$_{0.8}$Zn$_{0.2}$Fe$_2$O$_4$-Reduced Graphene Oxide (NZF-RGO) nanocomposites.

Synthesis of Ni$_{0.8}$Zn$_{0.2}$Fe$_2$O$_4$-Reduced Graphene Oxide (NZF-RGO) was performed by using the following steps: Step 1: Graphene oxide was synthesized by modified Hummer's and Offeman method [83]. Step 2: An *'in situ'* co-precipitation reduction based methodology has been developed where reduction of GO to RGO and formation of NZF nanoparticles from metal nitrates occurred simultaneously, which helped to anchor NZF nanoparticles on the sheets of RGO homogenously.

2.1.2.1 Synthesis of Graphene Oxide (GO):

Graphene Oxide was synthesized from Graphite powder according to the method reported by Hummers and Offeman [83]. Briefly, 1 g graphite and 0.6 g of $NaNO_3$ were mixed with 35 ml of H_2SO_4 (18 M) at 0 °C. The mixture was stirred for 6h. Then 3.8 g of $KMnO_4$ was added to the suspension very slowly. The temperature of the solution rises to 35 °C and was maintained for 8h so that complete oxidation takes place. Then 60 ml of distilled H_2O was slowly added, and the reaction temperature was increased to 98 °C. This temperature was maintained for 1h, and finally, 2 ml of 30 % H_2O_2 solution was added to the mixture and stirred for 0.5h. The mixture was centrifuged and washed with 10 % HCl solution and distilled H_2O. The yellowish brown precipitate of graphene oxide was obtained and dried at 60 °C.

2.1.2.2 Synthesis of Ni₀.₈Zn₀.₂Fe₂O₄-Reduced Graphene Oxide (NZF-RGO):

In a typical synthesis, an aqueous solution mixture containing the desired amount of metal nitrates salts (e.g., $Fe(NO_3)_3.9H_2O$, $Ni(NO_3)_2.6H_2O$, $Zn(NO_3)_2.6H_2O$) was prepared. In this mixture, an aqueous mixture containing well-dispersed GO powder was added. To this reaction mixture, an aqueous solution of NaOH (2M) was added dropwise till the pH reached ~ 8.5-9. This mixture was then refluxed at 120 °C for 12h, followed by cooling at room temperature. The black precipitate thus obtained was collected by ultracentrifugation and washed several times with distilled water. After separation, this precipitate was dried at 60 °C for 12h. Employing this preparation protocol NZF-RGO nanocomposites were prepared to have different weight ratio of RGO and NZF such as 85 wt.% NZF-15 wt.% RGO (85NZF-15RGO), 75 wt.% NZF-25 wt.% RGO (75NZF-25RGO), 50 wt.% NZF-50 wt.% RGO (50NZF-50RGO). Using this method pure $Ni_{0.8}Zn_{0.2}Fe_2O_4$ (NZF) nanoparticles were also synthesized where GO was not mixed. Except this, all parameters were kept same.

2.1.3 Catalytic Performance test of NZF-RGO towards decolorization of synthetic organic dyes with NaBH₄.

To study the catalytic activity of NZF-RGO, reduction reactions were performed for Methyl orange (MO), 4-Nitrophenol (4-NP), Rhodamine B (RhB), and Trifluralin. In a

typical run 4.5 ml of 9×10^{-5} (M) aqueous solution of 4-NP (in case of MO and Rh B the concentrations were 6×10^{-5} (M) and 2×10^{-5} (M) respectively and in case of trifluralin the concentration was 1.5×10^{-5} (M) in 1:1 ethanol and water mixture) was mixed with 2 ml H_2O and 1 ml 0.2 (N) $NaBH_4$ solutions. To this solution 0.5 ml, an aqueous suspension of the catalyst (1.25×10^{-2} gm/liter) was then added. 3-4 ml of the solution was then immediately transferred to a quartz cuvette. The colored solution faded gradually as the reaction proceeded. The reaction was monitored by recording absorption spectrum by a UV-vis spectrophotometer at an interval of 1 minute. Initially, the reduction reaction of 4-NP was investigated to obtain the effect type of the catalyst. UV-vis spectra of an aqueous solution of 4-NP showed the maximum absorption peak (λ_{max}) at 317 nm. This peak was red-shifted to 400 nm after addition of $NaBH_4$ due to the formation of bright yellow colored 4-nitrophenolate ions [252, 253].

After each cycle, the catalysts were separated from the reaction mixture by applying external magnetic field. After separating the catalyst from the reaction mixture, the catalyst was washed with alcohol, and it was observed that no unreacted dye molecule remained adsorbed in the catalyst. Then the catalyst was washed many time by the deionized water and dried for the next run. All the catalysis reactions were carried at room temperature (26 ± 1) °C, and the reactions were performed in triplicate.

It is well documented that, metal oxide nanoparticles catalyzed reduction reaction of dyes and herbicide like trifluralin in the presence of excess $NaBH_4$ proceed *via* pseudo-first-order kinetics [207,253-255]. As the absorbance of the dye is proportional to its concentration, the ratio of absorbance of the dye A_t (measured at time t) to A_o (at t=0) is equal to C_t/C_o (where C_t is the concentration of dye at time t, and C_o is the initial concentration of the dye). The apparent rate constant K_{app} was determined from the following equation: -

$$dC_t/dt = -k_{app}.C_t \qquad (2.1)$$
$$\ln(C_t/C_o) = \ln(A_t/A_o) = -k_{app}.t \qquad (2.2)$$

The value of k_{app} was calculated from $\ln(A_t/A_o)$ vs. time plot.

2.1.4 Magnetic separation and reusability test of the catalyst (NZF-RGO)

After completion of the catalysis reactions a permanent magnet (N35 grade NdFeB magnet having Energy product BH_{max} = 33-36 MGO) was held at the outside wall of the round-bottomed flask or beaker, where the reaction was conducted. The magnet attracted the catalyst nanoparticles. When all the catalyst nanoparticles were congregated near the magnet, the reaction mixture was separated by simple decantation. The catalyst was then washed several times with distilled water, dried over air oven at 100 °C for 6h and reused for the next cycle.

2.1.5 Microwave absorption measurement

The protocol for the measurement of microwave absorption of the synthesized nanocomposites has been described in Section 1.6 of Chapter 1.

2.2 Results and Discussion[11]

2.2.1 Structure and morphology of NZF-RGO nanocomposites

XRD pattern of GO showed an intense diffraction peak at 2θ = 9.76° and a small peak at 42.14° which corresponded to (001) and (101) planes of GO [256, 257]. In the case of pure RGO a broad peak around 2θ = 24° and a small peak at 43°, corresponding to (002) and (001) plane [60,163,164] were observed. NZF-RGO nanocomposite samples exhibited diffraction at 2θ = 30.35°, 35.72°, 37.83°, 43.32°, 53.94°, 57.20° and 62.89° correspond to (220), (311), (222), (400), (422), (511) and (440) planes of $Ni_{0.8}Zn_{0.2}Fe_2O_4$ with cubic spinel structure, respectively (JCPDS card No. 52-0277) (Fig. 2.1). The average crystallite size of NZF nanoparticles was found to be 14 nm, calculated by using Scherer's equation. In the XRD patterns of NZF-RGO composites, no peaks at 2θ = 9.76° and 42.14° were observed, which indicated that during the preparation of NZF-RGO composites, GO flakes were converted to RGO and RGO sheets were exfoliated [60, 61, 164, 258-261]. In this, '*in situ*' co-precipitation method, NaOH acted in a dual role. It not only precipitated hydroxides of metal ions, which eventually converted to NZF nanoparticles [262] but also converted GO to RGO during reflux [97, 263]. In this method, as the formation of NZF, occurred in the presence of RGO flakes, nanoparticles were expected to be well deposited on the surface of flakes.
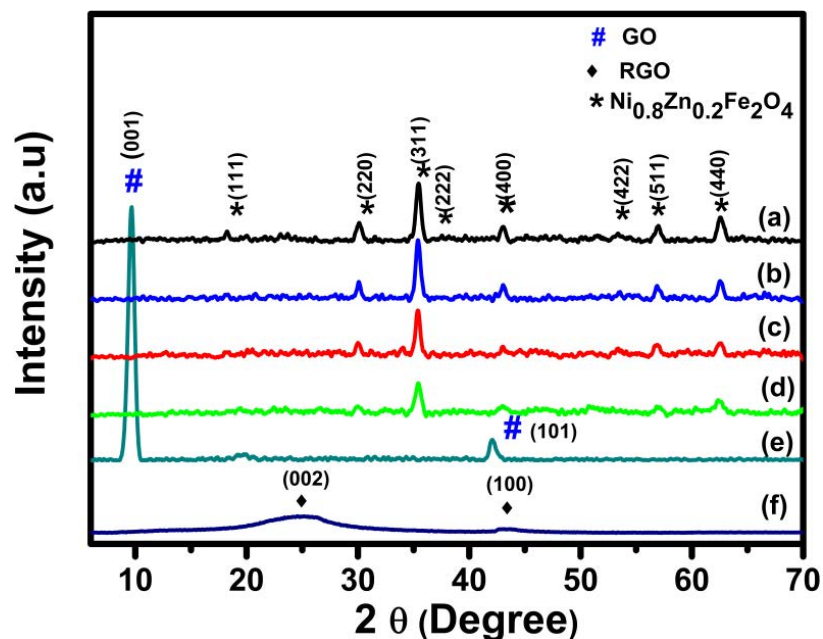
Fig. 2.1 Room temperature wide angle powder XRD pattern of (a) pure NZF, (b) 85NZF-15RGO, (c) 75NZF-25RGO, (d) 50NZF-50RGO (e) GO, and (f) RGO.

TEM micrographs of pure NZF and NZF-RGO nanocomposite (Fig. 2.2 (A, B)) also revealed that nanometer thin RGO sheets were well separated and NZF nanoparticles (~7-10 nm) were homogenously deposited on RGO sheets.
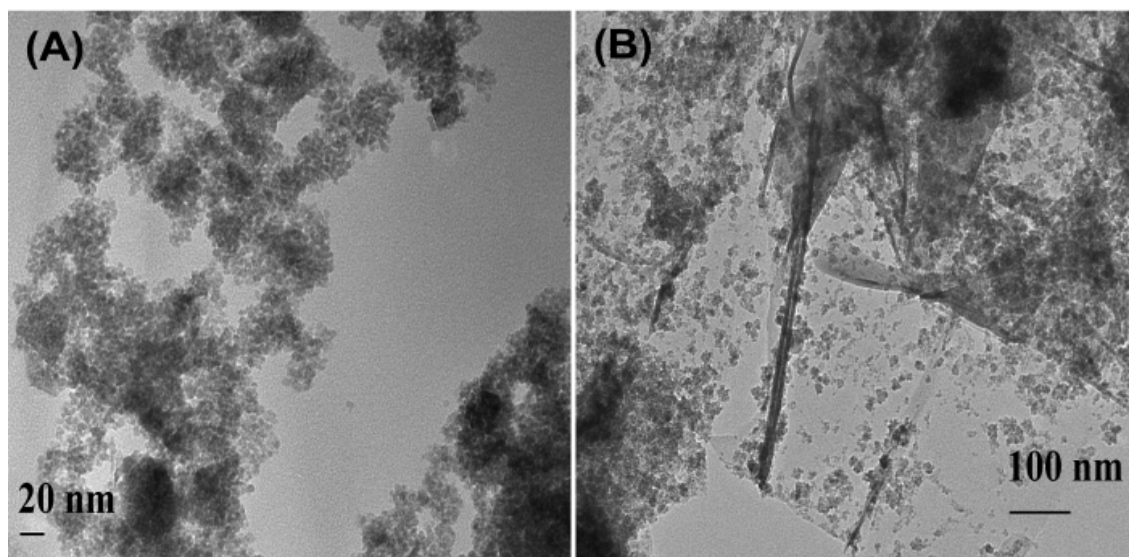
Fig. 2.2 (A) TEM images of pure NZF (B) TEM micrograph of 50NZF-50RGO.

EDX analysis of these nanocomposites also confirmed the composition of these composites (Fig. 2.3)
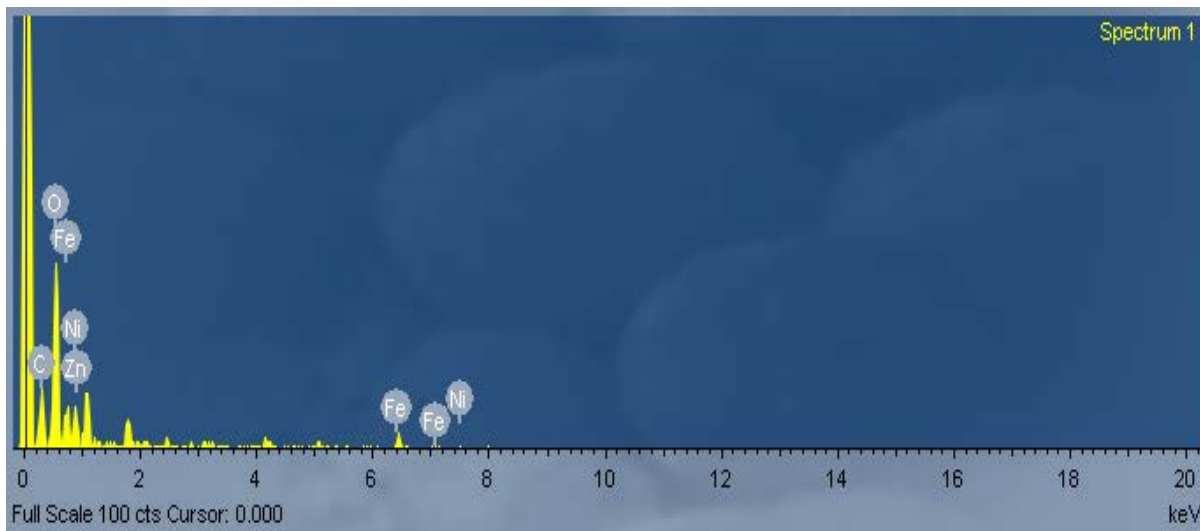
Fig. 2.3 EDX spectra of the synthesized 50NZF-50RGO nanocomposite.

TGA analysis of GO, RGO and NZF-RGO were performed in an air atmosphere in the temperature range of 30-850 °C with heat rate of 10 °C /min.. Fig. 2.4 shows TGA thermograms of pure GO and NZF-RGO nanocomposites having various compositions. In TGA thermograms following points were observed (i) in the temperature of 30-100°C, GO showed ~17% wt. loss, whereas RGO showed ~5 wt%, and 50NZF-50RGO ~9 wt% loss. These could be due to the evaporation of the surface adsorbed H$_2$O from the synthesized materials [61]. (ii) In the 100-200 °C temperature range, GO showed ~3% wt. loss and a sharp weight loss of ~ 25 wt % occurred in the range of 200-270 °C. This might be due to the removal of oxygen-containing groups (-OH, -CO$_2$H, -C=O, epoxy) from GO. (iii) In 325-625 °C temperature range, the oxidative decomposition of all carbon atoms of GO occurred. (iv) In case of pure RGO, a continuous weight loss till the complete decomposition of carbon occurred in the temperature range of 110-625 °C. In the case of 50NZF-50RGO, the carbon decomposition was observed in the range of 275-375 °C. After full decomposition of RGO component of the composite, ~50 wt% remained as undecomposed which was the NZF present in the composite. The lowering of the decomposition temperature of RGO in 50NZF-50RGO compared to pure RGO could be due to the presence of NZF in the composite, which might facilitate the oxidative decomposition of carbon. (v) In case of both RGO and 50NZF-50RGO, no distinguishable weight loss steps occurred in the temperature range of 100-200°C and

200-270 °C, which were observed in case of pure GO. This fact indicates that in pure RGO and 50NZF-50RGO, there is an absence of almost any oxygen -containing functional groups, which were present in pure GO. This is also indirect indication that, during synthesis of 50NZF-50RGO, GO was converted to RGO during reflux with NaOH. Similarly, for 85NZF-15RGO, 75NZF-25RGO and 50NZF-50RGO nanocomposites 85 wt%, 75 wt%, and 50 wt% NZF remained as a residue after thermal decomposition of the RGO component of the composites. So, we can also conclude that this '*in situ*' co-precipitation' method for NZF-RGO composite preparation is capable of producing composites with desired NZF and RGO composition.
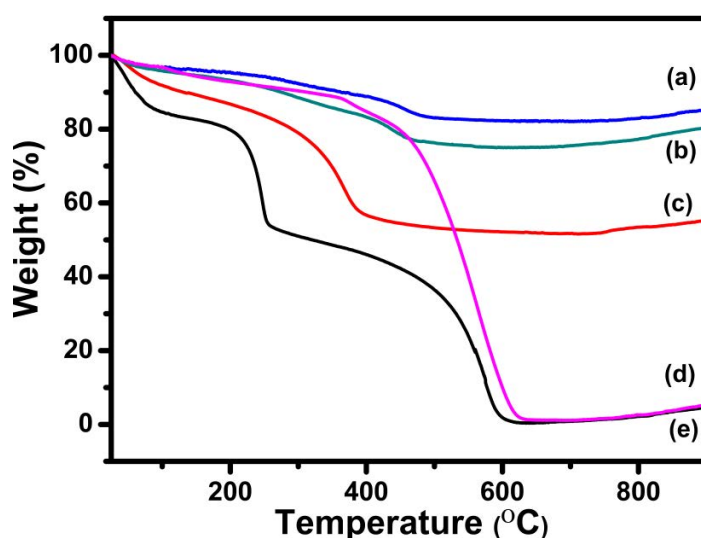
Fig. 2.4 TGA curves of (a) 85NZF-15RGO (b) 75NZF-25RGO (c) 50NZF-50RGO nanocomposite, and (d) GO.
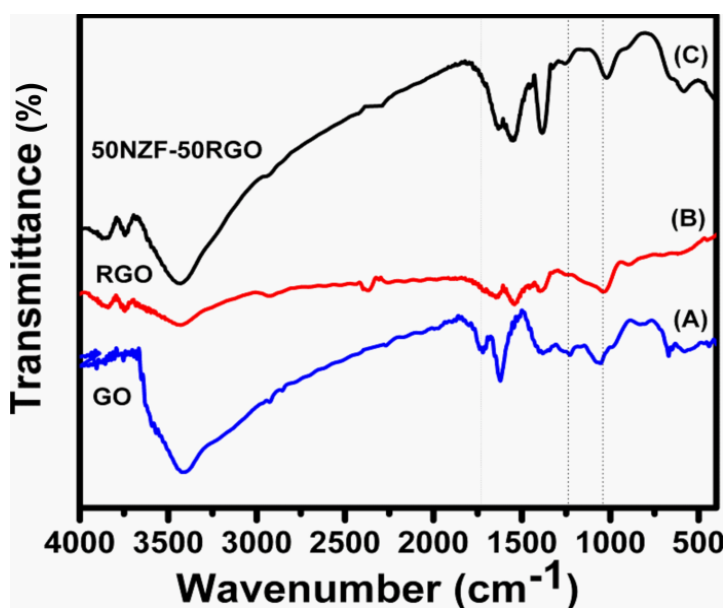
Fig. 2.5 FT-IR spectra of (A) GO (B) RGO, and (C) 50NZF-50RGO.

Fig. 2.5 shows FT-IR spectra of pure GO, pure RGO (prepared by refluxing GO at 120 °C for 12h) and 50NZF-50RGO. It was observed that in case of GO peaks appeared at (i) 1384 cm^{-1} corresponding to the stretching vibration of C-O of carboxylic group, (ii) 1720 cm^{-1} for a carbonyl group, (iii) 1226 cm^{-1} for C-O stretching vibration of epoxy group (iv) 1054 cm^{-1} for C-O stretching vibration [60,264]. This fact indicated the presence of an oxygen-containing functional groups (such as epoxy, carbonyl, carboxyl, and hydroxyl) on the surface of GO.

Moreover, the peak at 1621 cm^{-1} can be assigned to the contribution from the skeletal vibration of the graphitic domains [60,63,159,265]. In case of pure RGO it was observed that the peak at 1720 cm^{-1} (for carbonyl group) has disappeared and intensities of the peaks at 1226 and 1054 cm^{-1} (corresponding to C-O) have decreased. The appearance of a peak at 1544 cm^{-1} was also observed. The band at 1621 cm^{-1} (in GO sample), which can be assigned to the C=C skeletal vibration of graphitic domains of GO, has been redshifted to 1544 cm^{-1} for RGO and indicated the partial restoration of π-π conjugation of graphene sheet in RGO [159]. Absorption bands at the same positions were observed in FT-IR spectra of NZF-RGO nanocomposite samples. Here also carboxylic group vibration band ($\nu_{C=O}$ at 1720 cm^{-1}) was found to be disappeared and the absorption intensity corresponding to C-O at 1226, and 1054 cm^{-1} were decreased. These results implied that most of the oxygen-containing groups of GO, particularly carboxyl groups, had been removed and some of the hydroxyl and epoxy groups remained on the surface of RGO in NZF- RGO nanocomposites. Moreover, appearance of peak at 592 cm^{-1} indicated the presence of ferrite in NZF-RGO nanocomposite [60,63].

Raman spectroscopy, which is a sensitive and informative technique to probe disorder in sp^2 carbon materials, was used to determine the transformation of GO to RGO during formation of NZF-RGO nanocomposite. Fig 2.6 shows the Raman spectra of GO, Pure RGO, and NZF-RGO nanocomposite. In the Raman spectra of GO, characteristic peaks for D and G band were found at 1355 and 1599 cm^{-1} respectively, whereas in pure RGO the D band and G band shifted to 1338 and 1595 cm^{-1} [45]. The same kind of shifting was also observed in NZF-RGO nanocomposite (1349 and 1586 cm^{-1}) confirming the conversion of GO to RGO in the composites. In the case of pure GO, the value of I_D/I_G

was found to be 0.9 [64]. However, this ratio was increased to 1.33 in case of pure RGO and 1.03 for NZF-RGO composites, which can be attributed to the decrease in the average size of sp^2 domains upon reduction of GO during formation of RGO and NZF-RGO composites [45, 64].
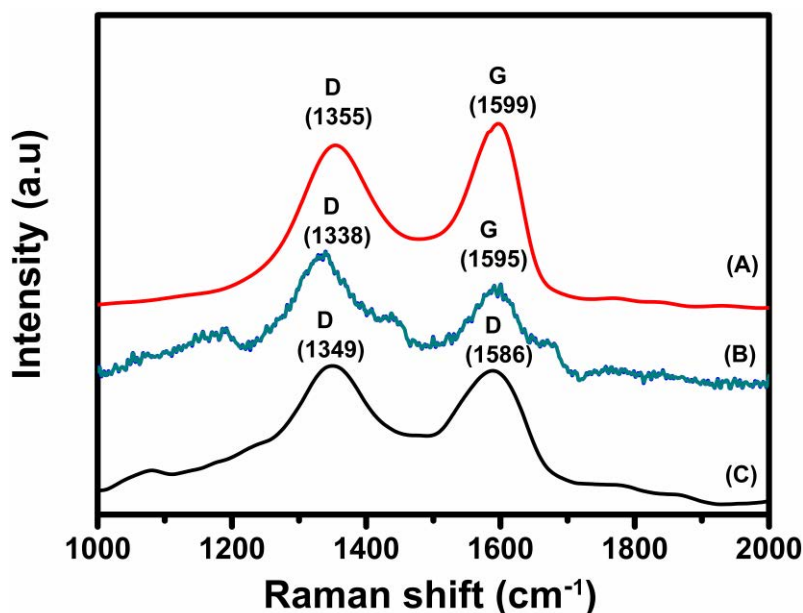
Fig. 2.6 Raman spectra of (A) GO, (B) RGO and (C) 50NZF -50RGO.

The results obtained from XRD, TGA, HRTEM, FT-IR and Raman spectroscopic measurement indicated that when the mixture of GO, metal nitrates, and NaOH was refluxed for 12 h at 120 °C, two reactions proceeded simultaneously, (i) reduction of GO to RGO and (ii) formation of Ni$_{0.8}$Zn$_{0.2}$Fe$_2$O$_4$ nanoparticles.

2.2.2 Formation mechanism of Ni$_{0.8}$Zn$_{0.2}$Fe$_2$O$_4$ nanoparticles

As proposed by Velmurugan et al. the formation of the Ni$_{0.8}$Zn$_{0.2}$Fe$_2$O$_4$ nanoparticles can be presented by the following reactions:[266]

$$0.8\ Ni^{2+} + 0.2\ Zn^{2+} + 2Fe^{3+} + 8OH^- \longrightarrow 0.8\ Ni(OH)_2.0.2\ Zn(OH)_2.2Fe(OH)_3 \downarrow \quad (2.3)$$

$$0.8\ Ni(OH)_2.0.2\ Zn(OH)_2.2Fe(OH)_3 \xrightarrow[\text{pH}\sim 9]{120\ °C,\ 12\ h} Ni_{0.8}Zn_{0.2}Fe_2O_4.\ 8H_2O \quad (2.4)$$
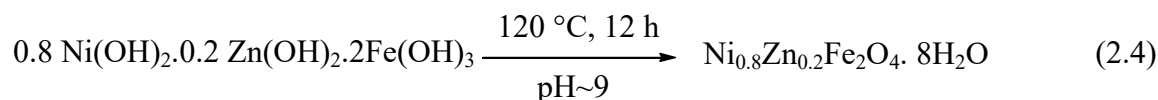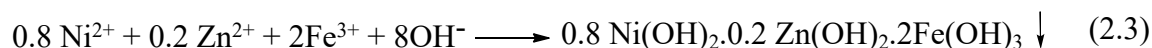
In the first step, during the addition of NaOH to the aqueous solutions of metal nitrate, formations of fine particles of metal hydroxides, takes place immediately (Equation 2.3) [266]. Then these fine hydroxide particles are converted to ferrite nanoparticles during reflux at 120 °C for 12 h [267].

2.2.3 Magnetic property of NZF-RGO

The magnetic properties (saturation magnetization (M$_s$) and coercivity (H$_c$)) of NZF-RGO nanocomposites were determined by VSM (Fig. 2.7(A)). It has been observed that with increasing RGO component M$_s$ value of the composites were decreased (Table 2.1). In these composites presence of nonmagnetic RGO along with several other factors (e.g., attachment of NZF nanoparticles on the surface of RGO sheets which might influence particle surface spin, disordered surface spin structure, dipolar interparticle interactions, etc. of NZF nanoparticle) [268-270] play important roles in determining their M$_s$ values. 50NZF-50RGO nanocomposites possessed M$_s$ and H$_c$ value of 14 emu g^{-1} and 0.361 O$_e$. This also indicated that the magnetic properties of these composites materials could also be tuned by changing the ratio of metal nitrate salts to GO [271].
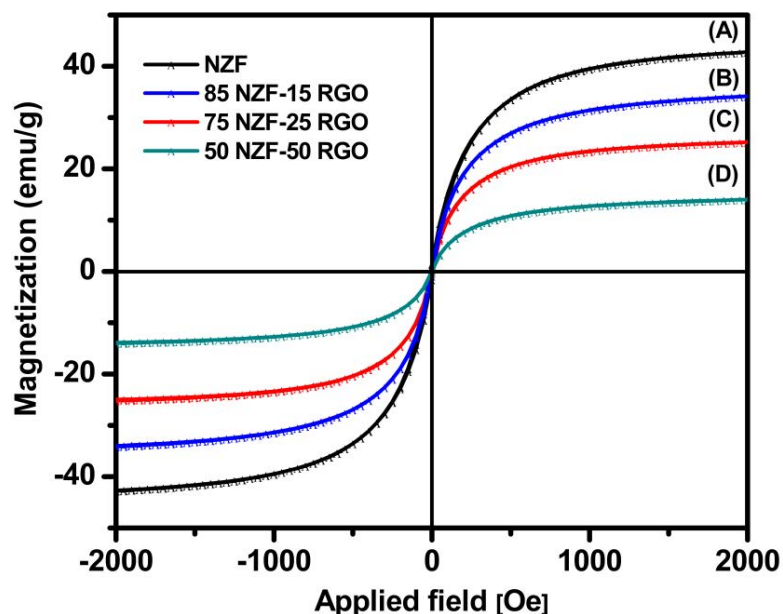
Fig. 2.7 (A) Room temperature magnetic hysteresis loops for (a) Pure NZF (b) 85NZF-15RGO (c) 75NZF-25RGO, and (d) 50NZF-50RGO

Table 2.1: Magnetic properties of NZF and NZF-RGO nanocomposites

Sample	M$_s$ (emu.g^{-1})	H$_c$ (O$_e$)
Pure NZF	42	7.674
85NZF-15RGO	34	4.101
75NZF-25RGO	25	2.389
50NZF-50RGO	14	0.361

2.2.4 Catalytic properties of NZF-RGO catalyst

To investigate the catalytic efficiency of the synthesized NZF-RGO nanocomposites, reduction of synthetic dyes (4-nitrophenol (4-NP), Methyl orange (MO), Rhodamine B (RhB)) in the presence of excess NaBH$_4$ in aqueous medium was investigated. To understand the effect of the presence of RGO in NZF-RGO composites the same reactions were performed with pure NZF nanocatalyst. Reduction of 4-NP was first performed in the presence of pure NZF, and it was observed that the reduction reaction was completed after 15 min. Similarly, in cases, MO and RhB, the times required for completion of reduction were 17 min and 19 min respectively. On the other hand, when the catalysis reaction was performed with pure RGO, RGO exhibited its inertness as a catalyst towards the reduction of the dye molecules. Fig 2.8(A) shows that reduction of the dyes did not occur even after 90 min when pure RGO was used as a catalyst. When NZF-RGO nanocomposites were used as catalysts progressive decrease of time, needed for the completion of the reaction, with increasing RGO content in the catalyst was observed. For example, when 50NZF-50RGO was used as a catalyst, the time needed to complete the reduction of 4-NP, MO, and RhB were 6, 5, and 7 min respectively (Fig. 2.8 (A-C) (Table 2.2)). The time-dependent UV-vis spectra of reduction of dyes when catalyzed by different NZF-RGO composites (i.e., NZF, 85NZF-15RGO, 75NZF-25RGO, 50NZF-50RGO, and 25NZF-75RGO) are provided in Fig. 2.9 and Table 2.3.
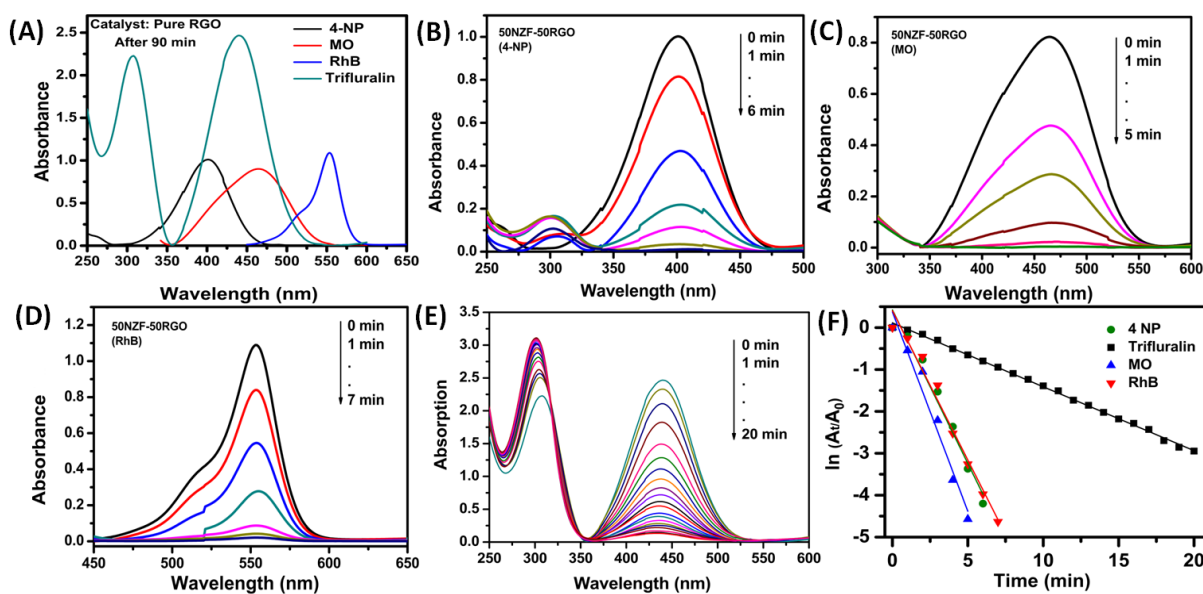
Fig. 2.8 Time-dependent UV-vis spectral changes of the reaction mixtures when catalyzed by (A) Pure RGO (the spectra of the reaction mixture were taken at 90 min after addition of RGO and spectra showed no reaction is happening), and (B-E) by 50NZF-50RGO in the presence of excess NaBH4 and (F) pseudo-first order kinetic plot of 4-NP, MO, RhB, and Trifluralin reduction catalyzed by 50NZF-50RGO.

Table 2.2: Completion time and rate constants of 50NZF-50RGO catalyzed reduction reactions.

Dyes	Completion Time (min)	Rate Constant (k$_{app}$) (min^{-1})	Correlation Coefficient
4-NP	6 ($\pm$0.14)	0.73 ($\pm$ 0.03)	0.96
MO	5 ($\pm$0.25)	0.95 ($\pm$ 0.05)	0.96
RhB	7 ($\pm$0.14)	0.71 ($\pm$ 0.02)	0.97
Trifluralin	20 ($\pm$0.5)	0.15 ($\pm$ 0.01)	0.99
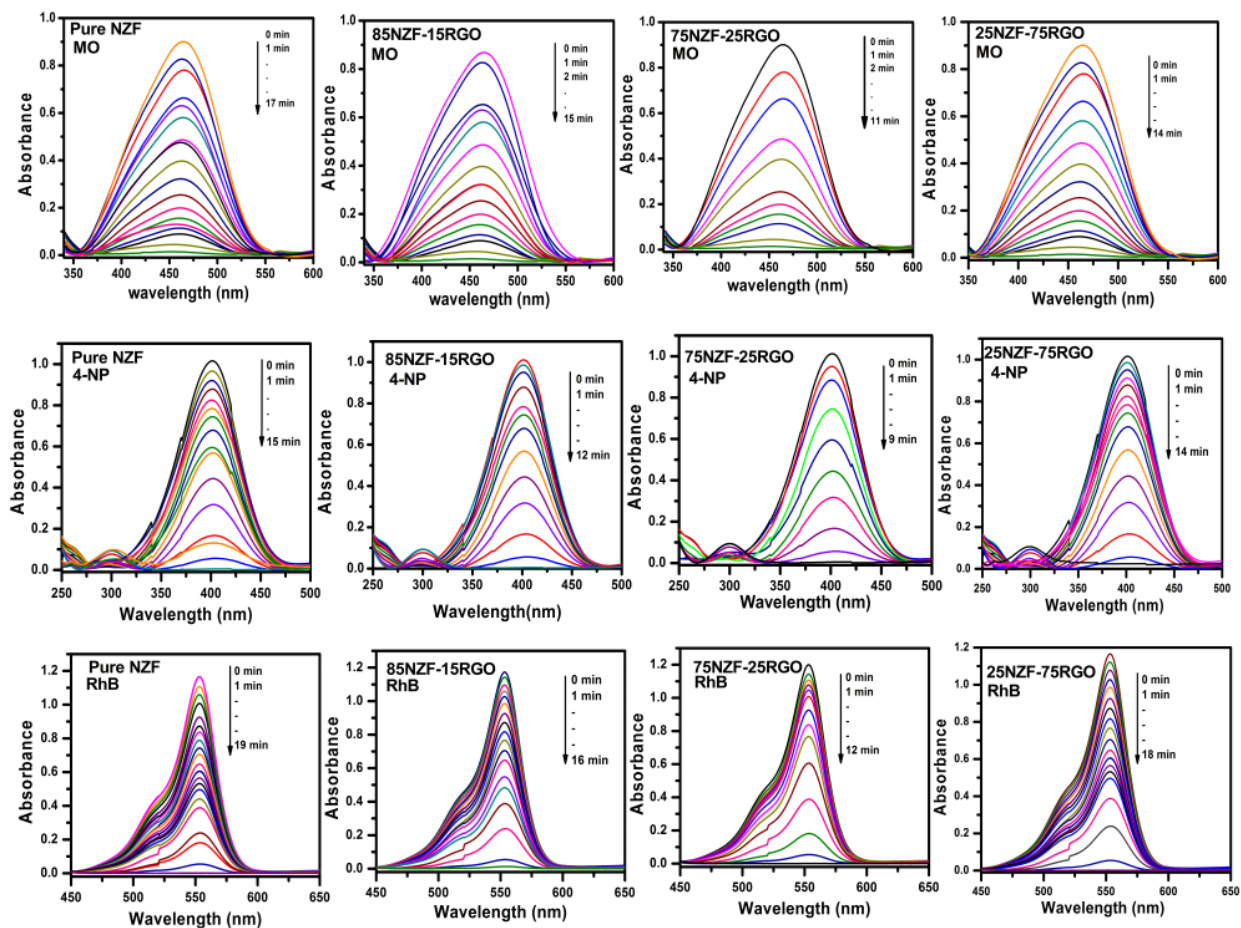
Fig. 2.9 Time-dependent spectral changes of the reduction reactions of various dyes catalyzed by NZF-RGO nanocomposites, having various compositions.

Table 2.3: Times required completing the reduction reaction of various dyes catalyzed by NZF and NZF-RGO composites.

Catalyst composition	Time required to complete the reaction		
	4-NP	**MO**	**RhB**
NZF	15 min	17 min	19 min
85NZF-15RGO	12 min	15 min	16 min
75NZF-25RGO	9 min	11 min	12 min
50NZF-50RGO	6 min	5 min	7 min
25NZF-75RGO	14 min	14 min	18 min

This enhancement of catalytic efficiency of NZF-RGO nanocomposites can be explained by considering following points: (i) these reduction reactions proceed via relaying of electrons from the BH$_4^-$ donor to the acceptor dye molecules [252,253,272-274]. In aqueous medium BH$_4^-$ was first absorbed on the surface of

42

the catalyst. The hydrogen atoms, which were formed from the hydride, transfer electrons to the dye molecule to reduce its functional groups (e.g.-NO$_2$ group for 4-NP, -N=N- group for MO, -C=N for RhB). This electron transfer (ET) induced hydrogenation of dye molecules occurred spontaneously, and NZF nanoparticles play a role in storing electrons after ET from hydride [252,275]. In case of NZF-RGO this nanocomposite, the synergistic effect between NZF and RGO sheets affects positively in the reduction of reaction time. Presence of RGO not only enhances the absorption of dye molecules onto the catalyst through π-π stacking but also facilitates the electron transfer to the dye molecule via electrostatic interaction [163,275,276]. However, the catalytic efficiency of NZF-RGO catalysts was found to be decreased when RGO component in the catalyst was more than 50 wt. % (Fig. 2.9 and Table (2.3)). This might be due to the decrease of NZF component in the catalyst [275]. As the concentration of NaBH$_4$ remains almost constant (because of its excess concentration) throughout the reaction, we have considered that this catalytic reaction follows pseudo-first-order kinetics [252] and values of apparent rate constant (k$_{app}$) were found to be 0.73 m^{-1}, 0.95 m^{-1}, and 0.71 m^{-1} for 4-NP, MO and RhB respectively when 50NZF-50RGO was used as catalyst (Fig. 2.8(E)). As it has been observed that, 50NZF-50RGO can act as an efficient catalyst towards the reduction of -NO$_2$ group of 4-NP, we have utilized this catalyst for reduction of trifluralin, which is a herbicide [277] and toxic in nature and present in water as residue. Trifluralin molecule contains two -NO$_2$ groups. It has been observed that 50NZF-50RGO is capable of decolorizing the aqueous solution of trifluralin by reducing its -NO$_2$ groups to -NH$_2$ group within 20 min in the presence of excess NaBH$_4$ (Fig. 2.8(D)).

As NZF is magnetic in nature, 50NZF-50RGO nanocatalyst offers an additional advantage along with its high catalytic activity. This catalyst can easily be separable from the reaction mixture after completion of the reaction by using a magnet externally. This easy magnetic separation of this catalyst helps to overcome the limitation of separation problem associated with nanoparticle catalysts. Fig 2.10 illustrates complete reduction reaction of the dyes catalyzed by 50NZF-50RGO composites in the presence of excess NaBH$_4$, resulting in decolorization of the dye solution and magnetic separation of the catalyst by employing a bar magnet externally.
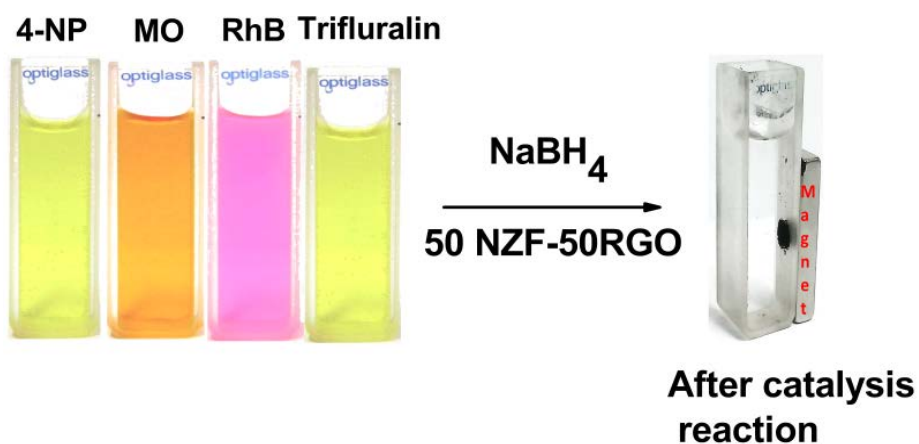
Fig. 2.10 Magnetic separation of the catalyst by applying a magnet externally after completion of the reaction.

2.2.5 Reusability of NZF-RGO nanocomposites

The reusability of the catalyst was tested after recovering the catalyst from the reaction mixture, and it was observed that 50NZF-50RGO retained its activity almost same till five cycles, and then slight decrease was observed (Fig. 2.11).
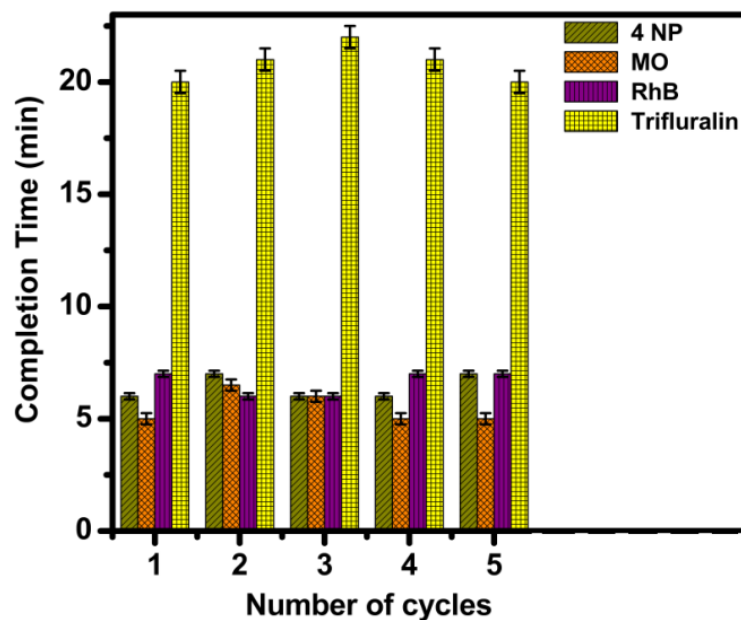
Fig. 2.11 Reusability of magnetically separable catalyst (50NZF-50RGO) for the reduction of 4-NP, MO, RhB, and Trifluralin.
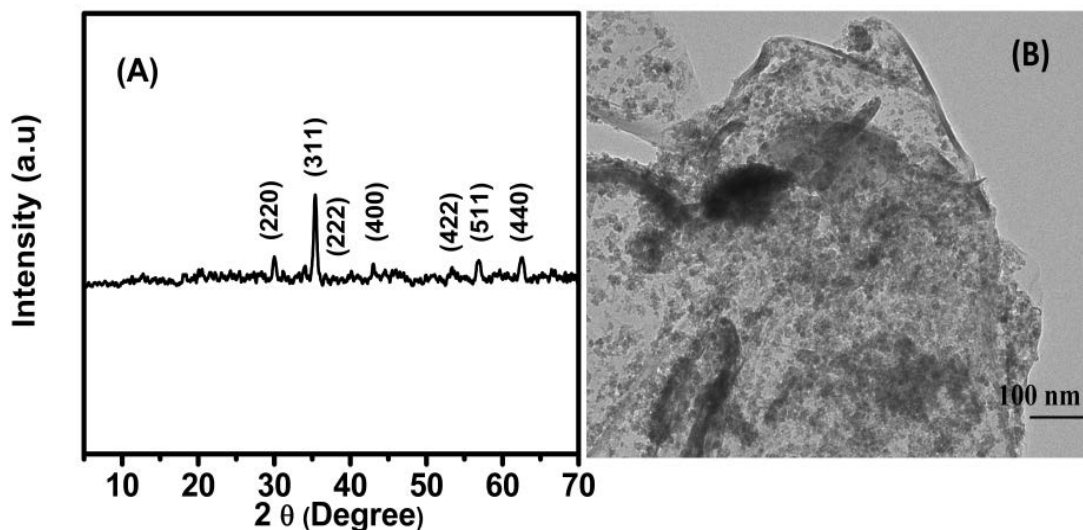
Fig. 2.12 (A) XRD and (B) TEM micrograph of the recycled catalyst 50NZF-50RGO.

XRD and TEM analysis of the recycled catalysts showed that after catalysis reactions any noticeable change in the crystal structure and microstructure of the catalyst did not occur (Fig. 2.12).

This high catalytic efficiency of 50NZF-50RGO towards the reduction of various dyes provoked us to investigate the microwave absorption property to demonstrate its capability to act as a multifunctional material.

2.2.6 Microwaves Absorption property of NZF-RGO nanocomposites

Microwave absorbing property of 50NZF-50RGO nanocomposites was investigated considering the fact that, RGO component of the composite will contribute towards microwave absorption due to the presence of residual defects and groups on the surface of the RGO sheets [60,278]. On the other hand, as the M$_s$ value of 50NZF-50RGO nanocomposites, is lower than that of pure NZF, the anisotropy energy of 50NZF-50RGO nanocomposites are higher than that of pure NZF. This higher anisotropy energy is expected to be helpful to enhance the microwave absorption properties of the composites [60,279-283].

From the measurement of ε', ε'', μ' and μ'' of pure NZF and 50NZF-50RGO nanocomposites over the frequency range of 8.2 to 12.4 GHz (X-band) (Fig 2.13) it was observed that (i) the values of ε' and ε'' were increased with increasing RGO content in the composite. This might be due to the fact that larger number of RGO sheets might enhance the electrical polarization and electrical conductivity of the samples because ε' is an expression of the polarizability of materials and consists of dipolar polarization and electric polarization at microwave frequency [45,60], (ii) the values of μ' and μ'' were found to be increased with increasing NZF content in the composite. Therefore, it is suggested that both dielectric loss and magnetic loss play important roles in microwave absorption of 50NZF-50RGO nanocomposite.
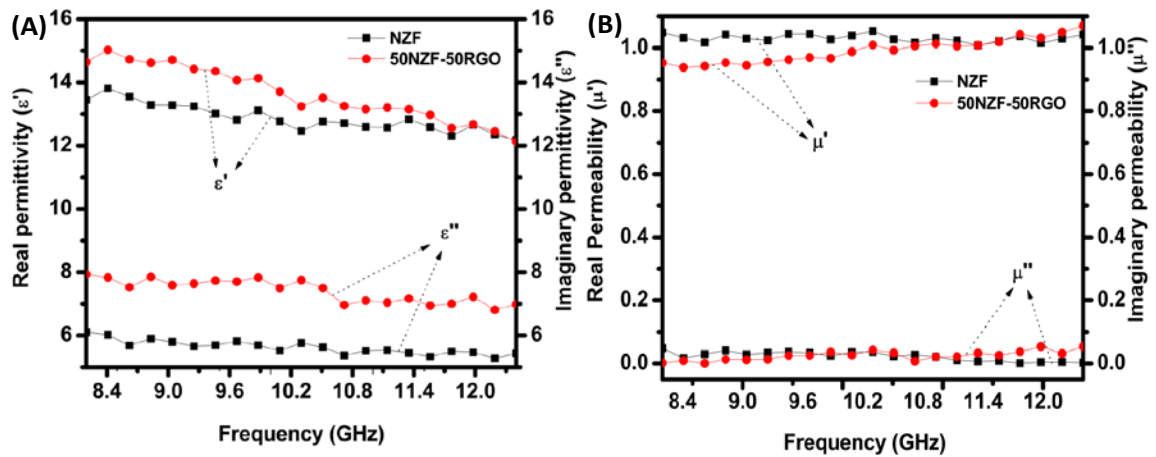
Fig. 2.13 Frequency dependence of (A) relative complex permittivity and (B) relative complex permeability of pure NZF and 50NZF-50RGO nanocomposite.

The reflection loss (RL) was calculated from the complex relative permeability and permittivity at a given frequency and specimen thickness using Equation 1.16 and 1.17 (Chapter 1). It has been observed that in X band region minimum RL values of these composites are greater than those of pure GO [105], RGO [92,106-108] (Table 1.1, Chapter 1) and NZF.

Pure NZF exhibited minimum reflection loss (RL) of -13.61 dB (~ 95% loss) at 10.72 GHz with effective bandwidth (i.e., minimum RL< -10dB) 9.8-12 GHz when absorber thickness was 1.9 mm (Fig. 2.14(A)). With increasing RGO content in 50NZF-50RGO nanocomposites minimum, RL was increased. The composite containing 50 wt% RGO,

i.e., 50NZF-50RGO, showed minimum RL of -19.99 dB (~ 99% loss) at 11.58 GHz with absorber thickness of 1.8 mm and effective bandwidth was 10.22-12.4 GHz (Fig. 2.14(B)). When thickness was increased from 1.8 to 1.95 mm, though minimum RL was decreased from -19.99 dB to -18.70 dB but effective bandwidth was increased from 10.22-12.4 GHz to 9.31-12.4 GHz. Hence, NZF-RGO nanocomposites have demonstrated that incorporation of RGO caused to enhance minimum RL value of the composites. As NZF-RGO composites possess heterogeneous structure, the accumulation of virtual charges at the interface between NZF-RGO, having different dielectric constant, leads to interfacial polarization (known as Maxwell-Wagner polarization). This might be one of the important factors which played a critical role in enhancing microwave absorption property of NZF-RGO compare to pure NZF [284,285].
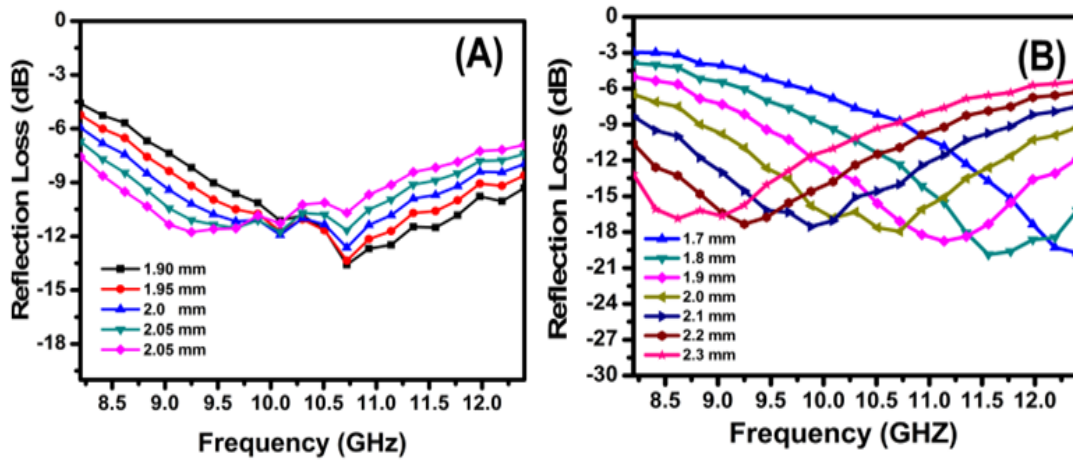
Fig. 2.14 Frequency dependence of reflection loss of synthesized (A) pure NZF and (B) 50NZF-50RGO nanocomposites by varying the thickness of the absorber.

2.3 Summary of results

(i)   In summary, we have described an *'in situ'* co-precipitation technique for preparation of NZF-RGO nanocomposites. Here, reduction of GO to RGO and formation of NZF nanoparticles from metal nitrates occurred simultaneously, which helped to anchor NZF nanoparticles on the sheets of RGO homogenously.

(ii)   The methodology employed to prepare these nanocomposites is very simple and does not require any elaborate setup.

(iii)   Moreover, in this method, no extra reducing agent was used to reduce GO. NaOH acted as a precipitating agent of metal hydroxides, which formed final NZF nanoparticle as well reducing agent to reduce GO to RGO.

(iv)   NZF-RGO nanocomposites having 50 wt.% RGO content (50NZF-50RGO) exhibited excellent catalytic activity towards decolorization of various dyes. The rates of the catalysis reactions are comparable and in some cases superior to the already reported catalysts [146,209,252-254,286-313]. This also showed its capability to reduce a toxic herbicide (trifluralin) which is frequently found in water as residue.

(v)   Magnetic nature of 50NZF-50RGO makes it a magnetically separable catalyst, which solves the separation related problem associated with the nanosized catalysts.

(vi)   50NZF-50RGO also exhibited ~ 99% minimum RL in the X-band region with effective bandwidth at 10.22-12.4 GHz. This nanocomposite not only shows higher minimum RL in comparison with pure NZF but also its light weight, (due to the presence of RGO) offers an added advantage.

(vii)   The heteroarchitectural structure of RGO-NZF composites caused to enhance its catalytic property as well as microwave absorption property.

(viii)   The minimum RL value of 50NZF-50RGO is comparable and in some cases greater than most of the ferrite and ferrite-RGO based composites [1-4,7,9-11,35, 52,59-64,107,109,126-134,139-143].

(ix)   50NZF-50RGO nanocomposites have demonstrated its capability to act as a multifunctional material in the area of the heterogeneous catalyst as well as microwave absorber.

Chapter 3

Synthesis of CoFe$_2$O$_4$-RGO: Excellent Microwave Absorber and Highly Efficient Magnetically Separable Recyclable Photocatalyst for Dye Degradation
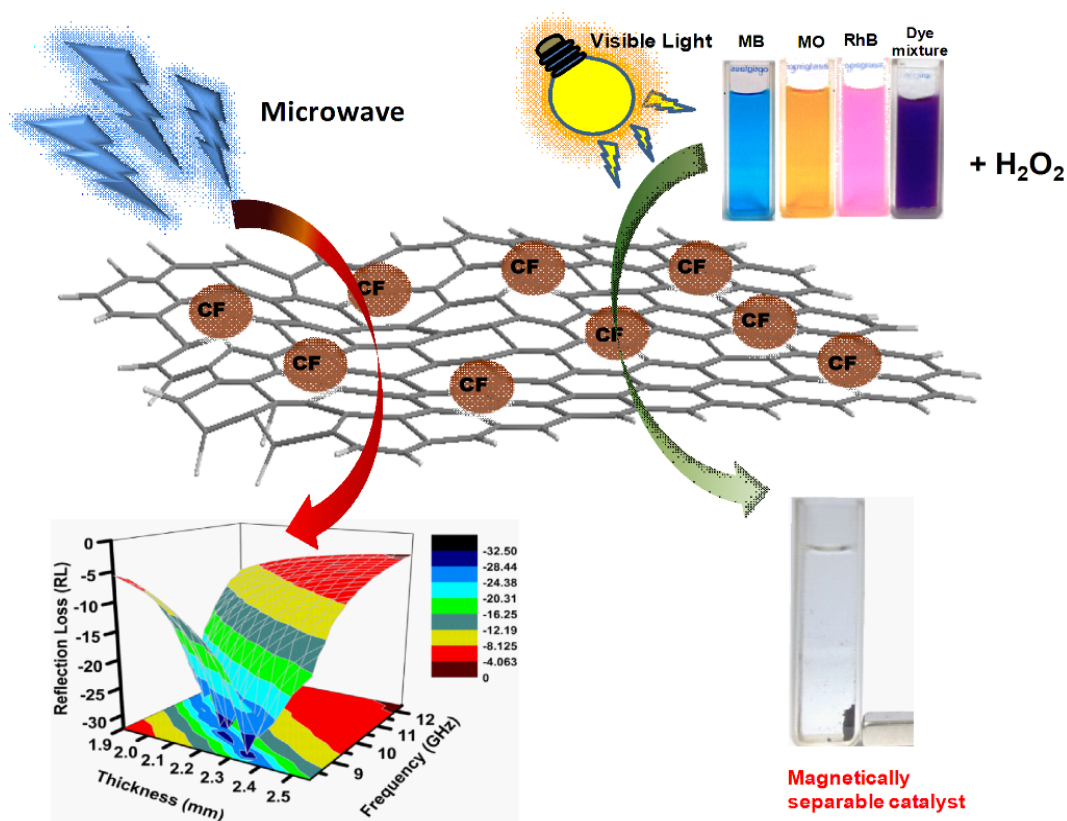
In this chapter an *'in-situ'* co-precipitation reduction method has been reported for the preparation of CoFe$_2$O$_4$-RGO (CF-RGO) nanocomposites with different weight ratios of CF and RGO. Their (i) structural characterizations, (ii) microwave absorption property in X-band region and (iii) photocatalytic activity towards degradation of synthetic organic dyes (e.g., Methyl Orange, Methylene Blue, Rhodamine B, and Dye mixture) were investigated under visible light generated from a 100W reading lamp in the presence of H$_2$O$_2$[7].

3.1 Experimental procedure[7]

3.1.1 Materials required

The chemicals used for synthesis of CF-RGO nanocomposites and photocatalysis tests are Cobalt nitrate Co(NO$_3$)$_2$.6H$_2$O (Merck, India), Iron nitrate Fe(NO$_3$)$_3$.9H$_2$O (Merck, India), Sodium hydroxide (NaOH) (Merck, India), Sodium nitrate (NaNO$_3$) (Merck, India), Sulphuric acid (H$_2$SO$_4$) (Merck, India), Potassium permanganate (KMnO$_4$) (Merck, India), 30% H$_2$O$_2$ (Merck, India), Polyethylene Glycol 400 (PEG 400) (S D Fine Chem Ltd). Methyl orange (Fisher scientific), Rhodamine-B (Fluka analytical), Methylene Blue (Fluka analytical), Graphite powder (Sigma Aldrich with a mean particle size of < 20 µm), Acetylene black (Sigma Aldrich), 1-Methyl-2-pyrrolidinone (Sigma Aldrich) and Poly (vinylidene fluoride) (Sigma Aldrich, Mw-180,000). All chemicals were used as received and without further purification. De-ionized water was used throughout the experiment.

3.1.2 Synthesis of CoFe$_2$O$_4$-Reduced Graphene Oxide (CF-RGO) nanocomposites

CoFe$_2$O$_4$-Reduced Oxide (CF-RGO) nanocomposites were synthesized by employing the same strategy which was used to prepare Ni$_{0.8}$Zn$_{0.2}$Fe$_2$O$_4$-Reduced Graphene Oxide (NZF-RGO) (Chapter-2).

3.1.2.1 Synthesis of Graphene Oxide (GO):

The protocol for the synthesis of Graphene Oxide has been described in section 2.1.2.1 of Chapter 2.

3.1.2.2 Synthesis of CoFe$_2$O$_4$–Reduced Graphene Oxide (CF-RGO) nanocomposites:

CoFe$_2$O$_4$-RGO nanocomposites were synthesized by employing an *'in situ'* co-precipitation reduction method using following steps: (i) In a round-bottomed flask stoichiometric amount of Co(NO$_3$)$_2$.6H$_2$O, and Fe(NO$_3$)$_3$.9H$_2$O were mixed with a PEG and H$_2$O mixture (PEG: H$_2$O weight ratio=1:5), (ii) In a separate beaker measured amount of graphene oxide (prepared by modified Hummer's method)[83] was well dispersed in de-ionized water using an ultrasonicator, (iii) This graphene oxide dispersion was then added to the mixture, which was prepared in step (i), (iv) In this mixture, an aqueous NaOH (2M) solution was added dropwise till pH was reached to ~11, (v) Then the temperature of the reaction mixture was raised to 160 °C and refluxed for 16h, (vi) After reflux, the reaction mixture was allowed to cool down at room temperature. The black color solid thus formed was separated from the mixture by applying a bar magnet externally. This solid was then washed with de-ionized water for several times, till pH of the washing became ~7. This solid was then dried at 60 °C for 10h. Using this protocol several CF-RGO nanocomposites, having different weight ratios of CF and RGO were prepared. Now onwards, nanocomposites having 5, 10, 15, 20, 25 and 50 wt. % RGO content will be referred as 95CF-5RGO, 90CF-10RGO, 85CF-15RGO, 80CF-20RGO, 75CF-25RGO and 50CF-50RGO respectively. Using this method pure CoFe$_2$O$_4$ (CF) nanoparticles were also synthesized where GO was not mixed. Except this, all parameters were kept same.

3.1.3 Photocatalytic activity test

To evaluate the photocatalytic activity of the synthesized CF-RGO nanocomposites towards photodegradation of methyl orange (MO), methylene blue (MB), rhodamine B (RhB) and dye mixture, photocatalyst reactions were conducted under visible light in the presence of H$_2$O$_2$. A 100 W reading lamp was used as a visible light source. In a typical photocatalysis reaction, 50 ml aqueous solution of 20 mg L^{-1} MO (in case of MB and Rh B the concentrations were 30 mg L^{-1} and 25 mg L^{-1} respectively) was mixed with 25 mg of catalyst in a 100 ml beaker. The mixture was then stirred mechanically in the dark for 1h to reach adsorption-desorption equilibrium between the dye and catalyst. Then, 2 ml of 30 % H$_2$O$_2$ was added to the reaction mixture, and the lamp (placed at a distance of 10 cm from the reaction mixture) was turned on. This point was considered as the starting point

(t=0) of the photochemical reaction. The change of concentration of dye in the reaction mixture with time was monitored spectrophotometrically (UV-vis spectrophotometer, V-570 Jasco, Japan) by following the decrease of absorbance at λ max (λ max (MO) = 464 nm, λ max (RhB) = 554 nm and λ max (MB) = 663 nm). As the absorbance of the dye is proportional to its concentration, the ratio of absorbance of the dye A_t (measured at time t) to A_o (at t = 0) is equal to C_t/C_o (where C_t is the concentration of dye at time t, and C_o is the initial concentration of the dye). After completion of the reaction, the catalyst was separated magnetically from the reaction mixture, washed several times with water and dried for recycling. Each catalysis reaction was performed three times, and reproducible results were obtained.

3.1.4 Magnetic separation and reusability test of the catalyst (CF-RGO)

After catalysis reactions, CF-RGO was magnetically separated from the reaction mixtures by applying a permanent magnet externally. Magnetic separation of the catalyst has been described in Section 2.1.4 of Chapter 2.

3.1.5 Microwave absorption measurement

The protocol for the measurement of microwave absorption of the synthesized nanocomposites has been described in Section 1.6 of Chapter 1.

3.2 Results and Discussion[7]

3.2.1 Structure and morphology of CF-RGO nanocomposites

XRD patterns of CF, pure GO, and CF-RGO nanocomposites are shown in Fig. 3.1. XRD of CF sample showed the diffraction peaks at 2θ= 18.23°, 30.35°, 35.72°, 37.83°, 43.32°, 53.94°, 57.20° and 62.89° corresponding to (111), (220), (311), (222), (400), (422), (511) and (440) planes of CoFe$_2$O$_4$ with cubic spinel structure, respectively [JCPDS card No. 22-1086]. XRD patterns of GO exhibited a strong peak at 2θ = 9.76°, and a small peak at 2θ = 42.14° for (001) and (101) planes of GO [60,256]. In the case of pure RGO a broad peak around 2θ = 24° and a small peak at 43°, corresponding to (002) and (001) plane [60,163,164] were observed. In the XRD patterns of CF-RGO nanocomposites following important points were observed:

(i) Presence of all the peaks corresponding to CF indicated the presence of CF nanoparticles in the composites, (ii) absence of peaks for GO (i.e., $2\theta = 9.76°$ and $42.14°$) indicated that during the preparation of CF-RGO composites, GO flakes were converted to RGO and RGO sheets were exfoliated [59,60,163,260]. This transformation of GO to RGO was also detected from the results obtained from TGA, FT-IR and Raman spectroscopy, which will be discussed later, (iii) no impurity peaks were detected, indicating the purity of CF-RGO nanocomposites. This is very important as presence of impurity phases significantly influences the magnetic, microwave absorption as well as photocatalytic activities of the composites, (iv) crystallite size of CF nanoparticles, calculated by Scherer's equation using (311) diffraction plane, was ~15 nm, (v) intensities of the peaks for CF were increased with increasing CF content in the composites.
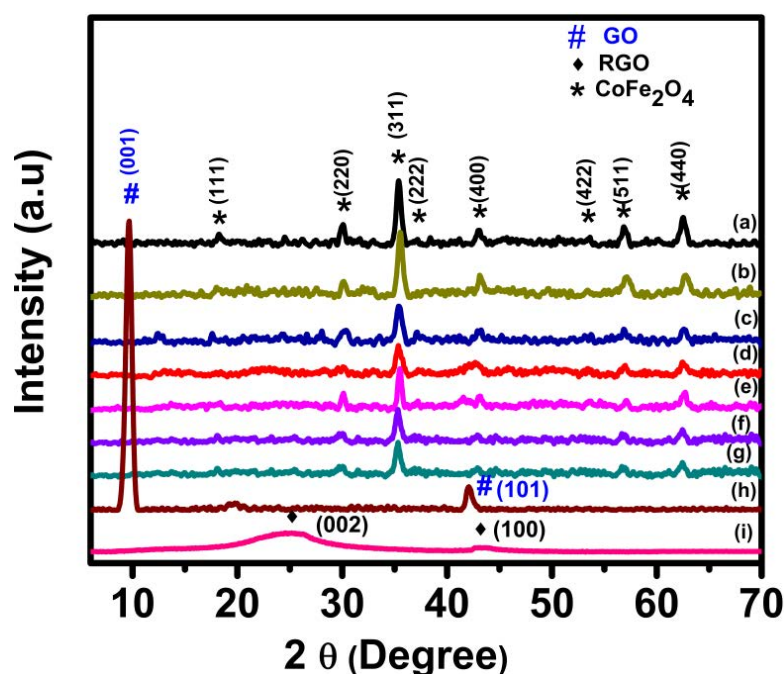
Fig. 3.1 Room temperature wide angle powder XRD patterns of (a) pure CF (b) 95CF-5RGO (c) 90CF-10RGO (d) 85CF-15RGO (e) 80CF-20RGO (f) 75CF-25RGO (g) 50CF-50RGO, and (h) GO.

Fig. 3.2 displays TEM micrographs of pure RGO (Fig. 3.2A and B), pure CF (Fig. 3.2C and D) and 85CF-15RGO nanocomposite (Fig. 3.2E and F). Fig. 3.2A shows a general view of RGO and a higher magnified image is shown in Fig. 3.2B. These micrographs exhibit the stacking of nanometer thin RGO flakes. Fig. 3.2C and D reveal that the average particle size of pure CF is ~ 15-20 nm. TEM images in Fig. 3.2E and F depict the general view and higher magnified image of 85CF-15RGO sample as

representative. These images show that CF nanoparticles are homogeneously embedded on the surface of nanometer thin RGO flakes. In HRTEM micrographs (Fig. 3.2G) well-resolved lattice fringes corresponding to (311) plane of CF were observed. SAED patterns (Fig. 3.2H) also show Debye-Scherrer diffraction rings for pure CF. EDAX analysis of the synthesized nanocomposites also confirmed the compositions of these composites (Fig. 3.3).
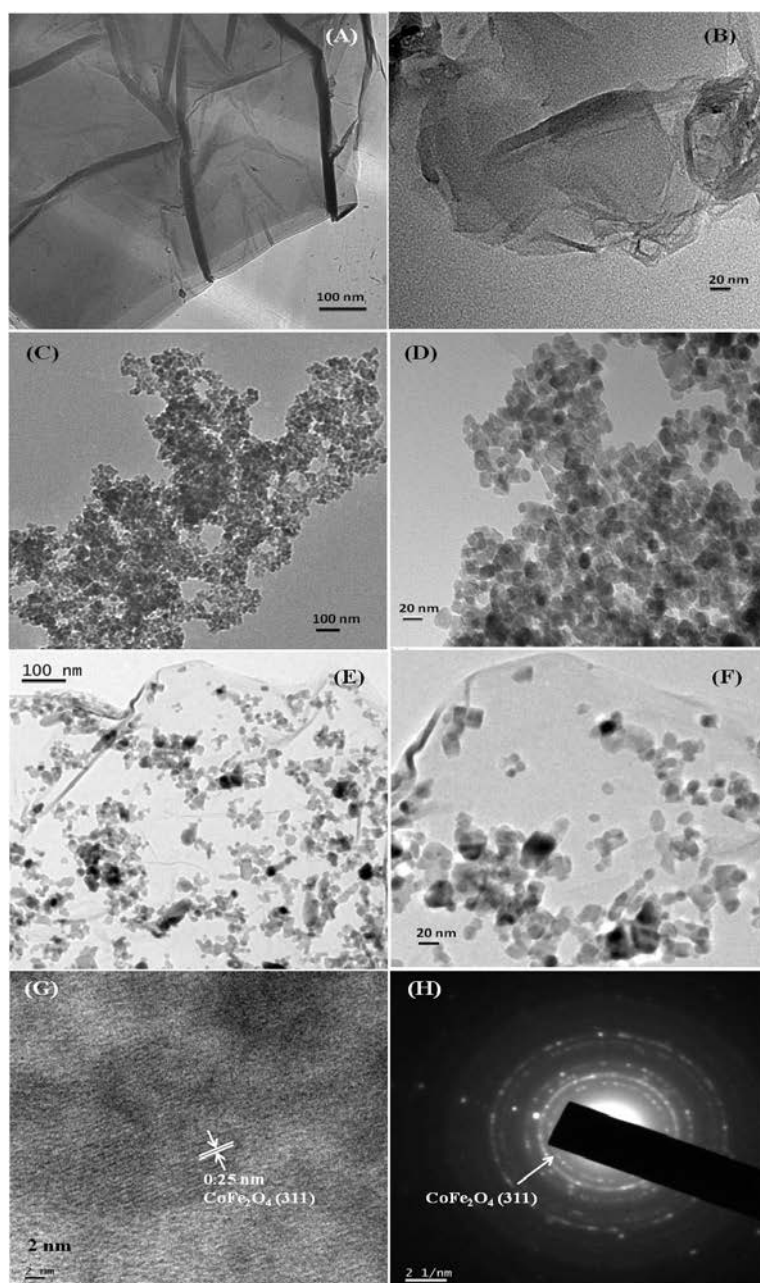
Fig. 3.2 TEM micrographs of synthesized RGO (A) and (B), Pure $CoFe_2O_4$ (C) and (D), 85CF-15RGO nanocomposites (E) and (F), HRTEM micrograph of 85CF-15RGO, (G) and SAED pattern of 85CF-15RGO (H).
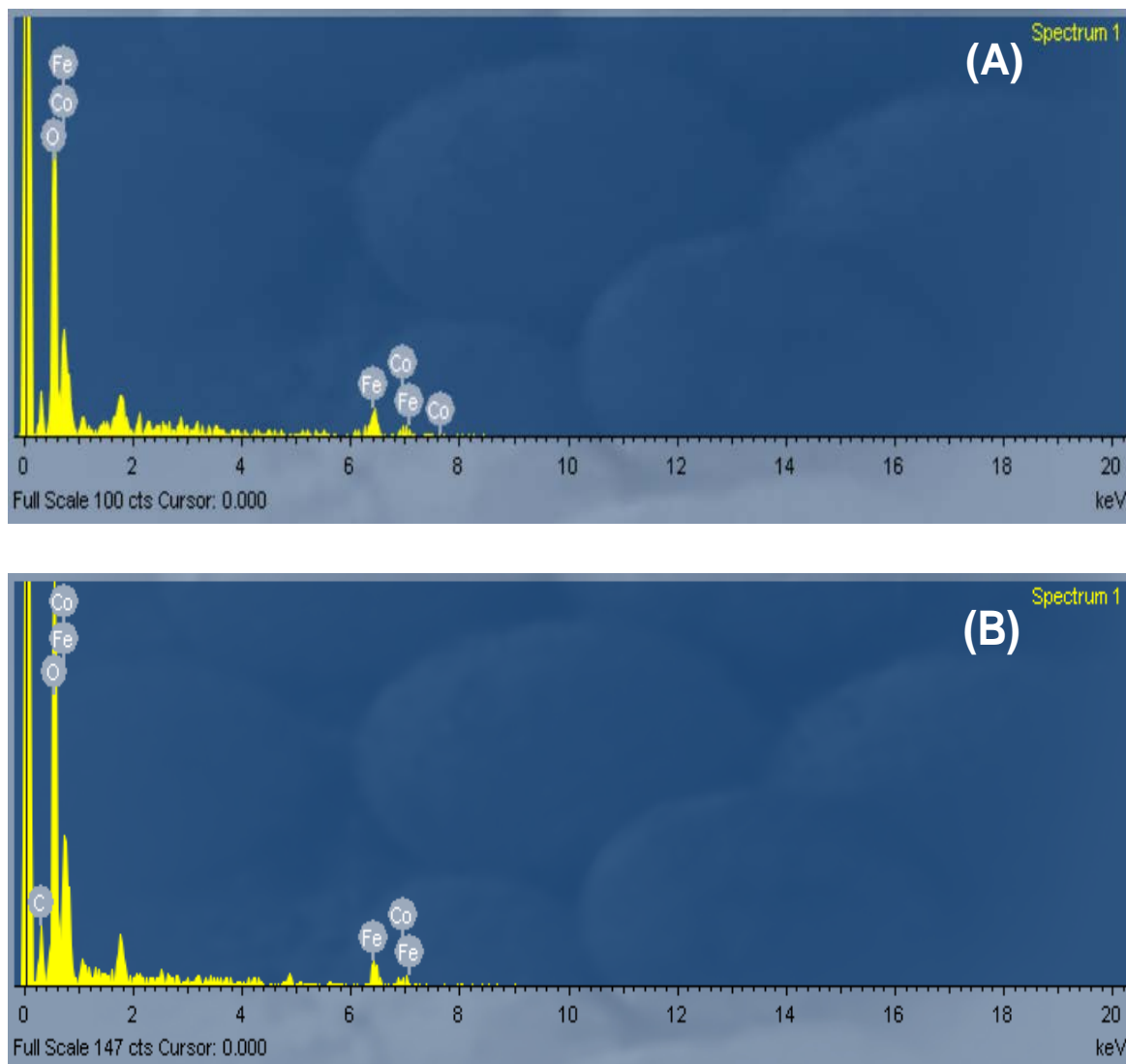
Fig. 3.3 EDAX spectra of (A) synthesized $CoFe_2O_4$ nanoparticles, and (B) $CoFe_2O_4$-RGO nanocomposite.

TGA analysis of GO and CF-RGO was performed in an air atmosphere in the temperature range of 30-850 °C with a heating rate of 10 °C/min. Fig 3.4 shows TGA thermograms of pure GO, pure CF, and CF-RGO nanocomposites having various compositions. In TGA thermograms following points were observed: (i) Pure CF is quite stable in the temperature range of 30-850 °C. (ii) In the temperature range of 30-100 °C, GO exhibited ~17% wt. loss, which might be due to evaporation of H_2O [60]. In this temperature range ~9% wt. loss occurred for 50CF-50RGO. (iii) In 100-200 °C temperature range, GO showed ~3% wt. loss and a sharp weight loss occurred in the range of 200-250 °C with 25% weight loss. This was due to the removal of oxygen-

containing groups from GO. However, only 9% wt. loss was observed for 50CF-50RGO. This fact clearly indicated that during synthesis of CF-RGO, GO was converted to RGO via reduction of oxygen-containing groups (e.g., carbonyl, carboxyl, epoxy groups, etc.) [60] during reflux with NaOH (iv) In 325-600 °C temperature range, the oxidative decomposition of carbon atoms of GO was observed whereas, in case of 50CF-50RGO, this decomposition of carbon occurred in the range of 275-375 °C. It was also observed that, ~50 wt. % CF remained undecomposed as residue. Similarly, for 85CF-15RGO and 75CF-25RGO nanocomposites 85 wt. % and 75 wt. % CF remained as a residue after thermal decomposition of the RGO component of the composites. So, we can also conclude that this *'in situ'* co-precipitation-reduction method for CF-RGO composite preparation is capable of producing composites with desired CF and RGO composition.
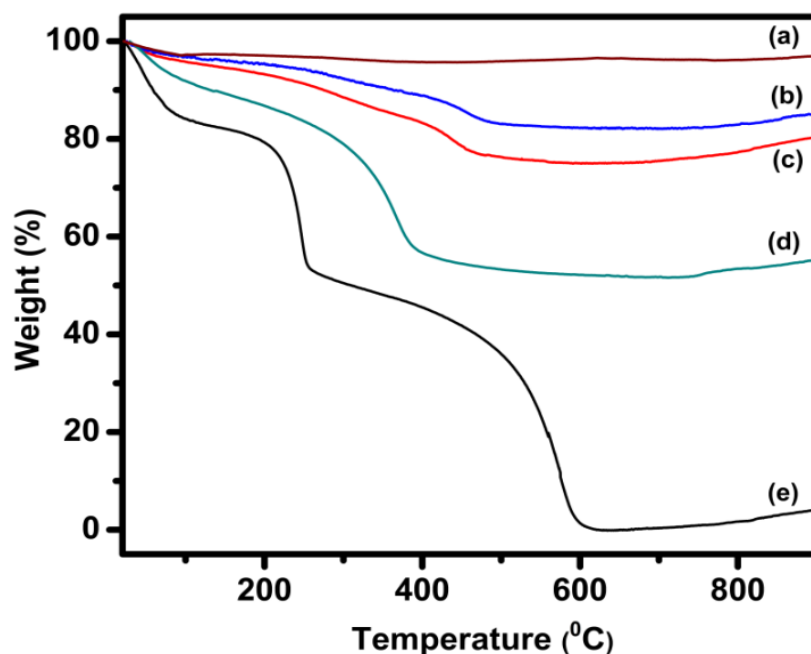
Fig. 3.4 TGA curves of (a) Pure CF, (b) 85CF-15RGO (c) 75CF-25RGO (d) 50CF-50RGO nanocomposite, and (e) GO.

Fig. 3.5 shows FT-IR spectra of pure GO, pure CF pure RGO (prepared by refluxing GO at 160 °C for 16h) and 85CF-15RGO. It was observed that in case of GO peaks appeared at (i) 1384 cm^{-1} corresponding to the stretching vibration of C-O of carboxylic group, (ii) 1720 cm^{-1} for a carbonyl group, (iii) 1226 cm^{-1} for C-O stretching vibration of epoxy group (iv) 1054 cm^{-1} for C-O stretching vibration [60,264]. This fact indicated the presence of oxygen-containing functional groups (e.g., epoxy, carbonyl, carboxyl, and hydroxyl) on the surface of GO. Moreover, the peak at 1621 cm^{-1} can be assigned to the

contribution from the skeletal vibration of the graphitic domains [60,63,159,265]. In case of pure RGO the peak at 1720 cm^{-1} (for carbonyl group) was found to be disappeared, and intensities of the peaks at 1226 and 1054 cm^{-1} (corresponding to C-O) have decreased. The appearance of a peak at 1544 cm^{-1} was also observed. The band at 1621 cm^{-1} (in GO sample), which can be assigned to the C=C skeletal vibration of graphitic domains of GO, has been redshifted to 1544 cm^{-1} for RGO and indicated the partial restoration of π-π conjugation of graphene sheet in RGO [159]. Absorption bands at the same positions were observed in FT-IR spectra of CF-RGO nanocomposite samples. Here also carboxylic group vibration band ($v_{C=O}$ at 1720 cm^{-1}) was found to be disappeared, and absorption intensities corresponding to C-O at 1226 and 1054 cm^{-1} were decreased. These results implied that most of the oxygen-containing groups of GO, particularly carboxyl groups, had been removed and some of the hydroxyl and epoxy groups remained on the surface of RGO in CF-RGO nanocomposites.
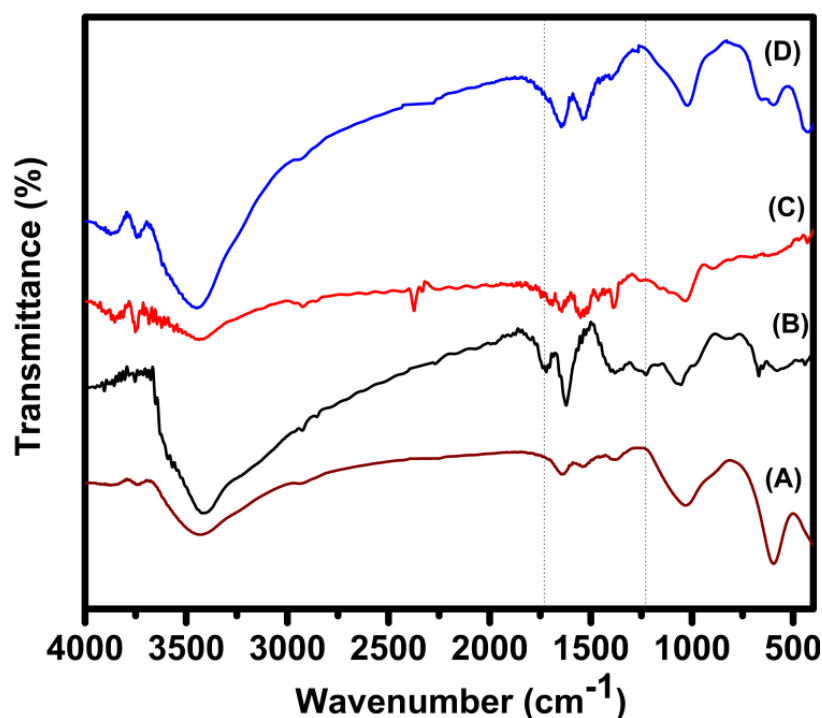
Fig. 3.5 FT-IR spectra of (A) Pure CF, (B) GO, (C) RGO, and (D) 85CF-15 RGO.

In the FTIR spectra of pure CF appearance of a peak at 591 cm^{-1}, could be ascribed to lattice absorption of M-O (M= Fe^{3+}, Co^{2+}), confirmed the formation of CoFe$_2$O$_4$ [142] Presence of this peak in CF-RGO samples indicated the existence of CoFe$_2$O$_4$ in CF-RGO nanocomposite [60,63].

Raman spectra of CF-RGO composites (Fig. 3.6A-B) also confirmed the presence of RGO in the composites. In Raman spectra of pure GO, characteristic peaks for D and G band were found at 1355 and 1599 cm^{-1} respectively. In case of 85CF-15RGO samples, these peaks appeared at 1349 and 1580 cm^{-1}. It has been reported that Raman shift of D and G bands shifts to lower values when GO is reduced to RGO [163]. I$_D$/I$_G$ ratio of 85CF-15RGO was found to be ~ 1.06 whereas this ratio was ~ 0.9 for pure GO [63]. This increase of I$_D$/I$_G$ value for 85CF-15RGO can be attributed to the decrease in the average size of sp^2 domains upon reduction of GO during formation of CF-RGO composite [45,63].
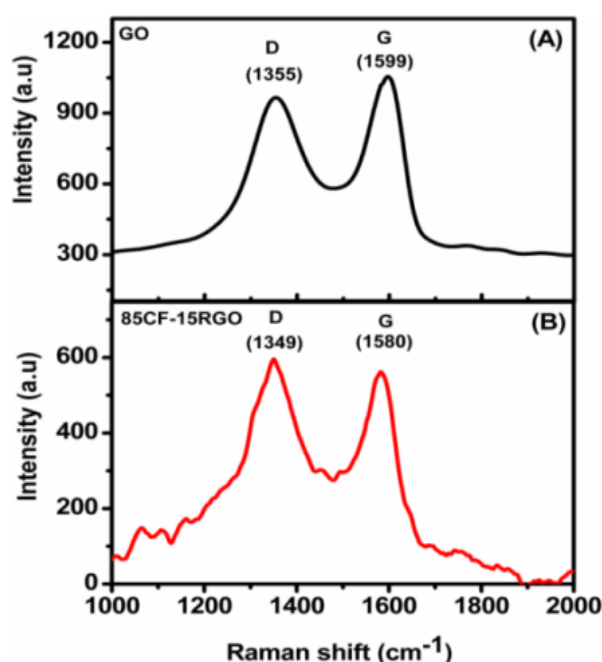
Fig. 3.6 Raman spectra of (A) GO and (B) 85CF-15RGO.

The results obtained from XRD, TGA, HRTEM, FT-IR, and Raman spectroscopic measurement indicated that when the mixture of GO, metal nitrates, and NaOH were refluxed for 16 h at 160 °C, two reactions proceeded simultaneously, (i) reduction of GO to RGO and (ii) formation of CoFe$_2$O$_4$ nanoparticles.

3.2.2 Formation mechanism of CoFe₂O₄ nanoparticles

To understand the growth mechanism of $CoFe_2O_4$ nanocrystals a set of the experiment were conducted, where the reaction mixtures of $Fe(NO_3)_3 \cdot 9H_2O$, $Co(NO_3)_2 \cdot 6H_2O$ and NaOH solutions were refluxed at 160 °C for different times (0 h to 12 h). The precipitates thus formed were analyzed by XRD to identify the crystal phases formed with changing reflux time. The precipitate, formed soon after the addition of NaOH solution at room temperature, (i.e., 0 h), was amorphous in nature. This brown precipitate was might be iron oxy-hydroxide (FeOOH), which is thermally stable at low temperature [314]. As pH of the reaction was high (pH 11-12), Co^{2+} ions were remained in solution due to the selective dissolution of $Co(OH)_2$ [315]. Precipitate, formed after 1 h of reflux, was mostly amorphous in nature. However, the formation of $CoFe_2O_4$ nanocrystals was started at this point as a small peak at $2\theta = 35.65°$ (311) plane of $CoFe_2O_4$ was observed in its XRD pattern. XRD patterns of the precipitates, obtained till 9 h of reflux, showed only the peak at $2\theta = 35.65°$, but with increasing reflux time the intensity of this peak was increased indicating the progressive increase of crystallite size from ~ 5 nm to 7 nm. XRD patterns are provided in Fig. 3.7

Formation of $CoFe_2O_4$ nanoparticles can be presented by the following reactions: [7,52]

$$Fe^{3+} + 3OH^- \longrightarrow FeOOH + H_2O \qquad (3.1)$$

$$2FeOOH + Co(OH)_2 \xrightarrow[16h]{160^0C} CoFe_2O_4 + 2H_2O \qquad (3.2)$$
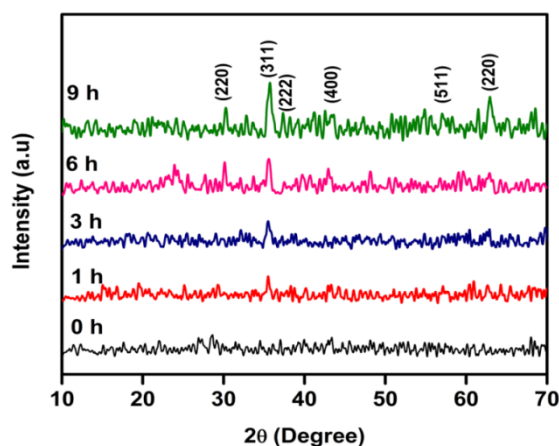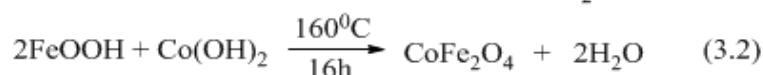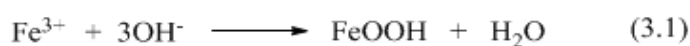
Fig. 3.7 Room temperature wide angle powder XRD pattern of the precipitates refluxed at 120 °C at a different time (0 h to 9h).

Formation of CF-RGO nanocomposites has been illustrated in Scheme-3.1.
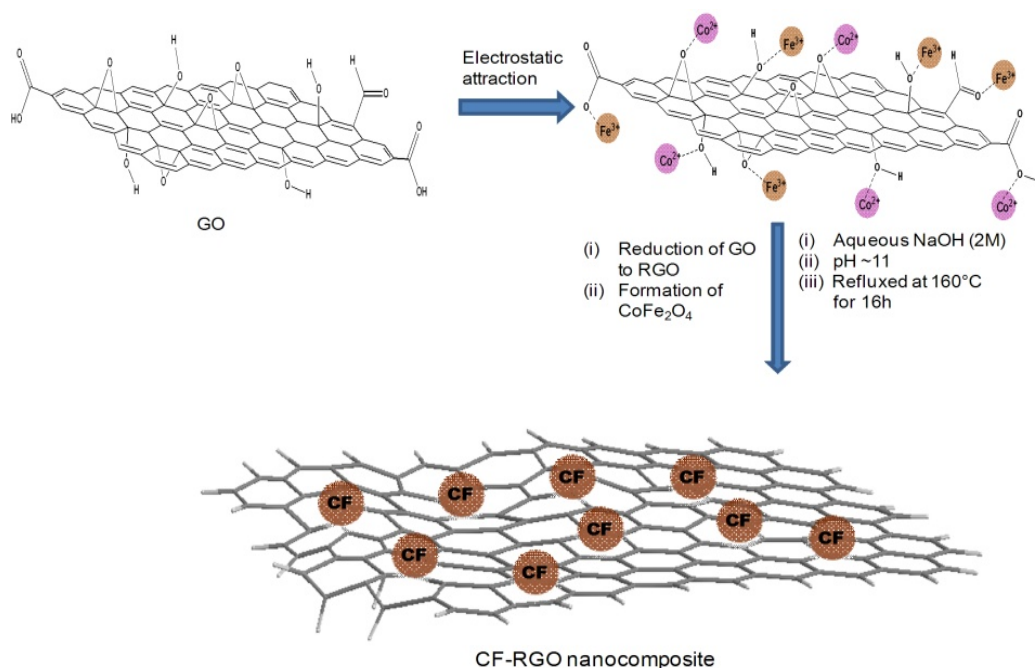
Scheme 3.1 Formation of CF-RGO nanocomposites in *'in situ'* co-precipitation reduction method.

As the formation of CF and RGO occurred simultaneously their interfacial interaction was expected to be superior to the composites where RGO and $CoFe_2O_4$ were prepared separately. As a consequence, CF nanoparticles were well dispersed on the surface of RGO. Presence of PEG in the reaction mixture during CF formation restricted the formation of large CF particles or agglomeration of CF nanoparticles.

3.2.3 Magnetic property of CF-RGO

Room temperature magnetic property measurement of synthesized CF and CF-RGO nanocomposites (Fig. 3.8) by Vibrating Sample Magnetometer (VSM) showed that with increasing RGO component saturation magnetization (M_s) and coercivity (H_c) values for pure CF were decreased. In these composites presence of nonmagnetic RGO along with several other factors (e.g., attachment of CF nanoparticles on the surface of RGO sheets which might influence particle surface spin, disordered surface spin structure, dipolar interparticle interactions, etc. of CF nanoparticles [63,268-270]) play important roles in determining their M_s values. This also indicated that the magnetic properties of these

composites materials could also be tuned by changing the ratio of metal nitrate salts to GO [271].
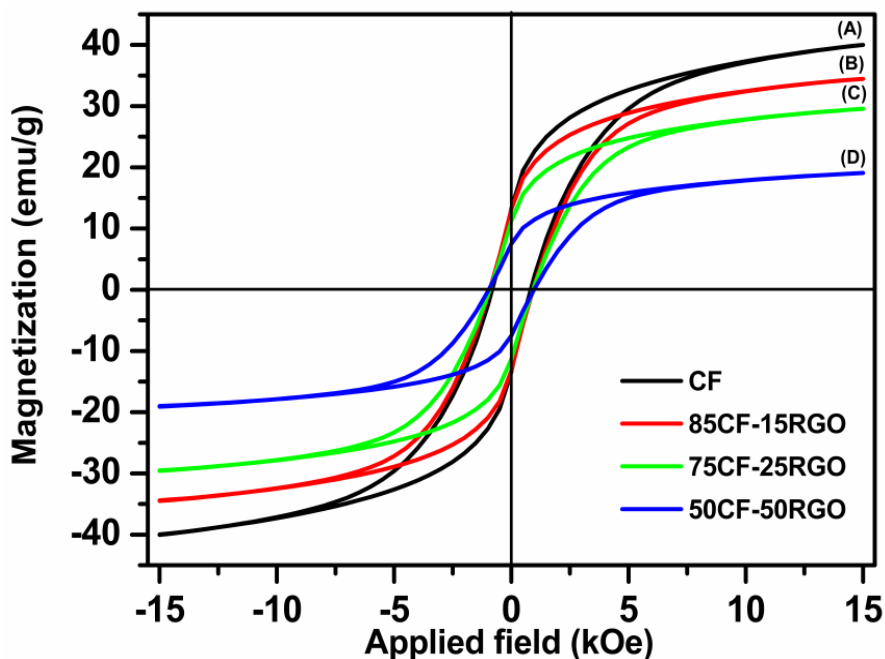
Fig. 3.8 Room temperature magnetic hysteresis loops for (A) pure CF, (B) 85CF-15RGO, (C) 75CF-25RGO, and (D) 50CF-50RGO.

Table 3.1: Magnetic properties of CF and CF-RGO nanocomposites

Sample	M_s (emu.g^{-1})	H_c (O_e)
Pure CF	39.96	820.04
85CF-15RGO	34.40	812.59
75CF-25RGO	29.50	789.26
50CF-50RGO	18.99	773.71

3.2.4 Photocatalytic activity of CF-RGO nanocomposites

The photocatalytic activities of $CoFe_2O_4$ nanocrystals and CF-RGO nanocomposites were evaluated by the degradation of dyes (MO, RhB, MB, and mixture of dyes) in the presence of H_2O_2 under visible light irradiation. The UV-vis spectra of these photocatalysis reactions are shown in Fig. 3.9. It has been observed that almost no

photocatalysis reaction occurred in the absence of catalyst (Fig. 3.10). Pure $CoFe_2O_4$ nanocrystals and RGO also exhibited their inertness as a catalyst towards these photocatalysis reactions. Photocatalysis reaction did not occur in the presence of (i) only visible light irradiation but absence of any catalyst and H_2O_2, (ii) visible light irradiation and H_2O_2 but without CF or catalyst, (iii) visible light irradiation, H_2O_2 and CF (iv) visible light irradiation and 75CF-25RGO but without H_2O_2 (Fig. 3.11), whereas the nanocomposites (CF-RGO) showed enhancement of photocatalytic activity dramatically in the presence of visible light and H_2O_2 (Fig. 3.10A). The photocatalytic activity of CF-RGO was increased with increasing RGO content in composites till 25 wt. % of RGO. The times required to degrade MO completely for the catalyst having 5, 10, 15 and 25 wt. % RGO were 270, 150, 120, and 60 mins, respectively. Further increase of RGO content caused to increase the completion time of the photocatalytic reaction. Fig. 3.10A shows the effect of different catalysts on photocatalytic degradation of MO. It has also been observed that the time required to complete photo-degradation of MO has decreased with increasing catalyst dose up to 500 mg L^{-1} and then no significant decrease of time was observed when more catalyst was used (Fig. 3.10B). Similarly, use of 2 ml of H_2O_2 was found to be optimum amount for the photocatalysis reaction (Fig. 3.10C).
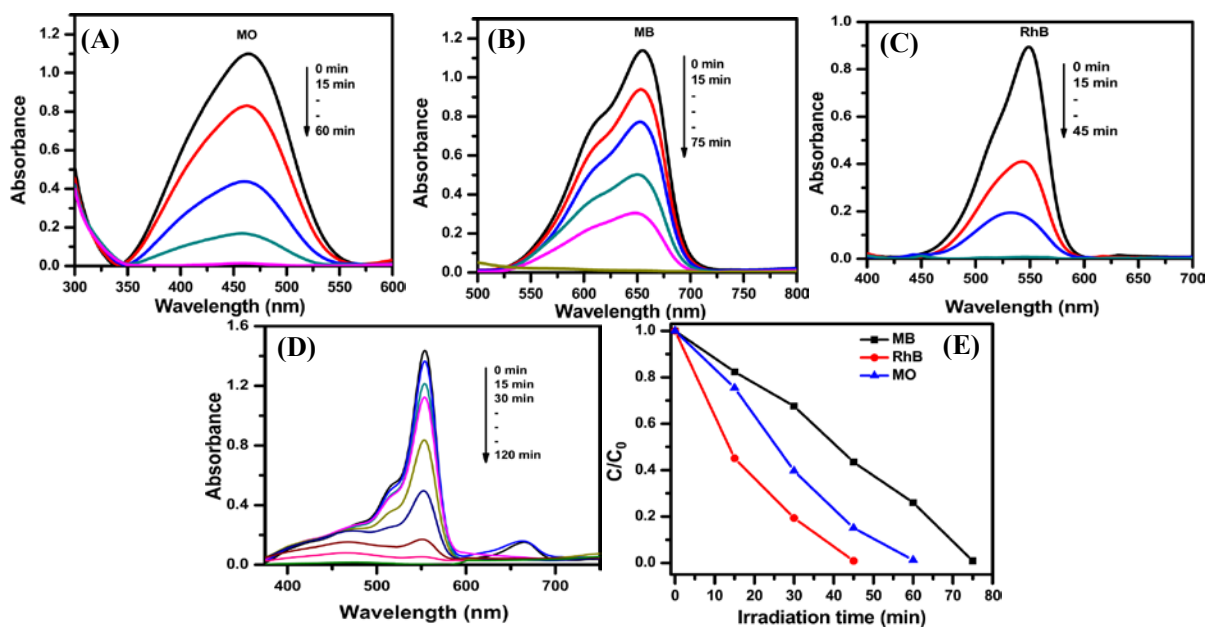
Fig. 3.9 Time-dependent UV-vis spectral changes of photocatalysis reactions for various dyes (A) Methyl orange, (B) Methylene blue, (C) Rhodamine B, and (D) mixture of dyes. (E) Photocatalytic degradation of different dyes catalyzed by 75CF-25RGO.
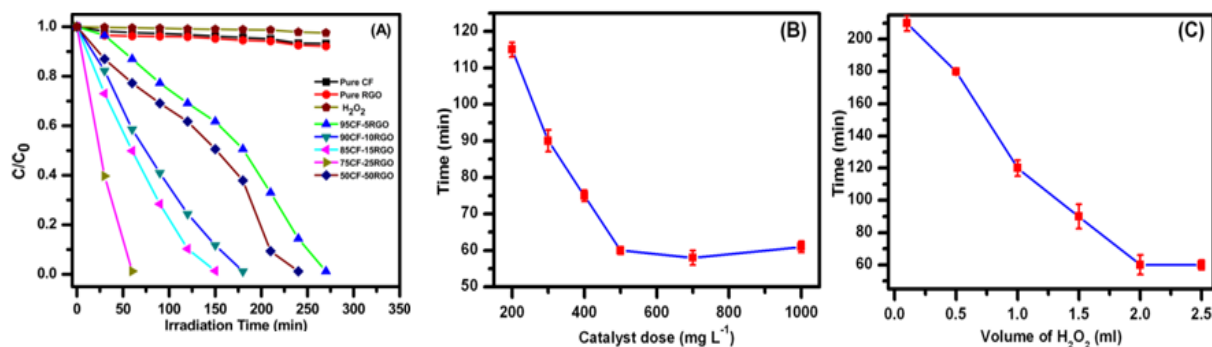
Fig. 3.10 (A) Effect of different catalysts and visible light on photocatalytic degradation of MO. Effect of (B) catalyst dose, and (C) H$_2$O$_2$ on the completion time of photocatalysis reaction of MO catalyzed by 75CF-25RGO.
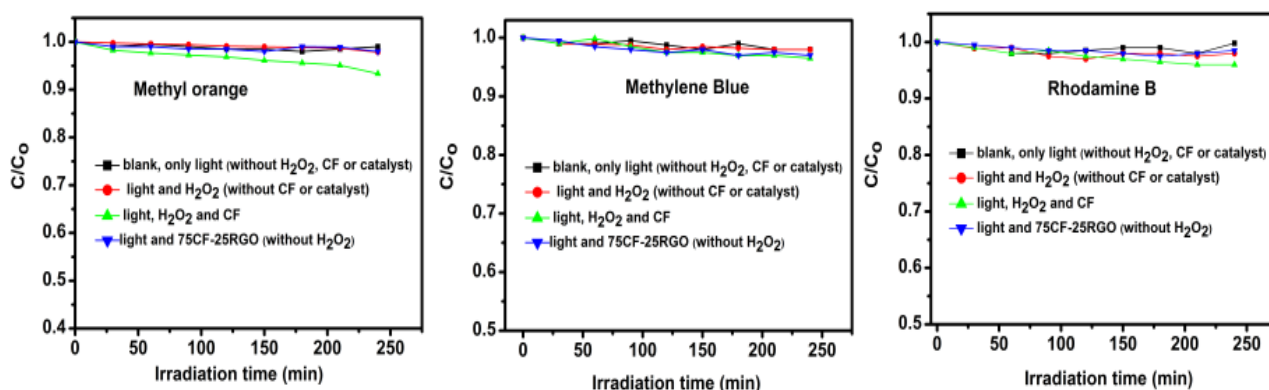
Fig. 3.11 These C/C$_0$ vs. Irradiation time plots show that photocatalysis reactions of dyes do not occur in the absence of CF-RGO and H$_2$O$_2$.

Hence to conduct photocatalysis reactions 500 mg L^{-1} of the catalyst does, and 2 ml of H$_2$O$_2$ were used for all the catalysis reactions. The photodegradation rates of MO using different CF-RGO nanocomposites under visible light irradiation decreased in the following order 75CF-25RGO > 85CF-15RGO > 90CF-10RGO > 50CF-50RGO > 95CF-5RGO. When 75CF-25RGO was used as a catalyst then times required to complete photodegradation of MO, MB, RhB, and a mixture of dyes by 75CF-25RGO were 60 min, 75 min, 45 min and 120 min respectively (Fig. 3.9).

As mentioned above CF-RGO nanocomposites exhibit higher photocatalytic activity than pure CF towards degradation of various dyes under visible-light irradiation. Fig. 3.12A shows the UV-vis absorption spectra, also named as diffuse reflectance spectra (DRS), of CF and 75CF-25RGO nanocomposite.

From absorption spectra, it was clearly observed that pure CF absorbs light in the entire range ~200 to 800 nm. However, the nanocomposites composed of RGO and CF (75CF-25RGO), absorbs more light energy in both near UV (300-400 nm) region and visible light region (400-800 nm). These features clearly suggest that incorporation of RGO into the system plays an important role in the optical absorption behavior of these nanocomposites in the near UV region and visible light region. UV-Vis spectra of the synthesized composites were recorded in diffuse reflectance mode (R = reflection intensity) and transformed to the absorbance coefficient (α) by Kubelka-Munk function F(R) [316]. The optical absorption coefficient (α) near the band edge follows the Kubelka-Munk function as :

$$F(R) = \frac{(1-R)^2}{2R^2} \qquad (3.3)$$

To calculate the band gap of the samples, the Kubelka-Munk function and Tauc plot were used (equation 3.4) [317]

$$\alpha h v = A \ (h v - E_g)^{n/2} \qquad (3.4)$$

where *h, v,* and E_g are Planck's constant, frequency of light and band gap, respectively. *A* is a constant.
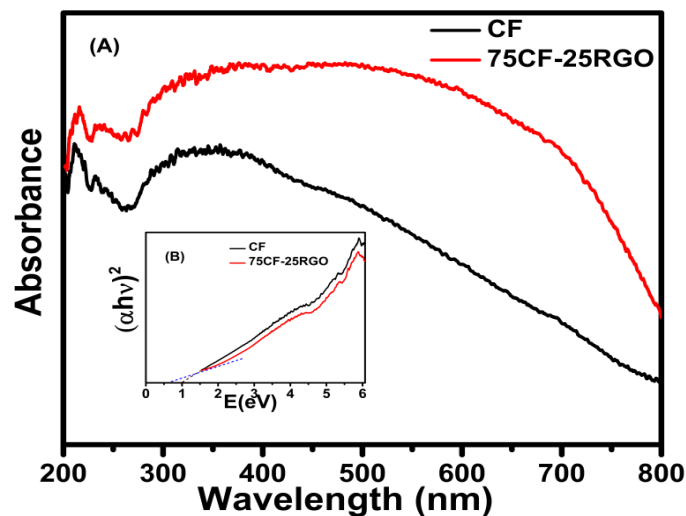
Fig. 3.12 (A) UV-vis absorption spectra of CF and 75CF-25RGO nanocomposite and (B) The inset is the plot of transformed Kubelka-Munk function versus the energy of light.

The plots of $(\alpha h v)^2$ versus hv for CF and 75CF-25RGO is shown as an inset in Fig. 3.12B and the band gap (E_g) values, determined from this plot, for CF and 75CF-25RGO are 1.08 and 0.85 eV respectively. These values are consistent with values reported by Gan et al. [318]. This decrease of band gap energy due to the incorporation of RGO is one of the key factors for enhancement of photocatalytic activity of CF-RGO nanocomposites.

Upon irradiation with visible light $CoFe_2O_4$ nanoparticles yield electrons (e) and holes (h) by charge separation (reaction-3.5).

$$CoFe_2O_4 \ + \ hv \ \longrightarrow \ CoFe_2O_4 \ (h+e) \qquad (3.5)$$

It was observed that $CoFe_2O_4$ is showing inertness as a catalyst towards photodegradation reaction. Recombination of holes and electrons which are photo generated in $CoFe_2O_4$ might be the main reason for this. Presence of highly conductive RGO in CF-RGO prevents the recombination of holes and electrons because electrons are quickly transferred to RGO sheets via a percolation mechanism (reaction-3.6).

$$CoFe_2O_4 \ (e) \ + \ RGO \ \longrightarrow CoFe_2O_4 \ + \ RGO \ (e) \qquad (3.6)$$
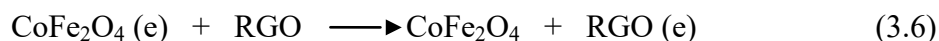
These electrons produce free radicals ($^{\bullet}OH$), superoxides ($O_2^{\bullet\ -}$) by reacting with H_2O_2, H_2O, dissolved O_2 (Reaction 3.7-3.11). Holes (generated in reaction-3.4) also produce $^{\bullet}OH$ when react with OH^- [319].

$$RGO \ (e) \ + \ O_2 \ \longrightarrow \ O_2^{\bullet\ -} \ + \ RGO \qquad (3.7)$$

$$O_2^{\bullet\ -} \ + \ H_2O \ \longrightarrow \ HO_2^{\bullet} \ + \ OH^- \qquad (3.8)$$

$$HO_2^{\bullet} \ + \ H_2O \ \longrightarrow \ H_2O_2 \ + \ ^{\bullet}OH \qquad (3.9)$$

$$H_2O_2 \ + RGO \ (e) \ \longrightarrow \ 2 \ ^{\bullet}OH \ + \ OH^- \qquad (3.10)$$

$$CoFe_2O_4 \ (h) \ + \ OH^- \ \longrightarrow \ CoFe_2O_4 \ + \ ^{\bullet}OH \qquad (3.11)$$
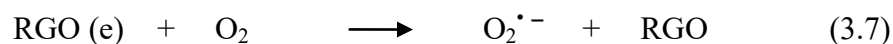
These free radicals and superoxide anions oxidize the dye molecules, which are adsorbed on the surface of the catalyst (Reaction-3.12).

$$\text{Dye} + {}^{\bullet}\text{OH (and / or } O_2{}^{\bullet\,-}) \longrightarrow \text{intermediates} \longrightarrow CO_2 + H_2O \qquad (3.12)$$
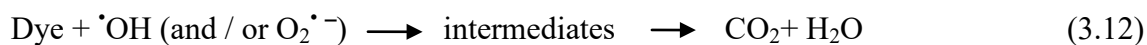
As shown in these reactions the RGO in RGO-CF catalysts prevents the hole-electron recombination, which in turns helps the formation of ${}^{\bullet}\text{OH}$, $O_2{}^{\bullet\,-}$. This explains the enhanced photocatalytic activity of CF-RGO nanocomposites.

To understand the synergistic effect between CF and RGO on the electrical conductivity of CF-RGO nanocomposites the electrochemical impedance measurements of pure CF, GO and CF-RGO nanocomposites were performed. The protocol for the electrochemical impedance measurements of the synthesized nanocomposites has been described in Section 1.6 of Chapter 1. The impedance plots of the synthesized materials are shown in Fig. 3.13.
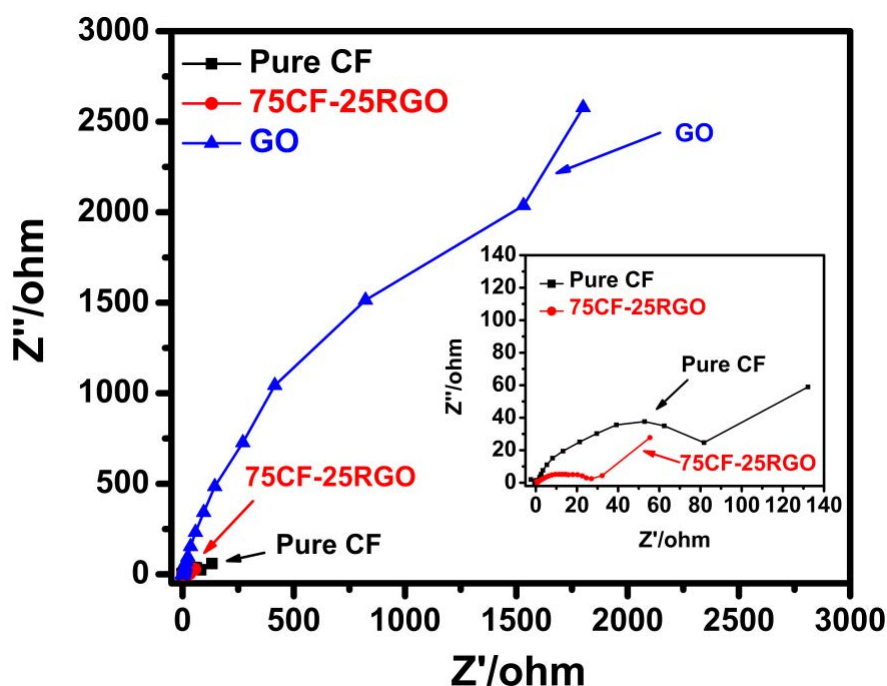
Fig. 3.13 The electrochemical impedance spectra (EIS) of 75CF-25RGO, pure CF, and GO. The spectrum in the inset is enlarged to show the impedance of 75CF-25RGO and pure CF.

It was observed that the impedance plot of 75CF-25RGO nanocomposite has a smaller radius than those of GO and pure CF. This fact indicates that charge transfer resistance of 75CF-25RGO has significantly reduced and GO has been reduced to RGO during the synthesis of CF-RGO nanocomposites [318]. This is because of graphene is a zero band gap semiconductor and a two-dimensional π conjugated system in which charge carriers behave as massless fermions, resulting in its unique electron transport properties [163,276,318]. Thus, the photogenerated electrons of CF could transfer easily from the conduction band to RGO and rapidly transport the instant that they formed. As a result of the great inhibition for the recombination of photogenerated electrons and holes, the photocatalytic activity of CF-RGO was significantly enhanced.

The lowering of band gap energy of $CoFe_2O_4$ in the presence of RGO in CF-RGO nanocomposites and the photodegradation of dye molecules catalyzed by CF-RGO composite are illustrated in Scheme-3.2
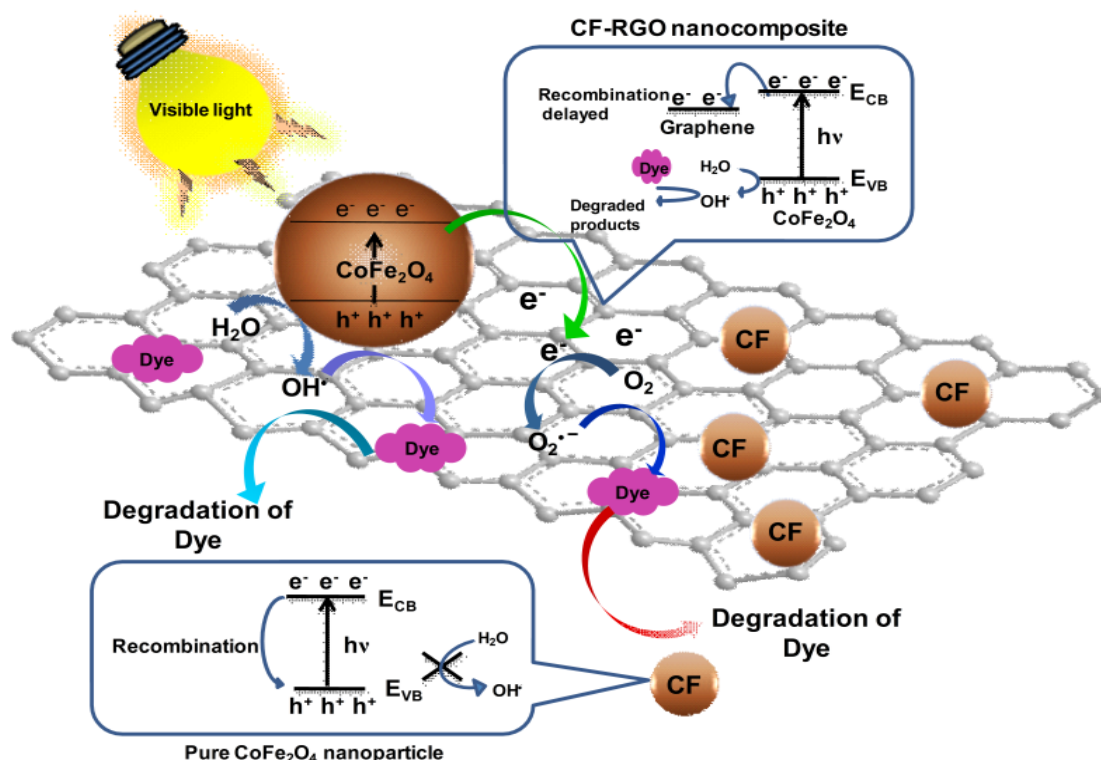
Scheme 3.2 Schematic illustration of the photocatalysis reaction mechanism of CF-RGO nanocomposites towards degradation of synthetic dye.

75CF-25RGO exhibited high catalytic efficiency towards degradation of a mixture of dyes. The dye mixture (MO, RhB, and MB) was decolorized (Fig 3.9D) within 120 min when treated with 75CF-25RGO ([catalyst] = 500 mg L^{-1}, [MO] = 20 mg L^{-1}, [MB] = 32 mg L^{-1} and [RhB] = 24 mg L^{-1} and [H_2O_2] = 40 ml L^{-1}). After separating the catalyst from the reaction mixture after the reaction, the catalyst was washed with alcohol, and it was observed that no unreacted dye molecule was remained adsorbed in the catalyst indicating complete photodegradation of dyes. As CF is magnetic in nature, 75CF-25RGO nanocatalyst offers an additional advantage along with the high catalytic activity.

The catalyst can be easily separable from the reaction mixture after completion of the reaction by using an external magnet. This easy magnetic separation of this catalyst also helps to overcome the limitation of separation problem associated with nanoparticles catalyst. Fig. 3.14 illustrates the complete decomposition of the dyes, resulting in decolorization of dye solution due to the photocatalytic reaction and magnetic separation of the catalyst by employing a bar magnet externally.
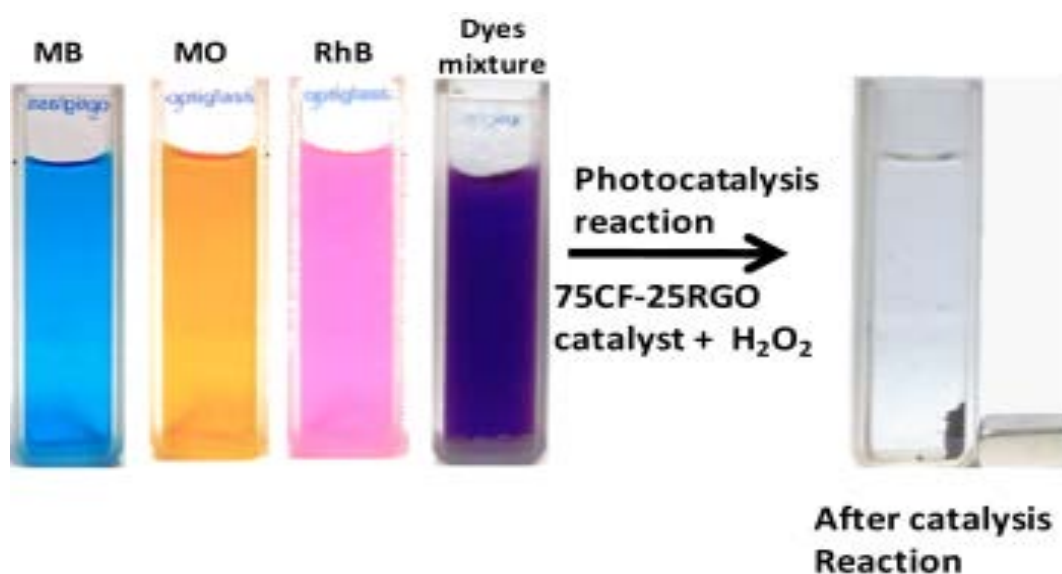
Fig. 3.14 Decolourization of dye solutions due to photocatalytic reaction and magnetic separation of the catalyst by applying a magnet after completion of reaction

3.2.5 Reusability of CF-RGO nanocomposites

After completion of the reaction, the catalyst was separated by applying an external magnetic. Then the catalyst was washed thoroughly by de-ionized water several times and dried at 90°C for 4h and reused. The experiment was repeated several times. The activity of the catalyst was found almost same up to 5 consecutive cycles (Fig. 3.15). XRD patterns and TEM micrograph of the reused catalyst also showed no significant change in their crystal structure as well as morphology compared to the fresh catalyst (Fig. 3.16A-B).
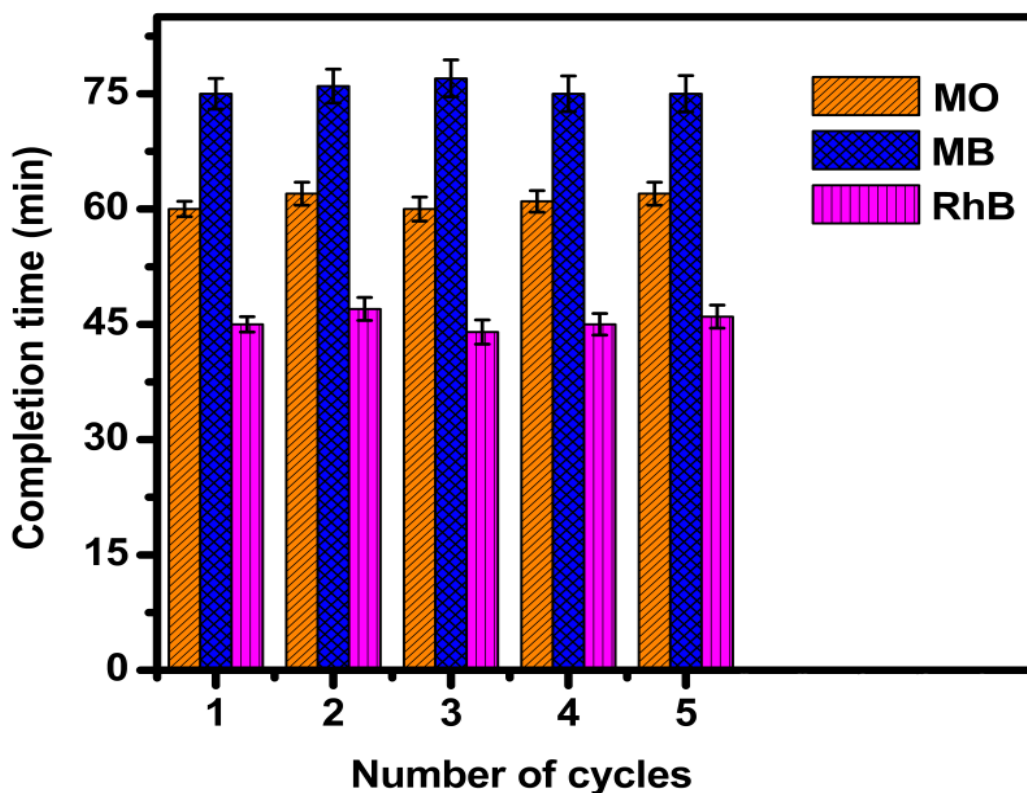
Fig. 3.15 Reusability of magnetically separable catalyst (75CF-25RGO) for the photodegradation of MO, MB, and RhB.
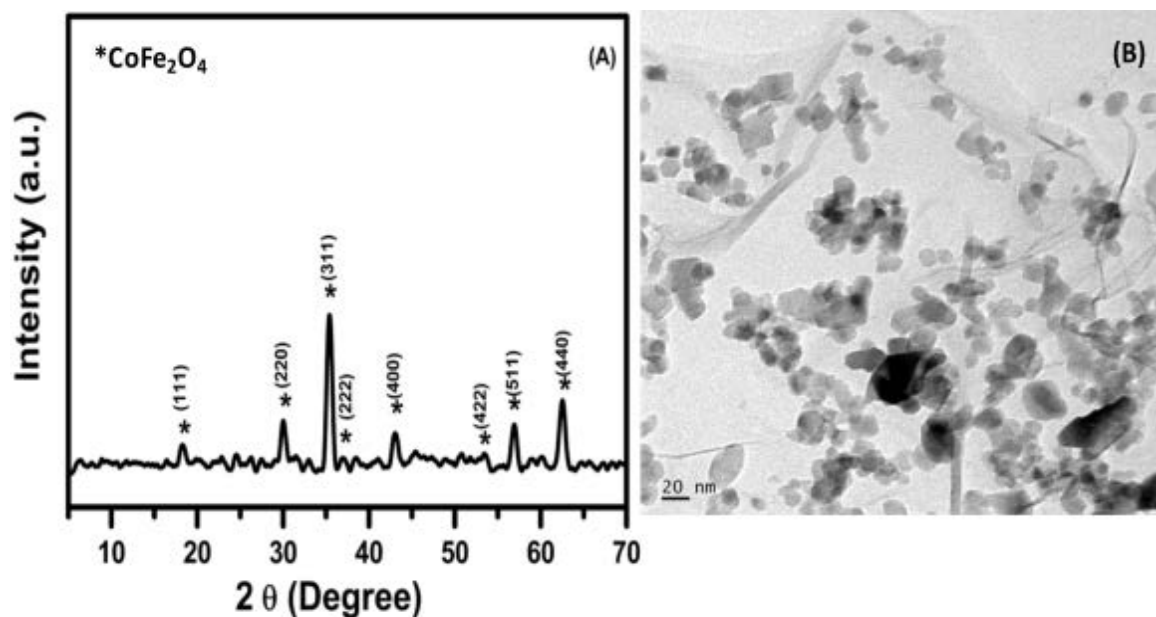
Fig. 3.16 (A) XRD and (B) TEM micrograph of the recycled 75CF-25RGO catalyst.

3.2.6 Microwaves Absorption property of CF-RGO nanocomposites

From the measurement of ε', ε'', μ' and μ'' of pure CF and CF-RGO nanocomposites over the frequency range of 8.2 to 12.4 GHz (X-band) (Fig. 3.17) it was observed that (i) the values of ε' and ε'' were increased with increasing RGO content in the composite. This might be due to the fact that larger number of RGO sheets might enhance the electrical polarization and electrical conductivity of the samples because ε' is an expression of the polarizability of materials and consists of dipolar polarization and electric polarization at microwave frequency [11,45,60]. (ii) Over the frequency range ε' and ε'' remained almost constant. (iii) The values of μ' and μ'' were found to be increased with increasing CF content in the composite and the values were decreased with increasing frequency from 8.2-12.4 GHz. Therefore, it is suggested that both dielectric loss and magnetic loss play important roles in microwave absorption of CF-RGO nanocomposite.
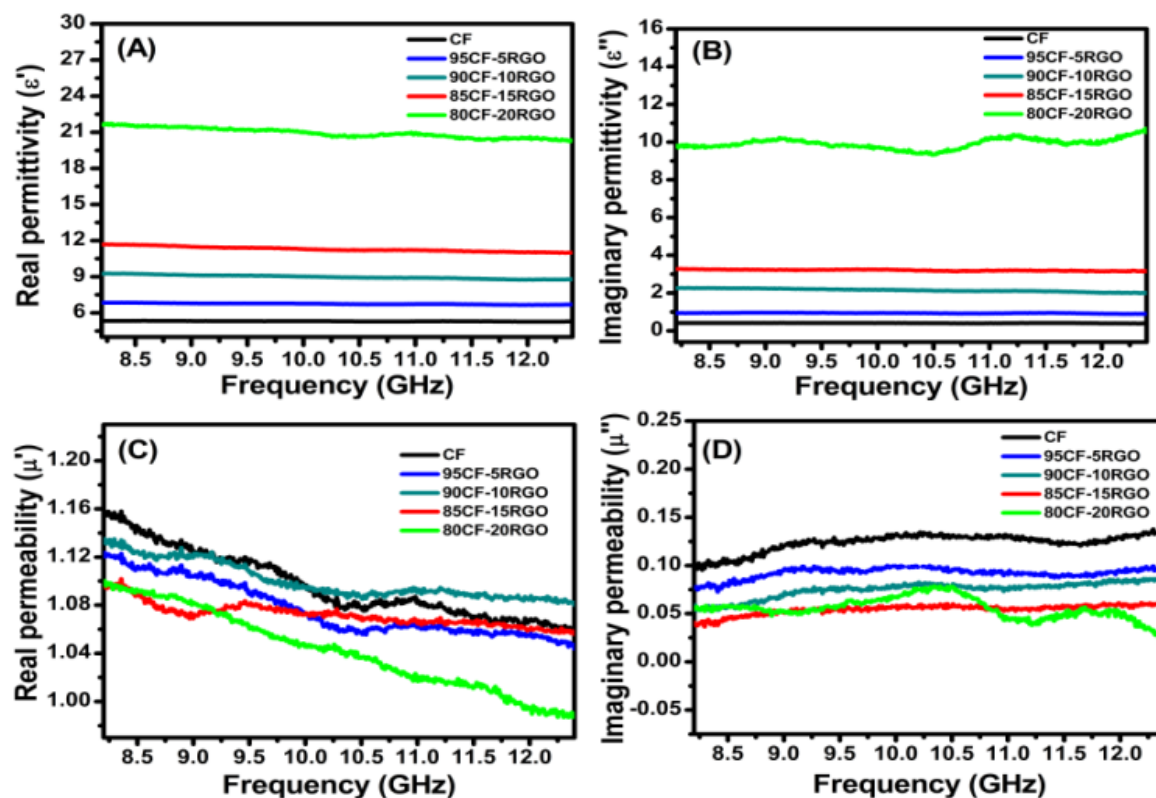
Fig. 3.17 Frequency dependence of relative complex permittivity: (A) real part and (B) imaginary part. Relative complex permeability (C) real part and (D) imaginary part of various compositions of CF-RGO nanocomposites

The reflection loss (RL) was calculated from the complex relative permeability and permittivity at a given frequency and specimen thickness using Equation 1.16 and 1.17 (Chapter 1).

For CoFe$_2$O$_4$ nanocrystals and CF-RGO nanocomposites, having various compositions, reflection loss (RL) values were calculated (Fig. 3.18) and following important points were observed: (i) Pure CF exhibited minimum RL value of -7.5 dB at 9.98 GHz when thickness was 3.2 mm (ii) With increasing RGO content in the composites minimum RL value was increased up to 15 wt. % of RGO. Beyond 15 wt. % of RGO content RL values were started to decrease. This might be due to the high permittivity value of composite having 20 wt. % RGO (80CF-20RGO), which is harmful to the impedance match and leads to intense reflection resulting in weak absorption [63]. (iii) Effective bandwidth (i.e., RL < -10 dB and > 90 % absorption) was found to be

increased with increasing RGO content in the composite. (iv) With increasing thickness of the absorber minimum RL values were increased up to certain value of thickness depending upon the composition of the composite. (v) With increasing thickness of the absorber the frequency, at which minimum RL was observed, was decreased. (vi) Composite having 85 wt. % CF and 15 wt. % RGO (85CF-15RGO) exhibited highest value of minimum RL of -31.31 dB (i.e., 99.94 % absorption) at 9.05 GHz when the thickness was 2.15 mm with effective bandwidth in 8.2-10.92 GHz range. This composite also exhibited minimum 99.5% microwave absorption (> -26.6 dB) for all the thickness (1.9-2.4 mm) at various frequencies in X-band region. The frequencies, at which minimum RL values were observed, were decreased with increasing thickness. The optimum reflection loss can be achieved by impedance matching, when $Z_{in} = Z_0$, where Z_0 and Z_{in} are free space impedance and absorber impedance respectively [320] and corresponding frequency and absorber thickness are known as matching frequency (f_m) and matching thickness (t_m). In the present case, Z_{in}/Z_0 was ~ 0.98 (Z_0 = 376.7 ohm [320] and Z_{in} = 368.58 ohm (calculated value)), when f_m was 9.05 GHz, and t_m was 2.15 mm.

Several factors play important roles in the enhancement of microwave absorption of CF-RGO nanocomposites such as (i) the existence of residual defects and functional groups in RGO, which favours the electromagnetic energy absorption [11,60], (ii) the high aspect ratio and high conductivity of RGO sheets provide its better absorbing ability [60], (iii) the interfaces between RGO sheets and CF nanoparticle, which cause the interfacial polarization (known as Maxwell-Wagner polarization [11]) and associated relaxation contribute to the dielectric loss of the CF-RGO nanocomposites. These important intrinsic physical properties of the hierarchical structure of the CF-RGO nanocomposites are responsible for their stronger microwave absorption ability than pure CF and pristine RGO.
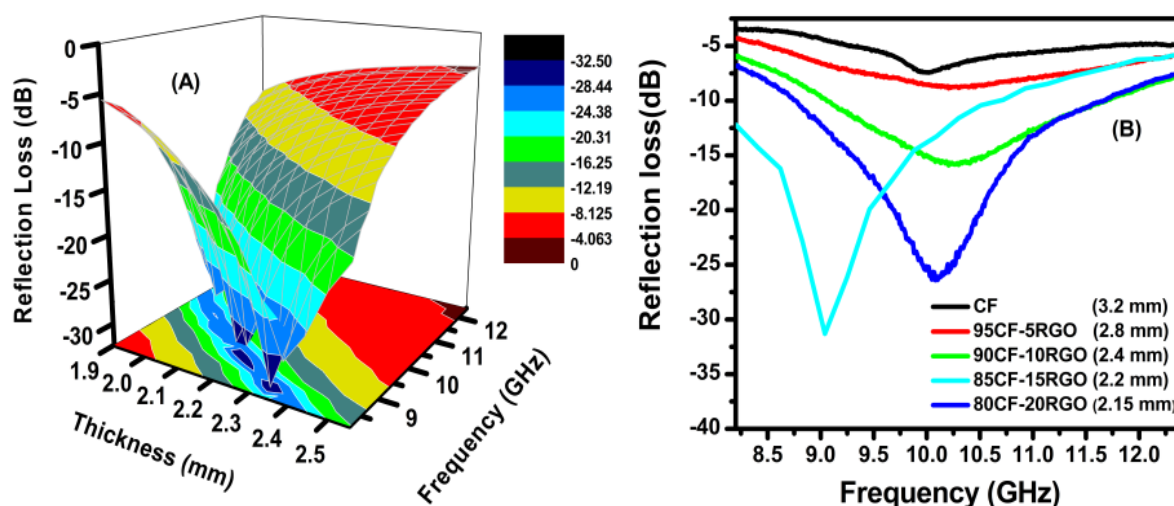
Fig. 3.18 Frequency dependence of reflection loss of synthesized (A) 85CF-15RGO nanocomposites by varying the thickness of the absorber and (B) Minimum reflection loss of $CoFe_2O_4$, and CF-RGO based composites with varying RGO loading percentage.

3.3 Summary of results

(i)   Here, we have described an *'in situ'* co-precipitation reduction method for preparation of CF-RGO nanocomposites with various compositions. In this method reduction of GO to RGO and formation of CF nanoparticles from metal nitrates occurred simultaneously, which helped to anchor CF nanoparticles on the sheets of RGO homogenously.

(ii)   The methodology employed to prepare these nanocomposites is very simple and does not require any elaborate setup.

(iii)   Here, NaOH acted the role of a precipitating agent during the formation of $CoFe_2O_4$ nanoparticles from metal ions, as well as a reducing agent to convert GO to RGO. In this synthetic methodology, no other reducing agent was used.

(iv)   The novelty of this technique lies in its simplicity, cost-effectiveness, and capability of large-scale production of $CoFe_2O_4$-RGO nanocomposites.

(v)   The synthesized $CoFe_2O_4$-RGO nanocomposites possess excellent microwave absorbing property as well as high photocatalytic activity towards degradation of various dyes under visible light irradiation generated from a 100W reading lamp.

(vi) The synthesized CF-RGO nanocomposites having 25 wt. % RGO content (75CF-25RGO) exhibited high photocatalytic efficiency towards the decolorization of individual dyes as well as a mixture of dyes under visible light generated from a 100W bulb.

(vii) The photocatalytic activity of 75CF-25RGO under visible light was found to be comparable and in some cases better than the various reported RGO-Ferrite composites [159,163,164,276,318,321-327].

(viii) Magnetic nature of 75CF-25RGO makes it a magnetically separable catalyst, which solves the separation-related problems associated with the nanosized catalysts.

(ix) 85CF-15RGO also exhibited ~99.94 % minimum RL (-31.31 dB) at 9.05 GHz in X-band region when the thickness was 2.15 mm with effective bandwidth in 8.2-10.92 GHz.

(x) To the best of our knowledge, the minimum RL value of 85CF-15RGO is comparable and even superior to most of the pure ferrites and ferrite-RGO composites [1-4,7,9-11,35,52,59-64,107,109,126-134,139-143].

(xi) This nanocomposite not only shows higher minimum RL in comparison with pure CF but also its lightweight, due to the presence of RGO, offers an added advantage.

(xii) The heteroarchitectural structure of RGO-CF composites caused to enhance its photocatalytic property as well as microwave absorption property. CF-RGO nanocomposites have demonstrated its capability to act as a multifunctional material as heterogeneous photocatalyst as well as microwave absorber.

Chapter 4

Synthesis of BiFeO₃ nanowire-RGO: Excellent Microwave Absorber and Versatile, Magnetically Separable and Reusable Catalyst towards Multiple Organic Reactions.
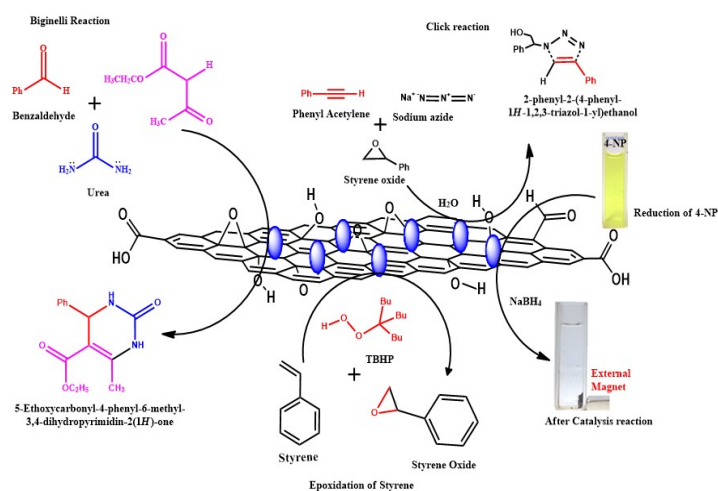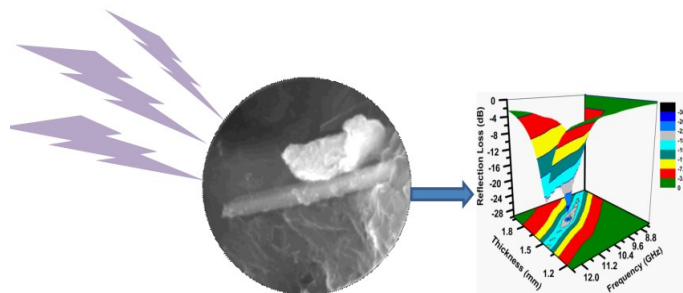
BiFeO₃ nanowire-RGO
nanocomposite

In this chapter, a hydrothermal method has been reported for the synthesis of $BiFeO_3$ nanowire-Reduced Graphene Oxide (BFO-RGO) with different weight ratios of BFO and RGO. Their (i) structural characterizations, (ii) microwave absorption property in X-band region and (iii) excellent catalytic activity towards Biginelli reaction, Click reaction, styrene epoxidation and decolorization of 4-nitrophenol and trifluralin via reduction reaction with $NaBH_4$ and magnetic separation of BFO-RGO after catalysis reactions and its reusability tests will be described. Here nanowire like structured BFO has been chosen to synthesize because, 1-D magnetic nanowires exhibit some fascinating properties due to high surface to volume ratio, high aspect ratio, efficient charge transfer via ballistic charge transfer mechanism along wire axis [62,142,328-332]. Moreover, polycrystalline BFO materials generally exhibit minimum reflection loss (RL) beyond X-band region [333-336]. Exploiting the interesting properties of BFO nanowires attempts has been made to develop (i) high performing microwave absorber, which can exhibit microwave absorption in X-band region, and (ii) active catalyst for various reactions. The work described in this chapter has been presented in reference [35,144].

4.1 Experimental procedure [35,144]

4.1.1 Materials required

Bismuth (III) nitrate pentahydrate $(Bi(NO_3)_3.5H_2O)$, Iron (III) chloride hexahydrate $(FeCl_3.6H_2O)$, Acetone, Ammonium hydroxide and 4-nitrophenol (4-NP) were purchased from Fischer Scientific, Sodium hydroxide, Sodium nitrate, Sulphuric acid, Potassium permanganate, Urea and 30% H_2O_2 solution were purchased from Merck, India, and Benzaldehyde, Phenylacetylene, Ethyl acetoacetate, Acetylacetone, Styrene, Styrene oxide, Cyclohexene oxide, tert-Butyl hydroperoxide (TBHP in 5-6 M decane), Sodium borohydride $(NaBH_4)$, Acetonitrile, Trifluralin and Graphite powder (mean particle size of < 20 μm) were purchased from Sigma Aldrich and used without further purification. Distilled water was used throughout the experiment.

4.1.2 Synthesis of BiFeO$_3$-Reduced Graphene oxide nanocomposite.

Synthesis of BiFeO$_3$-Reduced Graphene oxide nanocomposite (BFO-RGO) was performed by using the following steps: Step 1: Graphene oxide was synthesized by modified Hummer's method [83]. Step 2: A hydrothermal method was used to prepare BFO-RGO nanocomposites.

4.1.2.1 Synthesis of Graphene Oxide:

The protocol for the synthesis of Synthesis of Graphene Oxide has been described in section 2.1.2.1 of Chapter 2.

4.1.2.2 Synthesis of BiFeO$_3$-Reduced Graphene oxide nanocomposite.

We have employed a hydrothermal method to prepare BFO-RGO nanocomposites. The preparation of BFO-RGO nanocomposites is illustrated in Scheme 4.1. Synthesis of BFO-RGO was performed using the following steps: First step: 2.425 g Bi(NO$_3$)$_3$.5H$_2$O and 1.352 g FeCl$_3$.6H$_2$O were mixed in 50 mL of acetone (99.8%) and sonicated for 30 min. Second step: An aqueous dispersion of GO (0.03189 g in 50 ml) was then added to the mixture. Third step: 150 ml of H$_2$O and concentrated ammonia were added under vigorous stirring until the pH value of the solution reached 10-11. After filtering and rinsing with water, the red co-precipitate was re-dispersed in 40 ml water. Fourth step: Under vigorous stirring, 5 M NaOH aqueous solutions were added to the suspension. Fifth step: This solution was transferred in a stainless steel autoclave with a Teflon liner and heated at 140 °C for 24 hours. The final black powder was separated from the reaction mixture and washed with distilled water followed by drying at 60 °C. BFO-RGO nanocomposites with 1, 2, and 3 wt % RGO were prepared (confirmed by TGA vide infra) and designated as 99BFO-1RGO, 98BFO-2RGO, and 97BFO-3RGO respectively. We have also prepared pure BFO using the same method without adding GO.
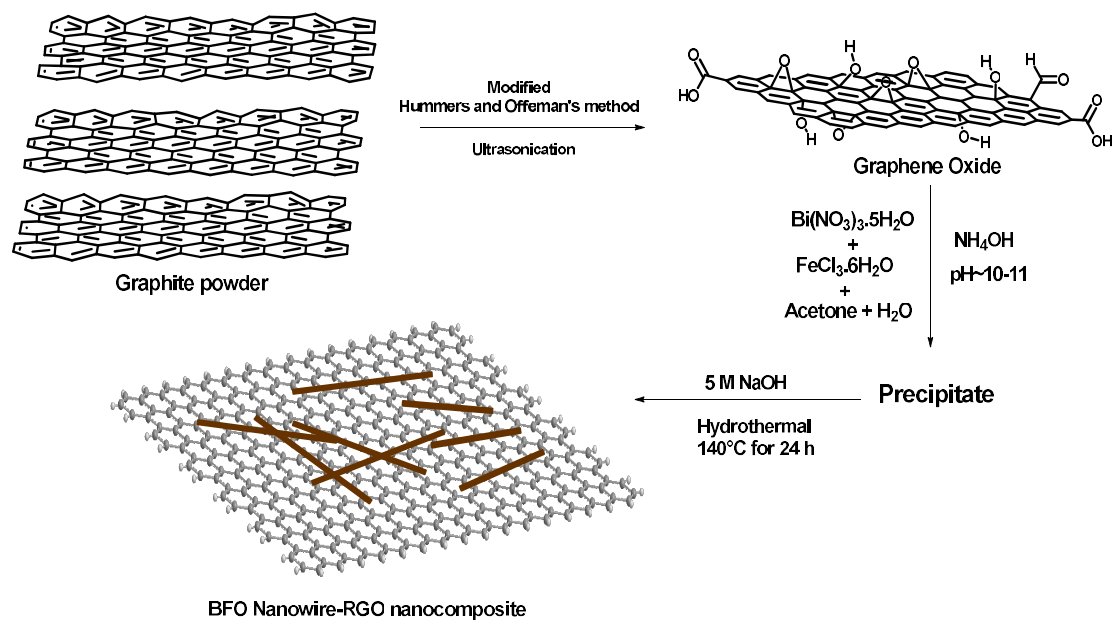
Scheme 4.1 Formation of BFO-RGO nanocomposites by hydrothermal method.

4.1.3 Catalytic Activity Tests

The catalytic activities of BFO-RGO have been tested for the following reactions:

(i) Synthesis of (5-Ethoxycarbonyl-4-phenyl-6-methyl-3,4-dihydropyrimidin-2(1H)-one and 5-Acetyl-6-methyl-4-phenyl-3,4-dihydropyrimidin-2(1H)-one) using Biginelli reaction in solventless condition.

(ii) Synthesis of 2-phenyl-2-(4-phenyl-1H-1,2,3-triazol-1-yl) ethanol and 2-(4-phenyl-[1,2,3] triazole-1-yl)- cyclohexanol using 'click reaction' in aqueous medium.

(iii) Epoxidation of styrene to styrene oxide.

(iv) Reduction of various dyes (4-Nitrophenol, and a herbicide (trifluralin) in the presence of excess NaBH₄.

4.1.3.1 Synthesis of 3,4-dihydropyrimidinone catalyzed by BFO-RGO nanocomposite.

We have performed the synthesis of 3,4-dihydropyrimidinone (5-Ethoxycarbonyl-4-phenyl-6-methyl-3,4-dihydropyrimidin-2(1H)-one and 5-Acetyl-6-methyl-4-phenyl-3,4-dihydropyrimidin-2(1H)-one) in solventless condition as representative of Biginelli

reaction. In typical synthesis, 1 mmol benzaldehyde (0.101 ml), 1.2 mmol urea (72 mg) and 1 mmol ethyl acetoacetate (0.126 ml) (or Acetylacetone (0.103 ml)) were mixed in a round bottom flask. To this mixture 25 mg of BFO-RGO catalyst was added and mixed thoroughly. The reaction mixture was then heated at 80 °C for 30 min. After cooling the reaction mixture was poured into ice-cooled water and the catalyst was separated by applying an external magnet. The product was then recrystallized. The same reactions were also conducted in the presence of pure BFO and pure RGO.

4.1.3.2 BFO-RGO catalyzed synthesis of 1, 4-disubstituted 1,2,3-triazoles by 'click reaction.'

For the synthesis of 1,4-disubstituted 1,2,3-triazoles by 'click reaction,' BFO-RGO was used as a catalyst. Here, 2-phenyl-2-(4-phenyl-1H-1,2,3-triazol-1-yl)ethanol and 2-(4-phenyl-[1,2,3] triazole-1-yl)- cyclohexanol were synthesized in aqueous medium as model reaction. In a typical synthesis, in a round-bottomed flask 1 mmol styrene oxide (0.115 ml) (or cyclohexene oxide (0.101 ml)), 1.1 mmol sodium azide (72 mg), 1 mmol phenylacetylene (0.110 ml) and 25 mg of BFO-RGO were mixed with 3 ml water. This mixture was then refluxed at 80 °C for 2h with constant stirring. Then the reaction mixture was allowed to cool down to room temperature, and the catalyst was separated magnetically. The product was separated by filtration followed by recrystallization. The same reactions were also conducted in the presence of pure BFO and pure RGO.

4.1.3.3 Epoxidation of styrene catalyzed by BFO-RGO

The catalytic reaction for styrene epoxidation was carried in a 50 ml two-necked flask fitted with a reflux condenser. 50 mg of the BFO-RGO catalyst, 4 ml of acetonitrile, and 5 mmol of styrene were added into the flask and stirred for 30 min under nitrogen atmosphere. Then 12.5 mmol of TBHP was added slowly under vigorous stirring, and then the reaction mixture was heated at 100 °C temperature. Samples were periodically collected from the reaction mixture and analyzed by a gas chromatograph (GC-2014 Shimadzu) equipped with a capillary column (30 M x 0.25 mm x 0.25 mm) and a FID detector. The same reactions were also conducted in the presence of pure BFO and pure RGO. It was observed that BFO-RGO acted as a catalyst for ~79% conversion of styrene and ~90% selectivity of styrene oxide after 5h of reaction.

4.1.3.4 Catalytic Performance test of BFO-RGO towards Reduction of 4-NP and trifluralin in the presence of excess NaBH$_4$

To study the catalytic activity of BFO-RGO, reduction reactions were performed for 4-Nitrophenol (4-NP) and Trifluralin. In a typical run, 4.5 ml of 9 x 10^{-5} M aqueous solution of 4-NP was mixed with 0.5 ml H$_2$O and 1 ml 0.2 M NaBH$_4$ solution. To this solution 2 ml aqueous suspension of the catalyst (0.4 gL^{-1}) was added. 4 ml of this reaction mixture was immediately transferred to a quartz cuvette. The colored solution faded gradually as the reaction proceeded. The reaction was monitored by recording absorption spectrum by a UV-vis spectrophotometer (V-570, Jasco) at an interval of 1 min. UV-vis spectra of an aqueous solution of 4-NP showed the maximum absorption peak (λ_{max}) at 317 nm. This peak was red-shifted to 400 nm after addition of NaBH$_4$ due to the formation of bright yellow colored 4-nitrophenolate ions. After addition of the catalyst gradually decrease of intensity of the peak at 400 nm indicated the progress of the reduction of 4-NP. Also, gradual development of small shoulder peak at 300 nm which is attributed to the absorption peak of 4-Aminophenol (4-AP) was observed. The reaction was carried out at room temperature (30 ± 1) °C.

The reduction of trifluralin was also conducted using the same procedure. For reduction of trifluralin, 4.5 ml of 0.75 mM trifluralin (in 1:1 ethanol and water (v/v)), 1 ml (0.2 M) NaBH$_4$, and 2 ml catalyst (0.4 g L^{-1}) were used. Reduction of trifluralin was monitored by observing the gradual disappearance of its λ_{max} at 437 nm.

All catalysis reactions were performed in triplicate. It is well documented that, metal oxide nanoparticles catalyzed reduction reaction of 4-NP in the presence of excess NaBH$_4$ proceed *via* pseudo-first order kinetics [11,207,252].

The apparent rate constant k$_{app}$ was determined from the equation discussed in Chapter 2 Section 2.1.3.

The purity of the products obtained by Biginelli reaction and Click Reaction was verified using ^{1}H NMR, FT-IR and melting point determination by DSC. (Details of spectral data of the synthesized compounds obtained from Biginelli, and click reaction are provided at the end of this chapter.

4.1.4 Magnetic separation and reusability test of the catalyst (BFO-RGO).

After catalysis reactions, BFO-RGO was magnetically separated from the reaction mixtures by applying a permanent magnet externally. Magnetic separation of the catalyst has been described in Section 2.1.4 of Chapter 2.

4.1.5 Microwave absorption measurement

The protocol for the measurement of microwave absorption of the synthesized nanocomposites has been described in Section 1.6 of Chapter 1.

4.2 Results and Discussion [35,144]

4.2.1 Structure and morphology of BFO-RGO nanocomposites

Room temperature wide angle powder XRD was employed to identify the phases which were present in (i) the precipitate, formed due to the reaction of NH_4OH with $Bi(NO_3)_3$ and $FeCl_3$, (ii) the final product formed after hydrothermal treatment of precipitate in aqueous NaOH medium, (iii) the product when hydrothermal process was carried out in the presence of the precipitate and GO in aqueous NaOH medium. XRD patterns are presented in Fig. 4.1.
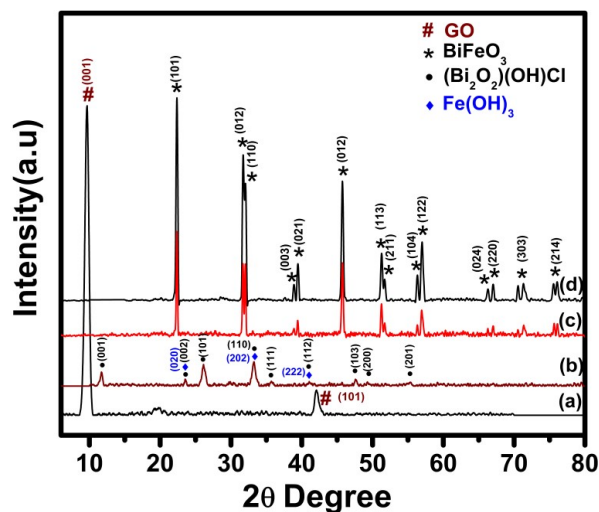
Fig. 4.1 Room temperature wide angle power XRD pattern of (a) pure GO, (b) the precipitate containing $Fe(OH)_3$ and $(Bi_2O_2)(OH)Cl$ phases, (c) BFO-RGO nanocomposite, and (d) Pure $BiFeO_3$.

It was observed that the reaction between NH_4OH with $Bi(NO_3)_3$ and $FeCl_3$ resulted in the formation of a precipitate containing small particles of $Fe(OH)_3$ and $(Bi_2O_2)(OH)Cl$ (Fig. 4.1b). Pure $BiFeO_3$ was formed due to the hydrothermal treatment of this precipitate. The diffraction peaks of pure BFO (Fig. 4.1d) can be assigned to the pure phase of $BiFeO_3$ (JCPDS No. 20-0169), which indicates its rhombohedral distorted perovskite structure with a space group of *R3c* and lattice parameters of $a = b = c = 5.62043$ Å and $\alpha = \beta = \gamma = 59.35381°$. These values are consistent with literature [331, 337]. XRD patterns of GO showed the diffraction peaks corresponding to (001) and (101) planes of GO [11,147] (Fig. 4.1a). In case of BFO-RGO, diffraction peaks corresponding to pure $BiFeO_3$ were observed (Fig. 4.1c). Here, the absence of peaks for GO indicated that during the preparation of BFO-RGO, GO flakes were converted to RGO and RGO sheets were exfoliated [11]. The important point here is that no impurity phase was detected. The synthetic method reported here showed its capability to produce BFO-RGO, where pure single phase BFO is present. According to the previously reported literature, synthesis of pure $BiFeO_3$ is a challenge [152]. Most of the reported methodologies produce either mixed phase $BiFeO_3$ or $BiFeO_3$ along with some impurity phases (e.g., $Bi_2O_2CO_3$, $Bi_{25}FeO_{40,}$ etc. [337-340]). However, when RGO content in BFO-RGO was increased to 3 wt. % and above, formation of an impurity phase $Bi_2O_2CO_3$ along with BFO were observed (Fig. 4.2).
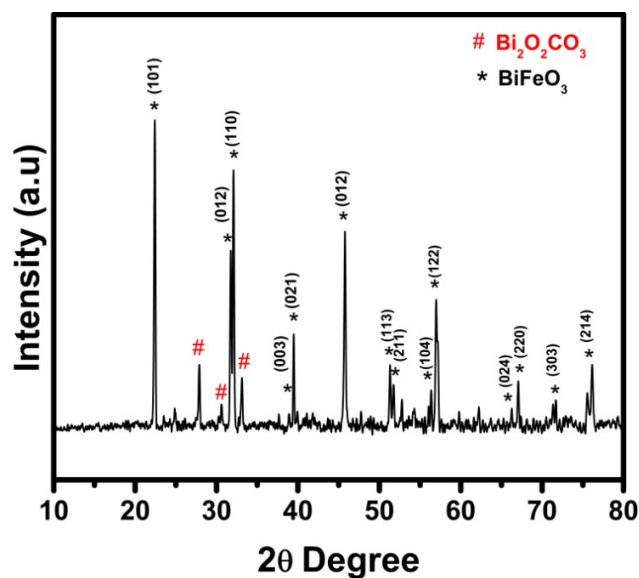
Fig. 4.2 Room temperature wide angle power XRD pattern of 97BFO-3RGO (3 wt. % RGO content $BiFeO_3$ nanowire).

Formation of $Bi_2O_2CO_3$ impurity phase occurred might be due to the limited migration of Bi^{3+} and Fe^{3+} in the compositions having higher RGO content [340]. Therefore we have not prepared BFO-RGO nanocomposite with more than 3 wt % RGO content.

This transformation of GO to RGO was further confirmed from the results obtained from FT-IR (Fig. 4.3), Raman spectroscopy (Fig. 4.4) and Thermogravimetry analysis (TGA) (Fig. 4.5).
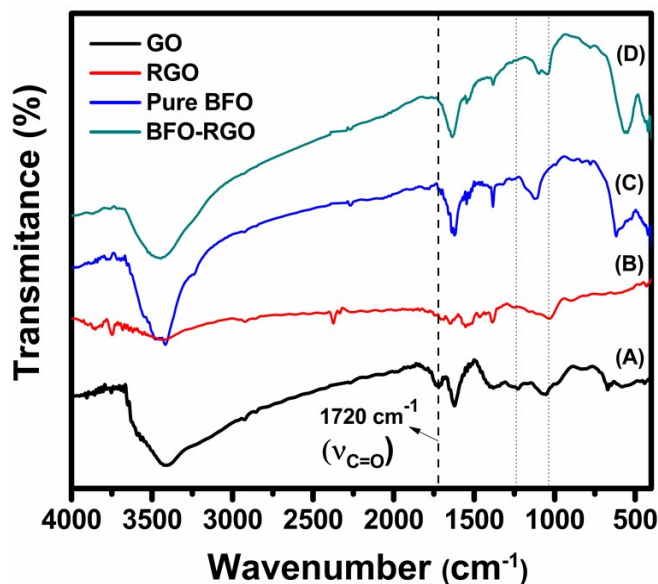
Fig. 4.3 FT-IR spectra of (A) GO, (B) RGO, (C) Pure BFO, and (D) 97BFO-3RGO nanocomposite.

The FT-IR spectra of pure GO, pure RGO, pure BFO, and BFO-RGO nanocomposite are presented in Fig. 4.3. The presence of oxygen-containing functional groups (e.g., epoxy, carbonyl, carboxyl, and hydroxyl) on the surface of GO was indicated by the FT-IR spectra of GO. Fig. 4.3 (A) shows FT-IR spectra of GO where bands at (i) 1384 cm^{-1} corresponding to the stretching vibration of C–O of carboxylic group, (ii) 1720 cm^{-1} for carbonyl group, (iii) 1226 cm^{-1} for C-O stretching vibration of epoxy group, (iv) 1054 cm^{-1} for C-O stretching vibration are present. A peak at 1621 cm^{-1} can be assigned to the contribution from the skeletal vibration of the graphitic domains [63,143]. In case of RGO (Fig. 4.3 (B)), the disappearance of 1720 cm^{-1} peak (for carbonyl group) and a decrease of intensities of peaks at 1226 and 1054 cm^{-1} (corresponding to C-O) were observed. In the same time, a peak at 1544 cm^{-1} appeared in RGO sample. The band at 1621 cm^{-1} (in GO sample), which can be assigned to the C=C skeletal vibration of

graphitic domains of GO, has been redshifted to 1544 cm^{-1} for RGO and indicated the partial restoration of π-π conjugation of graphene sheet in RGO. In the FTIR spectra of pure BFO (Fig. 4.3 (C)) a peak appears at 556 cm^{-1}, which can be ascribed to lattice absorption of M-O (M= Fe^{3+}, Bi^{3+}), confirmed the formation of BiFeO₃ [144]. In the FT-IR spectra of BFO-RGO nanocomposites absorption bands at the same positions were observed (Fig. 4.3 (D)). Here also carboxylic group vibration band ($v_{C=O}$ at 1720 cm^{-1}) was found to be disappeared, and absorption intensities corresponding to C-O at 1226 and 1054 cm^{-1} were decreased. These results implied that most of the oxygen-containing groups of GO, particularly carboxyl groups, had been removed and some of the hydroxyl and epoxy groups remained on the surface of RGO in BFO-RGO nanocomposite [144].

Raman spectroscopy, which is a sensitive and informative technique to probe disorder in sp^2 carbon materials, was used to determine the transformation of GO to RGO during formation of BFO-RGO nanocomposite. Fig. 4.4 shows the Raman spectra of GO, pure BFO, pure RGO and BFO-RGO nanocomposite.
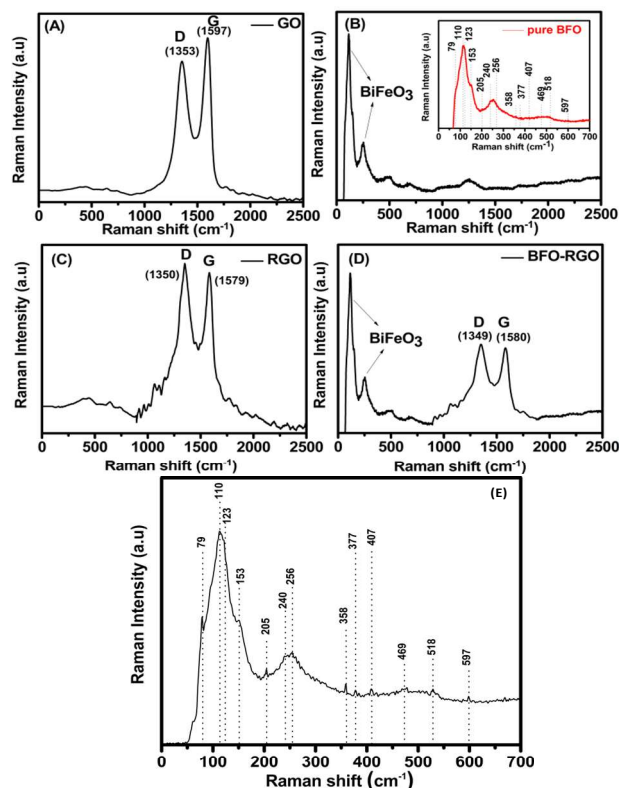
Fig. 4.4 Raman spectra of (A) GO, (B) Pure BFO, (C) pure RGO, and (D) BFO-RGO nanocomposite. (E) Enlarged Raman spectra of BFO showing all the 13 Raman active phonon modes of pure BFO.

In the Raman spectra of pure GO, characteristic peaks for D and G band were found at 1353 and 1597 cm^{-1} respectively, whereas in pure RGO the D band and G band shifted to 1350 and 1579 cm^{-1}. The same kind of shifting was also observed in BFO-RGO nanocomposite confirming the conversion of GO to RGO. I_D/I_G ratio for pure GO was found to be ~0.9 whereas this ratio was ~1.06 in BFO-RGO [63,144]. This increase of I_D/I_G value for BFO-RGO can be attributed to the decrease in the average size of sp^2 domains upon reduction of GO during formation of BFO-RGO composite [63,144]. The inset in Fig. 4.4 (B) shows all 13 Raman active phonon modes of pure BFO. These phonon modes appear at 123, 153, 205, 407, 240, 256, 358, 377, 469, 528, 597, 79 and 110 cm^{-1} and are characteristic peaks of A_1-1, A_1-2, A_1-3, A_1-4, E-1, E-2, E-3, E-4, E- 5, E-6, E-7, E-8 and E-9 modes respectively [144,341].
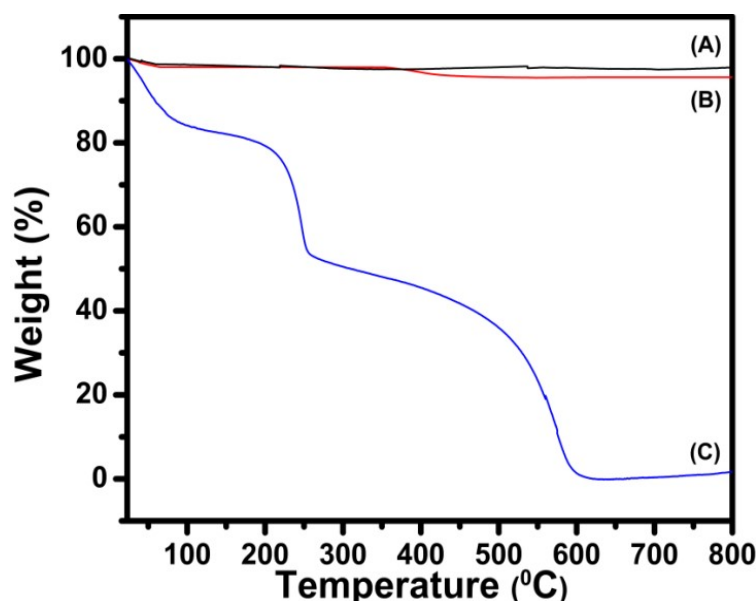
Fig 4.5 TGA curve of (A) pure BFO, (B) BFO-RGO nanocomposite, and (C) GO.

TGA analysis of GO and BFO-RGO was performed in an air atmosphere in the temperature range of 30–800 °C with a heating rate of 10 °C min^{-1}. Fig. 4.5 shows TGA thermograms of pure GO, pure BFO, and BFO-RGO nanocomposite. In TGA thermograms following points were observed: (i) pure BFO is quite stable in the temperature range of 30-800 °C. (ii) In the temperature range of 30-100 °C, GO exhibited ~17% wt loss, which might be due to evaporation of H_2O [7,60]. In this temperature range ~2% wt loss occurred for BFO-RGO. (iii) In 100-200 °C temperature range, GO showed ~3% wt loss and a sharp weight loss occurred in the range of 200-250 °C with

85

25% weight loss. This was due to the removal of oxygen-containing groups from GO. However, no such loss was observed for BFO-RGO. This fact clearly indicated that during synthesis of BFO-RGO, GO was converted to RGO via reduction of oxygen-containing groups (e.g. carbonyl, carboxyl, epoxy groups, etc. [7,60]). (iv) In 325-600 °C temperature range, the oxidative decomposition of carbon atoms of GO was observed whereas, in case of BFO-RGO, ~2 % weight loss was observed in the temperature range of 350-440 °C, which was due to the decomposition of carbon of RGO. From TGA thermogram it can be concluded that BFO-RGO nanocomposite is composed of ~2 wt % RGO and 98 wt% BFO.

Multiple point BET surface analysis of pure BFO and BFO-RGO (with 2 wt. % RGO) also showed that specific surface area of BFO was 28 m^2g^{-1} whereas that of BFO-RGO was 45 m^2g^{-1} (Fig. 4.6). N_2 adsorption-desorption isotherm of BET surface area analysis of these samples are shown in (Fig. 4.6). This increased surface area is ascribed to the synergistic effects between the RGO and BFO and resulted in enhancement of catalytic activity of RGO-BFO nanocomposite. The catalytic activities of BFO-RGO have been discussed in detail in Section 4.2.4.
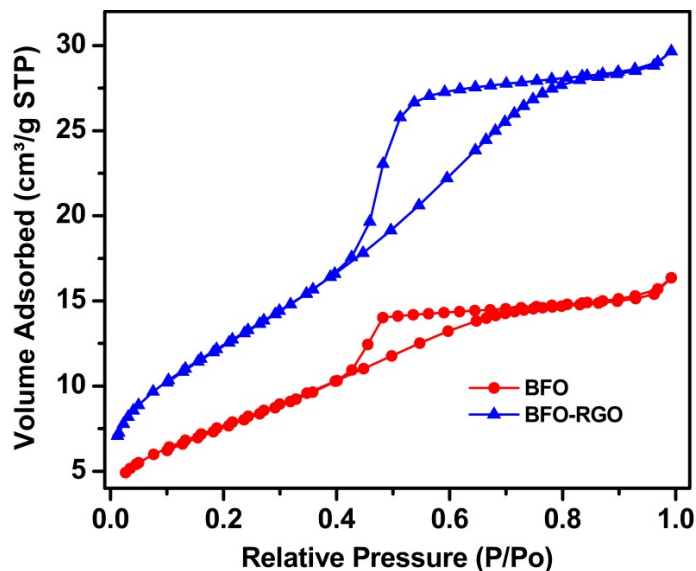
Fig. 4.6 N_2 adsorption-desorption isotherm of BFO and BFO-RGO nanocomposite.
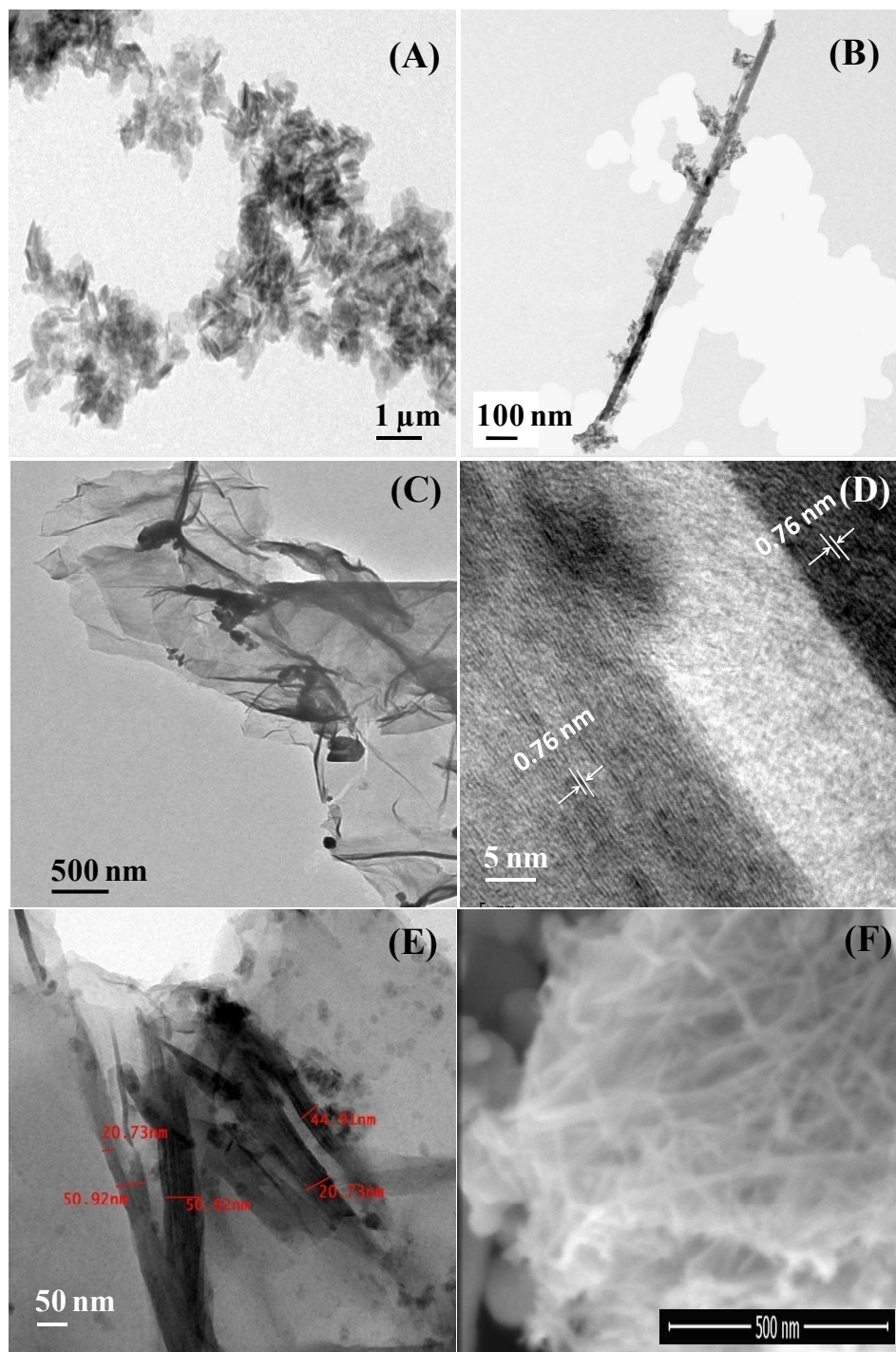
Fig. 4.7 TEM micrographs of synthesized (A) BFO, (B) individual BFO, (C) TEM micrograph and (D) HRTEM micrograph of a typical portion of GO, (E) and (F) TEM micrograph and FESEM micrograph of 97BFO-3RGO nanocomposite.

Representative TEM micrographs of as-synthesized pure BFO are presented in Fig. 4.7(A) and (B). These images clearly show that the BFO sample consists of uniform cylindrical structures with diameters between 40 to 200 nm and lengths varied from hundred nanometers to several microns. As these BFO samples have an aspect ratio (major axis /minor axis) in the range of 50-100, we have considered this synthesized $BiFeO_3$ as BFO nanowires [342].
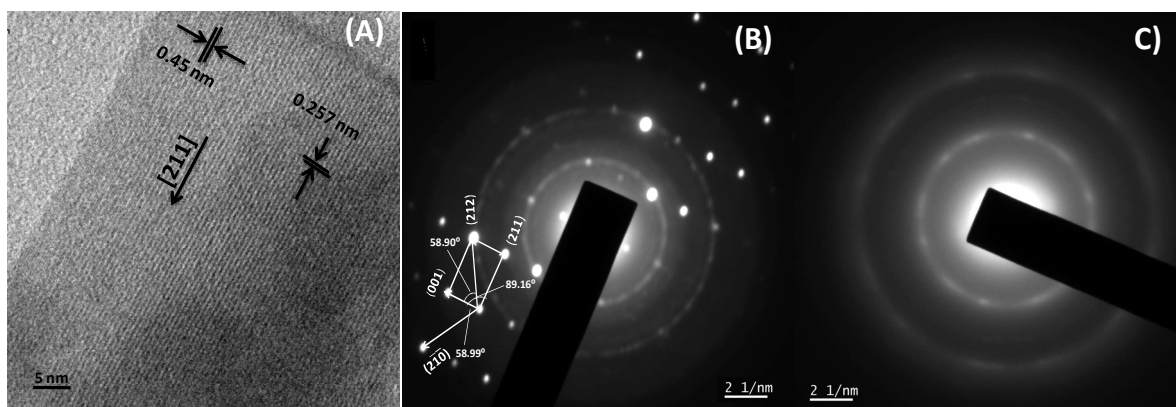
Fig. 4.8 (A) HRTEM image of BFO nanowire. SAED patterns of (B) BFO nanowire and (C) pure GO respectively.

The High Resolution Transmission Electron Microscopy (HRTEM) image (Fig. 4.8(A)) and selected area electron diffraction (SAED) pattern (Fig. 4.8(B)) of BFO show the planes with interplanar spacing of 0.257 and 0.45 nm representing (211) and (001) crystal face of $BiFeO_3$ nanowires respectively [336]. Fig. 4.7(C) shows nanometer thin sheet of pure GO. The SAED pattern for GO (Fig. 4.8(C)) shows the unresolved diffraction dots, indicating the GO sheets are amorphous in nature [63]. A HRTEM image of GO (Fig. 4.7(D)) shows the lattice fringe of 0.76 nm, which agrees well with the XRD pattern of GO [63]. Fig. 4.7 (E) and (F) show $BiFeO_3$ nanowire on the surface of nanometer thin RGO sheet.

EDX analysis of BFO-RGO nanocomposite (Fig. 4.9) also indicates the presence of Bi, Fe, O, and C in these composites.
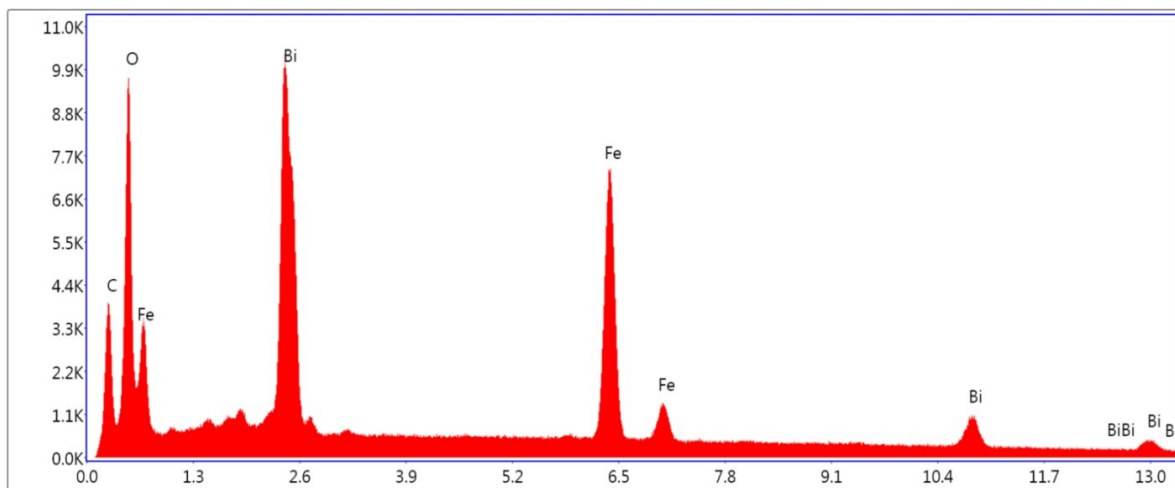
Fig. 4.9 EDX spectra of the synthesized 97BFO-3RGO nanocomposite.

The results obtained from XRD, HRTEM, FT-IR, Raman spectroscopy, and TGA clearly indicated the formation of $BiFeO_3$ nanowires and $BiFeO_3$ nanowire-RGO composite.

4.2.2 Formation mechanism of pure BiFeO₃ nanowire[35,144]

The precipitate, which forms due to the addition of NH_4OH in the mixture of $Bi(NO_3)_3$ and $FeCl_3$, contains small particles of $Fe(OH)_3$ and $(Bi_2O_2)(OH)Cl$ (Fig. 4.10A). It is important to note that, this precipitate does not contain any insoluble non-stoichiometric phases (e.g., bismuth subnitrate or bismuthyl nitrate $(Bi_2O_3.N_2O_5.2H_2O)$, etc.) which are generally formed in conventional methods employed for $BiFeO_3$ preparation [337,343]. These secondary phases create problem for single phase $BiFeO_3$ formation [337,343]. Hydrothermal treatment of $Fe(OH)_3$ and $(Bi_2O_2)(OH)Cl$ containing precipitate results in the formation of pure $BiFeO_3$.
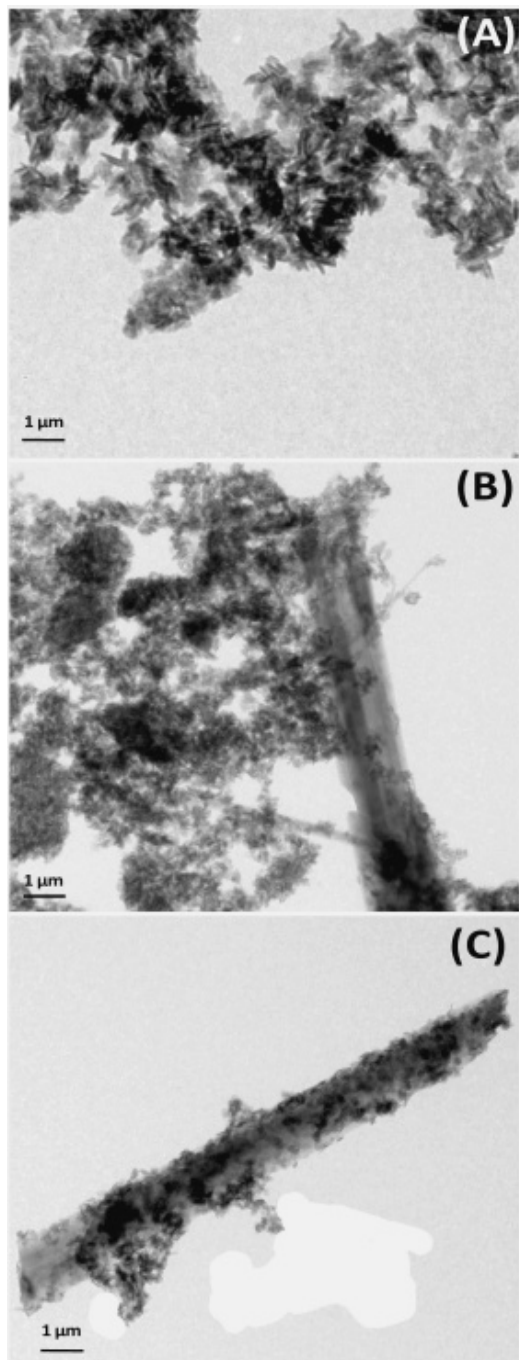
Fig. 4.10 TEM images of the aliquots of reaction mixtures taken from the hydrothermal reaction of BFO after (A) 0h, (B) 12h, and (C) 24h.

The reactions which are involved in $BiFeO_3$ single phase formation can be presented as follows:[35]

$$2\ Bi(NO_3)_3 + FeCl_3 + 7\ NH_4OH \longrightarrow (Bi_2O_2)(OH)Cl + Fe(OH)_3 + 6\ NH_4NO_3 + NH_4Cl + H_2O + HCl \quad (4.1)$$

$$(Bi_2O_2)(OH)Cl + 2\ Fe(OH)_3 \longrightarrow 2\ BiFeO_3 + 3\ H_2O + HCl \quad (4.2)$$
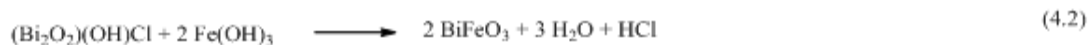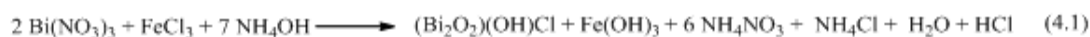
In this hydrothermal process, the growth of BFO nanowires is neither catalyst-assisted nor template directed. Based on the observation of TEM images for the aliquots of the reaction mixture, collected at regular intervals of 12h (Fig. 4.10), we propose that the growth of crystals in nanowire form might proceed via Oswald ripening process [341,344,345]. Before hydrothermal treatment the precipitate contains nanoparticles of $Fe(OH)_3$ and $(Bi_2O_2)(OH)Cl$ (as identified by XRD (Fig. 4.1b) and TEM (Fig. 4.10A). During hydrothermal treatment, these nanoparticles undergo aggregation and rupturing (as a result of Rayleing instability [342,346]), followed by dissolution due to high free energy. Then the crystal growth starts from the aggregates of smaller particles. Then longer nanowires grow at the cost of smaller particles as observed by TEM (Fig. 4.10B) of the sample collected after 12h of the hydrothermal process. Here, the reduction of surface energy is the primary driving force for the nanowire shaped crystal growth and morphology evolution. As the reaction proceeds after 12h, the nanoparticles start disappearing due to diffusion into growing nanowire. As a result, the formation of longer wires (Fig. 4.10C) occurs after 24h of the hydrothermal process. Similar mechanism was proposed by Lee et al. to explain the formation of $BaTiO_3$ and $SrTiO_3$ nanowires in a template-free hydrothermal synthesis method [342].

4.2.3 Magnetic property of BFO-RGO

Room temperature magnetic property measurements of synthesized BFO and BFO-RGO nanocomposites by vibrating sample magnetometer (VSM) show that saturation magnetization (M_s) values of the composites decrease with increasing RGO content in the composites (Fig. 4.11). M_s and coercivity (H_c) values of BFO and BFO-RGO composites are listed in Table 4.1. As in these composites, where BFO nanowires are anchored on the surface of nanometer-thin sheets of RGO, several factors play important roles in determining the M_s value of these composites. Some of these factors that influence the

magnetic properties are particle surface spin, disordered surface spin structure, dipolar interparticle interactions, etc. [7,63,268,269]. The magnetic properties of these composites can be tailored by simply manipulating the weight ratio of RGO and BFO in the composite.
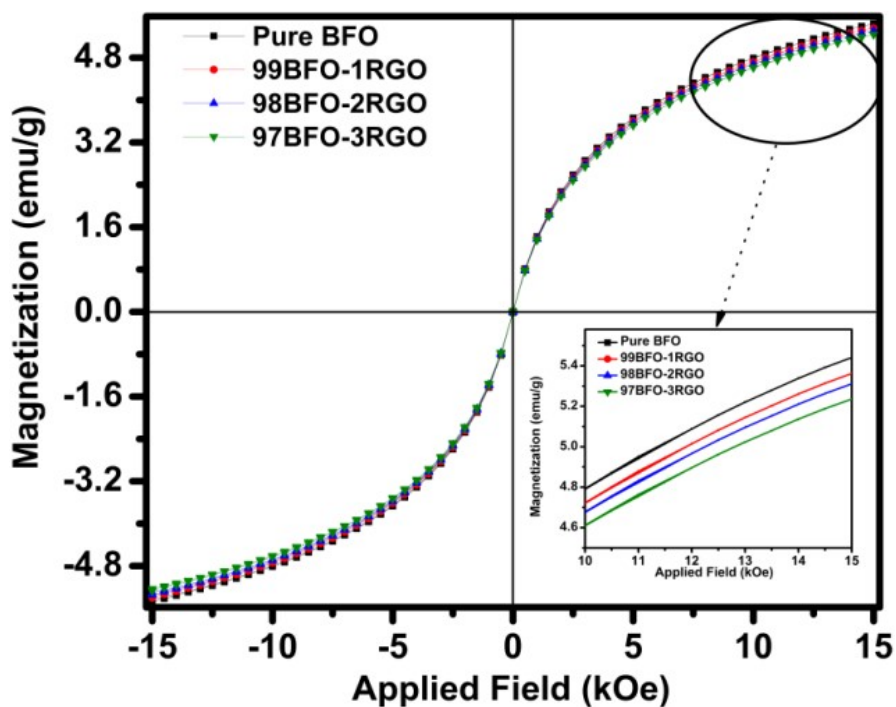
Fig. 4.11 Room temperature magnetic hysteresis loops of Pure BFO, 99BFO-1RGO, 98BFO-2RGO, and 99BFO-3RGO

Table 4.1: Magnetic properties of BFO and BFO-RGO nanocomposites

Material	Saturation magnetization (M_s) (emu/g)	Coercivity (H_c) (Oe)
BFO	5.42	4.20
99BFO-1RGO	5.35	4.30
98BFO-2RGO	5.30	4.15
97BFO-3RGO	5.22	4.14

4.2.4 Catalytic activity of BFO-RGO nanocomposite

4.2.4.1 Catalytic activity of BFO-RGO nanocomposite towards Reduction of 4-NP and trifluralin

To understand the effect of RGO on the catalytic activity of BFO-RGO nanocomposites, reduction reactions of 4-nitrophenol (4-NP) were performed in the presence of excess $NaBH_4$ with pure BFO (Fig. 4.12A) and BFO-RGO (Fig. 4.12B). A significant reduction of reaction completion time was observed when the reaction was catalyzed by BFO-RGO (6 min) compared to pure BFO (15 min) (Fig. 4.12). This enhancement of catalytic efficiency of BFO-RGO can be explained by considering following points: (i) this reduction reaction proceeds via relaying of electrons from BH_4^- donor to the acceptor 4-NP molecule. In aqueous medium BH_4^- is first absorbed on the surface of the catalyst. The hydrogen atoms, which are formed from the hydride, transfer electrons to 4-NP to reduce its functional group (e.g.-NO_2 group) [11,176,207]. This electron transfer (ET) induced hydrogenation of 4-NP occurs spontaneously, and BFO plays a role of storing electrons after ET from hydride. Presence of RGO not only enhances the adsorption of 4-NP onto the catalyst through π-π stacking but also facilitates the electron transfer to 4-NP via electrostatic interaction [11]. This reaction followed pseudo-first-order kinetics and values of apparent rate constant (k_{app}) were 0.72 min^{-1} for BFO-RGO, and 0.29 min^{-1} for pure BFO catalyzed reactions (Fig. 4.12D). k_{app} value of BFO-RGO catalyzed 4-NP reduction reaction is comparable with that of noble metal nanoparticle catalyzed the reaction. This high catalytic efficiency of BFO-RGO towards the reduction of -NO_2 group of 4-NP provoked us to investigate the reduction of a herbicide, trifluralin, *via* reduction of its –NO_2 groups. Trifluralin is used in various countries as a herbicide to control a variety of annual grass and broadleaf weed species. But, it remains in water as herbicide residue. As it is highly toxic in nature, it caused severe water pollution. BFO-RGO catalyst efficiently reduced trifluralin to its colorless form, where its –NO_2 groups were reduced to –NH_2 groups within 25 min.

As BFO-RGO nanocatalysts exhibited its enhanced catalytic efficiency towards dye degradation reaction in comparison with pure BFO, we have further explored the catalytic activity of BFO-RGO towards (i) Biginelli Reaction (ii) Click Reaction and (iii) styrene epoxidation reaction, by performing some model reactions. When these reactions were

performed in the presence of pure BFO and pure RGO, it was observed that no reaction occurred in the presence of RGO. When pure BFO was used as a catalyst, the reactions happened to some extent, but yields were significantly low in comparison with BFO-RGO catalyzed reactions.
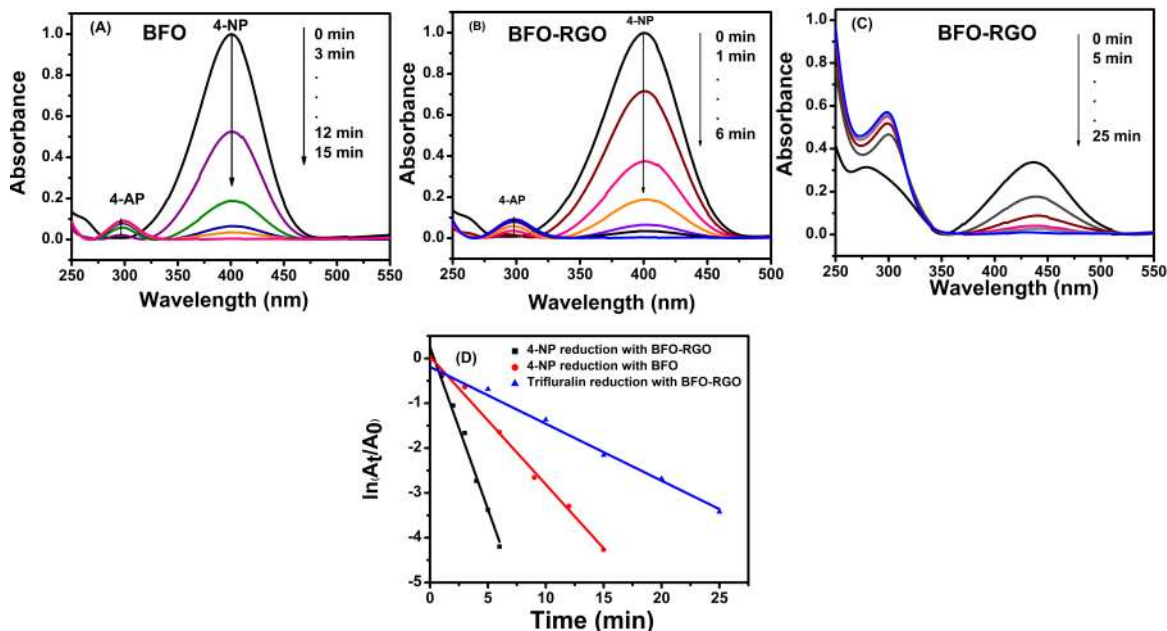
Fig. 4.12 Time-dependent UV-vis spectral changes of the reaction mixture of 4-NP catalyzed by (A) pure BFO, (B) BFO-RGO nanocomposite and (C) trifluralin catalyzed by BFO-RGO nanocomposite in presence of excess $NaBH_4$ and (D) pseudo first-order kinetic plot of 4-NP reduction with BFO and BFO-RGO nanocomposite and trifluralin reduction catalyzed by BFO-RGO nanocomposite

4.2.4.2 Catalytic activity of BFO-RGO nanocomposite towards Biginelli reaction.

In case of Biginelli Reaction, BFO-RGO catalyzed the reaction of aldehyde, urea and dicarbonyl compounds under solventless condition very efficiently to synthesize 3,4-dihydropyrimidin-2(1*H*)-ones. For example, 5-Ethoxycarbonyl-4-phenyl-6-methyl-3,4-dihydropyrimidin-2(1*H*)-one and 5-Acetyl-6-methyl-4-phenyl-3,4-dihydropyrimidin-2(1*H*)-one were synthesized with 93% and 90% yield respectively (Table 4.2). When these reactions were performed for a longer time (2h) neither increases in yield nor formation of any by-product at the cost of the main product was observed.

Table 4.2: BFO-RGO and pure BFO catalyzed the synthesis of 3,4-dihydro-pyrimidin-2(1H)-ones by Biginelli reaction.
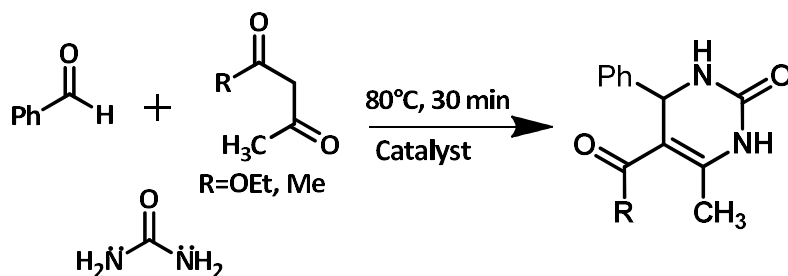
Entry	R	Product	Reaction Time (min)	[b]Yield(%) BFO-RGO	[b]Yield(%) BFO
1	OEt		30	93	65
2	CH₃		30	90	62

[a]Reaction Conditions: Benzaldehyde (1 mmol, 0.101 ml), Urea (1.2 mmol, 72 mg), 1,3-Diketone (1 mmol, 0.126 ml ethyl acetoacetate or 0.103 ml acetylacetone), BFO-RGO (25 mg), Solventless condition, reaction temperature 80 °C.

[b]Isolated yield.

The reaction proceeds via formation of an acylimine type intermediate, from the reaction of aldehyde and urea. This intermediate forms a complex with Bi^{3+}. The vacant d-orbital of Bi^{3+} promotes this complexation and stabilizes the intermediate, which intern enhances the rate of this key rate-limiting step. This intermediate complex then reacts effectively with β-diketone and the final product, dihydropyrimidin, forms following a cyclization and dehydration pathway [242,347]. Thus BFO present in BFO-RGO acted as a catalytically active center in Biginelli Reaction. The plausible mechanism of this reaction is shown in Scheme 4.2.
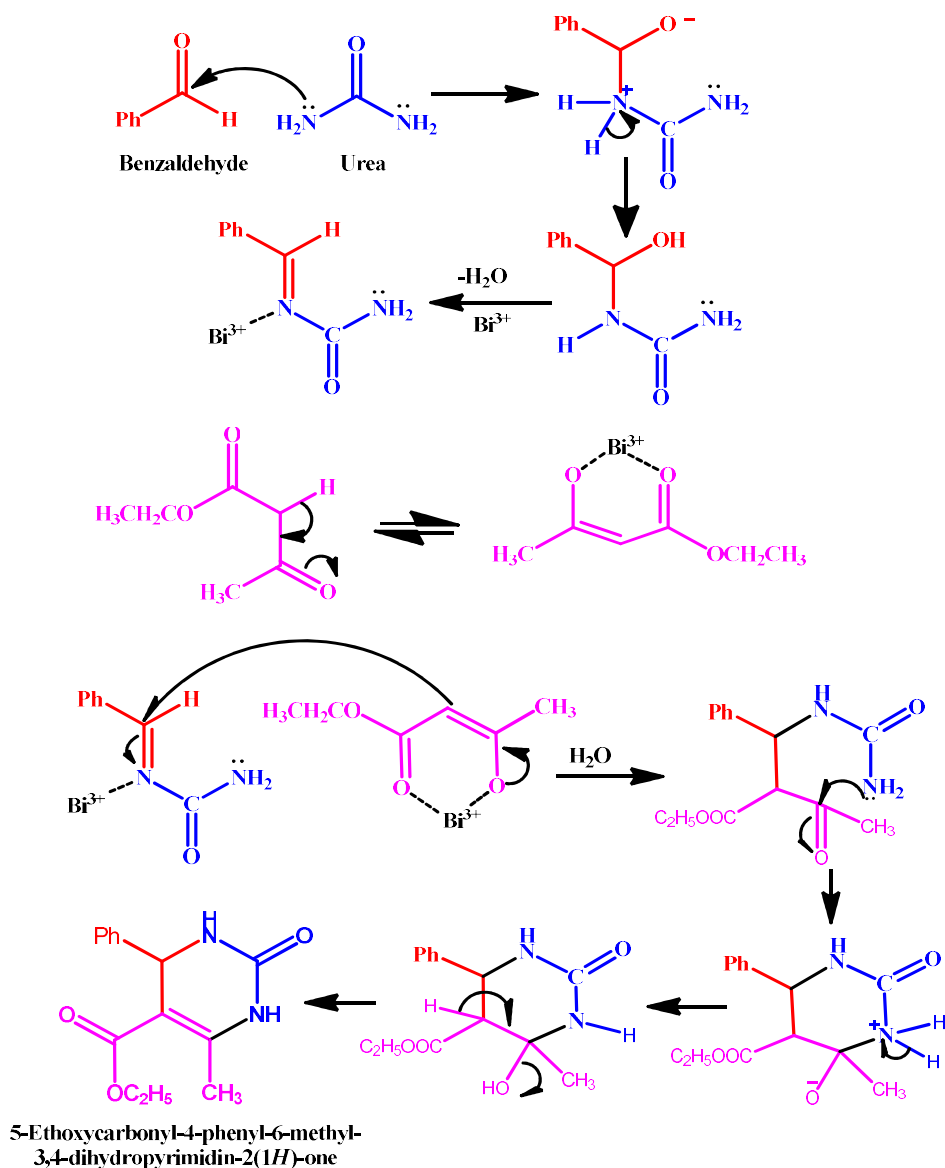
Scheme 4.2 The plausible mechanism involved in Biginelli Reaction catalyzed by BFO-RGO catalyst in the synthesis of 3,4-dihydropyrimidinone.

4.2.4.3 Catalytic activity of BFO-RGO nanocomposite towards click reaction.

To investigate the catalytic efficiency of BFO-RGO towards the synthesis of 1,2,3-triazole *via* click reaction, we have performed the three component click reaction involving sodium azide, epoxide and non-activated terminal alkynes in an aqueous medium. Here also, BFO-RGO exhibited its high catalytic activity towards synthesis of 2-

phenyl-2-(4-phenyl-1*H*-1,2,3-triazole-1-yl)ethanol (91% yield) and 2-(4-Phenyl-1*H*-1,2,3-triazol-1-yl)cyclohexanol (89% yield) (Table 4.3). Performing these reactions for a longer duration (~4h) did not affect the % of yield or formation of any other products.

Table 4.3: BFO-RGO and pure BFO catalyzed synthesis of 1,4-disubstituted 1,2,3-triazoles by 'click reaction.'
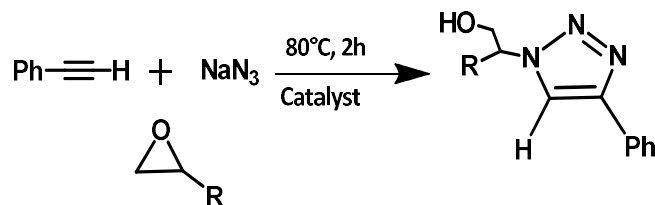
Entry	Epoxide	Triazole	Reaction Time (h)	[b]Yield (%) BFO-RGO	[b]Yield (%) BFO
1			2	91	65
2			2	89	60

[a]Reaction Conditions: alkyne (1 mmol, 0.110 ml), epoxide (1 mmol (styrene oxide 0.115 ml or, cyclohexene oxide 0.101 ml)), sodium azide (1.1 mmol, 72 mg), BFO-RGO (25 mg), water (3 ml), reaction temperature 80 °C.

[b]Isolated yield.

In this reaction, BFO-RGO plays a role of bifunctional catalyst. The formation of BFO-azide (to be specific Bi^{3+}-azide (intermediate-I)) as catalytically active species helps to activate epoxide and facilitates the delivery of azide during ring opening of epoxide [232]. Simultaneously another intermediate (intermediate-II) forms where acetylene coordinates with Bi^{3+} of BFO-RGO catalyst. This intermediate facilitates the 1,3-dipolar cycloaddition between -C≡C- bond (intermediate-II) and azide, to produce a triazole-BFO-RGO complex. Finally, the protonolysis of this complex in aqueous medium results

in the formation of β-hydroxy-1,2,3-triazole compounds [233]. The plausible mechanism of this reaction is shown in Scheme 4.3.
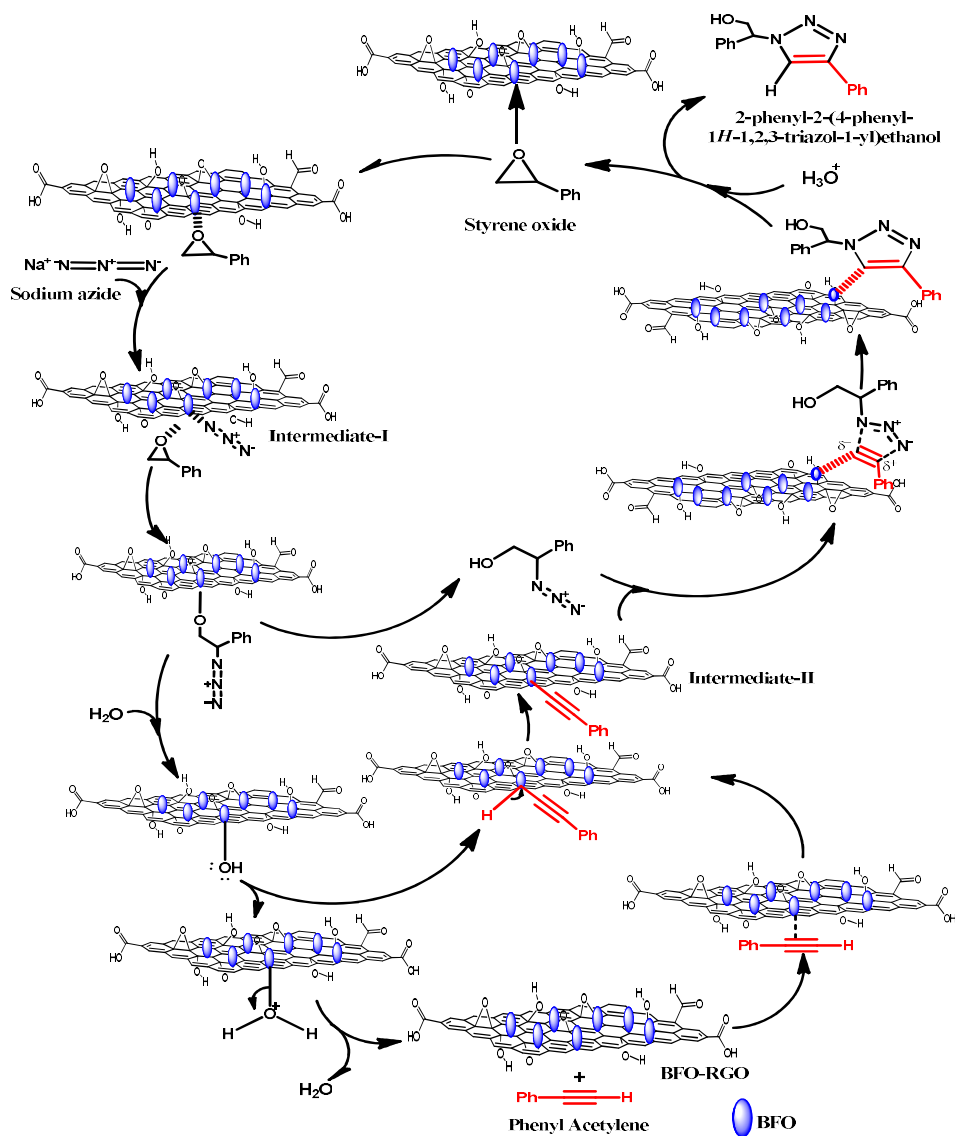
Scheme 4.3 The plausible reaction mechanism involved in click reaction catalyzed by BFO-RGO catalyst for synthesis of 1,4-disubstituted 1,2,3-triazoles.

4.2.4.4 Catalytic activity of BFO-RGO nanocomposite towards Epoxidation of styrene.

During exploration of the use of BFO-RGO as a catalyst for epoxidation of styrene in the presence of tert-Butyl hydroperoxide (TBHP), it was observed that styrene was converted to styrene oxide (Fig. 4.13) with very good ~90% selectivity and ~79% conversion (Fig. 4.14).
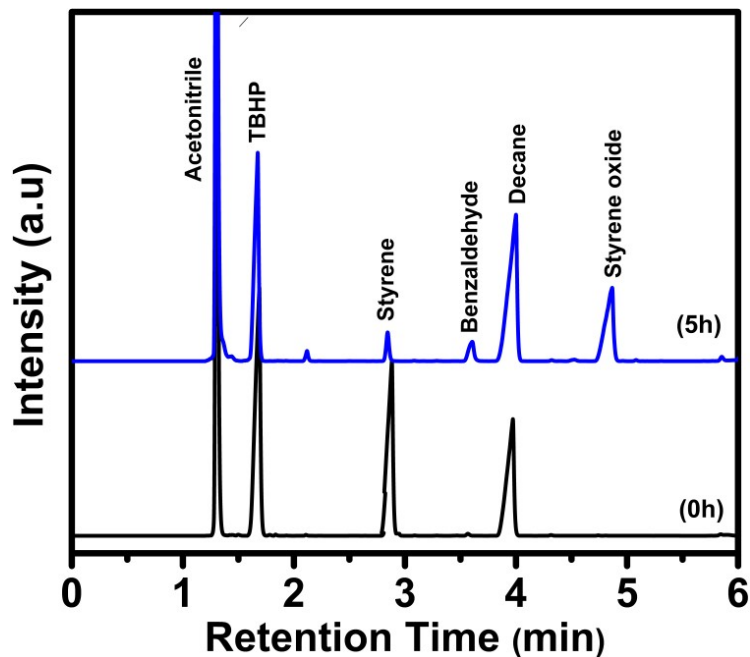
Fig. 4.13 Gas chromatogram analysis of styrene epoxidation reaction with BFO-RGO nanocatalyst.
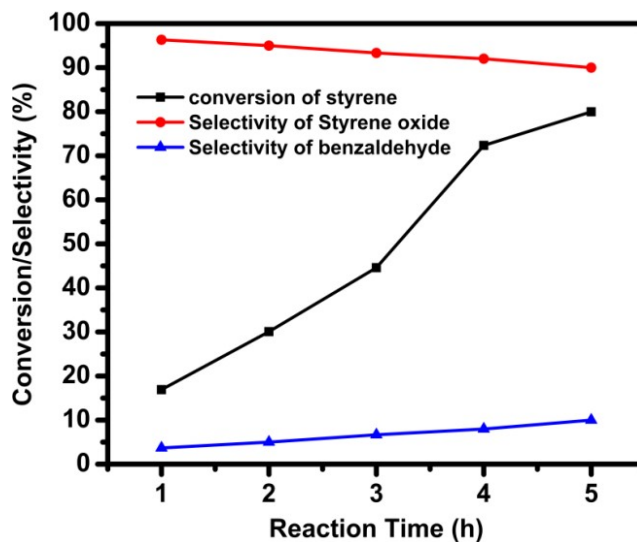
Fig. 4.14 Change of conversion and product selectivity with time in the BFO-RGO catalyzed epoxidation of styrene. Reaction condition: 50 mg catalyst, 5 mmol of styrene and 12.5 mmol of TBHP were stirred in 4 ml of acetonitrile at 100 °C for 5h.

Here, TBHP first couples with BFO to form a reactive species (intermediate A). Then intermediate A further interacts with –C=C- of styrene to develop a coordinated complex (intermediate B). Formation of Styrene oxide from intermediate B occurs *via* Sharpless type mechanism [348]. Here, the π-π interaction of RGO might accelerate the electron transfer between the benzene ring and sp^2 hybridized C-atoms of RGO [147, 148, 153, 349], which facilitates the combination of C-atoms of vinyl groups of styrene with O-atom of TBHP and results in the formation of an epoxidation product with improved conversion and selectivity. The detail mechanistic steps involved in the reaction are schematized in Scheme 4.4.
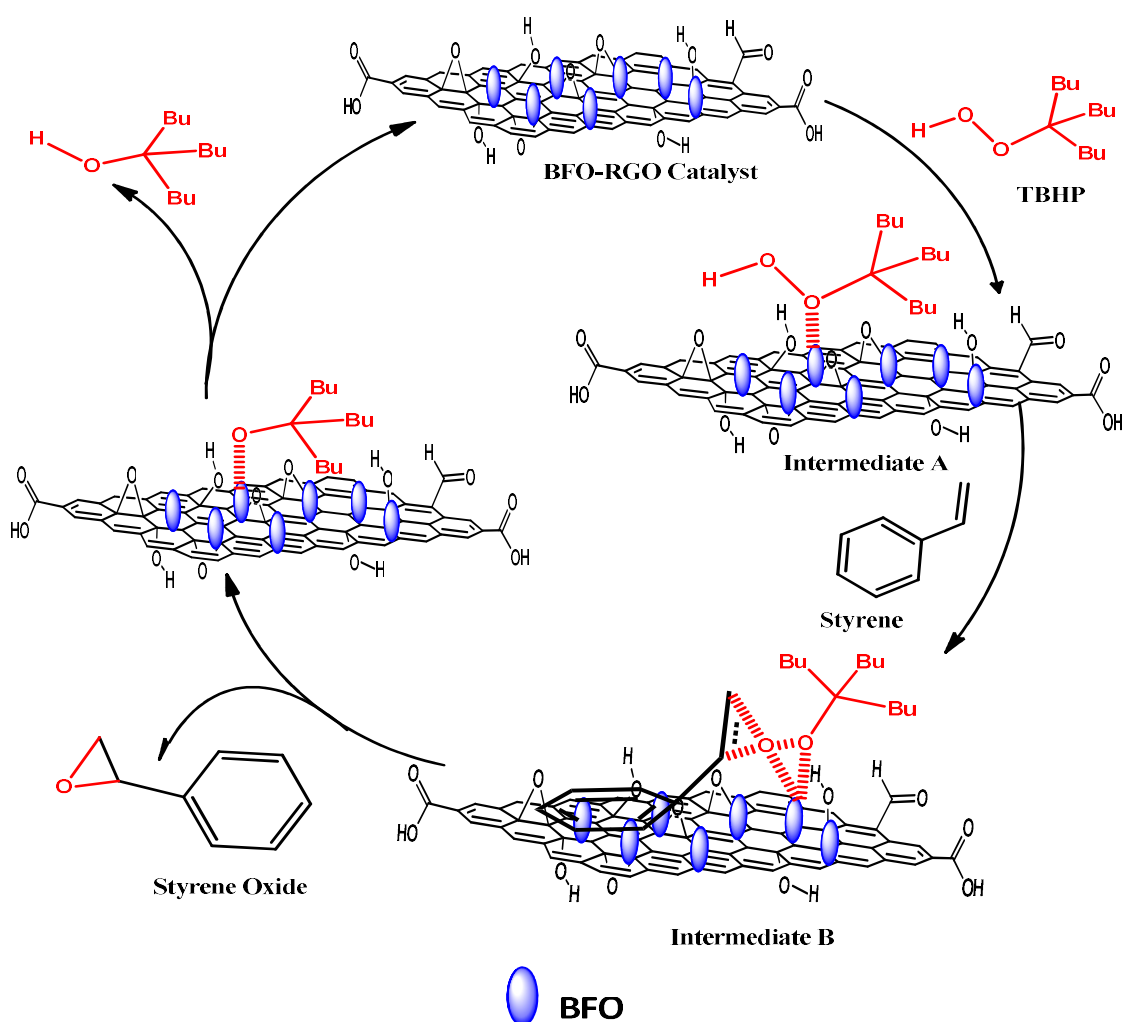
Scheme 4.4 The plausible mechanism involved in the BFO-RGO catalyzed the synthesis of styrene oxide from styrene in the presence of TBHP.

However, when the reaction mixture was allowed to react for more than 5h, it was observed that benzaldehyde was forming due to the reaction of styrene oxide and TBHP (Fig. 4.13). Formation of benzaldehyde proceeds via following mechanism [214] (Scheme 4.5):
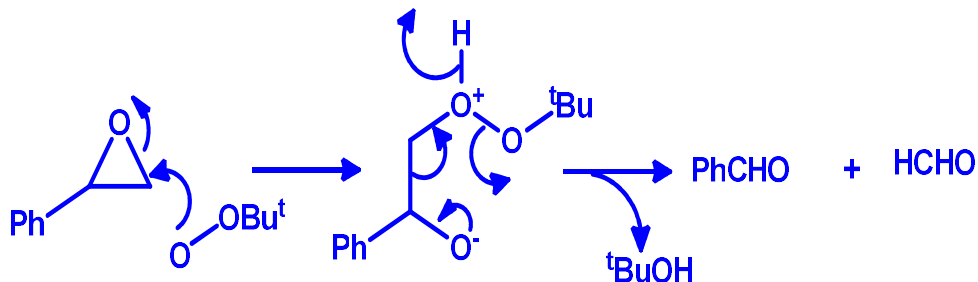
Scheme 4.5 The plausible reaction mechanism involved in the formation of benzaldehyde due to the reaction of styrene oxide and TBHP

The conversion and product selectivity were calculated as follows:

$$\text{Conversion (\%)} = \frac{\text{moles of reactant converted}}{\text{moles of reactant in feed}} \times 100 \qquad (4.3)$$

$$\text{Product Selectivity (\%)} = \frac{\text{Moles of the product formed}}{\text{Moles of the reactant converted}} \times 100 \qquad (4.4)$$

The catalyst can be easily separable from the reaction mixture after completion of the reaction by using an external magnet. This easy magnetic separation of this catalyst also helps to overcome the limitation of separation problem associated with nanoparticles catalyst. The presence of BFO introduces the magnetic character in BFO-RGO nanocatalyst. The superparamagnetic character of this catalyst allows their easy magnetic separation from the reaction mixture with an external magnet (Fig. 4.15)
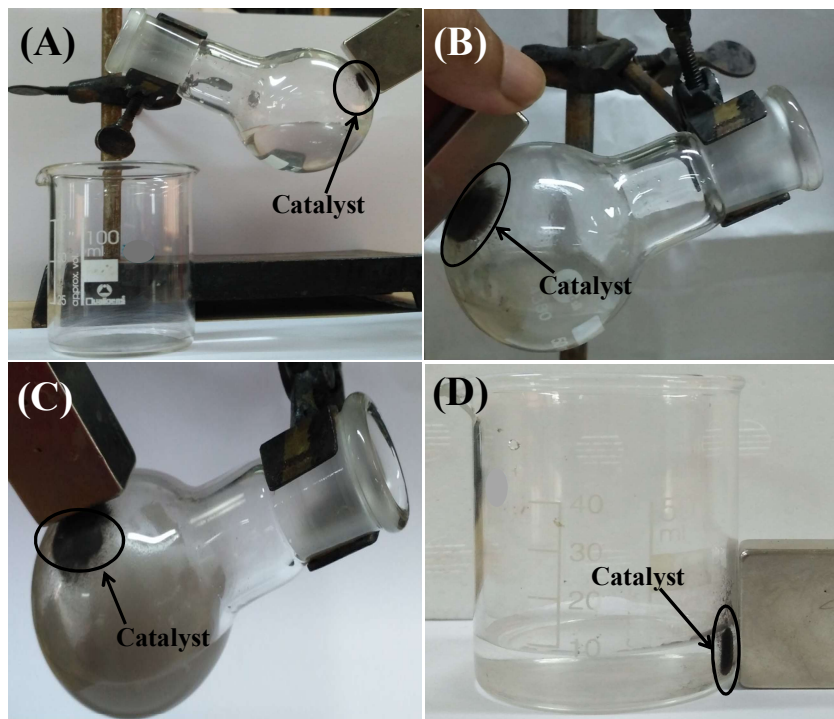
Fig. 4.15 Magnetic separation of BFO-RGO catalyst after completion of the (A) styrene epoxidation, (B) Biginelli, (C) click, and (D) 4-NP reduction reaction.

4.2.5 Reusability of magnetically separable BFO-RGO catalyst after catalysis reactions.

After completion of the reactions the catalyst, BFO-RGO, was magnetically separated, washed with water several times and dried. The recovered catalyst was again used for all reactions. It was observed that activity of the catalyst remained almost same up to 5 cycles. A slight decrease of catalytic activity for Biginelli, click reaction, and an epoxidation reaction was observed after 7th reactions (~2% decrease). For 4-nitrophenol reaction, BFO-RGO exhibited good activity after 10 cycles, with 100% conversion within 6-7 min. (Fig. 4.16). XRD patterns and FESEM image of the reused catalyst also showed no significant changes in their crystal structure as well as morphology compared to the fresh catalyst (Fig. 4.17 A and B)
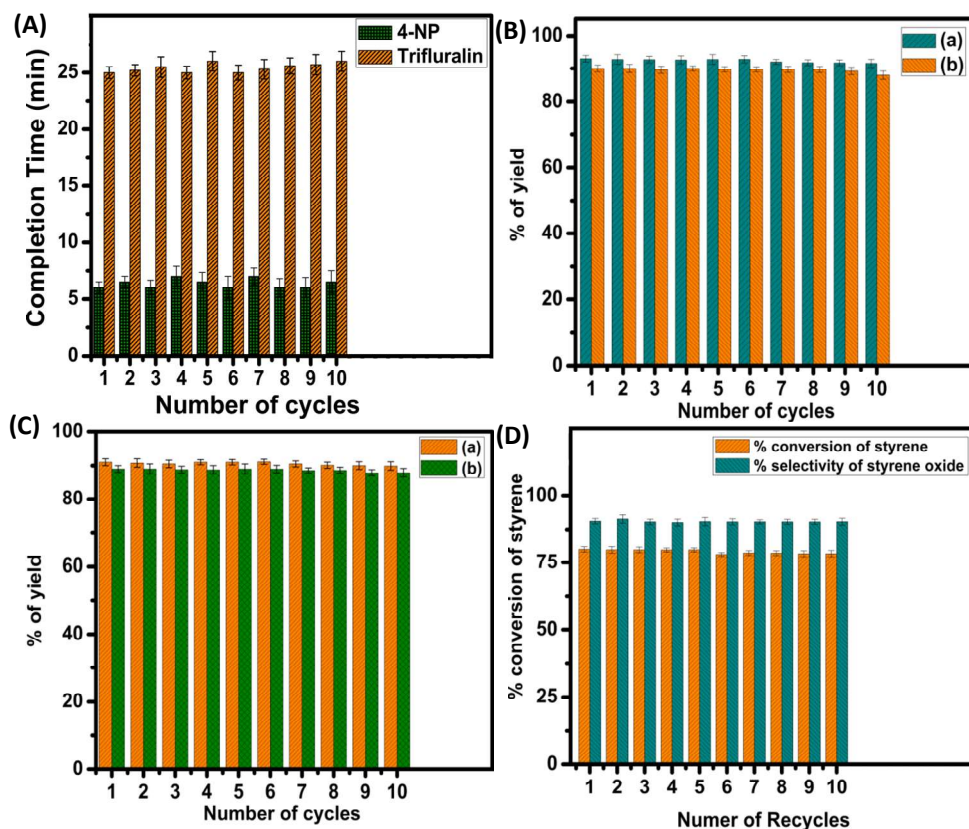
Fig. 4.16 Reusability of magnetically separable catalyst (BFO-RGO) for (A) reduction of 4-NP and trifluralin, (B) synthesis of (a) 5-Ethoxycarbonyl-4-phenyl-6-methyl-3,4-dihydropyrimidin-2(1H)-one and (b) 5-Acetyl-6-methyl-4-phenyl-3,4-dihydropyrimidin-2(1H)-one *via* Biginelli reaction, (C) synthesis of (a) 2-phenyl-2-(4-phenyl-1H-1,2,3-triazol-1-yl)ethanol and (b) 2-(4-Phenyl-1H-1,2,3-triazol-1-yl)cyclohexanol *via* Click reaction and (D) conversion of styrene and selectivity of styrene oxide.
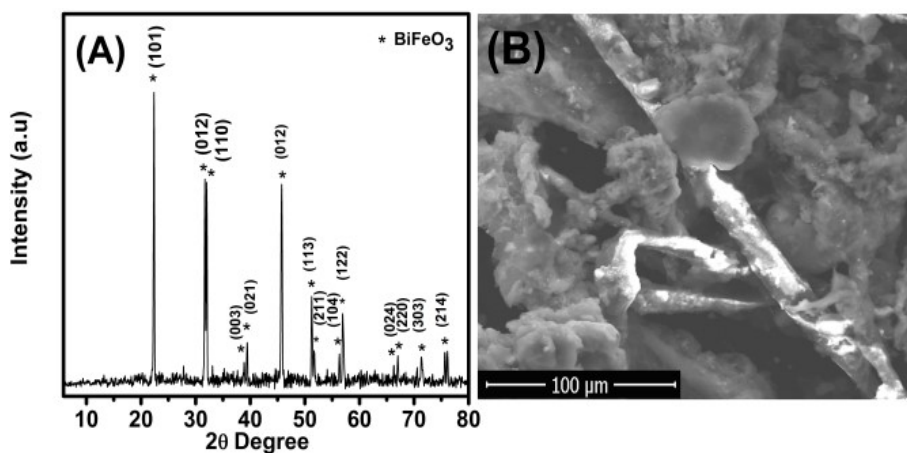
Fig. 4.17 (A) XRD and (B) FESEM image of the recycled BFO RGO catalyst.

4.2.6 Microwaves Absorption property of BFO-RGO nanocomposites

To evaluate microwave absorption properties of pure BFO and BFO-RGO nanocomposites, we have measured the complex permittivity and permeability of the samples by using Equation 1.1 and 1.9 respectively (as described in Section 1.2.1.2 of Chapter 1). Fig. 4.18 shows the complex permittivity and permeability for BFO and BFO-RGO nanocomposites with varying RGO content from (1 to 3 wt. %) in the X-band frequency range (8.2-12.4 GHz).
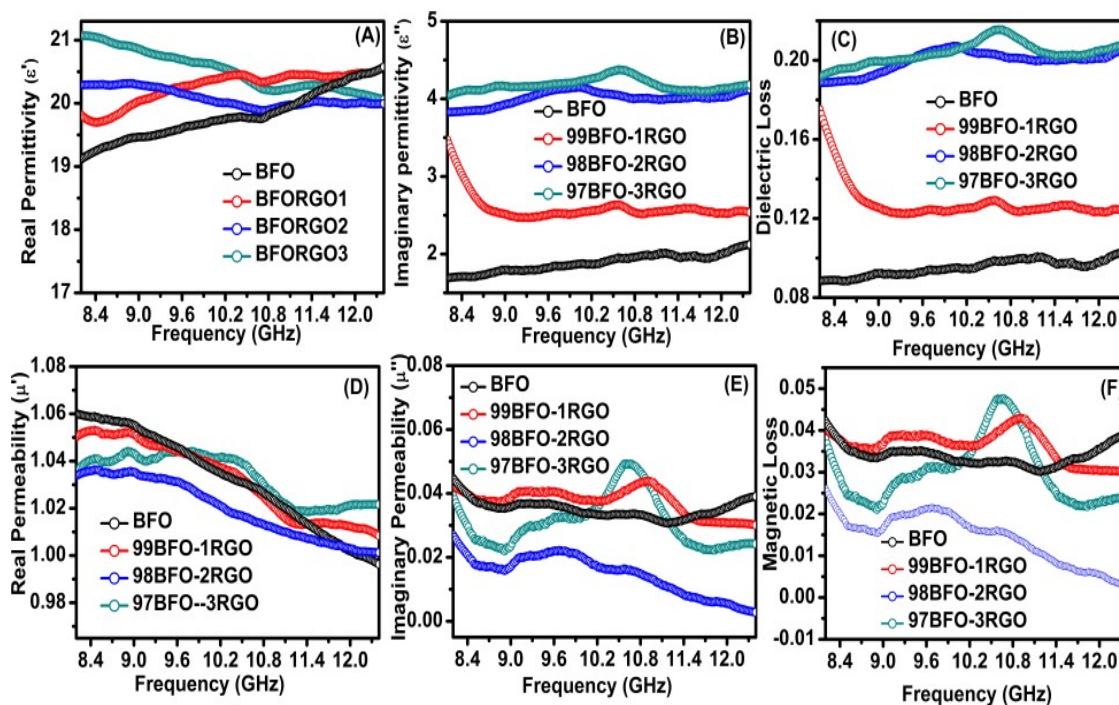
Fig. 4.18 Frequency dependence (A) real part and (B) imaginary part of relative complex permittivity, (C) Dielectric loss, (D) real part and (E) imaginary part of relative complex permeability and (F) magnetic loss values of pure BFO and BFO-RGO nanocomposites with different RGO content.

From Fig. 4.18 (A) and (B) it was observed that initial values of ε' and ε'' increased with increasing RGO content in the BFO-RGO nanocomposites. ε' values were in the range of 19.12-20.55 (pure BFO), 19.79-20.58 (99BFO-1RGO), 20.29-19.97 (98BFO-2RGO) and 21.08-20.08 (97BFO-3RGO). Similarly, ε'' values (Fig. 4.18 (B)) fall in the range of 1.69-

2.17 (pure BFO), 3.45-2.53 (99BFO-1RGO), 3.82-4.14 (98BFO-2RGO) and 4.04-4.20 (97BFO-3RGO). The fluctuation of values of ε' and ε'' became more and more pronounced with increasing RGO content in the composite. In ε'' versus frequency plots (Fig. 4.18 (B)) resonance peaks appeared in the range of 10.5-11.0 GHz for all RGO dominated composites. In the case of 97BFO-3RGO, a strong resonance peak was observed at 10.75 GHz. Therefore, it is clear that resonance peaks can be adjusted by varying the BFO and RGO ratio in the composite. The appearance of resonance peaks might be due to the displacement current lag caused by the interfaces between BFO and RGO in BFO-RGO nanocomposites [1,350,351]. Dielectric tangent loss (tan $\delta_\varepsilon = \varepsilon''/ \varepsilon'$) with changing frequency for pure BFO and BFO-RGO nanocomposites was also calculated and is shown in Fig. 4.18 (C). BFO-RGO nanocomposites possess higher dielectric loss than that of pure BFO. 97BFO-3RGO showed a strong resonance peak at 10.75 GHz. A resonance peak in the same region was also observed in ε'' versus frequency curve of 97BFO-3RGO (Fig. 4.18 (B)). These results suggest that BFO-RGO nanocomposites possess improved dielectric properties. Two important factors (i) conductivity loss and (ii) combined loss of the dipole polarization and interfacial polarization contribute to the dielectric loss of the absorber [1,3,9]. The contribution of conductivity loss, originating from the RGO content in the BFO-RGO nanocomposite, can be explained with the help of free electron loss theory. Although polarization plays a role in the imaginary part, free electrons also have significant effect on it, due to the good electrical conductivity of RGO [23,42-44]. According to the free electron theory [1,3,23,42-44], ε'' could, therefore, be obtained from equation 1.3 (as described in section 1.2.1.2 of chapter 1)

$$\varepsilon'' \approx \sigma(T)/2\pi\varepsilon_0 f \qquad (1.3)$$

where, $\sigma(T)$ is temperature-dependent electrical conductivity, f is frequency and ε_0 is the dielectric constant in a vacuum. Equation (1.3) shows that $\sigma(T)$ plays an important role in ε''. As with the increasing RGO content in BFO-RGO nanocomposites the resistivity of the nanocomposites decreases because of the high conductivity of RGO, it is expected that the composites having more RGO will exhibit higher conductance loss [3,45]. Present studies also revealed that 97BFO-3RGO exhibited highest ε'' value.

To explain the contribution of combined loss of the dipole polarization and interfacial polarizations towards dielectric loss of nanocomposites Debye theory [3] has been employed. The defects present in RGO are probably responsible for dipole polarization, whereas the interfacial polarization originates from the interfaces between BFO nanowire and RGO. In BFO-RGO nanocomposites the presence of large numbers of inner and outer surface interfaces causes the interfacial polarizations, which are associated with relaxation and contribute significantly to the dielectric loss [1,9,45].

Debye dipolar relaxation greatly influences the permittivity behaviors of microwave absorbers. According to Debye dipolar relaxation [1,3,45-47], the relative complex permittivity ε_r can be expressed by the equation 1.4, 1.5, 1.6 and 1.7 (as described in section 1.2.1.2 of Chapter 1):

Debye dipolar relaxation of microwave absorbers is generally determined from Cole-Cole semicircle plots of ε' versus ε''. Each semicircle represents one Debye relaxation process. The Cole-Cole plots of pure BFO and BFO-RGO nanocomposites are shown in Fig. 4.19. The presence of more than one semicircle for each sample suggests the existence of multiple Debye dipolar relaxation process [3]. Under alternating electromagnetic radiation, the lags of induced charges originating from BFO-BFO, BFO-RGO, and RGO-RGO interfaces, which meet the externally applied field, lead to the relaxation and transform the electromagnetic energy to thermal energy [2,3]. Furthermore, the lattice defects and functional groups in RGO also lead to self-doping [2,3]. This induces additional carriers between the RGO and BFO interface and is also beneficial to Debye relaxation.
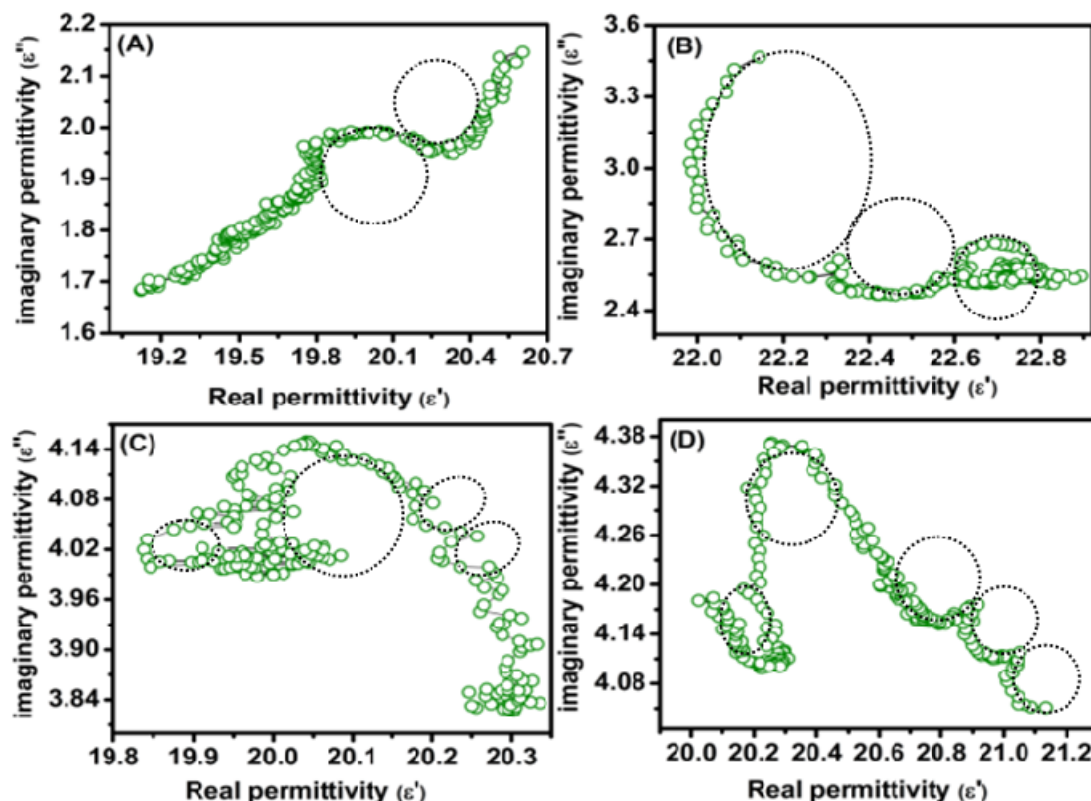
Fig. 4.19 Typical Cole-Cole semicircles for (A) BFO, (B) 99BFO-1RGO, (C) 98BFO-2RGO, and (D) 97BFO-3RGO in the frequency range 8-12 GHz.

These factors are responsible for multiple relaxation processes of BFO-RGO nanocomposites. Thus, during this process, the EM wave is attenuated to a certain degree. Moreover, besides the Debye relaxation effect, the Maxwell-Wagner relaxation due to the accumulation of bound charges at the heterogeneous interfaces also causes to absorb EM waves [1-3,45].

The magnetic loss is also an important factor that contributes to the EM wave attenuation in BFO-RGO nanocomposites. Fig. 4.18 (D) shows the changes of μ' values with varying RGO content in BFO-RGO composites. μ' values of pure BFO and BFO-RGO nanocomposites fall in the range of 1.059-0.990 (pure BFO), 1.050-1.007 (99BFO-1RGO), 1.030-1.002 (98BFO-2RGO) and 1.030-1.02 (97BFO-3RGO). Similarly, μ'' values (Fig. 4.18 (E)) fall in the range of 0.044-0.0399 (pure BFO), 0.041-0.030 (99BFO-1RGO), 0.026-0.003 (98BFO-2RGO) and 0.038-0.025 (97BFO-3RGO). 97BFO-3RGO composite shows a broad resonance peak at 8.7-11.5 GHz with a maximum value at 10.75

GHz. Fig. 4.18 (F) shows the change of magnetic tangent loss (tan $\delta_\mu = \mu''/\mu'$) with changing frequency for all the samples. tanδ_μ for pure BFO first declines in the frequency range 8.2-8.78 GHz, then remains constant with small fluctuations in the frequency range 8.78-11.21 GHz and finally increases in the frequency range of 11.21-12.4 GHz. But, in the case of 97BFO-3RGO, tan δ_μ first declines following a similar trend as pure BFO in the frequency range 8.2-8.78 GHz, followed by a broad resonance peak at 8.78-11.4 GHz with a maximum value at 10.68 GHz, and then remains almost constant in the frequency range 11.4-12.4 GHz.

Theoretically, the magnetic loss of magnetic materials is related to hysteresis loss, domain wall resonance, exchange resonance, eddy current loss, and natural resonance [3,34]. The effect of eddy current loss was estimated by using equation 1.11 and 1.12 (as described in section 1.2.1.2 of Chapter 1): [1-3,47,59]

$$\mu'' \approx 2\pi \mu_0 (\mu')^2 \sigma d^2 f / 3 \qquad (1.11)$$

$$C_0 = \mu'' (\mu')^{-2} f^{-1} = 2\pi \mu_0 d^2 \sigma \qquad (1.12)$$

where C_0 is eddy current coefficient, μ_0 is permeability in vacuum, d is the thickness of the absorber and σ is electrical conductivity of the composite. When the value of $\mu'' (\mu')^{-2} f^{-1}$ does not change with increasing frequency then it can be assumed that the eddy current loss is contributing towards magnetic loss [1,3]. Another important factor which contributes to the magnetic loss is the natural resonance and can be described by natural resonance equation (equation 1.13, 1.14 and 1.15 section 1.2.1.2 of Chapter 1): [1,3,59,60]

$$2\pi f_r = \gamma H_a \qquad (1.13)$$

$$H_a = 4|K_1|/3\mu_0 M_s \qquad (1.14)$$

$$K_1 = \mu_0 M_s H_c / 2 \qquad (1.15)$$

where H_a is anisotropy energy, γ is a gyromagnetic ratio, $|K_1|$ is anisotropy coefficient, μ_0 stands for permeability in free space ($4\pi \times 10^{-7}$ Hm^{-1}), H_c is coercivity, M_s is saturation magnetization and f_r is the resonance frequency.

Fig. 4.20 shows the change in eddy current coefficient (C_0) with increasing frequency for all the samples. In case of pure BFO, as the eddy current coefficient (C_0) changes with increasing frequency, it can be assumed that the magnetic loss is not caused by eddy current effect. In the case of BFO-RGO samples, it was observed that C_0 remains almost constant in the frequency range of 11.5 to 12.4 GHz and this might originate from eddy current loss. Additionally, C_0 values of the nanocomposites change in the frequency range from 8.2 to 11.5 GHz, and the resonance peaks are located at 10.90 GHz and 10.63 GHz for 98BFO-2RGO and 97BFO-3RGO respectively. This might be the contribution from natural resonance phenomena [1,3].

Therefore, we can conclude that magnetic loss in case of BFO-RGO nanocomposite comes up with a mixed mechanism comprised of both eddy current loss and natural resonance phenomenon. Furthermore, from equation 1.13, it is also clear that natural resonance depends upon anisotropic energy (H_a) and higher anisotropic energy favors the microwave absorption properties at high frequency. But this enhancement in H_a can be achieved by lowering M_s of the absorber (equation 1.14) [1,3,60]. In the present case, the M_s value of BFO-RGO nanocomposite decreases with the increasing RGO content in the composite and is lowest for 97BFO-3RGO (Fig. 4.11). Thus, the anisotropic energy for 97BFO-3RGO nanocomposite is highest among all BFO-RGO nanocomposites. So it is expected that due to high anisotropic energy 97BFO-3RGO can show enhanced microwave absorption properties compare to pure BFO.
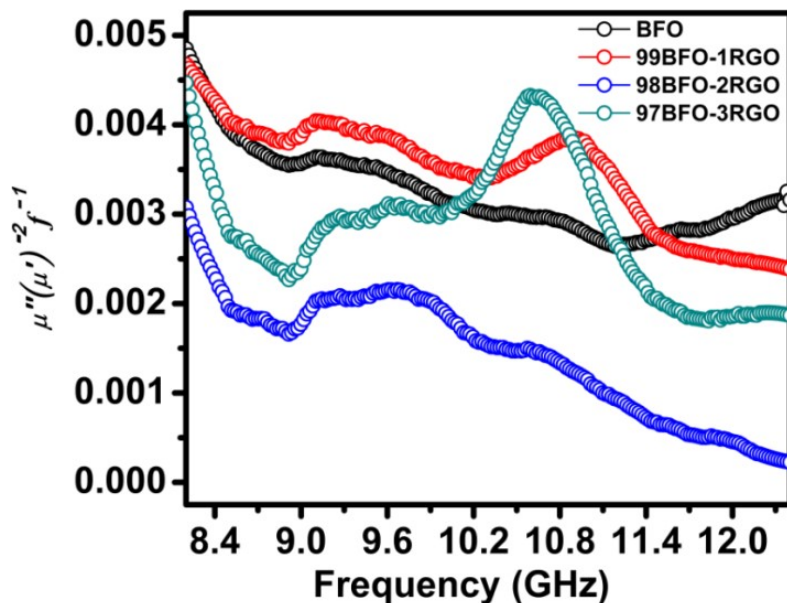
Fig. 4.20 Plots of μ'' $(\mu')^{-2}f^{1}$ *vs.* frequency for the sample BFO, 99BFO-1RGO, 98BFO-2RGO, and 97BFO-3RGO in the frequency range 8-12 GHz.

The reflection loss (RL) was calculated from the complex relative permeability and permittivity at a given frequency and specimen thickness using Equation 1.16 and 1.17 (as described in section 1.6 of Chapter 1).

The contribution of complex permittivity ($\varepsilon_r = \varepsilon' - j\varepsilon''$) and permeability ($\mu_r = \mu' - j\mu''$) in the lightweight absorber can be expressed by quarter-wavelength matching model equation 4.17: [3,47,56,139]

$$t_m = n\lambda/4 = nc/4f_m\ (\varepsilon_r\mu_r)^{1/2} \qquad n = 1, 2, 3\ldots \qquad (4.5)$$

where λ, f_m, and t_m are the wavelength of the materials, the frequency of complex permeability and complex permittivity and the absorber matching thickness at maximum microwave absorption. According to equation 4.5, absorbers with low thickness (t_m) possess a high value of ε_r. As ε_r is dependent on ε' and ε'', and the values of ε' and ε'' are influenced by the composition of the composites, the thickness of the absorber can be adjusted by judiciously selecting the composition of the absorber.
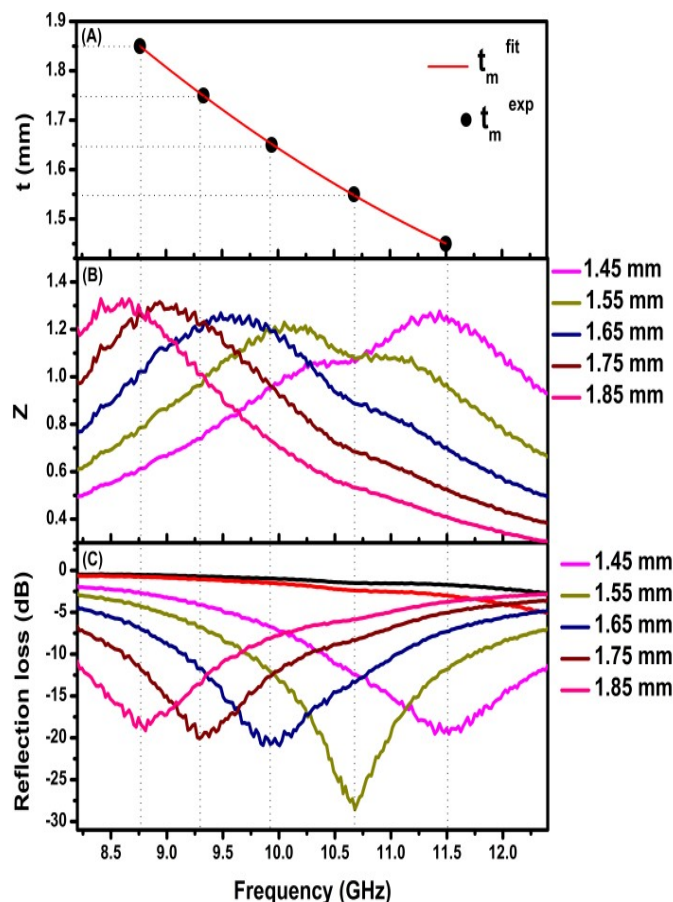
Fig. 4.21 (A) Comparison of the calculated matching thickness (t_m^{fit}) under n=1 to the t_m^{exp} obtained from RL values of 97BFO-3RGO, (B) the modulus of the normalized impedance Z, and (C) RL values of 97BFO-3RGO with different thickness.

It is clear from equation 1.16 and 1.17 that, in addition to good permittivity and permeability values, excellent impedance matching is another key factor for improving microwave absorption [46,139]. The modulus of the normalized characteristic impedance $Z = |Z_{in}/Z_0|$ has been calculated according to equation 1.16 and 1.17 (Fig. 4.21 (A)-(C)). It represents the ability of microwave to enter into the absorber and be converted to thermal energy or dissipated through interference. When the value of Z is equal or close to 1, it is beneficial for improving microwave absorption of the absorber [47, 139]. As t_m can be calculated from equation 4.5, a fitting curve was constructed by plotting t_m^{fit} (calculated from equation 4.5) versus frequency (Fig. 4.21 (A)). Matching thickness can also be obtained directly from RL curves (Fig. 4.21 (C)), which can be denoted as t_m^{exp}. When t_m^{exp} values (as black dots) were placed in t_m^{fit} curve (red line), it was observed that t_m^{fit} and

$t_m{}^{exp}$ are in good agreement. In the case of 97BFO-3RGO f_m was 10.68 GHz when t_m was 1.55 mm. Here Z was found to be very close to 1.

For pure BFO and BFO-RGO nanocomposites having various compositions, reflection loss (RL) values were calculated and shown in Fig. 4.22 (A) and (B).
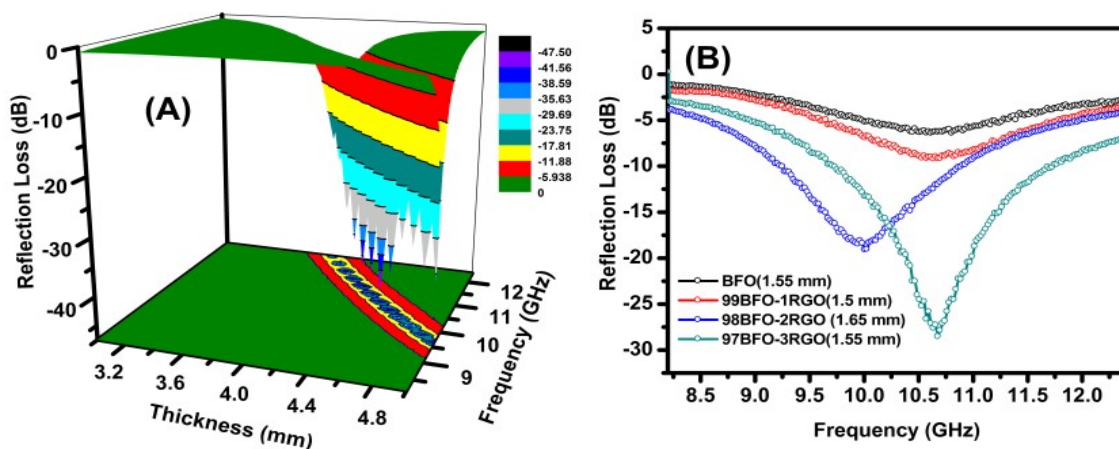
Fig. 4.22 Frequency dependence minimum reflection loss values for synthesized (A) BFO with a variation of thickness (3-5 mm) and (B) minimum reflection loss values of BFO and BFO-RGO nanocomposites with varying RGO content.

The important points are:

(i)   Pure BFO exhibited minimum RL of -45 dB (i.e., ~99.99%) at 10.78 GHz when the thickness was 4.5 mm (Fig. 4.22 (A)). Microwave absorption of the synthesized BFO nanowire in X-band region was found to be better than that of polycrystalline BiFeO₃ nanoparticles [14,352-355], which might be due to the 1-D nanowire like the structure of synthesized BFO. However, a thickness of 4.5 mm is quite large as a lightweight absorbing material. Moreover, the effective bandwidth was ~1 GHz which is also very low. When the thickness was lowered, the minimum RL values of BFO were decreased. When the thickness was 1.55 mm, minimum RL was -6.7 dB (~79 %) at 10.62 GHz (Fig. 4.22 (B)).

(ii)   With increasing RGO content in the composite minimum RL value was increased.

(iii)   Effective bandwidth (i.e., RL < -10 dB) was found to be increased with increasing RGO content in the composite.

(iv)   The composite is having 97 wt% BFO, and 3 wt% RGO (97BFO-3RGO) exhibited superior microwave absorption properties compare to pure BFO and other compositions of BFO-RGO nanocomposite. 97BFO-3RGO possessed highest value of minimum RL of -28.68 dB (i.e., 99.75% absorption) at 10.68 GHz when the thickness was 1.55 mm with effective bandwidth in the 9.6-11.7 GHz range.

To demonstrate the influence of thickness on microwave absorption properties, a 3D image map and a contour map of reflection loss in the frequency range 8-12 GHz for 97BFO-3RGO were plotted and are shown in Fig. 4.23 (A) and (B). It is important to note that 97BFO-3RGO exhibited minimum 99% microwave absorption (> -20.0 dB) for the thickness ranging from 1 to 2 mm at various frequencies covering the whole X-band region (8.2-12.4 GHz).
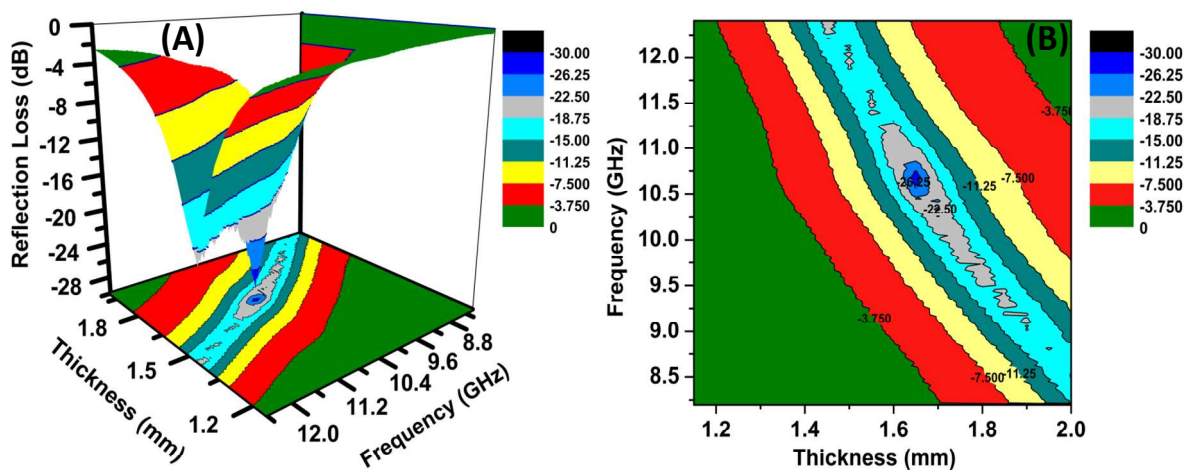
Fig. 4.23 (A) Three dimensional and (B) Two-dimensional contour representations of frequency dependence of reflection loss values of 97BFO-3RGO nanocomposites with the variation of thickness (1-2 mm).

Several factors are responsible for the enhanced microwave absorption property of BFO-RGO nanocomposites. Some of the important factors are (i) the existence of the residual defects and functional groups in RGO favor electromagnetic energy absorption, (ii) the high aspect ratio and high conductivity of RGO sheets provide better microwave absorption properties, (iii) the presence of interfaces between BFO-BFO, BFO-RGO and RGO-RGO causes interfacial polarization and associated Debye relaxation which contribute to the dielectric loss of BFO-RGO nanocomposites. At the same time, eddy current loss and natural resonance loss also contribute to the magnetic loss of the BFO-RGO nanocomposites. These factors play important roles in making BFO-RGO nanocomposites excellent microwave absorbing materials. To provide a visual demonstration of microwave absorbing mechanism of BFO-RGO, a schematic diagram is presented in Scheme 4.6.
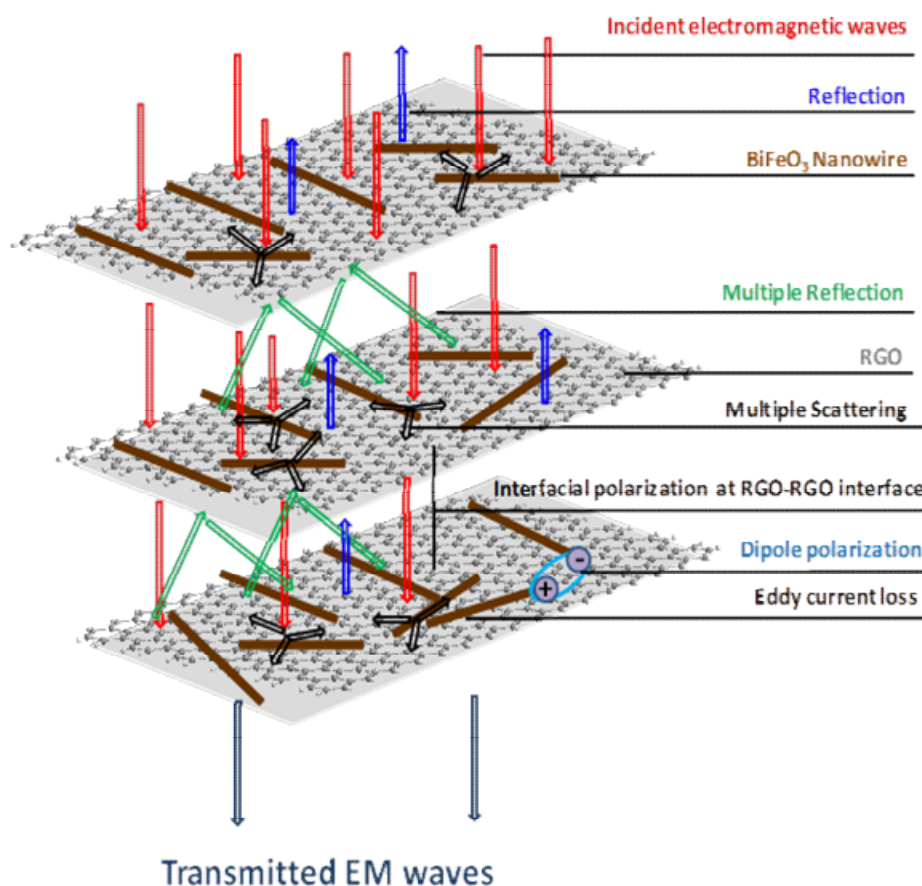
Scheme 4.6 Possible microwave absorbing mechanisms of the BFO-RGO nanocomposites.

To the best of our knowledge 1-D BiFeO$_3$ nanowire-RGO nanocomposite exhibited comparable and even superior microwave absorption property than most of the ferrite-based composite in X-band region [1-4,7,11,19-22,24,26,28-34].

4.3 Summary of results

(i)   Here, we have described a facile hydrothermal synthesis method to prepare BiFeO$_3$ nanowire-reduced graphene oxide (BFO-RGO) nanocomposites.

(ii)   The methodology employed to prepare these nanocomposites is very simple and does not require any elaborate setup.

(iii)   The synthesized BFO-RGO nanocatalyst consists of pure single phase BiFeO$_3$ nanowires, which are embedded on the surface of nanometer thin RGO sheets.

(iv)   The microwave absorption property of these nanocomposites has been improved with the increasing RGO content (up to 3 wt %) in the composites. The synergy of dielectric loss and magnetic loss along with multiple interfaces between RGO and BiFeO$_3$ nanowires are mainly responsible for the enhanced microwave absorption property of BFO-RGO nanocomposites.

(v)   The 1-D nanowire structure of BiFeO$_3$ greatly influences the microwave absorption properties of BFO-RGO nanocomposites. In the case of the nanocomposite containing 97 wt % BFO and 3 wt % RGO (97BFO-3RGO), proper impedance matching (Z close to 1) was observed.

(vi)   This composite exhibited minimum reflection loss of -28.68 dB (i.e., 99.75 % absorption) at 10.68 GHz with effective bandwidth 9.6-11.7 GHz with an absorber thickness of only 1.55 mm.

(vii)   Moreover, it also exhibited microwave absorption >-20 dB (99 % absorption) for the entire range of X-band (8.2-12.4 GHz) when the absorber thickness varied between 1 to 2 mm.

(viii)   BFO-RGO nanocomposites exhibit its potential as an efficient lightweight microwave absorber in the X-band region, which is important for radar absorption applications.

(ix)   1-D BiFeO$_3$ nanowire-RGO nanocomposite exhibited comparable and even superior microwave absorption property than most of the ferrites and ferrite based composites in X-band region [1-4,7,9-11,35,52,59-64,107,109,126-134,139-143].

(x) This BiFeO$_3$-RGO nanocomposite also showed its versatile catalytic activity towards (i) reduction of 4-nitrophenol (4-NP) and a herbicide, trifluralin in the presence of NaBH$_4$ (ii) Biginelli reaction (iii) epoxidation of styrene and (iv) Click reactions.

(xi) The excellent catalytic activity of this catalyst arises from the synergistic effect of RGO and BFO.

(xii) It is important to note that, as Biginelli reaction can be performed in solventless condition and click reaction in an aqueous medium, therefore, this catalyst promotes the environmentally green approach to conduct these organic synthesis reactions.

(xiii) The usefulness of BFO-RGO as a catalyst for various important organic reactions, its high catalytic efficiency, easy separation and good reusability make it an attractive nanocatalyst.

(xiv) 98BFO-2RGO nanocomposites exhibited excellent catalytic activity towards (i) reduction of 4-nitrophenol (4-NP), (ii) Biginelli reaction (iii) epoxidation of styrene, and (iv) 'click reactions.' The catalytic efficiency of 98BFO-2RGO nanocomposites is comparable and in some cases superior to the already reported catalysts [146-148,217,228,229,231-233,235,240,246-250,252,253,286-310,348-361].

(xv) This nanocomposite not only shows higher minimum RL in comparison with pure BFO but also its lightweight, due to the presence of RGO, offers an added advantage.

(xvi) The heteroarchitectural structure of RGO-BFO composites caused to enhance its catalytic property as well as microwave absorption property.

(xvii) BFO-RGO nanocomposites have demonstrated its capability to act as a multifunctional material as a heterogeneous catalyst as well as a good microwave absorber.

4.4 Spectral Data and plots of the products obtained from Biginelli reaction and Click reaction

5-Ethoxycarbonyl-4-phenyl-6-methyl-3,4-dihydropyrimidin-2(1*H*)-one:

Solid, m.p. 204-205°C (reported 205-206°C (Ref. 4), FTIR (KBr): 3434, 3235, 3111, 2932, 1711, 1647, 1575 cm^{-1}. ^{1}H NMR (CDCl$_3$, 400 MHz): δ (ppm) 1.18 (t, 3H), 2.37 (s, 3H), 4.10 (m, 2H), 5.42 (s, 1H), 5.69 (s, 1H), 7.29-7.34 (m, 5H), 7.95 (s, 1H).

5-Acetyl-6-methyl-4-phenyl-3,4-dihydropyrimidin-2(1*H*)-one:

Solid, m.p.236-237°C (reported 235-236°C. (Ref. 4) IR (KBr): 1616, 1701, 2920, 3116, 3294 cm^{-1}. ^{1}H NMR (DMSO-d$_6$, 400 MHz): δ (ppm) 2.11(s, 3H), 2.30 (s, 3H), 5.27 (s, 1H), 7.25-7.33 (m, 5H), 7.83 (s, 1H), 9.18 (s, 1H).

2-phenyl-2-(4-phenyl-1*H*-1,2,3-triazol-1-yl)ethanol:

Solid, m.p. 127-128°C (reported 125-127°C (Ref. 9), IR (KBr): 693, 755, 1057, 1084, 1223, 1431, 1455, 1493, 2939, 3029, 3089, 3123, 3427 cm^{-1}. ^{1}H NMR (CDCl$_3$, 400 MHz): δ (ppm) 3.62 (t, 1H), 4.25 (m, 1H), 4.68 (m, 1H), 5.70 (dd, 1H), 7.28-7.43 (m, 8H), 7.72 (s, 1H), 7.79 (d, 1H).

2-(4-Phenyl-1*H*-1,2,3-triazol-1-yl) cyclohexanol:

Solid, m.p. 172-174°C (reported 168.0-171.0°C (Ref. 9), IR (KBr): 696, 763, 1054, 1232, 1447, 2858, 2938, 3119, 3298 cm^{-1}. 1H NMR (CDCl$_3$, 400 MHz): δ (ppm) 1.42-2.27 (m, 8H), 3.91 (s, 1H), 4.14 (m, 2H), 7.28-7.39 (m, 3H), 7.67 (d, 2H), 7.75 (s, 1H).
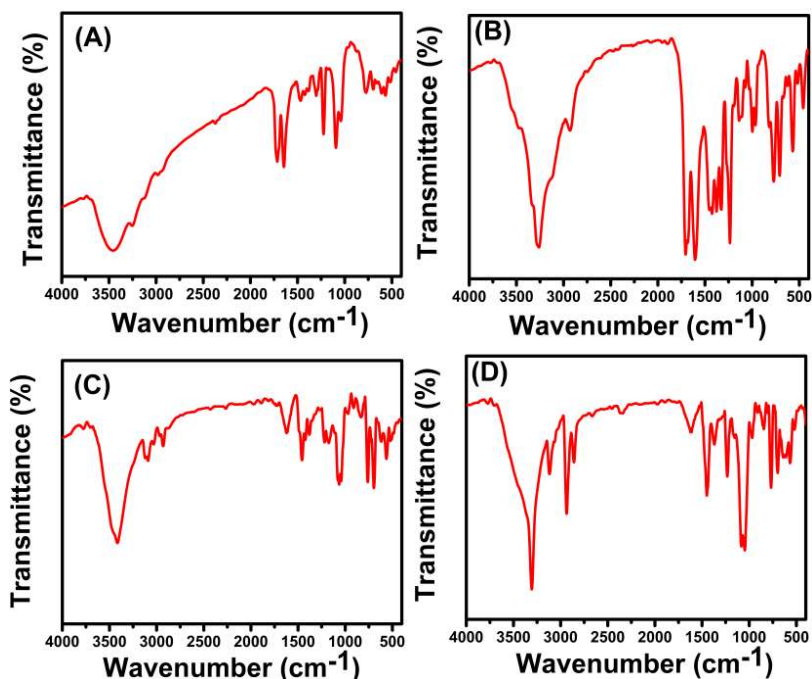
Fig. 4.24 FT-IR spectrum of (A) 5-Ethoxycarbonyl-4-phenyl-6-methyl-3,4-dihydropyrimidin-2(1*H*)-one, (B) 5-Acetyl-6-methyl-4-phenyl-3,4-dihydropyrimidin-2(1*H)*-one, (C) 2-phenyl-2-(4-phenyl-1*H*-1,2,3-triazol-1-yl)ethanol, and (D) 2-(4-Phenyl-1*H*-1,2,3-triazol-1-yl)cyclohexanol.
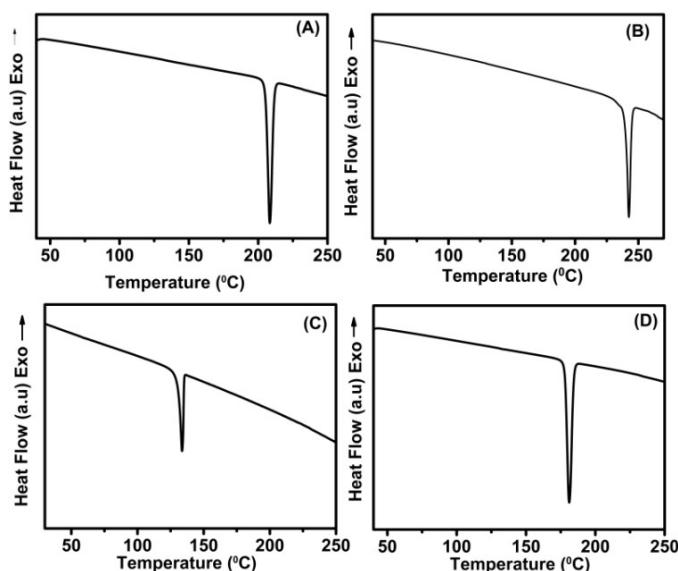
Fig. 4.25 DSC of (A) 5-Ethoxycarbonyl-4-phenyl-6-methyl-3,4-dihydropyrimidin-2(1*H*)-one, (B) 5-Acetyl-6-methyl-4-phenyl-3,4-dihydropyrimidin-2(1*H)*-one, (C) 2-phenyl-2-(4-phenyl-1*H*-1,2,3-triazol-1-yl)ethanol, and (D) 2-(4-Phenyl-1*H*-1,2,3-triazol-1-yl)cyclohexanol.
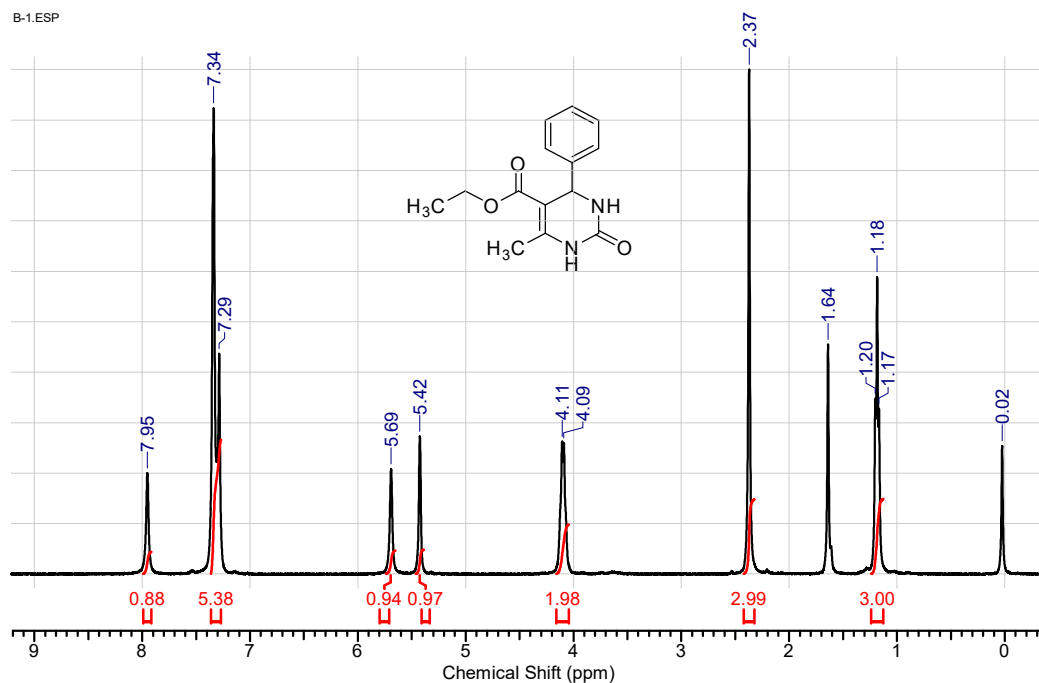
Fig. 4.26 ^{1}H NMR (CDCl₃, 400 MHz) spectrum of 5-Ethoxycarbonyl-4-phenyl-6-methyl-3,4-dihydropyrimidin-2(1H)-one.
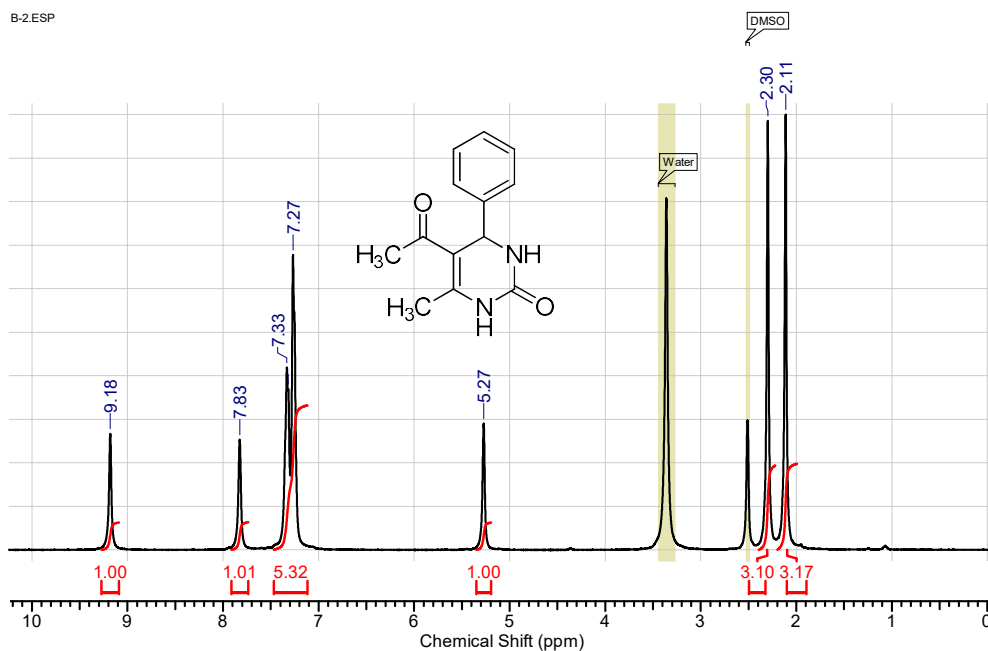
Fig. 4.27 ^{1}H NMR spectrum of 5-Acetyl-6-methyl-4-phenyl-3,4-dihydropyrimidin-2(1H)-one.
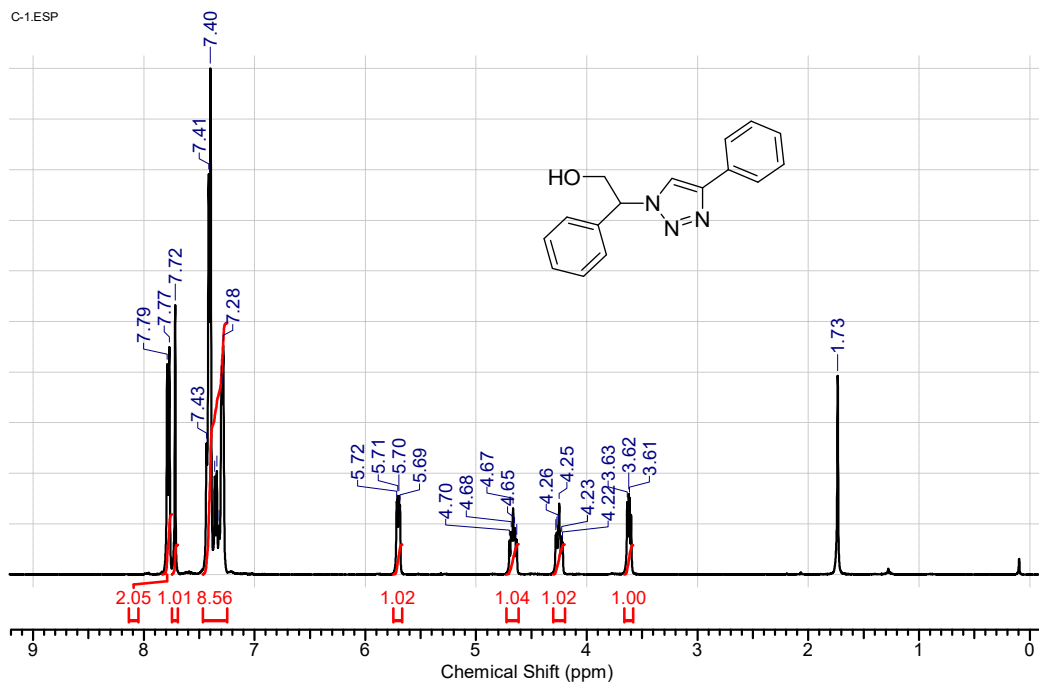
Fig. 4.28 ^{1}H NMR (CDCl₃, 400 MHz) spectrum of 2-phenyl-2-(4-phenyl-1H-1,2,3-triazole-1-yl) ethanol.
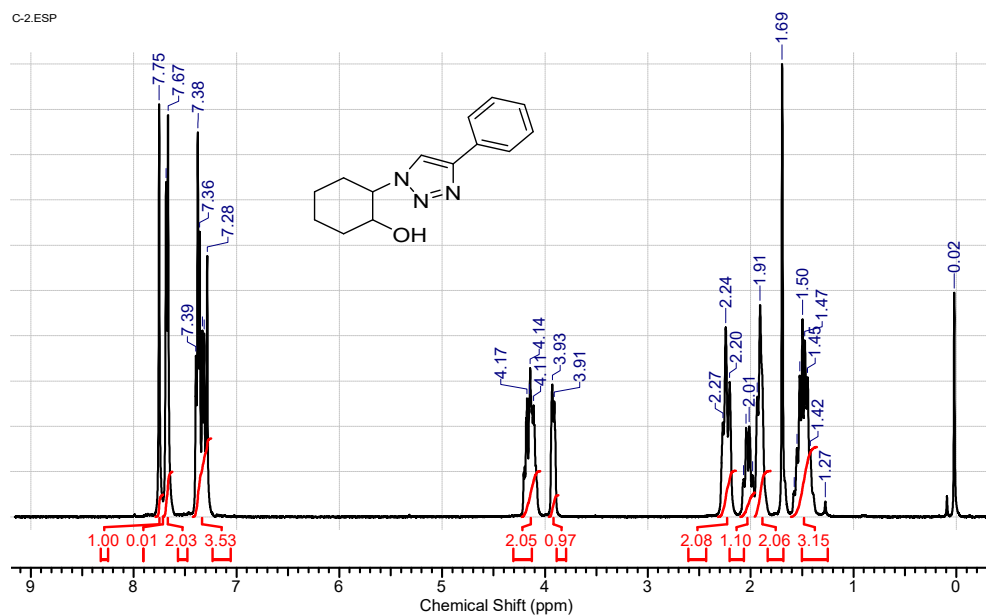
Fig. 4.29 ^{1}H NMR (CDCl₃, 400 MHz)spectrum of 2-(4-Phenyl-1H-1,2,3-triazol-1-yl) cyclohexanol.

Chapter 5
Conclusion

5.1 Summary of Results

(i)   The work, which is presented in this thesis, describes the synthesis of ferrite -
       RGO nanocomposites (e.g., $Ni_{0.8}Zn_{0.2}Fe_2O_4$-RGO, $CoFe_2O_4$-RGO, and $BiFeO_3$
       nanowire-RGO). An *'in situ'* co-precipitation technique was developed to
       prepare NZF-RGO and CF-RGO. A facile hydrothermal method was employed
       to prepare BFO-RGO.

       Comparisons of the catalytic activities and microwave absorption of
       these nanocomposites with the results reported by other researchers are
       summarized in Tables 5.1-5.7

(ii)   50NZF-50RGO and 98BFO-2RGO have shown excellent catalytic activity
       towards the reduction of 4-nitrophenol to 4-aminophenols in the presence of an
       excess aqueous solution of $NaBH_4$. 50NZF-50RGO also exhibited high catalytic
       activity towards decolorization of various dyes via $NaBH_4$ reduction.

(iii) 75CF-25RGO shows high catalytic activity towards photodegradation of
       synthetic dyes (e.g., Methyl orange, Methylene blue, Rhodamine B and a
       mixture of dyes) under visible light irradiation.

(iv)   Synthesized 98BFO-2RGO nanocomposite demonstrated its versatile catalytic
       activities towards multiple reactions such as Biginelli reaction, Click reaction,
       and epoxidation of styrene.

(v)   The catalytic activities of these catalysts were found to be comparable and in
       some cases better than various reported catalysts (Table 5.1-5.6).

(vi)   50NZF-50RGO, 85CF-15RGO, and 97BFO-3RGO nanocomposites also show
       excellent microwave absorption properties in the X band region (8.2-12.4 GHz).

(vii) From the results obtained from the microwave absorption study, following
       points were observed:

       ➢   All the nanocomposites exhibited more than 99% minimum RL in the
            X-band region (8.2-12.4 GHz).

       ➢   50NZF-50RGO showed minimum RL of -19.99 dB (~ 99% loss) at
            11.58 GHz with absorber thickness of 1.8 mm and effective
            bandwidth was 10.22-12.4 GHz.

       ➢   85CF-15RGO also exhibited ~99.94 % minimum RL (-31.31 dB) at
            9.05 GHz in X-band region when the thickness was 2.15 mm with

effective bandwidth in 8.2-10.92 GHz. This composite also exhibited minimum 99.5% microwave absorption (> -26.6 dB) for all the thickness (1.9-2.4 mm) at various frequencies in X-band region.

➢ 97BFO-3RGO possessed highest value of minimum RL of -28.68 dB (i.e., 99.75% absorption) at 10.68 GHz when the thickness was 1.55 mm with effective bandwidth in the 9.6-11.7 GHz range. The 1-D nanowire structure of $BiFeO_3$ greatly influences the microwave absorption properties of BFO-RGO nanocomposites

➢ Moreover, BFO-RGO nanocomposites also exhibited microwave absorption >-20 dB (99 % absorption) for the entire range of X-band (8.2-12.4 GHz) when the absorber thickness varied between 1 to 2 mm.

➢ It was observed that for all the composites with increasing RGO content minimum RL value was increased. The synergy of dielectric loss and magnetic loss along with multiple interfaces between RGO and NZF, CF and BFO are mainly responsible for the enhanced microwave absorption property of all the nanocomposites.

➢ Effective bandwidth (i.e., RL < -10 dB) was found to be increased with increasing RGO content in the composite.

➢ The synthesized nanocomposite not only shows higher minimum RL in comparison with pure ferrite but also its lightweight, due to the presence of RGO, offers an added advantage.

➢ The microwave absorption properties of all these nanocomposites in X-band region are comparable and even superior to many RGO-ferrite nanocomposites. (Table 5.7)

Table 5.1 Comparison of catalytic efficiency of different catalysts for the reduction of 4- nitrophenol to 4- aminophenol.

Catalyst	Completion time	Rate constant	Reference
Cu@SBA-15@CF	4 min	1.10 min^{-1}	[146]
Ag@CoFe$_2$O$_4$	4 min	1.18 min^{-1}	[252]
Ag10@SBA-15	5 min	1.274×10^{-2} s^{-1}	[253]
Au/Ag Bimetallic Nanocatalyst	535 s	6.07×10^{-3} s^{-1}	[286]
Au nanoparticle	-	9.19×10^{-3} s^{-1}	[287]
Ag nanoparticle	-	4.06×10^{-3} s^{-1}	[287]
Cu nanoparticle	45 min	0.09254 min^{-1}	[288]
Au@meso-SiO$_2$ hollow nanospheres	20 min	0.08 min^{-1}	[289]
Au@MSNs	20 min	0.18 min^{-1}	[290]
Ag-SBA-15	360 s	9.0×10^{-3} s^{-1}	[291]
Au/SBA-15	4 min	1.045 min^{-1}	[292]
Ni/SBA-15	18 min	0.003 s^{-1}	[293]
10%Cu/SBA-15	5 min	0.501 min^{-1}	[294]
CuFe$_2$O$_4$	3 min	0.846 min^{-1}	[295]
NiFe$_2$O$_4$	16 min	0.118 min^{-1}	[295]
dumbbell-like Au-Fe$_3$O$_4$	10 min	0.63 min^{-1}	[296]
Fe$_3$O$_4$/Cu	4 min	1.0655 min^{-1}	[297]
Fe$_3$O$_4$@Ag	6 min	0.87 min^{-1}	[298]
2.5Ru@SBA-15	5 min	0.81 min^{-1}	[299]
12.5Cu@SBA-15	4 min	1.04 min^{-1}	[300]
CuO@mTiO$_2$@CF	5 min	0.72 min^{-1}	[301]
Ag@mTiO$_2$@CF	4 min	1.08 min^{-1}	[302]
CuFe$_2$O$_4$	6 min	36.17 min^{-1}g^{-1}	[303]
mesoporous BiFeO$_3$	4 min	0.018 min^{-1}	[304]
RGO-Co	90 min	27.16±0.60 (×10^{-3} min^{-1})	[305]

RGO-Ni$_{25}$Co$_{75}$	30 min	93.22±3.78 (×10^{-3} min^{-1})	[305]
RGO-Ni	60 min	39.26±2.47(×10^{-3} min^{-1})	[305]
Ni/graphene	4 min	11.7×10^{-3} s^{-1}	[306]
Ag/RGO	120 s	17.15 (×10^{-3} s^{-1})	[307]
Ag$_{50}$Ni$_{50}$/RGO	60 s	48.40 (×10^{-3} s^{-1})	[307]
Ag/Fe$_3$O$_4$@C	4 min	1.03 min^{-1}	[308]
Pd/RGO/Fe$_3$O$_4$	1 min	0.051 s^{-1}	[309]
50NZF-50RGO	6 min	0.73 min^{-1}	Present work (Chapter-2)
98BFO-2RGO	6 min	0.72 min^{-1}	Present work (Chapter-4)

Table 5.2 Comparison of catalytic efficiency of different catalysts for decolorization of various synthetic dyes via reduction reaction with NaBH$_4$.

Dye	Catalyst	Completion time	Rate constant	Reference
Methyl Orange	Cu@SBA-15@CF	6 min	0.64 min^{-1}	[146]
	Au NPs/GO-G3PAMAM	150 s	19.1×10^{-3} s^{-1}	[209]
	Au/SBA-15	150 s	1.662 min^{-1}	[292]
	2.5Ru@SBA-15	5 min	0.66 min^{-1}	[299]
	12.5Cu@SBA-15	5 min	0.92 min^{-1}	[300]
	MnFe$_2$O$_4$@SiO$_2$@Ag	50 s	0.04 s^{-1}	[310]
	Ag nanoparticles	9 min	0.5853 min^{-1}	[311]
	Cu/CH-FP	13 min	0.2683 min^{-1}	[312]
	Au/TiO$_2$	-	3:89×10^{-3} s^{-1}	[313]
	50NZF-50RGO	5 min	0.95 min^{-1}	Present work (Chapter-2)

	Cu@SBA-15@CF	4 min	0.85 min^{-1}	[146]
	Ag@CoFe$_2$O$_4$	4 min	1.42 min^{-1}	[252]
	Ni/CPM	18 min	0.471 min^{-1}	[254]
	Fe$_3$O$_4$/Cu	3 min	1.0254 min^{-1}	[297]
Rhodamine	2.5Ru@SBA-15	5 min	0.91 min^{-1}	[299]
B	12.5Cu@SBA-15	5 min	1.04 min^{-1}	[300]
	Ag-Fe$_3$O$_4$@C	20 min	0.22 min^{-1}	[308]
	MnFe$_2$O$_4$@SiO$_2$@Ag	150 s	0.02 s^{-1}	[310]
	50NZF-50RGO	7 min	0.71 min^{-1}	Present work (Chapter-2)

Table 5.3 Comparison of catalytic efficiency of different catalysts for the preparation of 5-Ethoxycarbonyl-4-phenyl-6 methyl-3,4-dihydropyrimidin-2(1H)-one via Biginelli reaction.

Catalyst	Solvent	Time	% of Yield	Reference
Cu@SBA-15@CF	Solvent-free	90 min	90	[146]
Fe$_3$O$_4$@mesoporous SBA-15	absolute ethanol	6h	85	[240]
[DMEA][HSO$_4$]	Solvent-free	2h	94	[246]
cellulose sulfuric acid	CH$_3$CN	5h	80	[247]
ZnO	Solvent-free	10h	95	[248]
SiO$_2$–CuCl$_2$	Solvent-free	2h	94	[249]
Nafion-G	Solvent-free	1h	84	[250]
CuO@mTiO$_2$@CF	Solvent-free	60 min	96	[301]
Fe$_3$O$_4$/PAA-SO$_3$H	Solvent-free	120 min	90	[356]

triphenylphosphine	Solvent-free	10 h	70	[357]
L-tyrosine	Solvent-free	15 min	84	[358]
SiO$_2$-Cl	Solvent-free	3h	88	[359]
98BFO-2RGO	Solvent-free	30 min	93	Present work (chapter 4)

Table 5.4 Comparison of catalytic efficiency of different catalysts for the preparation of 2-phenyl-2-(4-phenyl-1H-1,2,3-triazole-1-yl) ethanol via Click reaction.

Catalyst	Solvent	Time	% of Yield	Reference
Cu@SBA-15@CF	water	2h	90	[146]
CuI–Zeolite	water	20h	77	[228]
[Cu^{II}-PhTPY]	water	1h	95	[229]
CuI	PEG-400	16h	83	[231]
copper(I)@phosphorated SiO$_2$	water	1h	94	[232]
CuNPs/C	water	8h	93	[233]
CuSO$_4$.5H$_2$O/Sodium ascorbate	water	4h	92	[235]
CuO@mTiO$_2$@CF	water	6h	89	[301]
Cu^{II}-hydrotalcite	water	5h	91	[360]
98BFO-2RGO	water	2h	91	Present work (chapter 4)

Table 5.5 Comparison of catalytic efficiency of different catalysts for epoxidation of styrene.

Catalyst	Oxidant	Reaction Temperature (°C)	Reaction Time (h)	Conversion of styrene (%)	Selectivity of styrene oxide (%)	Reference
SnO_2/RGO	H_2O_2	50	3	93.4	81.4	[147]
TiO_2/GO	TBHP	80	12	93.34	85.90	[148]
Au/Yb_2O_3	TBHP	97	3	63.5	54.8	[216]
CuO@mTiO_2@CF	TBHP	100	4	98.5	77.3	[301]
Ag@mTiO_2@CF	TBHP	100	10	98.1	94.5	[302]
Au-Silica	TBHP	80	48	98.5	82.8	[361]
Au-CNT	TBHP	82	10	67.2	77.5	[362]
TiO_2-Ag	TBHP	105	14	83.9	66.8	[363]
Ag-Fe_3O_4	TBHP	-	13	100	84	[364]
Au/BaTNT	TBHP	80	15	60.5	80.1	[365]
Ag/4A Zeolite	TBHP	100	48	80.08	89.2	[366]
Ag-$Mn_{0.42}Fe_{2.58}O_4$	TBHP	-	5	-	90.5	[367]
Ag-$Ni_{0.81}Fe_{2.19}O_4$	TBHP	-	5	-	84.8	[367]
Ag-γ-ZrP	TBHP	82	20	93.1	92.8	[368]
Ag/SBA-15	TBHP	80	9	64.5	51.7	[369]
98BFO-2RGO	TBHP	100	5	79	90	Present work (chapter 4)

Table 5.6: Comparison of photocatalytic activity of 75CF-25RGO nanocomposite with those of the other reported RGO-Ferrite and RGO based nanocomposites.

Composite	Preparation method	Amount of catalyst	Dye concentration	Source	Time	Dye	References
$CoFe_2O_4$-RGO (45 wt. %)	Ball milling for 6h at 25 sec^{-1}	0.01g /40mL	0 mg/L	Visible light Xe lamp 800W cutoff $\lambda > 420nm$.	180 min	MB, RhB, and MO	[159]
$ZnFe_2O_4$-RGO (20 wt. %)	Hydrothermal at 180 ºC for 12h	0.05g in 100 ml	20 mg/L	Visible light Xe lamp 500W cutoff $\lambda > 420nm$	90 min	MB	[163]
$CoFe_2O_4$-RGO (40 wt. %)	Hydrothermal at 180 ºC for 20h	25 mg in 100 ml	20mg/L	Visible light Xe lamp 500W cutoff $\lambda > 420nm$	240 min	MB (100%) MO (94%) RhB (71%)	[164]
(3%)P25/ $CoFe_2O_4$/RGO	Hydrothermal at 180 ºC for 20h	10 mg in 30 ml	40 mg/L	Visible light Xe lamp 500W cutoff $\lambda > 420nm$	240 min	MB	[276]
$CoFe_2O_4$-RGO (10wt. %)	Hydrothermal at 180 ºC for 12h	20 mg in 200 ml	10 mg/L	Tungsten halogen lamp 500W	180 min	MB	[318]
TiO_2-Fe_3O_4-RGO	Hydrothermal at 105 ºC for 24h	0.01g in 40 ml	0.0535 mmol/L	Visible Light Xe lamp 500W	120 min	MB	[321]
Fe_3O_4-RGO-TiO_2 composite	Hydrothermal at 200 ºC for 10h	1.5 g/L	10 mg/L	Visible light 300W UV-Vis Xenon Lamp > 400 nm	120 min	MB	[322]

CoFe$_2$O$_4$-TiO$_2$	Hydrothermal at 150 ºC for 24 h	20 mg in 5 ml	5 ppm aqueous solution (initial concentration)	UV light irradiation 8W UV –Hg lamp 5 sets.	6 h	MB	[323]
MnFe$_2$O$_4$-graphene (30 wt. %)	Hydrothermal at 180 ºC for 20 h	0.025 g in 100 mL	20 mg/L	500 W mercury and xenon lamp cutoff λ > 420nm Visible light	360 min	MB	[324]
RGO-MFe$_2$O$_4$ (M=Zn, Co, and Ni)	Hydrothermal at 200 ºC for 10 h	20 mg in 150 ml	10 mg/L	Tungsten lamp 500W	180 min	RhB and MB	[325]
CdFe$_2$O$_4$/ Graphene	Hydrothermal at 180 ºC for 12 h	100 mg in 100 ml	10 mg/L	Xe lamp 500W cutoff λ > 420nm Visible light	240 min	MB	[326]
Bi$_2$Fe$_2$O$_9$/RGO (4.5 wt.%)	Hydrothermal at 95 ºC 36 h	0.5mg/L	10mg/L	150W Xenon Arc Lamp Visible light	3 h	Bisphenol-A	[327]
75CF-25RGO	Co-precipitation followed by reflux at 160 ºC for 16 h	500 mg/L	20 mg/L	100 W Reading lamp Visible light	i) 60 min ii) 75min iii) 45min iv) 120min	i) MO ii) MB iii) RhB iv) Dye mixture	Present work (Chapter-3)

MB= Methylene Blue, MO= Methyl Orange, and RhB= Rhodamine B

Table 5.7 Comparison of microwave absorption properties of various ferrites and ferrite based composites**.**

Samples	Preparation Method	Minimum Reflection loss (dB)	Corresponding Frequency (GHz)	Absorber thickness (mm)	Effective bandwidth (RL < -10dB) (GHz)	Ref
Fe_3O_4/ graphene capsules (GCs)	Hydrothermal at 200 °C for 24 h	-32	8.76	3.5	5.4 to 17	[1]
$NiFe_2O_4$/r-GO	Hydrothermal at 180 °C for 24 h	-42	~6.5	5	5.3	[2]
Co-doped NiZn ferrite/graphene	Hydrothermal at 180 °C for 12 h	-53.5	9.6	3.1	4.8	[3]
$ZnFe_2O_4$ /RGO	Hydrothermal synthesis at 180 °C for12h	-29.3	16.7	1.6	2.6	[4]
60 wt % ZnO /$CoFe_2O_4$	Co-precipitation method 90 °C	-28.3	8.6	-	4.1 to 13	[9]
$NiFe_2O_4$	Hydrothermal at 180 °C for 6h	-24	9.5	3.5	8.5 to 13	[10]
$CoFe_2O_4$	Co-precipitation method 120 °C for 12h	-55	9.25	2	8.2 to 10.8	[52]

5 wt. % filler RGO/MnFe$_2$O$_4$/ PVDF	Hydrothermal at 140 °C for 12h	-29	9.2 z	3	8-12.88	[59]
RGO/ Fe$_3$O$_4$	One pot Co-precipitation at 80 °C for 2h	-44.6	6.6 G	3.9	4.3	[60]
Graphene-Fe$_3$O$_4$	Heated at 200 °C for 24h	-20	16	5		[61]
CoFe$_2$O$_4$ nanorod/Graphene	Hydrothermal 150 °C for 15h	-25.8	16.1	2.0	4.5	[62]
a) CoFe$_2$O$_4$ hollow/Graphene composites b) CoFe$_2$O$_4$ hollow	Hydrothermal at 160 °C for 24h followed by calcination 550 °C for 0.5h under argon atmosphere	a) -18.5 b) -11.7	a) 12.9 b) 7.2	a) 2 b) 2	a) 3.7 b) 1.3	[63]
BaFe$_{12}$O$_{19}$@RGO	Calcination at 900 °C for 2h	-32		3		[64]
RGO/ Fe$_3$O$_4$	Solvothermal method 200ºC for 8h	-26.4	5.3	4.0	2.8	[107]
(Mn$_{0.2}$Ni$_{0.4}$Zn$_{0.4}$Fe$_2$O$_4$)$_x$-(BaFe$_{12}$O$_{19}$)$_{1-x}$	One pot precursor based method 800 ºC for 4h	-25	8.2	3.5		[109]
30 wt.% hollow Fe$_3$O$_4$/RGO	Solvothermal method. 200 °C for 12h.	-24	12.9	2.0	4.9	[126]

Ni Zn ferrite	Calcined at 1200°C for 2h	-16	10.6	2		[127]
$(Ni_{0.4}Co_{0.2}Zn_{0.4})Fe_2O_4$	Sintered at 1250 °C for 2h.	-17.01	6.1	3		[128]
Ag core-shell $Ni_{0.5}Zn_{0.5}Fe_2O_4$	Hydrothermal at 180 °C for 3h.	-25	9.0	1-2		[129]
Rugby Shaped $CoFe_2O_4$	Hydrothermal at 160 °C for 30h followed by calcinations at 550 °C for 3h	-34.1	13.4	2.5	2.6	[130]
$Ni_{0.5}Co_{0.5}Fe_2O_4$	Co-precipitation at 85 °C	-18	2.47	1.5	-	[131]
$(NiFe_2O_4)_{0.85}$-$(SrFe12O19)_{0.15}$	One pot precursor based method 800 °C for 4h	-17	8.2	3.2	-	[132]
$(Ni_{0.65}Zn_{0.35}Fe_2O_4)_{0.85}$-$(BaFe_{12}O_{19})_{0.15}$	One pot precursor based method 800 °C for 4h	-21	9.86	3.05	-	[133]
$Co_{0.6}Zn_{0.4}Fe_2O_4$ nanofiber.	Calcination at 700 °C for 2h	-16	10.6	2.9	7.8 to 16.8	[134]
Fe_3O_4-Fe/G composite	Calcination at 420 °C for 3h	-30	4.72	2.0	6.2	[139]
Graphene/Fe_3O_4	Hydrothermal method 220 °C for 72h	-40.36	7.04	5.0	9.5	[140]

(RGO)/CoFe$_2$O$_4$ composite	One-pot hydrothermal route at 180 °C for 10h	-47.9	12.4	2.3	5.6	[141]
NiFe$_2$O$_4$ nanorod-graphene	Solvothermal 150 °C for 15h.	-29.2	16.1	2.0	13.6-18	[142]
10 wt. % filler RGO/Co$_3$O$_4$/Poly (vinylidene fluoride)	Hydrothermal at 140 °C for 12h.	-25	11.6	4	7.5-12	[143]
50N$_{0.8}$Z$_{0.2}$Fe$_2$O$_4$-50RGO nanocomposite	In situ Co-precipitation method at 120 °C for 12h	-19.99	11.58	1.8	10.22-12.4	Present work (Chapter-2)
85CF-15RGO	Co-precipitation reduction at 160 °C at 16 h	-31.13	9.05	2.15	2.72	Present work (Chapter-3)
97BFO-3RGO	Hydrothermal at 140 °C for 24h	-28.68	10.68	1.55	2.1	Present work (Chapter-4)

5.2 Conclusion

➤ The *'in situ'* co-precipitation technique which was developed to prepare NZF-RGO and CF-RGO nanocomposites, is a very simple technique compare to the most of the reported methods and to the best of our knowledge, this is the first time this technique was employed to synthesize NZF-RGO and CF-RGO.[7, 11] The advantages this *'in situ'* co-precipitation offers are (i) this method is very simple and does not require any special or complicated reaction set up (e.g., special

atmosphere, high-pressure equipment, etc.). (ii) The reactions can be performed in an aqueous medium; (iii) the starting materials (e.g., metal nitrates) are very cheap.

➤ A hydrothermal technique was developed to prepare BFO-RGO nanocomposite where BFO nanowires are immobilized on the surface of nanometer thin RGO sheets.

➤ NZF-RGO, CF-RGO, and BFO-RGO have exhibited excellent catalytic activities towards various reactions along with easy magnetic separation and high reusability.

➤ All the three nanocomposites (NZF-RGO, CF-RGO, and BFO-RGO) demonstrated their excellent microwave absorption properties in the X-band region (8.2-12.4 GHz).

➤ In summary, the synthesized nanocomposites have demonstrated their capability to act as multifunctional materials as excellent magnetically separable catalysts as well as high performing efficient microwave absorber.

5.3 Future scope of work

1) Investigations are required on the catalytic efficiencies of the synthesized catalysts towards decolorization/degradation of dyes of real effluents discharged from dye based industries.

2) Investigations on the usefulness of the synthesized ferrites-RGO nanocomposites as a catalyst for some other organic reactions are also required.

3) As the preparation of catalysts and tests on their catalysis activities have been performed in laboratory scale, further investigations are required for large-scale production of these catalysts and large-scale catalysis reactions to make these catalysts commercially viable.

4) Theoretical calculations and modeling of ferrite-RGO based nanocomposite need to be pursued to acquire in-depth understanding of the detailed electronic structures of these nanocomposites. This understanding will help to design advanced catalyst as well as high performing microwave absorber.

5) Other applications of the ferrites such as the construction of supercapacitors need to be explored.

References

1.   X. Jian, B. Wu, Y. Wei, S. X. Dou, X. Wang, W. He and N. Mahmood, *ACS Applied Materials & Interfaces*, 2016, 8, 6101-6109.

2.   J.-Z. He, X.-X. Wang, Y.-L. Zhang and M.-S. Cao, *Journal of Materials Chemistry C*, 2016, 4, 7130-7140.

3.   P. Liu, Z. Yao, J. Zhou, Z. Yang and L. B. Kong, *Journal of Materials Chemistry C*, 2016, 4, 9738-9749.

4.   Z. Yang, Y. Wan, G. Xiong, D. Li, Q. Li, C. Ma, R. Guo and H. Luo, *Materials Research Bulletin*, 2015, 61, 292-297.

5.   W. H. Organization, *Establishing a Dialogue on Risks from Electromagnetic Fields*, World Health Organization, 2002.

6.   J. C. Lin, *IEEE Microwave Magazine*, 2016, 17, 32-36.

7.   D. Moitra, M. Chandel, B. K. Ghosh, R. K. Jani, M. K. Patra, S. R. Vadera and N. N. Ghosh, *RSC Advances*, 2016, 6, 76759-76772.

8.   L. Wang, Y. Huang, X. Sun, H. Huang, P. Liu, M. Zong and Y. Wang, *Nanoscale*, 2014, 6, 3157-3164.

9.   J. Cao, W. Fu, H. Yang, Q. Yu, Y. Zhang, S. Liu, P. Sun, X. Zhou, Y. Leng and S. Wang, *The Journal of Physical Chemistry B*, 2009, 113, 4642-4647.

10.   W. Zhu, L. Wang, R. Zhao, J. Ren, G. Lu and Y. Wang, *Nanoscale*, 2011, 3, 2862-2864.

11.   D. Moitra, B. Ghosh, M. Chandel, R. Jani, M. Patra, S. Vadera and N. Ghosh, *RSC Advances*, 2016, 6, 14090-14096.

12.   J. R. Jauchem and K. L. Ryan, *Bioelectromagnetics*, 2000, 21, 159-166.

13.   B. Veyret, C. Bouthet, P. Deschaux, R. De Seze, M. Geffard, J. Joussot-Dubien, M. Le Diraison, J. M. Moreau and A. Caristan, *Bioelectromagnetics*, 1991, 12, 47-56.

14.   Y. Li, W.-q. Cao, J. Yuan, D.-w. Wang and M.-s. Cao, *Journal of Materials Chemistry C*, 2015, 3, 9276-9282.

15.   Y. Zhang, Y. Huang, T. Zhang, H. Chang, P. Xiao, H. Chen, Z. Huang and Y. Chen, *Advanced Materials*, 2015, 27, 2049-2053.

16.   T. Zhao, C. Hou, H. Zhang, R. Zhu, S. She, J. Wang, T. Li, Z. Liu and B. Wei, *Scientific Reports*, 2014, 4, 5619.

17.   P. Bhattacharya, S. Sahoo and C. Das, *Express Polymer Letter*, 2013, 7, 212-223.

18.   J.-S. Li, H. Huang, Y.-J. Zhou, C.-Y. Zhang and Z.-T. Li, *Journal of Materials Research*, 2017, 32, 1213-1230.

19.   M.-S. Cao, J. Yang, W.-L. Song, D.-Q. Zhang, B. Wen, H.-B. Jin, Z.-L. Hou and J. Yuan, *ACS Applied Materials & Interfaces*, 2012, 4, 6949-6956.

20.   P.-B. Liu, Y. Huang and X. Sun, *ACS Applied Materials & Interfaces*, 2013, 5, 12355-12360.

21.   P. Xu, X. Han, C. Wang, D. Zhou, Z. Lv, A. Wen, X. Wang and B. Zhang, *The Journal of Physical Chemistry B*, 2008, 112, 10443-10448.

22.   L. Yan, J. Wang, X. Han, Y. Ren, Q. Liu and F. Li, *Nanotechnology*, 2010, 21, 095708.

23.   H.-J. Yang, W.-Q. Cao, D.-Q. Zhang, T.-J. Su, H.-L. Shi, W.-Z. Wang, J. Yuan and M.-S. Cao, *ACS Applied Materials & Interfaces*, 2015, 7, 7073-7077.

24.   M.-M. Lu, W.-Q. Cao, H.-L. Shi, X.-Y. Fang, J. Yang, Z.-L. Hou, H.-B. Jin, W.-Z. Wang, J. Yuan and M.-S. Cao, *Journal of Materials Chemistry A*, 2014, 2, 10540-10547.

25.   X.-X. Wang, M.-M. Lu, W.-Q. Cao, B. Wen and M.-S. Cao, *Materials Letters*, 2014, 125, 107-110.

26.   B. Wen, X. Wang, W. Cao, H. Shi, M. Lu, G. Wang, H. Jin, W. Wang, J. Yuan and M. Cao, *Nanoscale*, 2014, 6, 5754-5761.

27.   J. Liu, W.-Q. Cao, H.-B. Jin, J. Yuan, D.-Q. Zhang and M.-S. Cao, *Journal of Materials Chemistry C*, 2015, 3, 4670-4677.

28.   H. Lv, Y. Guo, G. Wu, G. Ji, Y. Zhao and Z. J. Xu, *ACS Applied Materials & Interfaces*, 2017, 9, 5660-5668.

29.   H. Lv, Y. Guo, Z. Yang, Y. Cheng, L. P. Wang, B. Zhang, Y. Zhao, Z. J. Xu and G. Ji, *Journal of Materials Chemistry C*, 2017, 5, 491-512.

30.   X. Zhang, Y. Li, R. Liu, Y. Rao, H. Rong and G. Qin, *ACS Applied Materials & Interfaces*, 2016, 8, 3494-3498.

31.   Y. Yin, M. Zeng, J. Liu, W. Tang, H. Dong, R. Xia and R. Yu, *Scientific Reports*, 2016, 6, 25075.

32.   Y. Du, W. Liu, R. Qiang, Y. Wang, X. Han, J. Ma and P. Xu, *ACS Applied Materials & Interfaces*, 2014, 6, 12997-13006.

33.   M. Wu, Y. Zhang, S. Hui, T. Xiao, S. Ge, W. Hines, J. Budnick and G. Taylor, *Applied Physics Letters*, 2002, 80, 4404-4406.

34. B. Lu, X. Dong, H. Huang, X. Zhang, X. Zhu, J. Lei and J. Sun, *Journal of Magnetism and Magnetic Materials*, 2008, 320, 1106-1111.

35. D. Moitra, S. Dhole, B. K. Ghosh, M. Chandel, R. K. Jani, M. K. Patra, S. R. Vadera and N. N. Ghosh, *The Journal of Physical Chemistry C*, 2017, 121, 21290-21304.

36. C. Tian, Y. Du, P. Xu, R. Qiang, Y. Wang, D. Ding, J. Xue, J. Ma, H. Zhao and X. Han, *ACS Applied Materials & Interfaces*, 2015, 7, 20090-20099.

37. B. Qu, C. Zhu, C. Li, X. Zhang and Y. Chen, *ACS Applied Materials & Interfaces*, 2016, 8, 3730-3735.

38. A. Ansari and M. J. Akhtar, *RSC Advances*, 2016, 6, 13846-13857.

39. Y. Kang, Z. Jiang, T. Ma, Z. Chu and G. Li, *ACS Applied Materials & Interfaces*, 2016, 8, 32468-32476.

40. J. Tauc, R. Grigorovici and A. Vancu, *Physica Status Solidi B*, 1966, 15, 627-637.

41. J. Osepchuk, in *Kirk-Othmer Encyclopedia of Chemical Technology*, John Wiley & Sons, Inc., 2000, DOI: 10.1002/0471238961.1309031815190516.a01.pub2.

42. M.-S. Cao, W.-L. Song, Z.-L. Hou, B. Wen and J. Yuan, *Carbon*, 2010, 48, 788-796.

43. S. Ramo, J. R. Whinnery and T. Van Duzer, *Fields and Waves in Communication Electronics*, John Wiley & Sons, 2008.

44. Y.-J. Chen, G. Xiao, T.-S. Wang, Q.-Y. Ouyang, L.-H. Qi, Y. Ma, P. Gao, C.-L. Zhu, M.-S. Cao and H.-B. Jin, *The Journal of Physical Chemistry C*, 2011, 115, 13603-13608.

45. D. Chen, G.-S. Wang, S. He, J. Liu, L. Guo and M.-S. Cao, *Journal of materials chemistry. A, Materials for Energy and Sustainability*, 2013, 1, 5996-6003.

46. Y.-H. Chen, Z.-H. Huang, M.-M. Lu, W.-Q. Cao, J. Yuan, D.-Q. Zhang and M.-S. Cao, *Journal of Materials Chemistry A*, 2015, 3, 12621-12625.

47. N. Li, G.-W. Huang, Y. Li, H.-M. Xiao, Q.-P. Feng, N. Hu and S.-Y. Fu, *ACS Applied Materials & Interfaces*, 2016.

48. N. T. Correia and J. J. M. Ramos, *Physical Chemistry Chemical Physics*, 2000, 2, 5712-5715.

49. K. Chen, S. Yuan, P. Li, F. Gao, J. Liu, G. Li, A. Zhao, X. Lu, J. Liu and J. Zhu, *Journal of Applied Physics*, 2007, 102, 034103.

50. S. Biswas, I. Arief, S. S. Panja and S. Bose, *ACS Applied Materials & Interfaces*, 2017, 9, 3030-3039.

51. F. Qin and C. Brosseau, *Journal of Applied Physics*, 2012, 111, 4.

52. D. Moitra, S. Hazra, B. K. Ghosh, R. K. Jani, M. K. Patra, S. R. Vadera and N. N. Ghosh, *RSC Advances*, 2015, 5, 51130-51134.

53. J. Liu, M.-S. Cao, Q. Luo, H.-L. Shi, W.-Z. Wang and J. Yuan, *ACS Applied Materials & Interfaces*, 2016, 8, 22615-22622.

54. X. Dong, X. Zhang, H. Huang and F. Zuo, *Applied Physics Letters*, 2008, 92, 013127.

55. H. Lv, H. Zhang, J. Zhao, G. Ji and Y. Du, *Nano Research*, 2016, 9, 1813-1822.

56. H. Lv, H. Zhang, G. Ji and Z. J. Xu, *ACS Applied Materials & Interfaces*, 2016, 8, 6529-6538.

57. G. Tong, F. Liu, W. Wu, F. Du and J. Guan, *Journal of Materials Chemistry A*, 2014, 2, 7373-7382.

58. G. Wang, Z. Gao, G. Wan, S. Lin, P. Yang and Y. Qin, *Nano Research*, 2014, 7, 704-716.

59. X.-J. Zhang, G.-S. Wang, W.-Q. Cao, Y.-Z. Wei, J.-F. Liang, L. Guo and M.-S. Cao, *ACS Applied Materials & Interfaces*, 2014, 6, 7471-7478.

60. M. Zong, Y. Huang, Y. Zhao, X. Sun, C. Qu, D. Luo and J. Zheng, *RSC Advances*, 2013, 3, 23638-23648.

61. W.-d. Xue, R. Zhao, X. Du, F.-w. Xu, M. Xu and K.-x. Wei, *Materials Research Bulletin*, 2014, 50, 285-291.

62. M. Fu, Q. Jiao and Y. Zhao, *Materials Characterization*, 2013, 86, 303-315.

63. M. Fu, Q. Jiao, Y. Zhao and H. Li, *Journal of Materials Chemistry A*, 2014, 2, 735-744.

64. M. Verma, A. P. Singh, P. Sambyal, B. P. Singh, S. Dhawan and V. Choudhary, *Physical Chemistry Chemical Physics*, 2015, 17, 1610-1618.

65. C. e. N. e. R. Rao, A. e. K. Sood, K. e. S. Subrahmanyam and A. Govindaraj, *Angewandte Chemie International Edition*, 2009, 48, 7752-7777.

66. J. Fang, W. Zha, M. Kang, S. Lu, L. Cui and S. Li, *Journal of Materials Science*, 2013, 48, 8060-8067.

67. V. Georgakilas, M. Otyepka, A. B. Bourlinos, V. Chandra, N. Kim, K. C. Kemp, P. Hobza, R. Zboril and K. S. Kim, *Chemical Reviews*, 2012, 112, 6156-6214.

68. S. Stankovich, D. A. Dikin, R. D. Piner, K. A. Kohlhaas, A. Kleinhammes, Y. Jia, Y. Wu, S. T. Nguyen and R. S. Ruoff, *Carbon*, 2007, 45, 1558-1565.

69. G. Wang, M. Zhang, S. Liu, X. Xie, G. Ding, Y. Wang, P. K. Chu, H. Gao, W. Ren and Q. Yuan, *Advanced Functional Materials*, 2015, 25, 3666-3675.

70. K. S. Novoselov, A. K. Geim, S. V. Morozov, D. Jiang, Y. Zhang, S. V. Dubonos, I. V. Grigorieva and A. A. Firsov, *Science*, 2004, 306, 666-669.

71. P. Avouris and C. Dimitrakopoulos, *Materials Today*, 2012, 15, 86-97.

72. D. Li, M. B. Müller, S. Gilje, R. B. Kaner and G. G. Wallace, *Nature Nanotechnology*, 2008, 3, 101.

73. B. Wu, H. M. Tuncer, A. Katsounaros, W. Wu, M. T. Cole, K. Ying, L. Zhang, W. I. Milne and Y. Hao, *Carbon*, 2014, 77, 814-822.

74. M. J. McAllister, J.-L. Li, D. H. Adamson, H. C. Schniepp, A. A. Abdala, J. Liu, M. Herrera-Alonso, D. L. Milius, R. Car and R. K. Prud'homme, *Chemistry of Materials*, 2007, 19, 4396-4404.

75. S. Stankovich, R. D. Piner, X. Chen, N. Wu, S. T. Nguyen and R. S. Ruoff, *Journal of Materials Chemistry*, 2006, 16, 155-158.

76. S. Niyogi, E. Bekyarova, M. E. Itkis, J. L. McWilliams, M. A. Hamon and R. C. Haddon, *Journal of the American Chemical Society*, 2006, 128, 7720-7721.

77. M. P. Weir, D. W. Johnson, S. C. Boothroyd, R. C. Savage, R. L. Thompson, S. R. Parnell, A. J. Parnell, S. M. King, S. E. Rogers and K. S. Coleman, *Chemistry of Materials*, 2016, 28, 1698-1704.

78. A. V. Tyurnina, H. Okuno, P. Pochet and J. Dijon, *Carbon*, 2016, 102, 499-505.

79. Z.-Y. Juang, C.-Y. Wu, A.-Y. Lu, C.-Y. Su, K.-C. Leou, F.-R. Chen and C.-H. Tsai, *Carbon*, 2010, 48, 3169-3174.

80. Y. Zhang, L. Zhang and C. Zhou, *Accounts of Chemical Research*, 2013, 46, 2329-2339.

81. A. Reina, X. Jia, J. Ho, D. Nezich, H. Son, V. Bulovic, M. S. Dresselhaus and J. Kong, *Nano Letters*, 2009, 9, 30-35.

82. S. K. Hong, K. Y. Kim, T. Y. Kim, J. H. Kim, S. W. Park, J. H. Kim and B. J. Cho, *Nanotechnology*, 2012, 23, 455704.

83. W. S. Hummers Jr and R. E. Offeman, *Journal of the American Chemical Society*, 1958, 80, 1339-1339.

84. K. Koch and P. Krause, *Journal of Chemical Education*, 1982, 59, 973.

85. A. Simon, R. Dronskowski, B. Krebs and B. Hettich, *Angewandte Chemie International Edition*, 1987, 26, 139-140.

86. W. Gao, in *Graphene oxide*, Springer, 2015, pp. 61-95.

87.   J. Wu, W. Pisula and K. Müllen, *Chemical Reviews*, 2007, 107, 718-747.

88.   A. Jana, E. Scheer and S. Polarz, *Beilstein Journal of Nanotechnology*, 2017, 8, 688.

89.   S. Pei and H.-M. Cheng, *Carbon*, 2012, 50, 3210-3228.

90.   S. Stankovich, D. A. Dikin, G. H. Dommett, K. M. Kohlhaas, E. J. Zimney, E. A. Stach, R. D. Piner, S. T. Nguyen and R. S. Ruoff, *Nature*, 2006, 442, 282.

91.   C. Wang, X. Han, P. Xu, X. Zhang, Y. Du, S. Hu, J. Wang and X. Wang, *Applied Physics Letters*, 2011, 98, 072906.

92.   H. J. Shin, K. K. Kim, A. Benayad, S. M. Yoon, H. K. Park, I. S. Jung, M. H. Jin, H. K. Jeong, J. M. Kim and J. Y. Choi, *Advanced Functional Materials*, 2009, 19, 1987-1992.

93.   M. Periasamy and M. Thirumalaikumar, *Journal of Organometallic Chemistry*, 2000, 609, 137-151.

94.   G. Wang, J. Yang, J. Park, X. Gou, B. Wang, H. Liu and J. Yao, *The Journal of Physical Chemistry C*, 2008, 112, 8192-8195.

95.   Z.-S. Wu, W. Ren, L. Gao, B. Liu, C. Jiang and H.-M. Cheng, *Carbon*, 2009, 47, 493-499.

96.   X. Fan, W. Peng, Y. Li, X. Li, S. Wang, G. Zhang and F. Zhang, *Advanced Materials*, 2008, 20, 4490-4493.

97.   H.-P. Boehm, A. Clauss, G. Fischer and U. Hofmann, *Zeitschrift für anorganische und allgemeine Chemie*, 1962, 316, 119-127.

98.   M. J. Fernández-Merino, L. Guardia, J. Paredes, S. Villar-Rodil, P. Solís-Fernández, A. Martínez-Alonso and J. Tascon, *The Journal of Physical Chemistry C*, 2010, 114, 6426-6432.

99.   H. Han, Y. Chen and Z. Wang, *RSC Advances*, 2015, 5, 92940-92946.

100.   M. Zhou, Y. Wang, Y. Zhai, J. Zhai, W. Ren, F. Wang and S. Dong, *Chemistry-A European Journal*, 2009, 15, 6116-6120.

101.   H. Wang, J. T. Robinson, X. Li and H. Dai, *Journal of the American Chemical Society*, 2009, 131, 9910-9911.

102.   C.-Y. Chen, N.-W. Pu, Y.-M. Liu, S.-Y. Huang, C.-H. Wu, M.-D. Ger, Y.-J. Gong and Y.-C. Chou, *Composites Part B: Engineering*, 2017, 114, 395-403.

103.   F. Meng, H. Wang, F. Huang, Y. Guo, Z. Wang, D. Hui and Z. Zhou, *Composites Part B: Engineering*, 2018, 137, 260-277.

104. P. Sudeep, S. Vinayasree, P. Mohanan, P. Ajayan, T. Narayanan and M. Anantharaman, *Applied Physics Letters*, 2015, 106, 221603.

105. E. Ma, J. Li, N. Zhao, E. Liu, C. He and C. Shi, *Materials Letters*, 2013, 91, 209-212.

106. X. Wang, M. Yu, W. Zhang, B. Zhang and L. Dong, *Applied Physics A*, 2015, 118, 1053-1058.

107. X. Sun, J. He, G. Li, J. Tang, T. Wang, Y. Guo and H. Xue, *Journal of Materials Chemistry C*, 2013, 1, 765-777.

108. W.-Q. Cao, X.-X. Wang, J. Yuan, W.-Z. Wang and M.-S. Cao, *Journal of Materials Chemistry C*, 2015, 3, 10017-10022.

109. S. Hazra, B. K. Ghosh, H. R. Joshi, M. K. Patra, R. K. Jani, S. R. Vadera and N. N. Ghosh, *RSC Advances*, 2014, 4, 45715-45725.

110. Y. Sun, F. Xiao, X. Liu, C. Feng and C. Jin, *RSC Advances*, 2013, 3, 22554-22559.

111. R. Meena, S. Bhattachrya and R. Chatterjee, *Materials & Design*, 2010, 31, 3220-3226.

112. X. Gu, W. Zhu, C. Jia, R. Zhao, W. Schmidt and Y. Wang, *Chemical Communications*, 2011, 47, 5337-5339.

113. S. Hazra and N. Ghosh, *Journal of Nanoscience and Nanotechnology*, 2014, 14, 1983-2000.

114. M. Pardavi-Horvath, *Journal of Magnetism and Magnetic Materials*, 2000, 215, 171-183.

115. G. Datt, C. Kotabage and A. Abhyankar, *Physical Chemistry Chemical Physics*, 2017, 19, 20699-20712.

116. V. G. Harris, *IEEE Transactions on Magnetics*, 2012, 48, 1075-1104.

117. G. Tong, Y. Liu, T. Cui, Y. Li, Y. Zhao and J. Guan, *Applied Physics Letters*, 2016, 108, 072905.

118. Y. Yang, Y. Yang, W. Xiao, C. P. Neo and J. Ding, *Nanotechnology*, 2015, 26, 265704.

119. W. Zhang, X. Zuo, D. Zhang, C. Wu and S. R. P. Silva, *Nanotechnology*, 2016, 27, 245707.

120. N. Ranvah, Y. Melikhov, D. C. Jiles, J. E. Snyder, A. J. Moses, P. I. Williams and S. Song, *Journal of Applied Physics*, 2008, 103, 07E506.

121. J. Smit and H. Wijn, 1959.

122. P. Van der Zaag, *Journal of Magnetism and Magnetic Materials*, 1999, 196, 315-319.

123. A. Ghasemi, A. Hossienpour, A. Morisako, A. Saatchi and M. Salehi, *Journal of Magnetism and Magnetic Materials*, 2006, 302, 429-435.

124. A. Ghasemi, A. Hossienpour, A. Morisako, X. Liu and A. Ashrafizadeh, *Materials & Design*, 2008, 29, 112-117.

125. M. Sugimoto, *Journal of the American Ceramic Society*, 1999, 82, 269-280.

126. H.-L. Xu, H. Bi and R.-B. Yang, *Journal of Applied Physics*, 2012, 111, 07A522.

127. A. Miszczyk and K. Darowicki, *Anti-Corrosion Methods and Materials*, 2011, 58, 13-21.

128. D.-L. Zhao, Q. Lv and Z.-M. Shen, *Journal of Alloys and Compounds*, 2009, 480, 634-638.

129. C.-H. Peng, H.-W. Wang, S.-W. Kan, M.-Z. Shen, Y.-M. Wei and S.-Y. Chen, *Journal of Magnetism and Magnetic Materials*, 2004, 284, 113-119.

130. S. Zhang, Q. Jiao, Y. Zhao, H. Li and Q. Wu, *Journal of Materials Chemistry A*, 2014, 2, 18033-18039.

131. K. Khan, *Journal of Superconductivity and Novel Magnetism*, 2013, 27, 453-461.

132. S. Hazra, B. K. Ghosh, M. K. Patra, R. K. Jani, S. R. Vadera and N. N. Ghosh, *Journal of Nanoscience and Nanotechnology*, 2015, 15, 6559-6567.

133. S. Hazra, B. K. Ghosh, M. K. Patra, R. K. Jani, S. R. Vadera and N. N. Ghosh, *Powder Technology*, 2015, 279, 10-17.

134. X. Huang, J. Zhang, S. Xiao and G. Chen, *Journal of the American Ceramic Society*, 2014, 97, 1363-1366.

135. P. Fannin, C. Marin, I. Malaescu, N. Stefu, P. Vlazan, S. Novaconi, P. Sfirloaga, S. Popescu and C. Couper, *Materials & Design*, 2011, 32, 1600-1604.

136. W. Fu, S. Liu, W. Fan, H. Yang, X. Pang, J. Xu and G. Zou, *Journal of Magnetism and Magnetic Materials*, 2007, 316, 54-58.

137. R. Ji, C. Cao, Z. Chen, H. Zhai and J. Bai, *Journal of Materials Chemistry C*, 2014, 2, 5944-5953.

138. S.-Y. Tong, J.-M. Wu, M.-J. Tung, W.-S. Ko, Y.-T. Huang and Y.-P. Wang, *Journal of Alloys and Compounds*, 2012, 525, 143-148.

139. B. Qu, C. Zhu, C. Li, X. Zhang and Y. Chen, *ACS Applied Materials & Interfaces*, 2016.

140. T. Wang, Z. Liu, M. Lu, B. Wen, Q. Ouyang, Y. Chen, C. Zhu, P. Gao, C. Li and M. Cao, *Journal of Applied Physics*, 2013, 113, 024314.

141. M. Zong, Y. Huang, H. Wu, Y. Zhao, Q. Wang and X. Sun, *Materials Letters*, 2014, 114, 52-55.

142. M. Fu, Q. Jiao and Y. Zhao, *Journal of Materials Chemistry A*, 2013, 1, 5577-5586.

143. G.-S. Wang, Y. Wu, Y.-Z. Wei, X.-J. Zhang, Y. Li, L.-D. Li, B. Wen, P.-G. Yin, L. Guo and M.-S. Cao, *ChemPlusChem*, 2014, 79, 375-381.

144. D. Moitra, B. K. Ghosh, M. Chandel and N. N. Ghosh, *RSC Advances*, 2016, 6, 97941-97952.

145. J. Fang, B. Zhang, Q. Yao, Y. Yang, J. Xie and N. Yan, *Coordination Chemistry Reviews*, 2016, 322, 1-29.

146. B. K. Ghosh, S. Hazra and N. N. Ghosh, *Catalysis Communications*, 2016, 80, 44-48.

147. M. Liu, X. Wang, Y. Chen and L. Dai, *RSC Advances*, 2015, 5, 61481-61485.

148. G. Bian, P. Jiang, H. Zhao, K. Jiang, L. Hu, Y. Dong and W. Zhang, *ChemistrySelect*, 2016, 1, 1384-1392.

149. Z. Zhang, T. Sun, C. Chen, F. Xiao, Z. Gong and S. Wang, *ACS Applied Materials & Interfaces*, 2014, 6, 21035-21040.

150. A. S. Nia, S. Rana, D. Döhler, X. Noirfalise, A. Belfiore and W. H. Binder, *Chemical Communications*, 2014, 50, 15374-15377.

151. N. Salam, A. Sinha, A. S. Roy, P. Mondal, N. R. Jana and S. M. Islam, *RSC Advances*, 2014, 4, 10001-10012.

152. Z. Li, Y. Shen, Y. Guan, Y. Hu, Y. Lin and C.-W. Nan, *Journal of Materials Chemistry A*, 2014, 2, 1967-1973.

153. Y. Gao, P. Tang, H. Zhou, W. Zhang, H. Yang, N. Yan, G. Hu, D. Mei, J. Wang and D. Ma, *Angewandte Chemie International Edition*, 2016, 55, 3124-3128.

154. Y. Gao, X. Chen, J. Zhang, H. Asakura, T. Tanaka, K. Teramura, D. Ma and N. Yan, *Advanced Materials*, 2015, 27, 4688-4694.

155. L. Gan, S. Shang, C. W. M. Yuen, S.-x. Jiang and E. Hu, *Applied Surface Science*, 2015, 351, 140-147.

156. Y. Zhao, G. He, W. Dai and H. Chen, *Industrial & Engineering Chemistry Research*, 2014, 53, 12566-12574.

157. Y. Yao, Z. Yang, D. Zhang, W. Peng, H. Sun and S. Wang, *Industrial & Engineering Chemistry Research*, 2012, 51, 6044-6051.

158. Y. Fu, H. Chen, X. Sun and X. Wang, *AIChE Journal*, 2012, 58, 3298-3305.

159. G. He, J. Ding, J. Zhang, Q. Hao and H. Chen, *Industrial & Engineering Chemistry Research*, 2015, 54, 2862-2867.

160. R. R. Bacsa, I. Cameán, A. Ramos, A. B. Garcia, V. Tishkova, W. S. Bacsa, J. R. Gallagher, J. T. Miller, H. Navas and V. Jourdain, *Carbon*, 2015, 89, 350-360.

161. L. G. Devi and M. Srinivas, *Journal of Environmental Chemical Engineering*, 2017, 5, 3243-3255.

162. J. Feng, L. Su, Y. Ma, C. Ren, Q. Guo and X. Chen, *Chemical engineering journal*, 2013, 221, 16-24.

163. Y. Fu and X. Wang, *Industrial & Engineering Chemistry Research*, 2011, 50, 7210-7218.

164. Y. Fu, H. Chen, X. Sun and X. Wang, *Applied Catalysis B: Environmental*, 2012, 111, 280-287.

165. W. Zhang, B. Quan, C. Lee, S.-K. Park, X. Li, E. Choi, G. Diao and Y. Piao, *ACS Applied Materials & Interfaces*, 2015, 7, 2404-2414.

166. T. Soltani and B.-K. Lee, *Chemical Engineering Journal*, 2016, 306, 204-213.

167. P. Fei, M. Zhong, Z. Lei and B. Su, *Materials Letters*, 2013, 108, 72-74.

168. B. K. Ghosh, D. Moitra, M. Chandel and N. N. Ghosh, *Journal of Nanoscience and Nanotechnology*, 2017, 17, 4694-4703.

169. S.-Q. Liu, X.-L. Zhu, Y. Zhou, Z.-D. Meng, Z.-G. Chen, C.-B. Liu, F. Chen, Z.-Y. Wu and J.-C. Qian, *Catalysis Science & Technology*, 2017, 7, 3210-3219.

170. A. Hassani, G. Çelikdağ, P. Eghbali, M. Sevim, S. Karaca and Ö. Metin, *Ultrasonics Sonochemistry*, 2018, 40, 841-852.

171. Z. Cao, J. Zhang, J. Zhou, X. Ruan, D. Chen, J. Liu, Q. Liu and G. Qian, *Journal of Environmental Management*, 2017, 193, 146-153.

172. X. Wang, W. Mao, Q. Wang, Y. Zhu, Y. Min, J. Zhang, T. Yang, J. Yang, X. a. Li and W. Huang, *RSC Advances*, 2017, 7, 10064-10069.

173. D. Zhang and L. Zhang, *New Journal of Chemistry*, 2016, 40, 7171-7180.

174. M. Hu, Z. Yao and X. Wang, *Industrial & Engineering Chemistry Research*, 2017, 56, 3477-3502.

175. N. Zhang, Y. Zhang and Y.-J. Xu, *Nanoscale*, 2012, 4, 5792-5813.

176. H. Hu, J. H. Xin, H. Hu, X. Wang, D. Miao and Y. Liu, *Journal of Materials Chemistry A*, 2015, 3, 11157-11182.

177. S. P. Buthelezi, A. O. Olaniran and B. Pillay, *Molecules*, 2012, 17, 14260-14274.

178. Z. Aksu, *Process Biochemistry*, 2005, 40, 997-1026.

179. C. J. Ogugbue and T. Sawidis, *Biotechnology Research International*, 2011, 2011.

180. M. T. Yagub, T. K. Sen, S. Afroze and H. M. Ang, *Advances in Colloid and Interface Science*, 2014, 209, 172-184.

181. T. Robinson, G. McMullan, R. Marchant and P. Nigam, *Bioresource Technology*, 2001, 77, 247-255.

182. H. Zollinger, *Inc., New York*, 1987, 25-41.

183. A. Bafana, S. S. Devi and T. Chakrabarti, *Environmental Reviews*, 2011, 19, 350-371.

184. G. McMullan, C. Meehan, A. Conneely, N. Kirby, T. Robinson, P. Nigam, I. Banat, R. Marchant and W. Smyth, *Applied Microbiology and Biotechnology*, 2001, 56, 81-87.

185. R. Patel and S. Suresh, *Journal of Hazardous Materials*, 2006, 137, 1729-1741.

186. B. Manu and S. Chaudhari, *Bioresource Technology*, 2002, 82, 225-231.

187. K. Singh and S. Arora, *Critical Reviews in Environmental Science and Technology*, 2011, 41, 807-878.

188. A. Ahmad, S. H. Mohd-Setapar, C. S. Chuong, A. Khatoon, W. A. Wani, R. Kumar and M. Rafatullah, *RSC Advances*, 2015, 5, 30801-30818.

189. G. Divyapriya, I. M. Nambi and J. Senthilnathan, *Journal of Bionanoscience*, 2016, 10, 356-368.

190. V. Gupta, *Journal of Environmental Management*, 2009, 90, 2313-2342.

191. M. Joshi and R. Purwar, *Coloration Technology*, 2004, 34, 58-71.

192. M. Greluk and Z. Hubicki, *Chemical Engineering Research and Design*, 2013, 91, 1343-1351.

193. M. Coughlin, B. Kinkle, A. Tepper and P. Bishop, *Water Science and Technology*, 1997, 36, 215-220.

194. H. W. Hu, J. H. Xin and H. Hu, *ChemPlusChem*, 2013, 78, 1483-1490.

195. U. P. Azad, V. Ganesan and M. Pal, *Journal of Nanoparticle Research*, 2011, 13, 3951-3959.

196. W. Wang, F. Wang, Y. Kang and A. Wang, *Chemical Engineering Journal*, 2014, 237, 336-343.

197.   M. Bordbar, Z. Sharifi-Zarchi and B. Khodadadi, *Journal of Sol-Gel Science and Technology*, 2017, 81, 724-733.

198.   Y. Zheng and A. Wang, *Journal of Materials Chemistry*, 2012, 22, 16552-16559.

199.   H. Hu, J. H. Xin and H. Hu, *Journal of Materials Chemistry A*, 2014, 2, 11319-11333.

200.   Y. Junejo, A. Baykal, M. Safdar and A. Balouch, *Applied Surface Science*, 2014, 290, 499-503.

201.   C. Wen, M. Shao, S. Zhuo, Z. Lin and Z. Kang, *Materials Chemistry and Physics*, 2012, 135, 780-785.

202.   A. Amarjargal, L. D. Tijing, I.-T. Im and C. S. Kim, *Chemical Engineering Journal*, 2013, 226, 243-254.

203.   S. S. Hassan, A. R. Solangi, M. H. Agheem, Y. Junejo, N. H. Kalwar and Z. A. Tagar, *Journal of Hazardous Materials*, 2011, 190, 1030-1036.

204.   R. Dong, J. Xu, Z. Yang, G. Wei, W. Zhao, J. Yan, Y. Fang and J. Hao, *Chemistry-A European Journal*, 2013, 19, 13099-13104.

205.   Y. Zhang, P. Zhu, L. Chen, G. Li, F. Zhou, D. D. Lu, R. Sun, F. Zhou and C.-p. Wong, *Journal of Materials Chemistry A*, 2014, 2, 11966-11973.

206.   R. K. Narayanan, S. J. Devaki and T. P. Rao, *Applied Catalysis A: General*, 2014, 483, 31-40.

207.   T. Aditya, A. Pal and T. Pal, *Chemical Communications*, 2015, 51, 9410-9431.

208.   A. Saad, Y. Snoussi, M. Abderrabba and M. M. Chehimi, *RSC Advances*, 2016, 6, 57672-57682.

209.   R. Rajesh, S. S. Kumar and R. Venkatesan, *New Journal of Chemistry*, 2014, 38, 1551-1558.

210.   S. Naraginti, F. B. Stephen, A. Radhakrishnan and A. Sivakumar, *Spectrochimica Acta Part A: Molecular and Biomolecular Spectroscopy*, 2015, 135, 814-819.

211.   S. Gu, S. Wunder, Y. Lu, M. Ballauff, R. Fenger, K. Rademann, B. Jaquet and A. Zaccone, *The Journal of Physical Chemistry C*, 2014, 118, 18618-18625.

212.   N. Linares, C. Canlas, J. Garcia-Martinez and T. J. Pinnavaia, *Catalysis Communications*, 2014, 44, 50-53.

213.   A. Shehzad, S. Panneerselvam, M. Linow, M. Bocola, D. Roccatano, J. Mueller-Dieckmann, M. Wilmanns and U. Schwaneberg, *Chemical communications*, 2013, 49, 4694-4696.

214.   A. Wang and H. Jing, *Dalton Transactions*, 2014, 43, 1011-1018.

215.   Z. Li, S. Wu, D. Zheng, H. Ding, X. Wang, X. Yang, Q. Huo, J. Guan and Q. Kan, *ChemPlusChem*, 2014, 79, 716-724.

216.   V. Choudhary, D. Dumbre, N. Patil, B. Uphade and S. Bhargava, *Journal of Catalysis*, 2013, 300, 217-224.

217.   X. Huali, F. Yongxian, Z. Chunhui, D. Zexue, M. Enze, G. Zhonghua and L. Xiaonian, *Chemical and Biochemical Engineering Quarterly*, 2008, 22, 25-39.

218.   N. Patil, B. Uphade, P. Jana, S. Bharagava and V. Choudhary, *Journal of Catalysis*, 2004, 223, 236-239.

219.   V. R. Choudhary, R. Jha and P. Jana, *Catalysis Communications*, 2008, 10, 205-207.

220.   X. Zhang, S. Yang, D. Tang and R. Yang, *Materials Research Bulletin*, 2015, 70, 343-347.

221.   C. G. Freyschlag and R. J. Madix, *Materials Today*, 2011, 14, 134-142.

222.   X. Zhang, G. Wang, M. Yang, Y. Luan, W. Dong, R. Dang, H. Gao and J. Yu, *Catalysis Science & Technology*, 2014, 4, 3082-3089.

223.   V. R. Choudhary, R. Jha and P. Jana, *Green Chemistry*, 2006, 8, 689-690.

224.   Z.-Q. Shi, Z.-P. Dong, J. Sun, F.-W. Zhang, H.-L. Yang, J.-H. Zhou, X.-H. Zhu and R. Li, *Chemical Engineering Journal*, 2014, 237, 81-87.

225.   H. C. Kolb, M. Finn and K. B. Sharpless, *Angewandte Chemie International Edition*, 2001, 40, 2004-2021.

226.   A. N. Prasad, B. Thirupathi, G. Raju, R. Srinivas and B. M. Reddy, *Catalysis Science & Technology*, 2012, 2, 1264-1268.

227.   S. Jang, Y. J. Sa, S. H. Joo and K. H. Park, *Catalysis Communications*, 2016, 81, 24-28.

228.   T. Boningari, A. Olmos, B. M. Reddy, J. Sommer and P. Pale, *European Journal of Organic Chemistry*, 2010, 2010, 6338-6347.

229.   H. Sharghi, S. Ebrahimpourmoghaddam, M. M. Doroodmand and A. Purkhosrow, *Asian Journal of Organic Chemistry*, 2012, 1, 377-388.

230.   B. A. Kumar, K. H. V. Reddy, B. Madhav, K. Ramesh and Y. Nageswar, *Tetrahedron Letters*, 2012, 53, 4595-4599.

231.   G. Kumaraswamy, K. Ankamma and A. Pitchaiah, *The Journal of Organic Chemistry*, 2007, 72, 9822-9825.

232.   H. Naeimi and V. Nejadshafiee, *New Journal of Chemistry*, 2014, 38, 5429-5435.

233. F. Alonso, Y. Moglie, G. Radivoy and M. Yus, *The Journal of Organic Chemistry*, 2011, 76, 8394-8405.

234. S. Dıez-Gonzalez, E. Stevens and S. Nolan, *Chemical Communication*, 2008, 39, 4747-4749.

235. J. Yadav, B. S. Reddy, G. M. Reddy and D. N. Chary, *Tetrahedron Letters*, 2007, 48, 8773-8776.

236. L. Wan and C. Cai, *Catalysis Letters*, 2012, 142, 1134-1140.

237. M. Tavassoli, A. Landarani-Isfahani, M. Moghadam, S. Tangestaninejad, V. Mirkhani and I. Mohammadpoor-Baltork, *Applied Catalysis A: General*, 2015, 503, 186-195.

238. H. Sharghi, M. H. Beyzavi, A. Safavi, M. M. Doroodmand and R. Khalifeh, *Advanced Synthesis & Catalysis*, 2009, 351, 2391-2410.

239. G. C. Tron, T. Pirali, R. A. Billington, P. L. Canonico, G. Sorba and A. A. Genazzani, *Medicinal Research Reviews*, 2008, 28, 278-308.

240. J. Mondal, T. Sen and A. Bhaumik, *Dalton Transactions*, 2012, 41, 6173-6181.

241. H. G. Alvim, T. B. Lima, A. L. de Oliveira, H. C. de Oliveira, F. M. Silva, F. C. Gozzo, R. Y. Souza, W. A. da Silva and B. A. Neto, *The Journal of Organic Chemistry*, 2014, 79, 3383-3397.

242. B. K. Banik, A. T. Reddy, A. Datta and C. Mukhopadhyay, *Tetrahedron Letters*, 2007, 48, 7392-7394.

243. J. Javidi, M. Esmaeilpour and F. N. Dodeji, *RSC Advances*, 2015, 5, 308-315.

244. S. L. Jain, S. Singhal and B. Sain, *Green Chemistry*, 2007, 9, 740-741.

245. J. Safari and S. Gandomi-Ravandi, *Journal of Molecular Catalysis A: Chemical*, 2013, 373, 72-77.

246. A. Zhu, Q. Li, L. Li and J. Wang, *Catalysis Letters*, 2013, 143, 463-468.

247. A. Rajack, K. Yuvaraju, C. Praveen and Y. Murthy, *Journal of Molecular Catalysis A: Chemical*, 2013, 370, 197-204.

248. F. Tamaddon and S. Moradi, *Journal of Molecular Catalysis A: Chemical*, 2013, 370, 117-122.

249. G. Kour, M. Gupta, S. Paul and V. K. Gupta, *Journal of Molecular Catalysis A: Chemical*, 2014, 392, 260-269.

250. G. S. Prakash, H. Lau, C. Panja, I. Bychinskaya, S. K. Ganesh, B. Zaro, T. Mathew and G. A. Olah, *Catalysis Letters*, 2014, 144, 2012-2020.

251. Y. Naito and K. Suetake, *IEEE Transactions on Microwave Theory and Techniques,* 1971, 19, 65-72.

252. B. Naik, S. Hazra, D. Desagani, B. K. Ghosh, M. K. Patra, S. R. Vadera and N. N. Ghosh, *RSC Advances*, 2015, 5, 40193-40198.

253. B. Naik, S. Hazra, V. S. Prasad and N. N. Ghosh, *Catalysis Communications*, 2011, 12, 1104-1108.

254. P. Veerakumar, S.-M. Chen, R. Madhu, V. Veeramani, C.-T. Hung and S.-B. Liu, *ACS Applied Materials & Interfaces*, 2015, 7, 24810-24821.

255. B. Naik, V. S. Prasad and N. N. Ghosh, *Powder Technology*, 2012, 232, 1-6.

256. X. Zhang, Z. Zhou and C. Lu, *RSC Advances*, 2015, 5, 20186-20192.

257. C. Xu, X. Wu, J. Zhu and X. Wang, *Carbon*, 2008, 46, 386-389.

258. G. Goncalves, P. A. Marques, C. M. Granadeiro, H. I. Nogueira, M. Singh and J. Gracio, *Chemistry of Materials*, 2009, 21, 4796-4802.

259. A. Prakash, S. Chandra and D. Bahadur, *Carbon*, 2012, 50, 4209-4219.

260. Z. Yang, Y. Wan, G. Xiong, D. Li, Q. Li, C. Ma, R. Guo and H. Luo, *Materials Research Bulletin*, 2015, 61, 292-297.

261. J. Su, M. Cao, L. Ren and C. Hu, *The Journal of Physical Chemistry C*, 2011, 115, 14469-14477.

262. Z. Zhong, Q. Li, Y. Zhang, H. Zhong, M. Cheng and Y. Zhang, *Powder Technology*, 2005, 155, 193-195.

263. D. Luo, G. Zhang, J. Liu and X. Sun, *The Journal of Physical Chemistry C*, 2011, 115, 11327-11335.

264. G. S. Wang, Y. Wu, Y. Z. Wei, X. J. Zhang, Y. Li, L. D. Li, B. Wen, P. G. Yin, L. Guo and M. S. Cao, *ChemPlusChem*, 2014, 79, 375-381.

265. Y. Zhao, X. Song, Q. Song and Z. Yin, *CrystEngComm*, 2012, 14, 6710-6719.

266. K. Velmurugan, V. S. K. Venkatachalapathy and S. Sendhilnathan, *Materials Research*, 2010, 13, 299-303.

267. J.-G. Lee, H. M. Lee, C. S. Kim and O. Young-Jei, *Journal of Magnetism and Magnetic Materials*, 1998, 177, 900-902.

268. H. Lu, W. Zheng and Q. Jiang, *Journal of Physics D: Applied Physics*, 2007, 40, 320.

269. Z. Tang, C. Sorensen, K. Klabunde and G. Hadjipanayis, *Physical Review Letters*, 1991, 67, 3602.

270. R. Frison, G. Cernuto, A. Cervellino, O. Zaharko, G. M. Colonna, A. Guagliardi and N. Masciocchi, *Chemistry of Materials*, 2013, 25, 4820-4827.

271. Y. Zhan, F. Meng, X. Yang, R. Zhao and X. Liu, *Materials Science and Engineering: B*, 2011, 176, 1333-1339.

272. N. Pradhan, A. Pal and T. Pal, *Langmuir*, 2001, 17, 1800-1802.

273. S. Saha, A. Pal, S. Kundu, S. Basu and T. Pal, *Langmuir*, 2009, 26, 2885-2893.

274. A. K. Sinha, M. Basu, S. Sarkar, M. Pradhan and T. Pal, *Journal of Colloid and Interface Science*, 2013, 398, 13-21.

275. H. Zhang, S. Gao, N. Shang, C. Wang and Z. Wang, *RSC Advances*, 2014, 4, 31328-31332.

276. J. Sun, Y. Fu, P. Xiong, X. Sun, B. Xu and X. Wang, *RSC Advances*, 2013, 3, 22490-22497.

277. K. Mao, Y. Chen, Z. Wu, X. Zhou, A. Shen and J. Hu, *Journal of Agricultural and Food Chemistry*, 2014, 62, 10638-10645.

278. D. Chen, G.-S. Wang, S. He, J. Liu, L. Guo and M.-S. Cao, *Journal of Materials Chemistry A*, 2013, 1, 5996-6003.

279. X. Zhang, X. Dong, H. Huang, Y. Liu, W. Wang, X. Zhu, B. Lv, J. Lei and C. Lee, *Applied Physics Letters*, 2006, 89, 053115.

280. C.-C. Lee and D.-H. Chen, *Applied Physics Letters*, 2007, 90, 193102.

281. X. Liu, D. Geng, H. Meng, P. Shang and Z. Zhang, *Applied Physics Letters*, 2008, 92, 173117.

282. X. Liu, D. Geng and Z. Zhang, *Applied Physics Letters*, 2008, 92, 243110.

283. J. R. Liu, M. Itoh, T. Horikawa, K.-i. Machida, S. Sugimoto and T. Maeda, *Journal of Applied Physics*, 2005, 98, 054305.

284. J. Zhu, H. Gu, Z. Luo, N. Haldolaarachige, D. P. Young, S. Wei and Z. Guo, *Langmuir*, 2012, 28, 10246-10255.

285. S. He, G.-S. Wang, C. Lu, J. Liu, B. Wen, H. Liu, L. Guo and M.-S. Cao, *Journal of Materials Chemistry A*, 2013, 1, 4685-4692.

286. J. Huang, S. Vongehr, S. Tang, H. Lu, J. Shen and X. Meng, *Langmuir*, 2009, 25, 11890-11896.

287. A. Gangula, R. Podila, L. Karanam, C. Janardhana and A. M. Rao, *Langmuir*, 2011, 27, 15268-15274.

288. P. Deka, R. C. Deka and P. Bharali, *New Journal of Chemistry*, 2014, 38, 1789-1793.

289. J. Chen, Z. Xue, S. Feng, B. Tu and D. Zhao, *Journal of Colloid and Interface Science*, 2014, 429, 62-67.

290. J. Chen, R. Zhang, L. Han, B. Tu and D. Zhao, *Nano Research*, 2013, 6, 871-879.

291. J. Han, P. Fang, W. Jiang, L. Li and R. Guo, *Langmuir*, 2012, 28, 4768-4775.

292. A. T. Miah, S. K. Bharadwaj and P. Saikia, *Powder Technology*, 2017, 315, 147-156.

293. W. Pan, S. Zhang, F. He, S. Gai, Y. Sun and P. Yang, *CrystEngComm*, 2015, 17, 5744-5750.

294. J. Wang, X. Shao, G. Tian and W. Bao, *Journal of Porous Materials*, 2018, 25, 207-214.

295. A. Goyal, S. Bansal and S. Singhal, *International Journal of Hydrogen Energy*, 2014, 39, 4895-4908.

296. F.-h. Lin and R.-a. Doong, *The Journal of Physical Chemistry C*, 2011, 115, 6591-6598.

297. Z. Z. Wang, S. R. Zhai, B. Zhai and Q. D. An, *European Journal of Inorganic Chemistry*, 2015, 2015, 1692-1699.

298. G. Sharma and P. Jeevanandam, *European Journal of Inorganic Chemistry*, 2013, 2013, 6126-6136.

299. B. K. Ghosh, S. Hazra, B. Naik and N. N. Ghosh, *Journal of Nanoscience and Nanotechnology*, 2015, 15, 6516-6523.

300. B. K. Ghosh, S. Hazra, B. Naik and N. N. Ghosh, *Powder Technology*, 2015, 269, 371-378.

301. B. K. Ghosh, D. Moitra, M. Chandel, M. K. Patra, S. R. Vadera and N. N. Ghosh, *Catalysis Letters*, 2017, 147, 1061-1076.

302. B. K. Ghosh, D. Moitra, M. Chandel, H. Lulla and N. N. Ghosh, *Materials Research Bulletin*, 2017, 94, 361-370.

303. Y. Li, J. Shen, Y. Hu, S. Qiu, G. Min, Z. Song, Z. Sun and C. Li, *Industrial & Engineering Chemistry Research*, 2015, 54, 9750-9757.

304. I. Papadas, K. Subrahmanyam, M. G. Kanatzidis and G. Armatas, *Nanoscale*, 2015, 7, 5737-5743.

305. S. Bai, X. Shen, G. Zhu, M. Li, H. Xi and K. Chen, *ACS Applied Materials & Interfaces*, 2012, 4, 2378-2386.

306. Y.-g. Wu, M. Wen, Q.-s. Wu and H. Fang, *The Journal of Physical Chemistry C*, 2014, 118, 6307-6313.

307. R. Dhanda and M. Kidwai, *Journal of Materials Chemistry A*, 2015, 3, 19563-19574.

308. M. Zhu, C. Wang, D. Meng and G. Diao, *Journal of Materials Chemistry A*, 2013, 1, 2118-2125.

309. M. Atarod, M. Nasrollahzadeh and S. M. Sajadi, *Journal of Colloid and Interface Science*, 2016, 465, 249-258.

310. U. Kurtan, M. Amir, A. Yıldız and A. Baykal, *Applied Surface Science*, 2016, 376, 16-25.

311. N. Gupta, H. P. Singh and R. K. Sharma, *Journal of Molecular Catalysis A: Chemical*, 2011, 335, 248-252.

312. T. Kamal, S. B. Khan and A. M. Asiri, *Cellulose*, 2016, 23, 1911-1923.

313. M. M. Khan, J. Lee and M. H. Cho, *Journal of Industrial and Engineering Chemistry*, 2014, 20, 1584-1590.

314. C. H. Chia, S. Zakaria, M. Yusoff, S. Goh, C. Haw, S. Ahmadi, N. Huang and H. Lim, *Ceramics International*, 2010, 36, 605-609.

315. B. Jeyadevan, C. Chinnasamy, O. Perales-Perez, Y. Iwasaki, A. Hobo, K. Shinoda, K. Tohji and A. Kasuya, *IEEE Transactions on Magnetics*, 2002, 38, 2595-2597.

316. P. Kubelka and F. Munk, *Zeitschrift fur Technische Physik*, 1931, 12.

317. J. Tauc and A. Menth, *Journal of Non-Crystalline Solids*, 1972, 8, 569-585.

318. L. Gan, S. Shang, C. W. M. Yuen, S.-x. Jiang and E. Hu, *Applied Surface Science* 2015, 351, 140-147.

319. J. Li, Q. Xiao, L. Li, J. Shen and D. Hu, *Applied Surface Science*, 2015, 331, 108-114.

320. D. Moitra, S. Hazra, B. K. Ghosh, R. Jani, M. Patra, S. R. Vadera and N. N. Ghosh, *RSC Advances*, 2015, 5, 51130-51134.

321. Z.-Q. Li, H.-L. Wang, L.-Y. Zi, J.-J. Zhang and Y.-S. Zhang, *Ceramics International*, 2015, 41, 10634-10643.

322. X. Yang, W. Chen, J. Huang, Y. Zhou, Y. Zhu and C. Li, *Scientific Reports*, 2015, 5, 10632.

323. C. Haw, W. Chiu, S. A. Rahman, P. Khiew, S. Radiman, R. A. Shukor, M. A. A. Hamid and N. Ghazali, *New Journal of Chemistry*, 2016, 40, 1124-1136.

324. Y. Fu, P. Xiong, H. Chen, X. Sun and X. Wang, *Industrial & Engineering Chemistry Research*, 2012, 51, 725-731.

325.   S. Bai, X. Shen, X. Zhong, Y. Liu, G. Zhu, X. Xu and K. Chen, *Carbon*, 2012, 50, 2337-2346.

326.   D. Zhang, Q. Wang, L. Wang and L. Zhang, *Journal of Materials Chemistry A*, 2015, 3, 3576-3585.

327.   Z. T. Hu, J. Liu, X. Yan, W.-D. Oh and T.-T. Lim, *Chemical Engineering Journal*, 2015, 262, 1022-1032.

328.   R. Han, W. Li, W. Pan, M. Zhu, D. Zhou and F.-s. Li, *Scientific Reports*, 2014, 4, 7493.

329.   R.-B. Yang, W.-F. Liang, W.-S. Lin, H.-M. Lin, C.-Y. Tsay and C.-K. Lin, *Journal of Applied Physics*, 2011, 109, 07B527.

330.   J. Yang, J. Zhang, C. Liang, M. Wang, P. Zhao, M. Liu, J. Liu and R. Che, *ACS Applied Materials & Interfaces*, 2013, 5, 7146-7151.

331.   S. Li, J. Zhang, M. G. Kibria, Z. Mi, M. Chaker, D. Ma, R. Nechache and F. Rosei, *Chemical Communications*, 2013, 49, 5856-5858.

332.   H. Hong, L. Hu, M. Li, J. Zheng, X. Sun, X. Lu, X. Cao, J. Lu and H. Gu, *Chemistry-A European Journal*, 2011, 17, 8726-8730.

333.   Y. Li, H.-J. Yang, W.-G. Yang, Z.-L. Hou, J.-B. Li, H.-B. Jin, J. Yuan and M.-S. Cao, *Materials Letters*, 2013, 111, 130-133.

334.   Z.-L. Hou, H.-F. Zhou, L.-B. Kong, H.-B. Jin, X. Qi and M.-S. Cao, *Materials Letters*, 2012, 84, 110-113.

335.   Y.-Q. Kang, M.-S. Cao, J. Yuan and X.-L. Shi, *Materials Letters*, 2009, 63, 1344-1346.

336.   J. Yuan, Z.-L. Hou, H.-J. Yang, Y. Li, Y.-Q. Kang, W.-L. Song, H.-B. Jin, X.-Y. Fang and M.-S. Cao, *Ceramics International*, 2013, 39, 7241-7246.

337.   B. Liu, B. Hu and Z. Du, *Chemical Communications*, 2011, 47, 8166-8168.

338.   E. Aguiar, M. Ramirez, F. Moura, J. A. Varela, E. Longo and A. Simoes, *Ceramics International*, 2013, 39, 13-20.

339.   Y. Wang, G. Xu, L. Yang, Z. Ren, X. Wei, W. Weng, P. Du, G. Shen and G. Han, *Journal of the American Ceramic Society*, 2007, 90, 3673-3675.

340.   Z. Li, Y. Shen, C. Yang, Y. Lei, Y. Guan, Y. Lin, D. Liu and C.-W. Nan, *Journal of Materials Chemistry A,* 2013, 1, 823-829.

341.   R. Das, G. G. Khan, S. Varma, G. D. Mukherjee and K. Mandal, *The Journal of Physical Chemistry C*, 2013, 117, 20209-20216.

342.   U. A. Joshi and J. S. Lee, *Small*, 2005, 1, 1172-1176.

343. M. Popa, D. Crespo, J. M. Calderon-Moreno, S. Preda and V. Fruth, *Journal of the American Ceramic Society*, 2007, 90, 2723-2727.

344. S. H. Yu, B. Liu, M. S. Mo, J. H. Huang, X. M. Liu and Y. T. Qian, *Advanced Functional Materials*, 2003, 13, 639-647.

345. W. Wang, C. Xu, G. Wang, Y. Liu and C. Zheng, *Advanced Materials*, 2002, 14, 837-840.

346. D. Quéré, J.-M. Di Meglio and F. Brochard-Wyart, *Science*, 1990, 249, 1256-1260.

347. K. Ramalinga, P. Vijayalakshmi and T. Kaimal, *Synlett*, 2001, 2001, 0863-0865.

348. M. L. Kuznetsov, B. G. Rocha, A. J. Pombeiro and G. B. Shul'pin, *ACS Catalysis*, 2015, 5, 3823-3835.

349. J. An, L. Zhu, N. Wang, Z. Song, Z. Yang, D. Du and H. Tang, *Chemical Engineering Journal*, 2013, 219, 225-237.

350. X. Zhang, X. Dong, H. Huang, B. Lv, J. Lei and C. Choi, *Journal of Physics D: Applied Physics, 2007, 40, 5383.*

351. P. Watts, D. Ponnampalam, W. Hsu, A. Barnes and B. Chambers, *Chemical Physics Letters*, 2003, 378, 609-614.

352. Y. Li, H.-J. Yang, W.-G. Yang, Z.-L. Hou, J.-B. Li, H.-B. Jin, J. Yuan and M.-S. Cao, *Materials Letters*, 2013, 111, 130-133.

353. Z.-L. Hou, H.-F. Zhou, L.-B. Kong, H.-B. Jin, X. Qi and M.-S. Cao, *Materials Letters*, 2012, 84, 110-113.

354. Y.-Q. Kang, M.-S. Cao, J. Yuan and X.-L. Shi, *Materials Letters*, 2009, 63, 1344-1346.

355. J. Yuan, Z.-L. Hou, H.-J. Yang, Y. Li, Y.-Q. Kang, W.-L. Song, H.-B. Jin, X.-Y. Fang and M.-S. Cao, *Ceramics International*, 2013, 39, 7241-7246.

356. F. Zamani and E. Izadi, *Catalysis Communications*, 2013, 42, 104-108.

357. A. Debache, M. Amimour, A. Belfaitah, S. Rhouati and B. Carboni, *Tetrahedron Letters*, 2008, 49, 6119-6121.

358. A. Khaskel, P. Gogoi, P. Barman and B. Bandyopadhyay, *RSC Advances*, 2014, 4, 35559-35567.

359. H. N. Karade, M. Sathe and M. Kaushik, *Molecules*, 2007, 12, 1341-1351.

360. N. T. Thao, *Chemical Engineering Journal*, 2015, 279, 840-850.

361. J. Liu, F. Wang, S. Qi, Z. Gu and G. Wu, *New Journal of Chemistry*, 2013, 37, 769-774.

362. J. Liu, F. Wang, T. Xu and Z. Gu, *Catalysis letters*, 2010, 134, 51-55.

363. D. Yang, N. Yang and J. Ge, *CrystEngComm*, 2013, 15, 7230-7235.

364. D.-H. Zhang, G.-D. Li, J.-X. Li and J.-S. Chen, *Chemical Communications*, 2008, 3414-3416.

365. D. Nepak and D. Srinivas, *Applied Catalysis A: General*, 2016, 523, 61-72.

366. X. Hu, J. Bai, C. Li, H. Liang and W. Sun, *European Journal of Inorganic Chemistry*, 2015, 2015, 3758-3763.

367. D.-H. Zhang, H.-B. Li, G.-D. Li and J.-S. Chen, *Dalton Transactions*, 2009, 10527-10533.

368. J. Liu, F. Wang, Z. Gu and X. Xu, *Catalysis Communications*, 2009, 10, 868-871.

369. Y. Tang, M. Yang, W. Dong, L. Tan, X. Zhang, P. Zhao, C. Peng and G. Wang, *Microporous and Mesoporous Materials*, 2015, 215, 199-205.

List of Publications:

Publications related to thesis:

1. D. Moitra, B. K. Ghosh, M. Chandel, R. K. Jani, M. K. Patra, S. R. Vadera and N. N. Ghosh, Synthesis of a $Ni_{0.8}Zn_{0.2}Fe_2O_4$-RGO nanocomposite: an excellent magnetically separable catalyst for dye degradation and microwave absorber. *RSC Advances.* **2016**, 6, 17 14090-14096.

2. D. Moitra, M. Chandel, B. K. Ghosh, R. K. Jani, M. K. Patra, S. R. Vadera and N. N. Ghosh, A Simple *'in situ'* Co-precipitation Method for Preparation of Multifunctional $CoFe_2O_4$-Reduced Graphene Oxide Nanocomposites: Excellent Microwave Absorber and Highly Efficient Magnetically Separable Recyclable Photocatalyst for Dye Degradation. *RSC Advances.* **2016**, 6, 80, 76759- 76772.

3. D. Moitra, B. K. Ghosh, M. Chandel and N. N. Ghosh, Synthesis of a $BiFeO_3$ nanowire-reduced graphene oxide based magnetically separable nanocatalyst and its versatile catalytic activity towards multiple organic reactions. *RSC Advances.* **2016**, 6, 100 97941–97952.

4. D. Moitra, S. Dhole, B. K. Ghosh, M. Chandel, R. K. Jani, M. K. Patra, S. R. Vadera and N. N. Ghosh, Synthesis and Microwave Absorption Properties of $BiFeO_3$ Nanowire-RGO Nanocomposite and First-Principles Calculations for Insight of Electromagnetic Properties and Electronic Structures. *The Journal of Physical Chemistry C.* **2017***, 121, 39, 21290-21304.

5. D. Moitra, S. Hazra, B. K. Ghosh, R. K. Jani, M. K. Patra, S. R. Vadera and N. N. Ghosh, A facile low temperature method for the synthesis of $CoFe_2O_4$ nanoparticles possessing excellent microwave absorption properties. *RSC Advances.* **2015**, 5, 63, 51130–51134.

Publications not related to thesis

1.   D. Moitra, C. Anand, B. K. Ghosh, M. Chandel, N. N. Ghosh, 1-D $BiFeO_3$ nanowire-Reduced Graphene Oxide Nanocomposite as Excellent Supercapacitor Electrode Material. *ACS Applied Energy Materials.* **2018**, 1, 464−474.

2.   B. K. Ghosh, D. Moitra, M. Chandel, M. K. Patra, S. R. Vadera, N. N. Ghosh, CuO Nanoparticle Immobilised Mesoporous TiO_2 Cobalt Ferrite Nanocatalyst: A Versatile, Magnetically Separable and Reusable Catalyst. *Catalysis Letters.* **2017**, 147, 4, 1061–1076.

3.   B. K. Ghosh, D. Moitra, M. Chandel, H. Lulla, N. N. Ghosh, Ag nanoparticle immobilized mesoporous TiO_2-cobalt ferrite nanocatalyst: A highly active, versatile, magnetically separable and reusable catalyst. *Materials Research Bulletin.* **2017**, 94, 361–370.

4.   B. K. Ghosh, D. Moitra, M. Chandel, N. N. Ghosh, Preparation of TiO_2/Cobalt Ferrite/Reduced Graphene Oxide Nanocomposite Based Magnetically Separable Catalyst with Improved Photocatalytic Activity. *Journal of Nanoscience and Nanotechnology.* **2017**, 17, 7, 4694-4703.

5.   M. Chandel, B. K. Ghosh, D. Moitra, N. N. Ghosh, Barium Hexaferrite ($BaFe_{12}O_{19}$) Nanoparticles as Highly Active and Magnetically Recoverable Catalyst for Selective Epoxidation of Styrene to Styrene Oxide. *Journal of Nanoscience and Nanotechnology.* **2018**, 18, 5, 3478-3483.

6.   M. Chandel, B. K. Ghosh, D. Moitra, M. K. Patra, S. R. Vadera, N. N. Ghosh, Synthesis of Various Ferrite (MFe_2O_4) Nanoparticles and Their Application as Efficient and Magnetically Separable Catalyst for Biginelli Reaction. *Journal of Nanoscience and Nanotechnology.* **2018**, 18, 4, 2481-2492.

7.   B. Naik, D. Moitra, D. Dayananda, S. Hazra, B. K. Ghosh, S. V. Prasad, N. N. Ghosh, A facile method for preparation of TiO_2 nanoparticle loaded mesoporous γ-Al_2O_3: An efficient but cost-effective catalyst for dye degradation. *Journal of Nanoscience and Nanotechnology.* **2016**, 16, 8, 8544-8549.

Conferences:

1. D. Moitra, B. K. Ghosh, M. Chandel, R. K. Jani, M. K. Patra, S. R. Vadera and N. N. Ghosh, "Synthesis of a $Ni_{0.8}Zn_{0.2}Fe_2O_4$-RGO nanocomposite: an excellent magnetically separable catalyst for dye degradation and microwave absorber" *2nd INDO- UK INTERNATIONAL WORKSHOP ON ADVANCED MATERIALS AND THEIR APPLICATIONS IN NANOTECHNOLOGY (AMAN 2016)* BITS Pilani, KK Birla Goa campus January 11-12, 2016.

2. D. Moitra, M. Chandel, B. K. Ghosh, R. K. Jani, M. K. Patra, S. R. Vadera and N. N. Ghosh, "A Simple *'in situ'* Co-precipitation Method for Preparation of Multifunctional $CoFe_2O_4$-Reduced Graphene Oxide Nanocomposites: Excellent Microwave Absorber and Highly Efficient Magnetically Separable Recyclable Photocatalyst for Dye Degradation" *Royal Society of Chemistry (UK) West India Chapter Symposium on Recent Advancements in Chemical Sciences and Research Scholars' Meet-2016*, BITS Pilani, KK Birla Goa campus.

3. D. Moitra and N. N. Ghosh, 'Synthesis of BiFeO3 nanowire-Reduced Graphene Oxide based Magnetically Separable nanocatalyst and its Versatile Catalytic Activity towards Multiple Organic Reactions.' *2nd National Conference on New Frontiers in Chemistry From Fundamental to Applications (NFCFA 2015)*, BITS Pilani, KK Birla Goa Campus, 28-29 January, 2017.

BIO-DATA OF CANDIDATE

Personal details:

Name	Debabrata Moitra
Date of Birth	04-04-1985
Education	M.Sc. (Organic Chemistry)
	Assam University, Silchar (2009).
	B.Sc. (Chemistry)
	Alipurduar College, North Bengal University (2007).
Email	p20140403@goa.bits-pilani.ac.in

Scholarships and Awards:

i) Qualified entrance test of BITS Pilani, for institute research fellowship.

ii) (2nd Prize awarded for Poster Presentation) D. Moitra, M. Chandel, B. K. Ghosh, R. K. Jani, M. K. Patra, S. R. Vadera and N. N. Ghosh, "A Simple *'in situ'* Co-precipitation Method for Preparation of Multifunctional $CoFe_2O_4$-Reduced Graphene Oxide Nanocomposites: Excellent Microwave Absorber and Highly Efficient Magnetically Separable Recyclable Photocatalyst for Dye Degradation" *Royal Society of Chemistry (UK) West India Chapter Symposium on Recent Advancements in Chemical Sciences and Research Scholars' Meet-2016*, BITS Pilani, KK Birla Goa campus.

Publications during Ph.D Programme:

Total number of publications: 12

Listed in Appendix I.

BIO-DATA OF SUPERVISOR

Name	Dr. Narendra Nath Ghosh, FRSC (UK)
Current Position	Professor, Associate Dean for International Programmes and Collaboration, Department of Chemistry, Birla Institute of Technology and Science Pilani, K. K. Birla Goa Campus, City: Zuarinagar, State: Goa-403726, India.
Date of Birth:	01-01-1970
Education:	Ph. D. (Chemistry): IIT-Kharagpur (1999). M Sc (Chemistry): 1st Class-IIT-Kharagpur (1994).
Areas of Research:	(i) Nanostructured Magnetic materials (development of novel synthesis methodologies). (ii) Advanced catalysts (Mesoporous and nano-catalysts). (iii) Polymeric materials. (iv) Polymer-ceramic nano-composites (Novel preparation methods, Mechanical and Magnetic properties).

No. of Sponsored Research Projects

	(i) As PI:	11 (DST-UKIERI, DRDO, DST, BRNS, CSIR, UGC-DAE)
	(ii) As Co-PI:	04

No. of International journal Publications   88

No. of International conference proceedings   15

No. of Invited Book Chapter   7

No. of Invited Talks   11

Honors/Awards/Recognition

1.   Associate Dean for International Programmes and Collaboration.

2.   Fellow of Royal Society of Chemistry, UK.

3.   Visiting Professor in the School of Biomedical Sciences, University of Leeds, UK.

4. Visiting Research Professor in Chemical and Biological Engineering Department, Drexel University, USA.

5. Visiting Research Professor in Department of Chemistry, University of Tennessee Knoxville, USA.

6. Visiting Scientist Fellowship Award by "The Scientific and Technological Research Council of Turkey (TUBITAK)" 2006, 2009.

7. Member Expert in Chemistry for selection of candidates for Commonwealth Scholarship., UK Nominated by Ministry of Human Resource Development, Government of India.

8. Best Poster paper award "A Simple Chemical Technique for Synthesis of High Surface Area Mesoporous Silica Matrix and Iron-Oxide Incorporated Silicates" International Congress of Environmental Research (ICER 08) 2008.

9. Invited as Chairperson (for NANO-O9 and NANO-11 Sessions) in the 16th International Conference on Composites or Nano Engineering, ICCE-16, July 20-26, 2008 in Kunming, China.

10. Travel Grant Awards received from Indian National Science Academy, New Delhi, BITS- Pilani, Rajasthan, CSIR New Delhi, DST New Delhi. Appendix III.

11. Outstanding Scientist of 21st Century medal: Cambridge UK 2005.

12. Honorary appointment to the Research Board of Advisors of "The American Biographical Institute", USA. 2003.

13. Eminent Scientists of Today Medal by International Biographical Center Cambridge, U.K, 2002.

14. Biography has been published in several Who's Who in Science and Engineering from USA, UK.

15. The Royal Academy Of Engineering for Research Exchanges with China and India- Short Award for 2010.

16. Received a prestigious research grant under the DST UKIERI Thematic Partnership Scheme.